DISTRIBUTION STATEMENT A
Approved for Public Release
Distribution Unlimited

CHARACTERIZING THE PHYSICS OF PLANT ROOT GRAVITROPISM: A SYSTEMS MODELING APPROACH

by

THOMAS LYNN YODER, LtCol, USAF

B.S., United States Air Force Academy, 1982

M.S., University of Washington, 1983

M.S., Command and General Staff College, 1996

A 424 page thesis submitted to the

Faculty of the Graduate School of the

University of Colorado in partial fulfillment

of the requirement for the degree of

Doctor of Philosophy

DTIC QUALITY INSPECTED 4

Department of Aerospace Engineering Sciences

1999

19990907 171

REPORT DOCUMENTATION PAGE

Form Approved
OMB No. 0704-0188

Public reporting burden for this collection of information is estimated to average 1 hour per response, including the time for reviewing instructions, searching existing data sources, gathering and maintaining the data needed, and completing and reviewing the collection of information. Send comments regarding this burden estimate or any other aspect of this collection of information, including suggestions for reducing this burden, to Washington Headquarters Services, Directorate for Information Operations and Reports, 1215 Jefferson Davis Highway, Suite 1204, Arlington, VA 22202-4302, and to the Office of Management and Budget, Paperwork Reduction Project (0704-0188), Washington, DC 20503.

1. AGENCY USE ONLY *(Leave blank)*

2. REPORT DATE
3.Aug.99

3. REPORT TYPE AND DATES COVERED
DISSERTATION

4. TITLE AND SUBTITLE
CHARACTERIZING THE PHYSICS OF PLANT ROOT GRAVITROP

5. FUNDING NUMBERS

6. AUTHOR(S)
MAJ YODER THOMAS L

7. PERFORMING ORGANIZATION NAME(S) AND ADDRESS(ES)
UNIVERSITY OF COLORADO AT BOULDER

8. PERFORMING ORGANIZATION REPORT NUMBER

9. SPONSORING/MONITORING AGENCY NAME(S) AND ADDRESS(ES)
THE DEPARTMENT OF THE AIR FORCE
AFIT/CIA, BLDG 125
2950 P STREET
WPAFB OH 45433

10. SPONSORING/MONITORING AGENCY REPORT NUMBER
FY99-247

11. SUPPLEMENTARY NOTES

12a. DISTRIBUTION AVAILABILITY STATEMENT
Unlimited distribution
In Accordance With AFI 35-205/AFIT Sup 1

12b. DISTRIBUTION CODE

13. ABSTRACT *(Maximum 200 words)*

14. SUBJECT TERMS

15. NUMBER OF PAGES
424

16. PRICE CODE

17. SECURITY CLASSIFICATION OF REPORT

18. SECURITY CLASSIFICATION OF THIS PAGE

19. SECURITY CLASSIFICATION OF ABSTRACT

20. LIMITATION OF ABSTRACT

This thesis entitled:

Characterizing the Physics of Plant Root Gravitropism:

A Systems Modeling Approach

written by Thomas Lynn Yoder

has been approved for the Department of Aerospace

Engineering Sciences

_____

Paul Todd

_____

L. Andrew Staehelin

Date _____

The final copy of this thesis has been examined by the

signators, and we find that both the content and the form

meet acceptable presentation standards of scholarly work in

the above mentioned discipline.

Yoder, Thomas L. (Ph.D., Aerospace Engineering Sciences)

Characterizing the Physics of Plant Root Gravitropism: A Systems Modeling Approach

Thesis directed by Professor Paul Todd

Root gravitropism, a plant movement that keeps the root tip growing along the local gravity vector, is divided into three mechanisms; the gravity sensor, transduction, and differential growth. The gravitropic response has been duplicated with various mathematical constructs placed in series, but a coherent model based on systems engineering concepts does not exist. The goal of this research is to create models of the gravitropic sensor and differential growth response that are consistent with actual physical characteristics of these mechanisms. Additionally, a general feedback model of the overall response is created in order to infer characteristics within transduction.

The study initially establishes that the amyloplasts within the central columella cells of maize (*Zea mays* L.) are feasible gravity sensors; statoliths. Video-microscopy studies of live root cap sections were used to quantify the sedimentation dynamics of the putative statoliths. Extensive MATLAB analysis of amyloplast sedimentation indicates that an actin network interferes with the free sedimentation of the statoliths. This interference is most significant in the central region of the cell and less significant near the cell periphery including the cell's distal end. This central obstruction of actin creates a channeling behavior in all amyloplasts sedimenting through the cell's central region. The amyloplasts also appear to exhibit motions indicative of group action. Cytochalasin D mediates both the channeling and group behaviors, confirming that the

obstructive influence is indeed, at least in part, of actin origin. The video analysis methods produced a refined value for maize cytoplasmic viscosity. The diffusive motion of the statoliths in a vertical root appear insignificantly different than those oriented 10° to gravity, indicating that circumnutational oscillations may not be a result of root tip angle feedback.

Efforts to model the differential growth mechanism examined historical growth response data from numerous researchers. The RELEL (relative elemental elongation) approach to root growth applied to a model set analogous to bi-metallic bending is used to obtain the appropriate resolution for a model of this mechanism. Testing and analysis of the model highlights an extremely high sensitivity of curvature characteristics to all RELEL parameters. This sensitivity appears to be the reason for the large variety of deviations from "average" gravitropic responses that were seen both in the historical literature and in the 237 gravitropic responses accomplished for this research.

The newly observed gravitropic responses, along with historical data, are used to explore the gravitropic time response specifications as opposed to averaging individual time-curvature data into a single response. This approach highlights the significant disadvantages of time-averaging, low sampling rates, and a lack of frequency components being incorporated into the response. A single feedback "black box" model is created so that, along with the sensor and differential growth models, some inferences could be made about the elusive transduction mechanism. Both the current and historical gravitropic responses along with the inferences into transduction

indicate that the gravitropic mechanism is not a single-pathway system, but that at least 2 separate and parallel pathways exist within the system.

ACKNOWLEDGMENTS

The majority of this research was supported by NASA Grant NAG5-3967. Additional support including laboratory space, supplies, and training were provided by Professor L. Andrew Staehelin of the Molecular, Cellular, and Developmental Biology Department.

Several groups and individuals contributed significantly to this research. J. Genova of the BioServe Center for Space Commercialization aided in the design and supervised construction of all hardware required for this project. A graduate independent study in finite-element modeling was accomplished by B. Agoram and supervised by V. Barocas. Members of the Jones and Macintosh laboratories in the Molecular, Cellular, and Developmental Biology Department (MCDB) generously provided equipment, training, and software crucial for this project.

Thanks are extended to P. Todd, A. Staehelin, M. Balas, L.Stodieck, and D. Klaus for their support, guidance, and advice throughout this project. Additional thanks to A. Nebenfuhr and J. Meehl for their scientific and technical advice and assistance.

TABLE OF CONTENTS

ACKNOWLEDGMENTS vi
TABLE OF CONTENTS vii
LIST OF TABLES xi
LIST OF FIGURES xiii

CHAPTER 1 - INTRODUCTION AND METHODOLOGY 1-1
1.1 Introduction 1-1
1.2 Significance 1-7
1.3 Hypothesis and Objectives 1-8
1.4 The Quantitative Assumptions 1-11
1.4.1 The Columella Cell 1-11
1.4.2 Actin Parameters 1-13
1.4.3 Root Parameters 1-14
1.5 Thesis Organization 1-15
1.6 Summary 1-15

CHAPTER 2 - LITERATURE REVIEW 2-1
2.1 Introduction 2-1
2.2 Objective 2-2
2.3 Control Theory 2-2
2.4 The Gravitropic Response of Plants 2-15
2.4.1 The Sensor 2-23
2.4.1.1 Statoliths of the Columella Region 2-24
2.4.1.2 Studies of Agravitropic Lateral Roots 2-26
2.4.1.3 Studies of Starchless Amyloplasts 2-30
2.4.1.4 Results of Gravitational Research 2-37
2.4.2 The Differential Growth Response: The Elongation Zone 2-45
2.4.3 Transduction 2-49
2.4.3.1 The Role of Auxin 2-50
2.4.3.2 The Role of Calcium 2-57
2.4.3.3 Significance of Changes in Membrane Potential 2-62
2.5 Summary and Conclusions 2-66

CHAPTER 3 - THE GRAVITROPIC SENSOR 3-1
3.1 Introduction 3-1
3.2 Objective 3-4
3.3 Theory Development 3-9
3.3.1 Development of Statolith Feasibility 3-9
3.3.2 Development of a Force Balance Model 3-16
3.3.3 Development of a Second Order, Linear Equation of Motion 3-20
3.4 Experimental and Mathematical Procedures 3-26
3.4.1 Experimental Methods 3-26

3.4.2 Computational Techniques 3-32
3.5 Results 3-34
3.5.1 Analytical Results of the Force Balance Model 3-35
3.5.2 Observed Maize Amyloplast Sedimentation Dynamics 3-42
3.5.2.1 Amyloplast Sedimentation Position and Velocity Profiles 3-43
3.5.2.2 Quantification of Sedimentation Dynamics 3-48
3.5.2.3 Statistical Inferences from Sedimentation Studies 3-59
3.5.3 Viscosity Analysis and Diffusion Effects 3-72
3.5.4 Final EOM and Sensor Model Results 3-78
3.6 Discussion 3-88
3.7 Conclusions 3-91

CHAPTER 4 - CURVATURE BY DIFFERENTIAL ELONGATION 4-1
4.1 Introduction and Objective 4-1
4.2 Theory Development 4-2
4.2.1 Development of Elastic Curvature 4-5
4.2.2 Development of Plastic Curvature 4-6
4.3 Experimental and Mathematical Procedures 4-14
4.3.1 Experimental Methods 4-14
4.3.2 Computational Techniques 4-14
4.4 Results 4-18
4.4.1 Elastic Curvature: Experimental Results 4-18
4.4.2 Vertical Growth 4-19
4.4.3 Time-invariant, Gravistimulated Growth 4-22
4.4.3.1 Model Based on Two Averaged Data Sets 4-22
4.4.3.2 Sensitivity Analysis of RELEL Parameters 4-28
4.4.3.3 Model Based on Weighted Average of Selected RELEL Data 4-32
4.4.4 Time-variant, Gravistimulated Growth 4-34
4.4.5 Model of Circumnutation Effects 4-45
4.4.6 Transfer Function Model 4-50
4.5 Discussion 4-54
4.6 Conclusions 4-58

CHAPTER 5 - THE OVERALL GRAVITROPIC RESPONSE 5-1
5.1 Introduction 5-1
5.2 Objective 5-4
5.3 Theory Development 5-5
5.4 Experimental and Mathematical Procedures 5-13
5.4.1 Experimental Methods 5-14
5.4.2 Computational Techniques 5-18
5.5 Results 5-20
5.5.1 Historical Analysis Results 5-20
5.5.2 Current Experimental Results 5-31
5.6 Summary and Discussion 5-38
5.7 Conclusions 5-40

CHAPTER 6 - INFERENCES TO THE TRANSDUCTION MECHANISM 6-1
6.1 Introduction and Objective 6-1
6.2 Mathematical Techniques 6-2
6.3 Results and Discussion 6-5
6.3.1 Review and Discussion of Various s-Domain Models 6-5
6.3.2 Time-domain Characteristics of the Transduction Mechanism 6-10
6.3.3 Discussion of Possible Transduction Subsystems 6-16
6.4 Summary and Conclusions 6-22

CHAPTER 7 - SUMMARY AND CONCLUSIONS 7-1
7.1 Introduction 7-1
7.2 Overall Model 7-1
7.3 Sensor Model 7-3
7.4 Differential Growth Model 7-8
7.5 Inferences on Transduction 7-10
7.6 Summary 7-10
7.7 Conclusions 7-12

CHAPTER 8 - RECOMMENDED FURTHER RESEARCH 8-1
8.1 Introduction 8-1
8.2 Overall Model 8-1
8.3 The Sensor 8-4
8.5 Differential Elongation 8-5
8.6 Transduction 8-6
8.7 Summary and Conclusions 8-8

BIBLIOGRAPHY 8-9

APPENDIX I - MATLAB SCRIPT FILES FOR PROCESSING AMYLOPLAST SEDIMENTATION I-1
I.1 AMYLFALL.M I-1
I.2 AMYLFALL_SPEC.M I-27

APPENDIX II - MATLAB SCRIPT FILES FOR SIMULATING AMYLOPLAST SEDIMENTATION II-1
II.1 SEDIMENT.M II-1
II.2 STATE.M II-2

APPENDIX III - DERIVATION OF CURVATURE IN THE CANTILEVERED ROOT III-1

APPENDIX IV - DERIVATION OF ROOT THREE-POINT BENDING IV-1

APPENDIX V - DERIVATION OF CURVATURE DUE TO DIFFERENTIAL EXPANSION V-1

APPENDIX VI - MATLAB DIFFERENTIAL GROWTH AND RELEL SCRIPT FILES VI-1
VI.1 GROWTH.M VI-1
VI.2 RELEL.M VI-9
VI.3 RELEL_VERT.M VI-14

APPENDIX VII - PASCAL SOURCE CODE FOR PROCESSING EMPIRICAL ROOT CURVATURE RESPONSES VII-1

APPENDIX VIII - MATLAB SCRIPT FILES FOR CURVATURE RESPONSE ANALYSIS VIII-1
VIII.1 CURVEFIT.M VIII-1
VIII.2 TRANS_FUNC.M VIII-5
VIII.3 COMPENSATE.M VIII-7
VIII.4 AUTO_RESP_SPECS.M VIII-8

APPENDIX IX - DERIVATION OF PROPER 1-D CLINOSTAT PARAMETERS FOR MAIZE ROOTS IX-1

LIST OF TABLES

CHAPTER 1 - INTRODUCTION AND METHODOLOGY 1-1
Table 1.1 - Columella Cell Parameters 1-12
Table 1.2 - Derived Columella Cell Parameters 1-13
Table 1.3 - Actin Parameters 1-14

CHAPTER 2 - LITERATURE REVIEW 2-1
Table 2.1 - Performance Specifications 2-10
Table 2.2 - Growth Response Data 2-20
Table 2.3 - Elongation Rates of Maize Roots at Specific Times 2-21
Table 2.4 - Development of Lateral Root Columella Cells 2-29
Table 2.5 - Sweet Clover Columella Morphology Under Varying Gravitational Conditions 2-40
Table 2.6 - Elongation Rates and Level of IAA 2-56
Table 2.7 - Examination of the Electrical Properties of Gravistimulated Roots 2-65

CHAPTER 3 - THE GRAVITROPIC SENSOR 3-1
Table 3.1 - Summary of Statolith Velocity 3-61
Table 3.2 - Summary of t-Testing on Statolith Velocities 3-63
Table 3.3 - Summary of the Channeling Coefficient 3-65
Table 3.4 - Summary of t-Testing on Channeling Coefficient 3-65
Table 3.5 - Summary of the |x-Velocity| as a Function of x-Position 3-66
Table 3.6 - Summary of Group Behavior Formulations 3-69
Table 3.7 - Summary of t-Testing on Group Behavior Statistics 3-70
Table 3.8 - Summary of Velocity(μm/min.) as a Function of Vertical Position 3-71
Table 3.9 - Summary of t-Testing on Sector Velocities 3-72
Table 3.10 - Viscosity Analysis Summary 3-76
Table 3.11 - Diffusion Kinetics of the Maize Amyloplast 3-76
Table 3.12 - Vertical versus 10^0 Gravity Stimulated Statolith Movement 3-78

CHAPTER 4 - CURVATURE BY DIFFERENTIAL ELONGATION 4-1
Table 4.1 - RELEL Information 4-11
Table 4.2 - Elongation Rate Information 4-12
Table 4.3 - Deflection and Curvature on Cantilevered Roots 4-19
Table 4.4 - Barlow and Versel RELEL Data Processed for Simulation 4-23
Table 4.5 - Parameters Used in the Sensitivity Study 4-29
Table 4.6 - Results of Sensitivity Study 4-30
Table 4.7 - RELEL Parameters Obtained Through Weighted Average 4-33
Table 4.8 - Circumnutation Parameters 4-45

CHAPTER 5 - THE OVERALL GRAVITROPIC RESPONSE.....5-1
Table 5.1 - Order of Events During Gravitropism.....5-9
Table 5.2 - Summary of Time-domain Analysis on Graviresponses.....5-32
Table 5.3 - Summary of Significant t-Test Results.....5-34

CHAPTER 6 - INFERENCES TO THE TRANSDUCTION MECHANISM.....6-1
Table 6.1 - Derivation of $m_{effector}$ from Historical Data.....6-19

LIST OF FIGURES

CHAPTER 1 - INTRODUCTION AND METHODOLOGY 1-1
Figure 1.1 - Typical Control System for Space Heating 1-3
Figure 1.2 - Specialized Zones of Root Development 1-5

CHAPTER 2 - LITERATURE REVIEW 2-1
Figure 2.1 - Typical Control System 2-3
Figure 2.2 - The Spring-Mass-Damper System 2-4
Figure 2.3 - Horizontal Roots as a Step Function 2-7
Figure 2.4 - Example of a Root Gravitropic Response 2-7
Figure 2.5 - Dividing the Gravitropic System into Smaller Subsystems 2-9
Figure 2.6 - Relationship of Performance Specifications on the S-plane 2-11
Figure 2.7 - Elongation Rates During Root Graviresponse of Maize 2-21
Figure 2.8 - Possible Amyloplast-Cytoskeleton Interaction 2-43
Figure 2.9 - Specialized Zones of Root Development 2-46
Figure 2.10 - Indole-3-Acetic Acid (IAA) 2-51

CHAPTER 3 - THE GRAVITROPIC SENSOR 3-1
Figure 3.1 - Statolith Model 3-5
Figure 3.2 - Possible Models of Statolith-Cytoskeletal Interaction 3-7
Figure 3.3 - Flowchart for Objective #1 Accomplishment 3-8
Figure 3.4 - The Balance of Forces Acting on the Amyloplast 3-17
Figure 3.5 - Spring-Mass-Damper System 3-21
Figure 3.6 - Microscope Mount 3-30
Figure 3.7 - Coordinate System Used for Amyloplast Sedimentation Kinetics 3-32
Figure 3.8 - Simulated Amyloplast Dynamics - Initial Displacement Only 3-36
Figure 3.9 - Simulated Amyloplast Dynamics - TEXUS Experiment 3-39
Figure 3.10 - Simulated Amyloplast Dynamics - 1-g Gravity Only 3-41
Figure 3.11 - Distal-to-Side Sedimentation Profile of 7 Plastids 3-43
Figure 3.12 - Side-to-Side Sedimentation Profile of 9 Plastids 3-44
Figure 3.13 - Distal-to-Basal Sedimentation Profile of 7 Plastids 3-45
Figure 3.14 - Distal-to-Side Velocity Profile 3-46
Figure 3.15 - Side-to-Side Velocity Profile 3-47
Figure 3.16 - Distal-to-Basal Velocity Profile 3-48
Figure 3.17 - Channeling Behavior Formulation #1 3-51
Figure 3.18 - Channeling Coefficient with Specificity 3-52
Figure 3.19 - Channeling Behavior Formulation #2 3-54
Figure 3.20 - Group Behavior Test Formulation #1 3-56
Figure 3.21 - Group Behavior Formulation #2 3-57
Figure 3.22 - Vertical Velocity as a Function of Vertical Position 3-59
Figure 3.23 - Identifying an Unobstructed Statolith during Sedimentation 3-75
Figure 3.24 - Network Model Set 3-80
Figure 3.25 - Actin Grid Forces 3-82

Figure 3.26 - Network Model Dynamics with 3% Actin by Volume.....3-83
Figure 3.27 - Finite-element Model of Falling Amyloplasts.....3-85
Figure 3.28 - Amyloplast Group Effect on the Actin-Grid Model 3-86
Figure 3.29 - 1st-Order, s_Domain Model for Tension Redistribution.....3-88

CHAPTER 4 - CURVATURE BY DIFFERENTIAL ELONGATION.....4-1
Figure 4.1 - Differential Elongation Produces Curvature 4-2
Figure 4.2 - Flowchart for Chapter Four Objective.....4-4
Figure 4.3 - Changes in Curvature with Model Resolution.....4-8
Figure 4.4 - Overall Elongation Rates on the Top and Bottom of the Maize Root..4-13
Figure 4.5 - Vertical Growth RELEL Model.....4-20
Figure 4.6 - Vertical Root Growth Simulation.....4-21
Figure 4.7 - A Gravistimulated RELEL with Two Averaged Data Sets.....4-24
Figure 4.8 - The RELEL Surface Curve Interpreted 4-25
Figure 4.9 - Further Interpretation of the RELEL Surface Curve.....4-26
Figure 4.10 - Root Curvature for Two Averaged Data Sets.....4-27
Figure 4.11 - Explanation of the S-shape Curvature Effect 4-28
Figure 4.12 - Eliminating the S-shaped Growth Characteristic.....4-31
Figure 4.13 - Root Curvature for Weighted Average Data Sets 4-34
Figure 4.14 - Root Curvature for Time-variant, Weighted Average Data Sets.....4-36
Figure 4.15 - RELEL Surface Plots for Selected Times of Time-variant Model 4-38
Figure 4.16 - RELEL Maximum ($RELEL_{max}$) Time History.....4-40
Figure 4.17 - RELEL Position (μ) Time History.....4-41
Figure 4.18 - RELEL Standard Deviation (σ) Time History 4-42
Figure 4.19 - RELEL Surface Plots for Selected Times of Empirical Model 4-43
Figure 4.20 - Root Curvature for Time-variant, Empirical Model 4-44
Figure 4.21 - Circumnutations on a Vertical Root 4-47
Figure 4.22 - Circumnutating Gravitropic Response Rates and Curvature.....4-48
Figure 4.23 - Circumnutating Gravitropic Root 4-49
Figure 4.24 - S-domain Model of Circumnutating, Vertical Root.....4-50
Figure 4.25 - S-domain Model of Graviresponding Root 4-51
Figure 4.26 - S-domain Model of Both Circumnutation and Gravitropism 4-53

CHAPTER 5 - THE OVERALL GRAVITROPIC RESPONSE.....5-1
Figure 5.1 - Simple Imitative Model Time-Response Curve.....5-2
Figure 5.2 - Flowchart for Objective 3.....5-5
Figure 5.3 - Simple Model Set for Gravitropism.....5-7
Figure 5.4 - Model Set with Further Details 5-8
Figure 5.5 - Dual Path Model Set for Gravitropism 5-11
Figure 5.6 - The Plant Growth Chamber/Shadow Box (GC/SB) 5-16
Figure 5.7 - Measurement of the Root Cap Angle 5-17
Figure 5.8 - Maize Merit Graviresponse Curve.....5-21
Figure 5.9 - Curve Matching with Residuals for Maize Merit.....5-22
Figure 5.10 - Transfer Function Fit to Maize Merit Data 5-23
Figure 5.11 - Frequency Analysis of the Maize Merit Data 5-25

Figure 5.12 - Maize Merit as Higher Order Transfer Functions.....5-27
Figure 5.13 - Low Sampling Rate Problem.....5-29
Figure 5.14 - Time-Averaging with Offset Initial Conditions.....5-30
Figure 5.15 - Yellow Dent Overall Model.....5-36
Figure 5.16 - Frequency Components of the Yellow Dent Model.....5-37
Figure 5.17 - Block Diagram Conversion of s-Domain Model.....5-39

CHAPTER 6 - INFERENCES TO THE TRANSDUCTION MECHANISM.....6-1
Figure 6.1 - Development of the Transduction Model.....6-3
Figure 6.2 - Differential Growth Gravitropic - Step Response OLTF.....6-7
Figure 6.3 - Overall, Closed-Loop Model Step Response.....6-10
Figure 6.4 - Summary of s-Domain Models.....6-11
Figure 6.5 - Complete Open-Loop Differential Growth Model.....6-13
Figure 6.6 - Open-Loop Transduction Dynamics.....6-14
Figure 6.7 - Altered Open-Loop Transduction Dynamics.....6-16
Figure 6.8 - Proposed Ionic Signal Properties.....6-20

CHAPTER 7 - SUMMARY AND CONCLUSIONS.....7-1
Figure 7.1 - The Evolving Model of Plant Root Gravitropism.....7-11

CHAPTER 8 - RECOMMENDED FURTHER RESEARCH.....8-1
Figure 8.1 - Circumnutations During Gravitropism.....8-7

CHAPTER 1

INTRODUCTION AND METHODOLOGY

1.1 Introduction

The ability of plants to detect and respond to gravity is an essential characteristic for their survival. On Earth, the plant must direct its emerging roots downward in order to acquire the best possible chance of obtaining moisture and nutrients. When a seed germinates in any position other than with its root directly downward, the root and stem undergo a gravitropic response. Statoliths (gravity-sensing organelles) within the root cap respond to the gravitational force and, through a process that is yet not fully understood, induce differential growth along the root's elongation zone so that the root curves toward the downward direction. Research to date suggests that the statoliths perceive the off-vertical gravity signal by altering the tension and/or position of the cell's cytoskeletal components. This alteration produces a cascade of ion activity and cellular changes that leads to the differential growth pattern. Cells on the top side of the root elongate rapidly while those below are inhibited from growth. The general goal of this study is to model the plant root gravitropic response using classical controls and system identification principles. Specific objectives of this research include:

(1) the development of a mathematical model of the physical principles governing the plant root gravity sensor (the statolith),

(2) the development of a mathematical model for the differential growth response within the plant root's elongation zone,

(3) the development of an overall (gravity input-to-curvature output) model through empirical analysis, and

(4) the development of a model for the transduction mechanism through block diagram reduction.

A brief review of the literature pertinent to the objectives of this thesis follows while a thorough literature review of plant gravitropism is found in Chapter 2 of this thesis. It is most likely that the plant root gravitropic response is a closed loop regulatory process. Although immensely more complex, this control system is similar to a typical home heating system shown in Figure 1.1. When the occupants get cold they turn up the reference temperature on the thermostat. This creates a differential between the sensed temperature and the requested temperature and therefore produces a non-zero control signal that turns on the furnace. The furnace flame produces a very high temperature in the combustion chamber that must then be distributed or "transduced" to the rest of the house. The distribution mechanism which includes the circulation fan, the ducting system, and various forms of heat transfer will eventually result in a temperature increase at locations throughout the house which again is received by the temperature sensor in the thermostat. When the temperature equals the reference temperature, the control signal is returned to zero and the furnace shuts off.

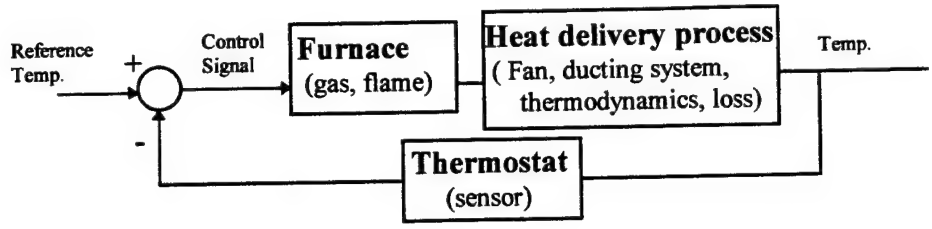

Figure 1.1 - Typical Control System for Space Heating

The gravitropic curvature of a horizontally placed root is the result of differential growth between the root's upper side and lower side. Specifically, to curve downward the upper side must have a higher growth rate than the lower side. This can be achieved in a variety of ways: (1) growth acceleration along the upper side; (2) growth inhibition of the lower side; (3) both (1) and (2); or (4) a combination of accelerations and inhibitions on opposite sides that result in the observed redirected growth (Konings, 1995).

In 1987, Selker and Sievers showed that roots develop a positive curvature by accelerating growth on the top side and diminishing growth on the bottom side in comparison to vertically growing controls. Their work used intact roots of *Lepidium sativum* which were photographed at 1.5-6 min. intervals before and after being tilted from a vertical to a horizontal position (Selker & Sievers, 1987). Further work with maize (*Zea mays*) was accomplished by Barlow *et al.* in 1993 who compared the steady-state properties of the graviresponse to the amplitude of the input signal (the size of the angle of displacement from vertical). Primary roots of maize were oriented at various angles from the vertical ranging from 90 to 1 degrees and their subsequent bending was analyzed from filmed records. The maximum rate of bending and the

time before onset of bending both varied two-fold, but showed no correlation with the initial angle of tip displacement (Barlow *et al.*, 1993). Roots oriented to small initial angles (<40 deg.) often overshot the vertical and proceeded to oscillate around this orientation, whereas roots oriented to large initial angles (>60 deg.) often failed to achieve the vertical. Roots in this latter group resumed bending after an indeterminate time, or did so immediately after a second displacement of their tip, showing that they were not intrinsically unable to bend.

From the viewpoint of the controls analyst, the perception of the gravity signal is accomplished by one or more sensors. The classical postulation for a gravity sensor within the root is the starch-statolith hypothesis. "Statolith" comes from the Greek *statos*, meaning "standing" or "placed" and the Greek *lithos*, meaning "stone". This stone (or mass) that stands (or seeks) gravity has long been held as the gravity sensor within the plant root. Since 1901, the amyloplasts of the root cap's columella region have been postulated as the root's statoliths. Early investigations showed that these starch-filled plastids were the only organelle that consistently sedimented in response to a gravity signal. Experiments accomplished throughout the 1970's and 1980's continued to support the idea that the amyloplasts acted as statoliths within the columella cells of the central root cap. These columella cells are dubbed statocytes; cells with statoliths. These experiments correlated the motion of the amyloplasts with the graviresponse. First, close correlation was found between the presence of the sedimenting amyloplasts within the root cap and the root's ability to exhibit gravitropism. Second, the presentation time of a root's graviresponse was closely

correlated with the sedimentation time of the amyloplasts (Salisbury & Ross, 1992b). In 1985, Sack *et al.* measured amyloplast sedimentation kinetics in roots of *Zea mays* L.. Initial sedimentation velocities were found to be 19.1 μm/min. at 5.9 seconds (Sack *et al.*, 1985).

In 1995, Ishikawa and Evans defined specialized regions of the plant root that are extremely useful in dividing the root's gravitropic control system into manageable pieces. Their morphological descriptions of the root included the cap, apical meristem, the cell elongation zone, and the maturation zone (Ishikawa & Evans, 1995). Their morphological definitions of the root zones are summarized in Figure 1.2.

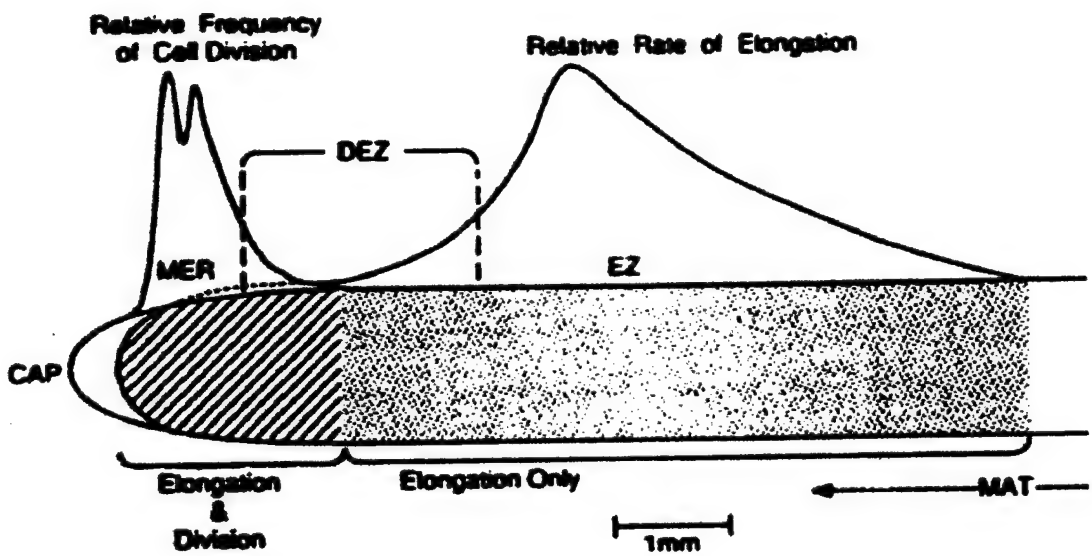

Figure 1.2 - Specialized Zones of Root Development
Relative rates of cell division and cell elongation are shown from the root cap (CAP), through the meristem region (MER), into the elongation zone (EZ), and, finally, into the maturation zone (MAT). The distal elongation zone (DEZ) is shown as a continuum between the meristem and elongation zones. Scale is appropriate for a typical root of maize (Ishikawa & Evans, 1995).

In 1991, Ishikawa *et al.* used computer-based digitized video to analyze the gravitropic response in maize roots. The study found that a major factor causing the downward curvature during graviresponse is the induction of a very rapid elongation of cells in the DEZ on the top side of the root. The rate of elongation in these cells prior to gravistimulation is low with the majority of elongation occurring in the more basal portions of the elongation zone. In contrast, the rate of elongation of cells in this main portion of the elongation zone is inhibited by gravistimulation, especially in those cells on the bottom portion of the root (Ishikawa *et al.*, 1991).

The transduction mechanism which receives the gravity signal perceived by the sensor and eventually induces the differential growth response within the DEZ and elongation zone is most elusive of the three mechanisms that make up the gravitropic system. Transduction involves a complex chain of biochemical signals, with, more than likely, some signals operating in parallel to others. Much work in the field of molecular biology is required to piece together the structure and chemistry of this mechanism. Some components of this structure and chemistry are presumed. Auxin is believed to be the primary agent for differential growth (Taiz & Zeiger, 1991). At a microscopic level, the auxins create membrane hyperpolarization and by stimulating the plasma membrane's H^+ ATPase, creates cell wall acidification. This brings about cell wall loosening and promotes elongation growth in these tissues (Millner, 1995). Indole-3-acetic acid (IAA) is the most important of the naturally occurring hormones in the gravitropic process. Much evidence exists pointing to IAA as the growth response effector (Bandurski *et al.*, 1984; Lee *et al.*, 1984; Evans *et al.*, 1986;

McClure & Guilfoyle, 1989; Cosgrove, 1990; Nick *et al.*, 1990; Young *et al.*, 1990; Evans, 1991). Calcium and membrane potentials are also most certainly involved with the transduction mechanism (Lee *et al.*, 1983; Lee *et al.*, 1983; Lee *et al.*, 1984; Moore, 1986; Moore *et al.*, 1987; Stinemetz *et al.*, 1987; Hasenstein & Evans, 1988; Leopold & Wettlaufer, 1988; Wendt & Sievers, 1989; Wayne *et al.*, 1990; Bjorkman & Cleland, 1991; Ishikawa & Evans, 1992; Suzuki *et al.*, 1994; Zieschang & Sievers, 1994).

1.2 Significance

The ability of plants to sense and respond to gravity is essential for their survival. The graviresponse of the roots of various species has been well documented, but a coherent view of the underlying mechanisms that sense the gravity input, transduce this signal to the growth zone of the root, and produce the eventual curvature continues to elude investigators. The significance of this research lies in bringing a systems approach to the problem of identifying the mechanisms underlying the root gravitropic response. There have been numerous attempts to create imitative mathematical models (Stockus, 1994), but this research takes gravitropism and separates it into subsystems with various levels of definition and applies modeling to those systems that are fairly well defined. While imitative models can be adjusted to correlate extremely well with the gravitropic response, they give no insight into the underlying mechanisms nor do they build a broad picture of the actual systems at work to create the gravitropic curvatures. This research uses a systems approach that allows the overall gravitropic mechanism to be broken into smaller systems with model

sets (general forms) that match the actual biology and engineering behind the system. This systems approach creates insight into the overall design and interaction of the various mechanisms (known and unknown) that act together to produce the gravitropic response. Specifically, this research provides the general model set and parameter identification for the putative gravitropic sensor, the columella cell, and shows that the gravitropic response is the result of parallel path of mechanisms.

Knowledge of the mechanisms underlying gravitropism can lead to the eventual control and exploitation of these mechanisms to optimize secondary metabolite production and overexpress beneficial biochemical pathways within the plant. Finally, the understanding and eventual control of the plant root gravitropic response will greatly reduce the design challenges associated with microgravity applications requiring prolific plant growth such as in Controlled Ecological Life Support Systems (CELSS).

1.3 Hypothesis and Objectives

The hypothesis underlying this thesis is that the gravitropic response of plant roots can be effectively modeled using control theory and system identification techniques. A gravitropic response is initiated in a germinating seedling when the seed germinates in any position other than with its root directly downward. Currently, it is believed that starch-filled plastids, amyloplasts, within the root cap act as the plant's statoliths (gravity-sensing organelles). Sedimentation of the amyloplast "detects" the gravity signal and through a cascade of other, less understood mechanisms, the signal is transduced into a pattern of differential growth along the root's elongation zone.

The end result is that the root curves toward the downward position. A similar mechanism operates in a complementary fashion to direct the emerging shoot opposite the gravity vector. Research to date suggests that the statoliths perceive the off-vertical gravity signal by altering the tension and/or position of the cell's cytoskeletal components. This alteration produces a cascade of ion activity and biochemical changes that leads to the differential growth pattern. Cells on the upper side of the root elongate rapidly while those on the lower side of the root are inhibited from growth. The application of classical control and system identification techniques to the study of this complex perception-transduction-reaction mechanism has been extremely limited. At question is whether the use of such techniques can provide the necessary insights into the electromechanical and biochemical apparatuses that comprise the gravitropic response. The general goal of this study is to model the gravitropic response of the plant root through development of a series of models associated with the three phases of the response: perception, transduction, and growth response. This development requires the following specific objectives:

Objective 1. Develop a mathematical model of the physical principles governing the plant root's putative gravity sensor.

Objective 2. Develop a mathematical model of the plant root's differential elongation and curvature.

Objective 3. Develop an empirical model of the plant root's overall gravitropic response.

Objective 4. Develop a "black-box" model of the plant root's transduction mechanisms.

Of all the mechanisms modeled in this work, Objective 1 involves the most quantitative identification of parameters. A free body diagram of the putative gravity sensor, the root cap's columella cell, is developed. Force balance analysis is performed on the model to produce the sensor's equations of motion and these are analyzed using state space techniques. The sedimentation dynamics of the putative gravity-sensing mass, the amyloplast, was analyzed to develop velocity and acceleration profiles for the amyloplasts. The data are used to develop and confirm the accuracy of the proposed model.

Based upon purely historical empirical data, Objective 2 requires the use of plate and shell theory and differential elongation data from past experimenters. A model is developed that describes curvature for a given differential elongation within the cells of the root's elongation zone. The model development includes differential elongation for a given gradient of auxin.

Objective 3 requires the use of MATLAB's System Identification and Controls toolboxes along with both historical and current gravitropic response data. Appropriate empirical models are constructed for the complete response. Current gravitropic response data are acquired using maize seedlings in various stages of development to bring a more robust nature to this model.

Objective 4 creates a inferred model of transduction from the results of Objectives 1 through 3 detailed in preceding paragraphs. By applying the

mathematical model for the sensor from objective (1) and the mathematical model for the final growth response from objective (2) to the overall model achieved in objective (3), a simple input/output model (the transfer function) of the root's transduction processes is obtained. Inferences are drawn as to the most likely chain of biochemical/molecular mechanisms that could produce the response function identified by this model.

1.4 The Quantitative Assumptions

To model various components of the gravitropic mechanism, certain parameters as to the morphology of the various cells, organelles, and biochemical reactions are assumed. Numerous laboratory results over the years have produced varied estimates of these morphological values, but these were chosen because of their specificity to corn, the weight of their statistical significance, and confirmation from secondary sources. This section is broken into three sections which separately document the assumed parameters concerning columella structure, the structure of actin, and the whole root structure.

1.4.1 The Columella Cell

Table 1.1 details the general morphology parameters of the corn columella cell. These values primarily come from some very detailed work accomplished by Randy Moore at Baylor University, Texas.

Table 1.1 - Columella Cell Parameters

Item	Value	Reference
Cellular Volume	17900 μm^3	(Moore, 1986)
Inferred Dimensions:	*(estimated from volume above)*	
Height (distal-basal)	33.2 μm	
Width (side-side)	23.2 μm	
Depth (posterior-anterior)	23.2 μm	
Relative volume of amyloplasts	7.57 %	(Moore, 1986)
Number of amyloplasts	29	(Moore, 1986)
V_{amyl} - Volume of single amyloplast	28 μm^3	(Moore, 1986)
s - Starch volume in amyloplast	66 %	(Moore, 1986)
ρ_{cyto} - Cytoplasmic density	1.015 g/cm^3 1.015×10^3 kg/m^3	(Wayne *et al.*, 1990) (Bjorkman, 1988)
ρ_{starch} - Starch density	1.5 g/cm^3	(Wayne *et al.*, 1990) (Leach & Schoch, 1961)
ρ_{stroma} - Stroma density	1.1 g/cm^3	(Robinson, 1985)
η - Cytoplasmic viscosity	1-20 cp 1-20 $\times 10^{-3}$ Pa-s 1-20 $\times 10^{-9}$ kg/μm-s	(Sack *et al.*, 1985)
g - gravity acceleration of 1 g	9.81 m/s^2	

Other parameters are initially derived from these basic values. This research assumes that the amyloplast is a spherical body with a volume defined by equation 1-1.

$$V_{amyl} = \frac{4}{3}\pi r_{amyl}^{\ 3} \tag{1-1}$$

This assumption allows computation of the amyloplast radius (r_{amyl}). Both the stroma density and starch density along with the relative volume (RV) of starch to stroma in the amyloplast is required to compute the total density of the amyloplast as shown in Equation 1-2.

$$\rho_{amyl} = (RV)_{starch} * \rho_{starch} + (RV)_{stroma} * \rho_{stroma} \tag{1-2}$$

The mass of the amyloplast is then computed using Equation 1-3.

$$m_{amyl} = V_{amyl} * \rho_{amyl} \tag{1-3}$$

Table 1.2 summarizes the results of these initial parameter computations.

Table 1.2 - Derived Columella Cell Parameters

Parameter	Value
r_{amyl} - radius of amyloplast	1.884 μm
ρ_{amyl} - density of amyloplast	1.364 g/cm^3 1.364x10^{-15} kg/μm^3
$\Delta\rho$ - difference between amyloplast and cytoplasmic densities	3.49x10^{-16} kg/μm^3
m_{amyl} - mass of amyloplast	3.82x10^{-14} kg

1.4.2 Actin Parameters

Table 1.3 summarizes the structural parameters assumed in this thesis to apply to the actin fiber. Calculation of Young's Modulus (E) assumes homogeneity in the structure of the actin fiber. This, of course, is not precisely accurate since the F-actin fiber is composed of a helix of G-actin molecules each consisting of a polypeptide 375 amino acids long (Alberts *et al.*, 1994). But, since the scale of motion and deformation applied to this structure is many orders a magnitude larger than the size of these peptides, the assumption of homogeneity is acceptable. The cross-section of the actin fiber is assumed to be elliptical with a moment of inertia (I) defined by the equations 1-4 and 1-5. The $I_{average}$ for the entire elliptical cross-section is assumed to be the average of the two values; I_1 - flex along the major axis and I_2 - flex along the minor axis.

$$I_1 = ab^3 \frac{\pi}{4} \text{ ; a, b - semimajor, semiminor axis} \tag{1-4}$$

$$I_2 = a^3 b \frac{\pi}{4} \text{ ; a, b - semimajor, semiminor axis} \tag{1-5}$$

Table 1.3 - Actin Parameters

Parameter	Value	Reference
EI - Structural Rigidity	7.29×10^{-26} Nm^2	(Gittes *et al.*, 1993)
r - radius of actin fiber r_a - semimajor axis r_b - semiminor axis	4 nm 4.5 nm 3 nm 2 nm	(Alberts *et al.*, 1994) (Janmey *et al.*, 1991) (Gittes *et al.*, 1993)
elliptical area ($\pi r_a r_b$)	1.88×10^{-5} μm^2	derived
average maximum length	17.7 μm	(Gittes *et al.*, 1993)
maximum strain to rupture	<20%	(Janmey *et al.*, 1991)
I_1 ($r_a r_b^3 \pi/4$)	1.89×10^{-35} m^4	derived
I_2 ($r_a^3 r_b \pi/4$)	4.24×10^{-35} m^4	derived
I_{avg}	3.07×10^{-35} m^4	derived
E_1 - Young's Modulus E_2 E_{avg}	3.87 GPa 1.72 GPa 2.8 GPa	derived " "

1.4.3 Root Parameters

The parameters and assumptions involving the root as a whole are based on a typical 20-30 mm maize root. The cap, meristem, distal elongation zone, elongation zone, and maturation zone are the general regions traversed while moving from the root tip to the seed. The cap is less than a millimeter in length, with the elongation zone nearly 3 millimeters from the root tip. Growth parameters for various regions of the root are quite extensive and are both spatially and temporally dependent. Because of this complexity, the assumptions used for the root growth parameters are introduced in Chapter 4 as the differential growth model is developed.

1.5 Thesis Organization

Organization of this dissertation follows the objectives listed in Section 1.3. Following this introductory chapter, Chapter Two reviews the current literature pertaining to the state of research into plant root gravitropism. Chapters Three through Six detail the methodology, results, and discussion pertaining to Objectives 1 through 4. Chapter Seven summarizes the conclusions of the research and Chapter Eight highlights the directions for future research.

1.6 Summary

This thesis approaches the task of modeling the plant root gravitropic mechanism not from a imitative approach, but from a systems engineering approach. Instead of creating mathematical functions that imitate the results of gravitropism, models are developed based on what is known of the underlying physics and processes at work in the plant. The task is not trivial, since data are still missing, especially for many events in the transduction pathways. This thesis builds on what is known, adds some new findings, and begins the process of modeling gravitropism based on the processes actually occurring within the root tip. Based on this spectrum of what is known and what is not known, individual models for the various pieces of the entire gravitropic response are developed to various resolution. The results of this "first brush" while not complete, provide an excellent starting point for further refinement and increased model resolution.

CHAPTER 2

LITERATURE REVIEW

2.1 Introduction

The ability of plants to detect and respond to gravity is vital for their survival. Plants respond to the Earth's gravity field by redirecting growth of their roots toward gravity and redirecting growth of their shoots opposite to the gravity vector. This ensures that the root penetrates into regions that ensure its best chance to gather nutrients and water. The shoot grows to ensure its best chance to receive light energy. Responding to the local gravity signal requires the plant to have a control system that can detect the signal, transduce the signal to the area of the plant where growth occurs, and, finally, produce a growth response that redirects the root appropriately with the growth response ending when the root is growing toward gravity. Detection of the signal requires a sensor that can detect gravity or the contact forces, tensions, or pressures that result from the organism being in a gravity field. This sensor must be able to detect the gravity signal to a specific level of sensitivity and also detect it through a background of interfering noise such as thermal activity in the cytoplasm of the organism. Transduction of the signal to the growth region of the plant is most likely accomplished by a cascade of primary and secondary biochemical messengers. The gravitropic response of plant roots has been the subject of innumerable experiments over the past 100 years, but a coherent knowledge of the complete regulatory system involved with this tropism still eludes the scientific community.

2.2 Objective

The objective of the research described in this thesis consists of establishing a paradigm that uses modern control theory techniques to analyze the plant gravitropic system. By dividing the entire gravitropic system into small "blocks" and using the myriad of gravitropic data available to model those blocks, insights into the model viability or modifications to whole root gravitropic models can be attained.

2.3 Control Theory

It is most likely that the plant root gravitropic response is a closed loop regulatory process. Although immensely more complex, this control system is similar to a typical home heating system shown in Figure 2.1. When someone gets cold they turn up the reference temperature on the thermostat. This creates a differential between the sensed temperature and the requested temperature and therefore produces a non-zero control signal that turns on the furnace. The furnace flame produces a very high temperature in the combustion chamber that must then be distributed or "transduced" to the rest of the house. The distribution mechanism which includes the circulation fan effects, the ducting system, and various applications of thermodynamics will eventually result in a temperature increase at locations throughout the house which again is received by the temperature sensor in the thermostat. When the temperature equals the reference temperature, the control signal is returned to zero and the furnace shuts off.

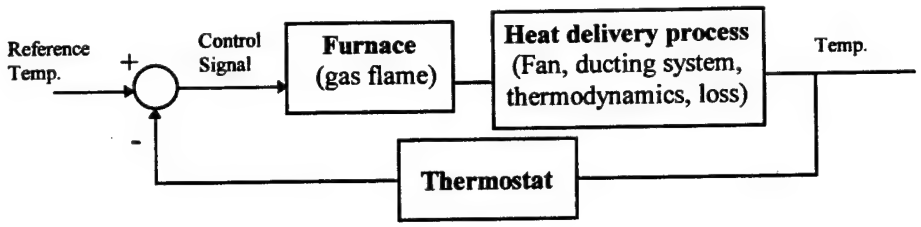

Figure 2.1 - Typical Control System

The application of control theory to the mechanism of plant root gravitropism is a logical step in the decades of research accomplished on this plant response. The field of "controls" provides a large array of analysis and modeling techniques that has been historically applied to areas ranging from machination and traffic control to robotics and medical instrumentation. Application of control theories to biological processes such as the function and regulation of the heart have given us many insights into the inner workings of such complex physiological regulatory mechanisms (Milhorn, 1966). Since this thesis will apply controls analysis to the mechanism of root gravitropism, this section outlines some of the important background of control theory and analysis techniques.

Controls analysis can proceed in two general directions. If the dynamics and processes of the mechanism under investigation are known, then this system is modeled and controls techniques are used to study the response of the system to various stimuli and develop what steps can be taken to modify the system to act in a desired way. Alternatively, if the system is unknown, controls techniques known as "system identification" attempt to develop a working description of the system and

gain insight into the hidden structures and dynamics within the mechanism. The following paragraphs outline the analysis tools in these two different approaches.

If the system under investigation has a known structure, controls analysis may begin by defining the system with differential equations. Figure 2.2 shows the classic spring-mass-damper system.

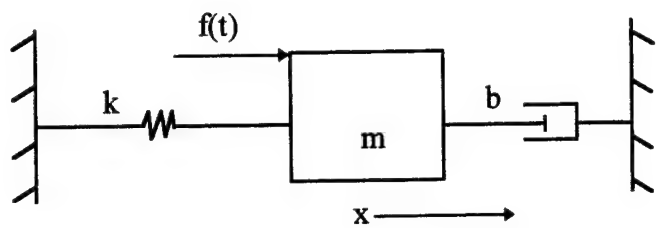

Figure 2.2 - The Spring-Mass-Damper System

This system is easily described by summing the forces in the x-direction and equating to the (mass x acceleration) along that axis according to Newton's Second Law:

$$\sum F_x = ma_x$$
$$\equiv m\ddot{x}$$

The spring constant (k), in MKS units (kg/s^2), provides an opposing force to any displacement along the x-axis. The damping constant (b), in MKS units (kg/s), provides an opposing force to any velocity along the x-axis. The force, f(t), is any externally applied force along the x-axis.

$$\sum F_x = m\ddot{x}$$
$$-F_{spring} - F_{damper} + f(t) = m\ddot{x}$$
$$f(t) - kx - b\dot{x} = m\ddot{x}$$

$$\therefore \quad \ddot{x} + \frac{b}{m}\dot{x} + \frac{k}{m}x = f(t) \qquad (2\text{-}1)$$

Therefore, the differential equation [2-1] describes the motion of the system. Given any values for f, b, and k along with the system's initial conditions, the position, velocity, and acceleration of the system can be computed. The solution of this second-order, linear differential equation is developed as follows:

$$x(t) = x_h + x_P$$

where, x_h - homogeneous solution

x_p - particular solution

The homogeneous solution is the solution with the forcing function, f(t), set to zero while the particular solution is the response due to the forcing function. They can simply be added for the complete solution because the differential equation is linear. For the homogeneous solution, the roots of the auxiliary equation, $r^2 + \frac{b}{m}r + \frac{k}{m} = 0$, are found. This polynomial has two roots (r_1,r_2) and the form of these roots drives the form of the system's response. The roots may be distinct real, repeated real, or complex conjugate.

$$x_h = c_1 e^{r_1 t} + c_2 e^{r_2 t} \text{ ; for distinct real roots}$$

$$x_h = c_1 e^{r_1 t} + c_2 t e^{r_2 t} \text{ ; for repeated real roots}$$

$$x_h = e^{at}(c_1 \cos(bt) + c_2 \sin(bt)) \text{ ; for complex conjugate roots } a \pm bi$$

Coefficients c_1 and c_2 are found given system initial conditions. The x_p solution depends on the form of f(t) and is found through a variety of methods such as variation of parameters or undetermined coefficients. For example, for b=5 kg/s, m=1 kg, k=6 kg/s, and $f(t)=e^{-t}$:

$$\ddot{x} + \frac{b}{m}\dot{x} + \frac{k}{m}x = f(t)$$

$$\ddot{x} + 5\dot{x} + 6x = e^{-t}$$

$$r^2 + 5r + 6 = 0 \text{ ; } r_1 = -3,\ r_2 = -2$$

$$\therefore \quad x_h = c_1 e^{-3t} + c_2 e^{-2t} \quad \Leftarrow$$

$$x_p = ke^{-t}$$

$$ke^{-t} + 5(-ke^{-t}) + 6(ke^{-t}) = e^{-t}$$

$$(k - 5k + 6k) = 1$$

$$2k = 1 \;\; ; \;\; k = 1/2$$

$$\therefore \;\; x_p = \frac{1}{2}e^{-t} \;\; \Leftarrow$$

$$\therefore \;\; x(t) = c_1 e^{-3t} + c_2 e^{-2t} + \frac{1}{2}e^{-t}$$

The family of curves given by the solution provides a means with which to analyze and predict the response of this simple system. This approach to system description is only useful if the system is known. Also, one can easily see that as the complexity of the system increases beyond this point, a differential equation description becomes burdensome.

Another basic tool of control theory is the transfer function (TF). The TF is a ratio of the system's output to its input given initial conditions of zero. This tool is useful both if the system is known or if the system is unknown. The transfer function requires the use of the Laplace Transform which transforms the system description from the time domain to the s-domain, where s=a+bi. The transformation is $L\{f(t)\} = \int_0^\infty e^{-st} f(t)dt$. From the previous example, the spring-mass-damper differential equation ($\ddot{x} + \frac{b}{m}\dot{x} + \frac{k}{m}x = f(t)$) transforms to a polynomial: $s^2 + \frac{b}{m}s + \frac{k}{m} = F(s)$. The transformation allows analysis of polynomials instead of

differential equations. If the system is unknown, the transfer function can be found by analyzing the system's output given a known input, $TF = \frac{Out}{In} \equiv G(s) = \frac{R(s)}{F(s)}$.

The plant root gravitropic response is typically initiated by placing the root horizontally. This input is equivalent to a step function with an amplitude equal to 1 g as shown in Figure 2.3.

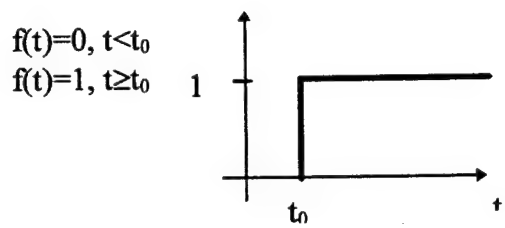

Figure 2.3 - Horizontal Roots as a Step Function

At time $t=t_0$, the gravity vector is applied laterally across the root. The Laplace transform of the step function is $F(s)=1/s$. If the response of the root is measured as degrees of curvature (θ) over time, Figure 2.4 shows a representative response.

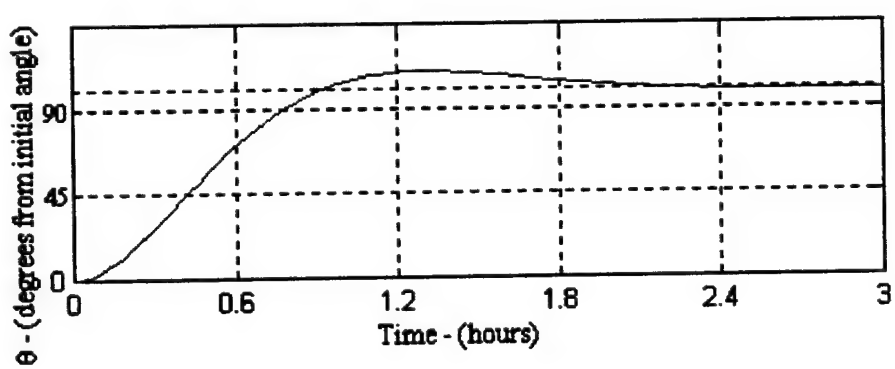

Figure 2.4 - Example of a Root Gravitropic Response

The figure denotes the system output and can be reduced to a second order, linear differential equation or a polynomial in the s-domain. This specific curve is described as $R(s) = \frac{10s}{s(s^2 + 3.6s + 9)}$. Therefore, the transfer function as show in Figure 2.4 is $G(s) = \frac{R(s)}{F(s)} = \frac{10/s(s^2+3.6s+9)}{1/s} = \frac{10}{s^2+3.6s+9}$. G(s) is therefore the derived transfer function which attempts to describe the root's gravitropic mechanism. In this form, it tells us little about the complexities within the root that make the connection between sensing the gravity signal and producing the curvature, but it is a start. Once this transfer function is known, the structure and functions within the system may be analyzed and inferred. Continuing the process of system identification, this transfer function can be further dissected or expanded into deeper dynamics within the root.

Another useful tool in controls analysis is required at this point; the block diagram. The block diagram is used to break a larger complex mechanism into smaller, more manageable sections. If the larger system is difficult to model or study, the smaller sections may be easier to identify and afterward, the system is combined back together through various block diagram algebra rules. Figure 2.5 shows the next logical step in identifying the gravitropic system.

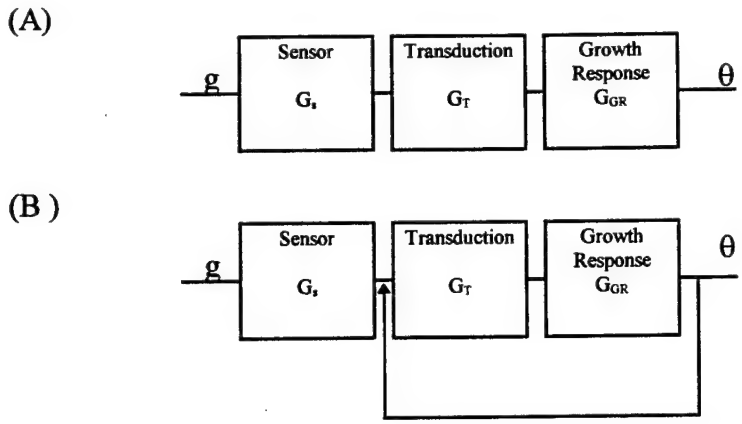

Figure 2.5 - Dividing the Gravitropic System into Smaller Subsystems
(A) shows one of the myriad of ways that the root gravitropic system may be further divided. (B) shows another example with a feedback loop.

Block diagram algebra dictates that the complete system description for (A) is: $G(s)=G_S*G_T*G_{GR}$. On the other hand, the complete description for (B) is: $G(s)=G_S*(\frac{G_T*G_{GR}}{1+G_T*G_{GR}})$. This demonstrates that even a small change in the way that the individual sections feed forward or backward into other sections can make a large difference in the system description. In the process of system identification, the field of controls uses many analysis tools that may be useful in developing these transfer functions.

A system, whether known or unknown a priori, produces various responses to various inputs that may be analyzed in order to gain insight into the system description. One such analysis is accomplished on the s-plane, better known as the root-locus. From Figure 2.4, various specifications can be derived that can aid in constructing a model for the system responsible for creating the example response

found in the figure. Some of the performance specifications found in Table 2.1 are time-domain while others are s-domain (Laplace variable).

Table 2.1 - Performance Specifications

Symbol	Name	Performance Domain	Description
FV	Final Value	Time	the steady-state value of the response following all transient activity
T_R	Rise Time	Time	the time between 10% and 90% of the FV
T_p	Peak Time	Time	the time from input to maximum
PO	Percent Overshoot	Time	(maximum-FV)/FV *100 %
T_S	Settling Time	Time	time for the response to settle to within ±2 % of the FV
e_{ss}	Steady-state error	Time	difference between input amplitude and the FV
W_n	Natural Frequency	s	undamped natural frequency
W_d	Damped Frequency	s	damped natural frequency
ζ	Damping Ratio	s	

The analytical relationships between these time-domain and s-domain performance specifications allow parts of the system transfer function to be developed. Since the response in Figure 2.4 showed an oscillatory nature, we can attempt to model the response as a second-order system forced by a step function. The general form of the second-order system is:

$$G(s) = \frac{kW_n^2}{s^2 + 2\zeta W_n s + W_n^2}$$

The FV gives us the value for k. The other constants are estimated using the following relationships:

$$PO = 100e^{-\zeta\pi/\sqrt{1-\zeta^2}} \text{ ; find value for } \zeta$$

$$T_R = \frac{1}{W_d}\left[\pi - \tan^{-1}(\sqrt{(1-\zeta^2)/\zeta})\right] \text{ ; find value for } W_d$$

$$T_S = \frac{4}{\sigma} \text{ ; find value for } \sigma$$

$$W_n^{\ 2} = \sigma^2 + W_d^{\ 2} \text{ ; find value for } W_n$$

Analysis of these specifications can alternatively be done graphically on the root-locus. Figure 2.6 shows the relationship between the specifications and the transfer function's root locations on the s-plane. The root-locus is a locus of all points in the s-plane that represents the location of all possible closed-loop poles of a transfer function as a feedback loop is closed around the transfer function and the gain is increased. The beginning point of the root-locus is the location of all the open-loop poles (i.e. the roots of G(s)). These open-loop poles are all we need be concerned about when attempting to model the natural gravitropic response of the root because we don't plan on enhancing the system gain.

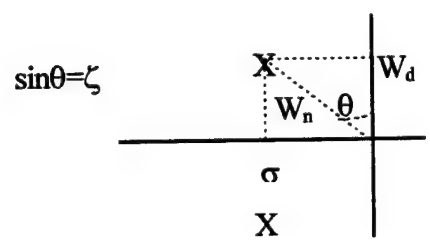

Figure 2.6 - Relationship of Performance Specifications on the S-plane

For example, if a damped frequency was noted in the response that would lead us to a value for W_d and if an exponential decay was noted in the response oscillations, that would lead to a value for σ. Once these values are known, the pole pair could be

plotted on the s-plane, giving us estimates of the other unknown parameters such as W_n and ζ.

The transfer function is a good tool for systems with a single input and single output (SISO). When describing a root's curvature angle to a gravity input, this form of system representation works well on a minimal level. However, many systems, including the plant gravitropic mechanism, are much more complex than can be effectively described by transfer functions. State space techniques provide a vehicle from which a multiple input, multiple output (MIMO) system may be represented and analyzed.

The arrival of numerical processors that can manipulate large matrices of data has allowed state space representation of systems to gain greater utility. The "system state" is the smallest amount of information about the system that must be known at some initial time, along with all inputs, in order to determine system behavior for all future time. "State variables" are the set of variables required to define the system state. Individually, these state variables or "states" are one of possibly infinite variables used to describe a parameter within the system. A minimum representation of a system requires a minimum number of states that, taken together, can fully describe the system from one point in time to another. The states are represented in a "state vector" ($\underline{x}$). The state space representation of a system takes a nth-order differential equation that describes a system and converts it to n, 1st-order differential equations. This process is shown in the following example which converts the spring-mass-damper system from Figure 2.2 into state space.

$$\ddot{x}+\frac{b}{m}\dot{x}+\frac{k}{m}x=f(t) \qquad \text{Let: } x_1 = x \text{ and } x_2 = \dot{x}$$

$$\therefore\ \dot{x}_1 = \dot{x} \equiv x_2$$

$$\dot{x}_2 = \ddot{x} = -\frac{b}{m}\dot{x}-\frac{k}{m}x+f(t) \equiv -\frac{b}{m}x_2-\frac{k}{m}x_1+f(t)$$

State Space Representation:

$$\underline{\dot{x}} = \mathbf{A}\underline{x}+\mathbf{B}\underline{u}$$

$$\begin{bmatrix}\dot{x}_1\\ \dot{x}_2\end{bmatrix} = \begin{bmatrix}0 & 1\\ -\frac{k}{m} & -\frac{b}{m}\end{bmatrix}\begin{bmatrix}x_1\\ x_2\end{bmatrix} + \begin{bmatrix}0\\ 1\end{bmatrix}f(t)$$

where, **A** - state dynamics matrix (n x n); n = # of states (nth order)

B - control distribution matrix (n x r); r = # of controls (inputs)

The states chosen to completely represent this simple system were position and velocity of the mass. The states that could be used to represent the root's gravitropic system might include:

$$\underline{x} = \begin{bmatrix}\theta\\ c_{DEZ}\\ c_{cap}\\ A_{DEZ}\\ A_{cap}\\ L_{elong_{top}}\\ L_{DEZ_{top}}\\ L_{mer_{top}}\\ \dot{L}_{elong_{top}}\\ \dot{L}_{DEZ_{top}}\\ \dot{L}_{mer_{top}}\\ L_{elong_{bot}}\\ \vdots\end{bmatrix}$$

where; θ - angle of root cap from vertical

c_{DEZ} - intracellular Ca^{++} level in DEZ

c_{cap} - " " " cap

A_{DEZ} - auxin gradient in DEZ
$L_{DEZ\text{-}top}$ - length of the DEZ segment on the top
etc.

Depending on the states chosen to represent the system and the sensors available in the system, not all states may be directly observed. The system output $(\underline{y})_{mz1}$ represents what can be observed directly: $\underline{y} = C\underline{x} + D\underline{u}$; where C is the state distribution matrix and D is the control output coupling matrix. If the only sensor on the spring-mass-damper system was a ruler to measure displacement, x, then the C-matrix is: [1 0] while the D-matrix is zero.

Once the C-matrix is defined, transfer functions between specific inputs and outputs can also be computed from the state space descriptions:

$$G(s)_{mxn}=C[sI-A]^{-1}B+D$$

The complete root gravitropic response is initially divided into the three separate mechanisms or "blocks." The first block, the sensor, initially detects the gravity signal. Classically this sensor is believed to be the starch-filled amyloplasts acting as statoliths within the columella cells of the root cap. Upon detection of gravity a signal is passed to the second block, transduction, which converts the signal into various plant physiological processes that relay the signal to the area of the root where differential growth occurs. The final block is the growth differential that occurs in the root to redirect its growth. Before each of these blocks can be modeled with identification theory, an in-depth study is made of the current quantitative data involved with the gravitropic response. Initially, we will examine the time response specifications to provide a vital starting point for an attempt at modeling the response.

Following that, literature pertaining to the gravity sensor is discussed and, finally, various primary and secondary messengers, proposed as key components of the transduction process, are discussed.

2.4 The Gravitropic Response of Plants

The gravitropic curvature of a horizontally placed root is the result of differential growth between the root's upper side and lower side. Specifically, to curve downward the upper side must have a higher growth rate than the lower side. This can be achieved in a variety of ways: (1) growth acceleration along the upper side; (2) growth inhibition of the lower side; (3) both (1) and (2); or (4) a combination of accelerations and inhibitions on opposite sides that result in the observed redirected growth (Konings, 1995). In order to formulate a proper model of gravitropism it is necessary to elucidate how the gravireception signal is transduced, how and when the bending begins, the time response characteristics of the bending, the steady-state conditions of the roots, the presentation time of the root, and any nuances of bending motions of the root that may contribute to or mask the gravitropic response.

In 1987, Selker and Sievers showed that roots develop a positive curvature by accelerating growth on the top side and diminishing growth on the bottom side in comparison to vertically growing controls. Their work used intact roots of *Lepidium sativum* which were photographed at 1.5-6 min. intervals before and after being tilted from a vertical to a horizontal position (Selker & Sievers, 1987). Relative extension rates were calculated for segments of the root by measuring the rate of movement of charcoal particles on the surface of the root. Curvature was measured at points

separated by 0.8 mm, from the tip to the root hair zone. For the first hour after the root was tilted to a horizontal position, the relative extension rate for the side of the root producing the outer side of the curve was higher than that during vertical growth. The relative rate for the inner side fell to near zero during the first hour in the horizontal position. For most of the second hour, the two sides had approximately equal relative rates of extension. In the last 12 min. of the second hours, as the root tip is moving the final distance to a vertical position, the rate on the inner side showed a high extension rate. The gradient in extension rate from the inner to the outer side of the curve had thus become negative during the second hour. This reversal in the extension gradient is necessary to prevent the root from continuing to grow in a circle past the point where the root tip is vertical. Curvature units are expressed in reciprocals of the radius of curvature in millimeters. Curvature reached maximal values of 0.7 mm^{-1} to 1.2 mm^{-1} for the inner side and 0.5 mm^{-1} to 0.7 mm^{-1} for the outer side. Although this work did not investigate the presentation time for *Lepidium*, earlier work by Behrens *et al.* found this to be from 12 to 30 seconds (Behrens *et al.*, 1982). Selker and Sievers also found that the overall elongation of the graviresponding roots was unaltered from vertical controls. Zeischang and Sievers also found in 1991 that the overall elongation in gravistimulated roots of *Phleum pratense* was unchanged compared to vertical controls (Zieschang & Sievers, 1991).

Zeischang photographed roots of *Pheleum pratense* L. during vertical growth and gravitropic bending and was able to estimate the number of cells responsible for

the initial curvature response. The gravitropic response was divided into phases according to growth rate values (Zieschang & Sievers, 1991):

1. An increase in rates on the upper side and a decrease on the lower side during the first 1-1 1/2 hours
2. A transient equality of the rates on both sides
3. 2-3 hr after the beginning, the growth gradient is inverted
4. After about 4 hrs , the growth rates on both flanks are roughly equal again.

Curvature began about 15-20 min after horizontal placement of the root. When the group plotted curvature vs. arc length, one maximum value appeared during the first 2 hours. After 2-2 1/2 hours, two maximum values were observed, the apical one near the root tip always keeping the same distance from the tip, the other one drifting basipetally relative to the growing tip. A group of six rhizodermal cells on each side of the root was identified as the first cells showing gravitropic bending. These cells are located at the beginning of the elongation zone, enclosing the region 480-680 μm from the root tip. These cells might be the initial target cells for the signal which the site of graviperception sends to the growth response zone. A model of gravitropism that relies on a simple redirection of auxin predominately into the lower portion of the graviresponding root cannot explain this response of specialized cells in an apparently very small region of the elongation zone.

Further difficulties with the simple auxin redistribution theories included findings that the growth responses are apparently multimodal in nature. In 1991, Ishikawa *et al.* used a video digitizer system to measure surface extension and

curvature of maize roots in graviresponse (Ishikawa *et al.*, 1991). Downward curvatures began 25 ± 7 min. from stimulation and resulted from both an increased growth rate on the top and a decreased growth rate on the bottom relative to vertical controls. Curvature rate was 1.4 ±0.5 deg/min. but the pattern of curvature varied somewhat. A final angle of 90 deg was reached in 110 ± 35 min. after the start. In about 65% of the samples, backward curvature was noted; in 15% of those, this period of backward curvature occurred before the root reached 90 deg. Following transient backward curving, downward curvature resumed and the root approached 90 deg. In 65 % of the reverse curvature cases, the roots curved steadily past the vertical, reaching a maximum curvature about 205 ±65 min. after stimulation. The direction reversed back toward vertical and after one or two oscillations about the vertical, the roots obtained a vertical orientation. Periods existed during the response when the normally unimodal growth-rate distribution within the elongation zone became bimodal with two zones of rapid elongation separated by a region of reduced elongation rate. This occurred at different times on the convex and concave sides of the root. During the period of steady downward curvature, the elongation zone along the convex side extended farther toward the tip than in the vertical control. During the period of reduced rate of curvature, the zone of elongation extended farther toward the tip along the concave side of the root. The data shows that the gravitropic response pattern varies with time and involves changes in localized elongation rates as well as changes in the length and position of the elongation zone. Models of root

gravitropic curvature based on simple unimodal inhibition of growth along the lower side cannot account for these complex growth patterns.

Further work with maize was accomplished by Barlow *et al.* in 1993 who compared the steady-state properties of the graviresponse to the amplitude of the input signal (the size of the angle of displacement from vertical). Primary roots of maize were oriented at various angles from the vertical ranging from 90 to 1 degrees and their subsequent bending was analyzed from filmed records. The maximum rate of bending and the time before onset of bending both varied two-fold, but showed no correlation with the initial angle of tip displacement (Barlow *et al.*, 1993). Roots oriented to small initial angles (<40 deg.) often overshot the vertical and proceeded to oscillate around this orientation, whereas roots oriented to large initial angles (>60 deg.) often failed to achieve the vertical. Roots in this latter group resumed bending after an indeterminate time, or did so immediately after a second displacement of their tip, showing that they were not intrinsically unable to bend. The apparently spontaneous resumption of bending after a temporary plagiotropic phase is suggested by Barlow *et al.* as being due to noise in the graviperception system in the root cap. The tips of roots growing vertically downwards showed oscillatory bending movements up to 10 deg. either side of vertical. This angle corresponds to the minimum angle of displacement which induces gravitropic bending. Only when roots were oriented 10-20 deg. from vertical did they begin unequivocally to show a gravitropism since at such angles the deflection of their tips exceeded that due to their natural oscillation.

Because of different experimental methods and varying purposes for the research, it becomes difficult to compare the graviresponse data of various species from a common point of reference. Table 2.2 is an attempt to summarize the growth response data of the three species discussed in this section. The table shows that many deficiencies exist in some important quantitative data required for a system identification analysis. The detailed and quantitatively oriented research accomplished with *Zea mays* (corn) indicates that system identification is more likely to be successful with this species.

Table 2.2 - Growth Response Data

Species	T_{min} (min.)	T_1 (min.)	$\theta_{min.}$ (deg)	δ_{max} (deg)	PO (%)	α_{ss} (deg)
Lepidium sativum (cress)	0.2-0.5	9-10	10	10	?	0
Phleum pratense	?	15-20	?	?	?	0
Zea mays (corn)	4	25-30	10	10	θ=10° : 150 θ=20° : 85 θ=40° : 19 θ=90° : 0	0-10

T_{min} is known as the presentation time which is the minimum time the root can be subjected to an off-vertical component of gravity and still produce a gravicurvature. T_1 is the time until the beginning of the gravicurvature response is detected. $\theta_{min.}$ is the minimum angle off-vertical required to induce a graviresponse in the root. This is related to the minimum gravity signal that can be sensed by the plant, but is not equal to it. δ_{max} is the amplitude of any oscillations about the vertical noted in vertically growing roots. θ is the initial angle of displacement from the vertical. PO is the percent overshoot from the vertical as calculated from (angle past vertical / initial angle of displacement [θ]). α_{ss} is the steady-state angle reached by the root as measured in degrees from vertical. Note the lack of numerous data.

The growth response data available on maize is much more extensive than that of other species. The work of Ishikawa *et al.* elucidated the time history of elongation

rates along the upper and lower side of the graviresponding root. Figure 2.7 displays the elongation data (Ishikawa *et al.*, 1991) and Table 2.3 summarizes the data at key times.

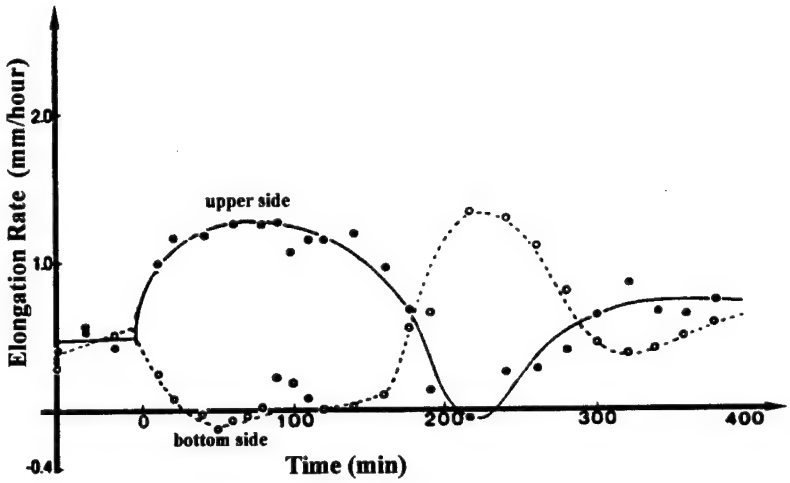

Figure 2.7 - Elongation Rates During Root Graviresponse of Maize
Data from Ishikawa *et al.*, 1991.

Table 2.3 - Elongation Rates of Maize Roots at Specific Times

	Maize Elongation Rates (mm/hr)			
	Vertical	**1 hour**	**2 hours**	**3 hours**
Upper Side:	0.5	1.2	0.9	0.0
Lower Side:	0.5	0.0	0.1	1.2
Curvature (deg/min.):	0.0	1.2	-0.6 to 0.6 Dependent on the presence of an overshoot condition	

The Cholodny-Went Theory provides the earliest hypothesis as to the mechanism that creates the graviresponse in roots. Although the hypothesis has been eroded during recent decades, the basic landscape remains the same. Went stated their hypothesis in a 1937 work on phytohormones:

> Growth curvatures, whether induced by internal or by external factors, are due to an unequal distribution of auxin between the two sides of the curving organ. In

the tropisms induced by light and gravity, the unequal auxin distribution is brought about by a transverse polarization of the cells, which results in lateral transport of the auxin (Went & Thimann, 1937).

One of the key features of the hypothesis is that the curvature is the result of an unequal distribution of auxin between the upper and lower side of the graviresponding root. According to this hypothesis, gravity induces redistribution of auxin toward the lower side of the organ and this causes the growth asymmetry that leads to reorientation. Arguments against the C-W hypothesis that were based primarily on concerns over the timing and magnitude of the development of hormone asymmetry are countered by recent evidence that such asymmetry develops early and is sufficiently large to account for curvature (Evans, 1991). Thus, it appears that the C-W hypothesis is fundamentally valid. However, recent comparative studies of the kinetics of curvature and the timing of the development of hormone asymmetry indicate that this hypothesis alone cannot account for the intricacies of the gravitropic response. These studies, such as those of Ishikawa described earlier and those of Evans, indicate that time-dependent gravity-induced changes in hormone sensitivity as well as changes in sensitivity of the gravity receptor play important roles in the response (Evans, 1991).

With the quantitative specifications of the graviresponse detailed, these data will provide the means to verify the models for each of the three sections of the control system; the sensor (perception), transduction, and the growth response. Modeling will also require a firm foundation in the present understanding of the plant root's morphological structure, specialized zones, and functions. Morphological data are

abundant concerning the putative sensor region of the root and the regions of differential growth within the elongation zone of the root. Therefore, the morphological considerations concerning the statoliths and the differential growth regions are explored in the following section.

2.4.1 The Sensor

From the viewpoint of the controls analyst, the perception of the gravity signal is accomplished by one or more sensors. The classical postulation for a gravity sensor within the root is the starch-statolith hypothesis. "Statolith" comes from the Greek *statos*, meaning "standing" or "placed" and the Greek *lithos*, meaning "stone". This stone (or mass) that stands (or seeks) gravity has long been held as the gravity sensor within the plant root. This hypothesis has been alternatively supported and rejected throughout the twentieth century. Early in the twentieth century it seemed clear that the site of gravity perception was in the root cap. Reports showed that roots of pea, lentil, and broadbean would not respond to gravity when their root caps were removed. The careful microsurgical technique that removes the cap did not inhibit root growth, but gravitropism was absent until the root regenerated the root cap (Salisbury & Ross, 1992b). On the surface, the conclusion that the perception of gravity occurs within the root cap appears legitimate, but when viewed from the context of the complete control system proposed in this thesis this conclusion appears hasty. The root cap is necessary for graviresponse, but not proven as necessary for gravity perception. The root cap's role could also be solely or partially involved with the signal transduction portion of our control model. In a 1989 review article, Poff and

Martin discuss two lines of evidence that support the assertion that the root cap is the sole site of gravireception in the root. The first evidence is based on surgical removal of the cap, which abolishes the response to gravity. Although sufficient to conclude that the cap is required for gravitropism, they also conclude that the evidence does not prove it is the site of perception. The second evidence is from centrifuge experiments where different parts of the root were subjected to different forces. Poff and Martin also effectively refute this evidence because it appears on closer examination that the experiment really proved that the perception of gravity occurs throughout the root tip (Poff & Martin, 1989). Although subject to considerable debate, the statolith hypothesis is the mostly widely accepted. Numerous experiments have been undertaken to quantify the structure and effect of the statoliths.

2.4.1.1 Statoliths of the Columella Region

Since 1901, the amyloplasts of the root cap's columella region have been postulated as the root's statoliths. Early investigations showed that these starch-filled plastids were the only organelle that consistently sedimented in response to a gravity signal. Experiments accomplished throughout the 1970's and 1980's continued to support the idea that the amyloplasts acted as statoliths within the columella cells of the central root cap. These columella cells are dubbed statocytes; cells with statoliths. These experiments correlated the motion of the amyloplasts with the graviresponse. First, close correlation was found between the presence of the sedimentable amyloplasts within the root cap and the root's ability to exhibit gravitropism. Second, the presentation time of a root's graviresponse was closely correlated with the

sedimentation time of the amyloplasts (Salisbury & Ross, 1992b). In 1985, Sack *et al.* measured amyloplast sedimentation kinetics in roots of *Zea mays* L. (Sack *et al.*, 1985). Sedimentation kinetics were analyzed by measuring the change in angle from the center of the cell to each amyloplast as an index of sedimentation. Angular change in amyloplasts was found to occur within a mean of 5.9 sec after gravistimulation. Initial sedimentation velocities were found by multiplying the instantaneous angular velocities (radians/min.) by the position vector to the amyloplast from the cell center. These initial sedimentation velocities were found to be 19.1 μm/min. at 5.9 seconds. The following year, Sack reported an average sedimentation velocity of 5.5 ± 1.0 μm/min. including a maximum velocity of 18 μm/min. (Sack *et al.*, 1986). When seedlings were gravistimulated at 90^0 for 5-40 min. periods, a plot of curvature against the logarithm of duration of stimulation yielded a regression line with a correlation coefficient of 0.98. Extrapolating this line to the abscissa gives a presentation time of 4.1 minutes. The empirical presentation time for maize, as introduced in the previous section, is 4 minutes. Therefore, the sedimentation time of amyloplasts within maize is found to be highly correlated with the presentation time of maize gravitropism. Thirdly, when roots were treated with agents that remove the amyloplast starch, the gravitropic behavior ceased. In 1969, Iversen's group made roots of garden cress seedlings starchless by treatment with gibberellic acid and kinetin for 29 hours at 35^0 C in the dark. The starch depleted roots elongated at 0.48 mm/hr but were unable to respond to gravity following a 3 hour temperature adaptation at 21^0 C. Control roots placed under the same temperature conditions but placed in plain water elongated at

0.64 mm/hour at 21^0 C and 0.33 mm/hour at 35^0 C. Illuminating the hormone-treated seedlings caused starch to reform within 20-24 hours; simultaneously graviresponsiveness returned (Iversen, 1969). This final finding from Iversen's group describes the fourth correlation in that gravitropic sensitivity reappears at a correlated time as that of starch grains reforming within the amyloplasts or root cap regeneration following removal of the cap. Of course, the effect of gibberellic acid or kinetin on the signal transduction or growth response portions of the control model must also be considered when establishing any possible correlations these results appear to produce. The use of cytoskeletal poisons such as kinetin or cytochalasin derivatives is further discussed in a following section on gravitational research. These studies provide insight into the infrastructure that allows the statolith to interact and communicate with the rest of the statocyte.

2.4.1.2 Studies of Agravitropic Lateral Roots

Morphological analysis of agravitropic lateral roots also appears to support the statolith hypothesis in some cases and counter it in others. In 1983 Ransom and Moore investigated the roots of *Phaseolus vulgaris*. The primary roots of this species are positively geotropic, while lateral roots are unresponsive to gravity. In order to elucidate any structural basis for this lack of graviresponse, they performed a qualitative and quantitative analysis of the structure of columella cells within primary and lateral roots of this species. The columellas of primary roots are more extensive than those of lateral roots. The volumes of columella cells of primary roots are approximately twice those of columella cells of lateral roots. However, columella cells

of primary roots contain greater absolute volumes and numbers of all cellular components examined than do those of lateral roots. Also, the relative volumes of cellular components in columella cells of primary and lateral roots are statistically indistinguishable. The ER is sparse and distributed randomly in both types of columella cells. Both types of columella cells contain numerous sedimented amyloplasts, none of which, in their observations, contact the cell wall or form complexes with other cellular organelles. Therefore, they concluded that positive geotropism by roots must be due to a factor(s) other than the presence of sedimented amyloplasts alone (Ransom & Moore, 1983).

Other evidence exists that indicates that the ultrastructure of the columella cell is not a sufficient requirement for positive gravitropism. In 1984, Moore and Pasieniuk investigated the roots of *Ricinus communis*. Horizontally oriented primary roots of *Ricinus communis*, the castor bean, are more graviresponsive than similarly oriented lateral roots. The more pronounced graviresponsiveness of primary roots is positively correlated with their caps having a more extensive columella tissue than caps of lateral roots. Individual columella cells of primary roots contain 2.6 times more protoplasm than do columella cells of lateral roots. Similarly, the absolute volumes of all cellular components in columella cells of primary roots are larger than those of lateral roots. However, there are no statistically significant differences in the relative volumes of any cellular component in columella cells of primary vs. lateral roots. ER is distributed randomly in columella cells of both types of roots. Columella cells of primary and lateral roots contain numerous sedimented amyloplasts which do not

consistently contact any cellular structure. Nuclei tend to be located in the middle thirds of the columella cells and the vacuole is found in largest concentrations in the middle and upper thirds of columella cells of both types of roots. There is no significant difference in the intracellular distributions of organelles in columella cells of both types of roots (Moore & Pasieniuk, 1984). Primarily because of the similar relative organelle volumes, they also concluded that the differing graviresponsiveness of primary vs. lateral roots is probably due to factors other than the structures of their individual columella cells.

It interesting to note that both the Ransom and Moore publications base their conclusions on the relative organelle volumes and presence of sedimented amyloplasts. Both groups did find significant differences in absolute volumes of all organelles, including the plastids, between the primary and lateral roots. As a sensor, the absolute size of the sensing mass is important as it provides gain to the sensor's ability to detect gravity above the background noise. Moore's group realized this and produced a follow-on article in the same year which took the next step in analyzing the lateral root structure. They compared the structure of the lateral root while it was agravitropic and compared it to the structure it has in its morphological development when it achieves gravitropic capability. The castor bean has an interesting gravitropic behavior. Primary roots are strongly gravitropic. After branching from the main root, secondary roots grow laterally for 15 to 20 mm and are agravitropic. At this point, they become gravitropic and bend downward. This provides an excellent study into what causes the lateral root to become gravitropic at that point in its development.

Moore and Pasieniuk found that the columella tissues of primary (graviresponsive) roots are (a) 4.3 times longer, (b) 2.95 times wider, (c) 37.4 times more voluminous, and (d) composed of 17.2 times more cells than those of lateral roots growing laterally at a length of 10 mm. The onset of positive gravitropism by lateral roots, which occurs at a length of 15-20 mm, is positively correlated with a (a) 2.99-fold increase in length, (b) 2.63-fold increase in width, and (c) 20.7-fold increase in volume of their columella tissues. Table 2.4 summarizes these findings and relates the parameters at the point of lateral root positive gravitropism with primary roots. These data appear to indicate a collective effect of the various morphological parameters toward producing a viable gravity sensor. This investigation reversed their original conclusions and they concluded that the minimal graviresponsiveness of lateral roots in this species is due to the small size of their columella tissues. They further postulate that this smaller size of agravitropic lateral roots results in their caps being unable to (a) establish a concentration gradient of the effector sufficient to induce gravicurvature and (b) produce as much of the effector as caps of graviresponsive roots (Moore & Pasieniuk, 1984).

Table 2.4 - Development of Lateral Root Columella Cells

	Primary Roots / Agravitropic Lateral Roots at 10 mm	**Increases to the Lateral Root up to Positive Gravitropism**	**Lateral Root Percentage of Primary Root at Positive Gravitropism**
Length	**4.3**	**2.99**	**69.4 %**
Width	**2.95**	**2.63**	**89.3 %**
Volume	**37.4**	**20.7**	**55.3 %**
# of Plastids	**17.2**	**10.52**	**61.3 %**

From a volumetric standpoint, the gravitropism of the lateral roots begins when their absolute volumes come within approximately 55% of the volumes of primary root columella cells. But again, these morphological differences between primary and lateral roots can be interpreted as effecting the signal transduction portion of the gravitropic control system and not just the sensor mechanism as Moore and Pasieniuk's final conclusion indicates. In order to truly identify the amyloplast as the sole statolith with the plant root, specific investigations into the amyloplast itself is required.

2.4.1.3 Studies of Starchless Amyloplasts

Work with starchless mutants, while initially appearing to rule out the single statolith hypothesis, still leaves room for the classic starch-statolith postulation. Caspar et al. created a serious setback for the single statolith hypothesis in 1985 when they presented a poster at the annual meeting of the American Society of Plant Physiologists. Their work was on a starchless mutant of *Arabidopsis*. The mutant could not synthesize starch and therefore the amyloplasts were starchless. However, the root continued to respond to gravity (Salisbury & Ross, 1992b). This was serious evidence against the statolith hypothesis of graviperception. Four years later Caspar and Pickard published results that continued to question the validity of the starch-statolith theory of gravity reception. After verifying the starchless nature of the mutant's plastids, the compared wild-type (WT) and mutant gravitropism. In WT seedlings, starch-filled plastids in the starch sheath of the hypocotyl and in three of the

five columellar layers of the root cap were piled on the cell floors, and sedimented to the ceilings when the plants were inverted. However, starchless plastids of the mutant were not significantly sedimented in these cells in either upright or inverted seedlings. Gravitropism of light-grown seedlings was vigorous: e.g. 10° curvature developed in mutants rotated on a clinostat following a 5 min induction at 1 g, compared with 14° in the WT. Curvatures induced during intervals from 2.5 to 30 min were 70% as great in the mutant as the WT. Their conclusion was that the presence of starch and the sedimentation of plastids are unnecessary for reception of gravity for these roots (Caspar & Pickard, 1989).

Three years later, in work accomplished by Kiss and Sack, the mutant's gravitropism was not found as normal, but severely inhibited. Although the graviresponse was present in these mutant roots, the response was significantly diminished. Kiss and Sack compared the kinetics of gravitropism in the starchless mutant (TC7) and the wild-type (WT). WT roots were more responsive to gravity than TC7 roots as judged by several parameters:

1. Vertically grown TC7 roots were not as oriented with respect to the gravity vector as WT roots,

2. In the time response of gravicurvature, curvature in TC7 roots was delayed and reduced compared to WT roots,

3. TC7 roots curved less than WT roots following a single, short period of gravistimulation, and WT, but not TC7, roots curved in response to a 1 min. period of horizontal exposure, and

4. WT roots curved much more than TC7 roots in response to intermittent stimulation (repeated short periods of horizontal exposure); WT roots curved in response to 10 sec of stimulation or less, but TC7 roots required 2 min. of stimulation to produce a curvature.

However, the growth rates were equal for both genotypes (Kiss *et al.*, 1989). Their conclusion was that the wild-type root was more sensitive to gravity than the starchless roots. Furthermore, through centrifugation studies, they found that the starchless plastids are still relatively dense and are still the most movable component in the TC7 columella cells. Therefore, their findings indicated that starch is not required for gravity perception in TC7 roots, but is necessary for full sensitivity; thus it is still a viable hypothesis that amyloplasts function as statoliths in wild-type roots of *Arabidopsis*.

The starchless plastids may still function as the statolith within the classic statolith model. In 1989, Moore accomplished work on the starchless mutant of *Arabidopsis thaliana* L. that confirmed these earlier conclusions. He found that the primary roots of the mutant are strongly graviresponsive despite lacking amyloplasts in their columella cells. The ultrastructures of calyptrogen (i.e. meristematic) and peripheral cells (i.e. peripheral) in the wild-type (WT) as compared to mutant seedlings are not significantly different. The largest difference in cellular differentiation in caps of mutant and WT roots is the relative volume of plastids in columella cells. Plastids occupy 12.3% of the volume of columella cells in WT seedlings, but only 3.69% of columella cells in mutant seedlings. He drew three conclusions based on these data:

1. Amyloplasts and starch are not necessary for root graviresponsiveness;

2. The increase in relative volume of plastids that usually accompanies differentiation of columella cells is not necessary for root graviresponsiveness; and

3. The absence of starch and amyloplasts does not affect the structure of calyptrogen (i.e. meristematic) and secretory (i.e. peripheral) cells in root caps.

His investigation also found that the plastids in columella cells of mutant roots are distributed throughout the cells and do not move appreciably when the root is reoriented (Moore, 1989). These results could suggest that plastids are not the gravisensors in roots. However, one can always argue that only a minute movement or a tension applied to the cytoskeletal network rather than complete sedimentation of plastids can suffice for perception of gravity.

Moore also accomplished similar work on a starch-deficient cultivar of maize. In the primary roots of *Zea mays* L. cv. vp-7 wild type, starch occupies only 4.2% of the volume of plastids in calyptrogen cells. Plastids in calyptrogen cells are distributed randomly around large, centrally located nuclei. The differentiation of calyptrogen cells into columella cells is characterized by cellular enlargement and the sedimentation of plastids to the bottom of the cells. He found that the sedimented plastids in columella cells do not contain significantly more starch than those in calyptrogen cells, but still continued to sediment and the primary root exhibited graviresponsiveness. Since maize amyloplasts have a normal starch content of 41.7%, a conclusion may be drawn that the sedimentation of plastids in columella cells of this cultivar of maize must involve factors other than their density resulting from increased starch content

alone. Although not mentioned in Moore's work, cytoskeletal modification that alters the medium in which the amyloplast sediments could also play an important role in this result. Moore also found that the onset of root gravicurvature is not associated with a significant change in the distribution of plastids in columella cells. He did not detect any significant movement of the amyloplasts in columella cells by the onset of gravicurvature, which began approx. 15 min. after reorienting the roots. Although his observations were qualitative, he observed over 200 columella cells, and could not detect any significant change in the distribution of plastids that correlated with the onset of gravicurvature (Moore, 1987).

In 1994, Sack continued the debate over whether gravity sensing relies on the amyloplasts sedimenting. Sack argued that starch and significant amyloplast sedimentation are not necessary for reduced sensing in mutant roots, but the plastids might function as a sensor if the ER was a specialized sensor for plastid mass. Alternatively, components in addition to the amyloplasts might provide mass for sensing, such as the nucleus. However, he did question that if the entire weight of the protoplast functioned in sensing, why would there be specific cytological specializations favoring sedimentation rather than cell mass? Therefore, he postulated that there may be more than one mechanism of gravity sensing (Sack, 1994). In support of the classical statolith hypothesis he cites the following:

1. Essentially perfect correlation between the presence of gravitropism and amyloplast sedimentation in untreated, wild-type plants. No gravitropic organs or cells above algae that lack amyloplast sedimentation.

2. Only one organelle that sediments consistently in plants is the amyloplast.

3. Amyloplast sedimentation is under highly specific spatial and temporal control. The amyloplast sedimentation only occurs in cells in very specific locations (center of the root cap or the starch sheath of stems) and sedimentation only occurs at a specific developmental stage of the cell (not present in young or old cells).

4. Columella cells have other specializations that favor sedimentation.

-- nucleus near proximal end of cell and doesn't sediment

-- ER located almost entirely in the cell periphery and is more enriched near the distal end of cell

-- amyloplasts are smaller than storage type plastids

-- starch not easily mobilized from these plastids

Sack's ideas for revising the classical statolith hypothesis are as follows:

1. Starchless mutants still have gravitropism, but not full sensing of the gravity signal.

2. Look at the mass itself versus the need for sedimentation.

3. The mass sensor could be receptors in the ER or the cytoskeleton.

4. The mass could be the nucleus or maybe the entire cell.

More recently, Kiss *et al.* (Kiss *et al.*, 1996) studied gravitropism in roots of wild-type (WT) *Arabidopsis thaliana* L. along with three starch-deficient mutants that were generated by T-DNA insertional mutagenesis. One of these mutants was starchless while the other two were intermediate mutants, which had 51% and 60%, respectively, of the WT amount of starch as determined by light and electron

microscopy. The four parameters used to assay gravitropism were: orientation during vertical growth, time course of curvature, induction, and intermittent stimulation experiments. Again, the Kiss group found that WT roots were much more responsive to gravity than were roots of the starchless mutant. Additionally, they found that the intermediate starch mutants exhibited an intermediate graviresponse. Their data suggest that lowered starch content in the mutants primarily affects gravitropism rather than differential growth because both phototropic curvature and growth rates were approximately equal among all four genotypes. Since responses of the intermediate-starch mutants were closer to the WT response than to that of the starchless mutant, it appears that 51%-60% of the WT-level of starch is near the threshold amount needed for full gravitropic sensitivity.

Although the current state of research by no means negates the classical statolith hypothesis, alterations to the simple specifics of the theory are indeed in order. The complete mass of the amyloplast, or even the entire columella cell, could provide the potential energy required to serve as the root's sensor. Current data indicate that sedimentation of the amyloplasts is possibly not required, but that gravity can be perceived through a change in cytoskeletal tensions, where the amyloplasts provide a gain control on such a sensor. The mass of the amyloplast along with the elastic modulus within the columella cell itself combine to adjust the sensor's gain (sensitivity) to the gravity signal. Perbal and Driss-Ecole investigated such ideas using gravitational research in 1994. They contend that although the amyloplasts are considered the perceptors of gravity, their displacement and the starch they contain

may not be required for gravisensing. It is well known that the amplitude of the stimulus is dependent upon the intensity of the acceleration and the inclination of the root with respect to gravity. This strongly supports the hypothesis that the stimulus results in a mechanical effect (pressure or tension) on a cellular structure. Perbal and Driss-Ecole (Perbal & Driss-Ecole, 1994) proposed three cellular components as candidates for a role in the gravity sensing mechanism: actin filaments, ER, and the plasma membrane with its ion channels. Their space flight experiments are one of the growing number of studies that use gravitational research to explore the mechanisms of the plant's gravity sensor.

2.4.1.4 Results of Gravitational Research

The use of space flight and the presence of microgravity has become an invaluable tool for investigating the putative gravity-sensing mechanism within the plant root. Volkmann *et al.* (Volkmann *et al.*, 1991) have contributed to the subject of the plant gravity sensor through innovative space flight research coupled with ground-based analysis. They flew *Chara globularia* (a green alga) and *Lepidium sativum* (cress) aboard a series of TEXUS sounding rockets. These rockets provide a parabolic trajectory that produces a state of microgravity for approximately 6 minutes (Dutcher *et al.*, 1994). The statoliths within the *Chara* rhizoid consist of membrane vesicles filled with $BaSO_4$ crystals, while the proposed statoliths within the cress roots are amyloplasts filled with starch grains. Earlier work done with *Chara* rhizoids on space flights included the experiment performed by Buchen *et al.* (Buchen *et al.*, 1991) that used video microscopy to show that the cytoplasmic streaming in *Chara* rhizoids

was affected by 10^{-4} g gravity. Both the acropetal and basipetal streaming velocities increased when subjected to microgravity. The endogenous difference in the velocities of the opposing streams was maintained in microgravity, yet the difference was less since the basipetal velocity increased more than the acropetal velocity. The group also found that the structure and orientation of the microfilaments labeled by rhodamine-phalloidin had not changed after 6 minutes of microgravity. The work of Volkmann *et al.* (Volkmann *et al.*, 1991) showed that the statoliths moved basipetally (away from the original 1 g vector) when subjected to microgravity. This movement was rapid and couldn't be attributed to simple diffusion effects. The statoliths relocated nearly twice as far from the distal cell wall as the statoliths within the ground or flight controls. The statolith distribution within the statocyte also became more irregular. The Volkmann group concluded that the results suggest that the position of statoliths depends not only on the gravity vector, but buoyancy forces and forces mediated by microfilaments. They proposed that the microfilaments may tug the statoliths both basipetally and acropetally and, along with the gravity vector, create an equilibrium position in the statolith. They conclude by proposing that a disturbance in this balance of forces might provide the mechanism for gravity sensation in the statocyte. Further work must be accomplished to verify and quantify the statolith-cytoskeletal relationship. Also, if the amyloplast is truly a mechanism of the plant's gravity-sensing system, biological adaptation would suggest that the plant gravity sensor would undergo morphological changes to adapt to the gravitational environment. Such

research is invaluable in quantifying the complete perception mechanism within the root.

In-depth morphometric studies of the columella cells under the condition of microgravity along with tight controls are needed to correlate the structure of the statoliths to gravity conditions. Early gravitational researchers reported both increases and decreases in amyloplast volume during root growth under microgravity conditions (Moore, 1986; Perbal & Driss-Ecole, 1989). With the intent of producing definitive work on columella cell morphology under varying gravitational conditions, Smith (Smith, 1996) combined stringent experimental control specimens with advanced serial sectioning techniques and computer-generated three-dimensional reconstructions of columella cells and their organelle distributions. His work compared sweet clover grown in 1 g, microgravity, and on a clinostat. The three-dimensional reconstructions produced morphological data on the effects of gravity on amyloplast structure. Smith's research showed that microgravity does not produce a significant increase or decrease in the number of amyloplasts per cell, but both the amyloplast volume and the total amyloplast volume per cell was significantly increased under microgravity conditions. His data are summarized in Table 2.5.

Table 2.5 - Sweet Clover Columella Morphology Under Varying Gravitational Conditions

Gravity	Cell Volume (μm^3)	Nucleus Volume (μm^3)	Amyloplast Number/Cell	Amyloplast Volume (μm^3)	Total Amyloplast Volume/Cell (μm^3)
1 g controls	3215 ± 343	116 ± 20	13.3 ± 1.5	16.0 ± 6.2	235 ± 114
microgravity	3872 ± 331	133 ± 24	13.0 ± 0.7	17.7 ± 9.0	253 ± 149
clinostat	3990 ± 475	125 ± 42	13.2 ± 1.3	15.6 ± 6.4	199 ± 66

The data was obtained from three-dimensional reconstructions of twelve columella cells in each gravity condition. Values shown are the statistical mean (±SD). Amyloplast volume is significantly greater in microgravity (ANOVA; $p<0.001$) and total amyloplast volume is significantly dependent on gravity condition (ANOVA; $p=0.039$). Data from Smith, 1996.

An interesting conclusion that arises from this research is that the amyloplast does adapt to its gravity conditions, becoming larger during a lack of gravity signal. This would increase the gain of the sensor mechanism allowing the root's gravitropic system to increase its sensitivity to gravity. If the amyloplast is indeed the statolith, or at least a segment of the root's gravity sensor, this is exactly what would be expected of the plant as it adapts to its surroundings.

In the area of amyloplast-cytoskeletal interaction, Todd (Todd, 1994) analyzed the kinetic data on statolith polarity and motion of *Chara* and cress subjected to microgravity and developed a quantitative analysis of the statocyte's effective elastic modulus. He found that statolith action is consistent with gravitational sedimentation opposed by elastic deformation of an intracellular material. The time required for a statolith to sediment to equilibrium was calculated on the basis of its buoyant density and compared with observed sedimentation times. The relative response times to shifts in the gravity vector showed that the statoliths are within a cytoskeleton of

extremely low elastic modulus (non-stiff). He analyzed the force balances with $F_{buoyant}$, $F_{gravity}$, F_{drag}, and $F_{elastic}$. An expression for the terminal velocity of the sedimenting statoliths worked out to be: $v=[4a^2 (\rho-\rho_0)g-3aE]/[18\eta]$ where a is radius of the statolith, ρ is density of the statolith, ρ_0 is the density of the cytoplasm, and η is viscosity. Elastic modulus (E) is then found by: $E=6\eta v/a$. From the spaceflight data on the sedimentation times and ground experiments, the E_{chara}=0.1 dyne/cm^2 and E_{cress}=0.03 dyn/cm^2. These are very low values with *Chara* being much stiffer (by a factor of 3). Such experiments that utilize both microgravity and simulated gravity with centrifuges help establish the interaction between the amyloplast and the rest of the statocyte.

In 1986, Wendt and Sievers worked to establish the kinematics of the cytoskeletal network by using centrifugation. Their experiments showed that when cress roots are centrifuged, the structural polarity of the statocytes is altered. At low centrifugation (3000 g-min.), the stratification of organelles depends upon the statocyte's position. Central columella cells are affected more than lateral ones. Higher doses of centrifugation (60,000-360,000 g-min.) create a more uniform stratification in all statocytes. When exposed to normal gravity again following centrifugation, the endoplasmic reticulum (ER) is relocated parallel to the periclinal cell walls within a few minutes. This ER relocation is independent of the direction of gravity in relation to the root axis and independent of the applied dose of centrifugation. Cytochalasin B application before and during centrifugation totally inhibits the relocation of the ER. After removing the drug by rinsing, the statocytes

restore cell polarity and relocate their ERs. This supports the hypothesis that organelle distribution is controlled in part by the cytoskeleton and possibly a cellular program. When centrifuged roots are exposed to 1 g in the horizontal position, the latent period of gravitropism increases by 8-10 min. relative to controls, regardless of the previous level of centrifugation. The kinetics of the gravicurvature are virtually identical. The time needed for the statocytes to restore the distal cell polarity of organelles correlates with this increase in latent period (Wendt & Sievers, 1986). These findings indicate that the central columella cells of the cress root cap have a lower elastic modulus than those of the lateral columella regions. This is consistent with the idea that the effective elastic modulus of the cell changes temporally with the development and differentiation of the root cell. Wendt and Sievers' findings also confirm the idea of statoliths within a matrix of cytoskeletal filaments. It is still unknown if such an interaction occurs with direct amyloplast attachment to the microfilaments or whether they move and rest within a "bed" of cytoskeletal proteins as shown in Figure 2.8.

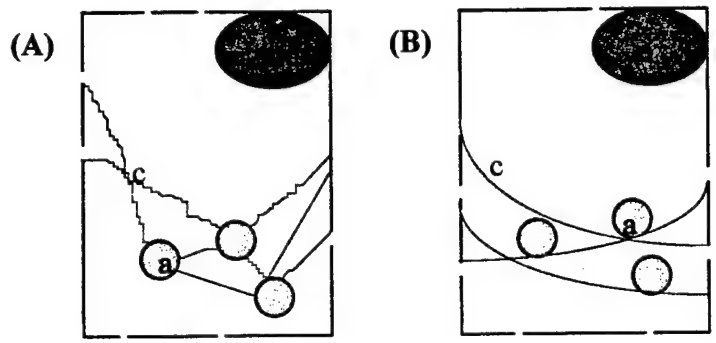

Figure 2.8 - Possible Amyloplast-Cytoskeleton Interaction
Shown are: n - nucleus shown in the typical position within columella cells, a - amyloplasts in a sedimented equilibrium position, and c - cytoskeletal microfilaments. (A) shows actual connections between the amyloplasts and the cell membrane and other amyloplasts via the cytoskeletal proteins while (B) shows the amyloplasts resting within a network of microfilaments.

In 1989, Sievers *et al.* investigated the presence of the cytoskeletal network within rhizoids of green algae and higher plants. Microfilaments were demonstrated in rhizoids of *Chara fragilis*. Each contains thick microfilament-bundles arranged longitudinally in the basal region. Much thinner bundles exist in apical regions which contact the statoliths and encircle them in the form of a dense envelope. In root statocytes of *Lepidium sativum* L., they detected the presence of an actin network as indicated by the fact that application of cytochalasin B resulted in an approximately threefold increase in the statolith sedimentation rate relative to controls (Sievers *et al.*, 1989).

In 1993, Guikema *et al.* studied the distribution of organelles within columella cells of sweet clover following growth under static or clinorotating conditions with the use of transmission electron microscopy. Developmentally conditioned polarity was observed; proximal location of the nucleus and distal accumulation of the ER. This

polarity was insensitive to clinorotation. In contrast, clinorotation altered the location of the amyloplasts. Cytoskeletal poisons had a profound effect on the extent, location, and structure of the ER during clinorotation. They also found that cytoskeletal interaction with the amyloplasts occurs on the amyloplast envelope. The envelope fraction had 17 polypeptides isolated using immobilized antibody technology. Clinorotation at 1 to 4 rpm disrupted the polarity of cytochalasin-treated columella cells as the amyloplasts were found distributed throughout the cytoplasm of rotated cells. No difference in nucleus location was noted. Cytochalasin D and colchicine were was used to disrupt microfilaments and microtubules, respectively. Taxol and phalloidin were used to restabilize microfilaments and microtubules, respectively. Only cytochalasin D disrupted the normal polarity under static conditions; the nucleus sedimented. All treatments disrupted the polarity under clinorotated conditions. Their conclusions included that the microfilaments maintain the ER and statoliths under tension (Guikema *et al.*, 1993).

It is clear that experiments in microgravity can provide a unique insight, that is not possible in 1 g, into the gravity-sensing mechanism within the plant root. In an article in Advances in Space Research, Kordyum (Kordyum, 1994) summarized the findings of several space flight experiments. In generalizing the effect of microgravity on the cellular level he concluded that three responses occur in microgravity:

1. Rearrangements of cytoplasmic organelles and calcium balance.
2. Physical-chemical properties of the plasmalemma are changed.
3. Enzyme activity is often enhanced.

These three responses serve to provoke acceleration of growth and differentiation of the cells subjected to microgravity. He also concluded that the plant gravireceptive apparatus still forms in space, but is non-functional.

2.4.2 The Differential Growth Response: The Elongation Zone

In 1995, Ishikawa and Evans wrote an article in which they defined specialized regions of the plant root that are extremely useful in dividing the root's gravitropic control system into manageable pieces. Their morphological descriptions of the root included the cap, apical meristem, the cell elongation zone, and the maturation zone. Relative frequency of cell division is plotted through the meristem and into a region called the distal elongation zone (DEZ). Relative rate of elongation is plotted through the meristem, through the DEZ, and into the elongation and maturation zones. The short article described the DEZ in detail and discussed the effect on the DEZ by various tropisms, auxin, electrical, and water stress. Data show that the differential growth response occurs initially and primarily within the specialized cells of the DEZ (Ishikawa & Evans, 1995). Their morphological definitions of the root zones are summarized in Figure 2.9 and is used throughout this thesis.

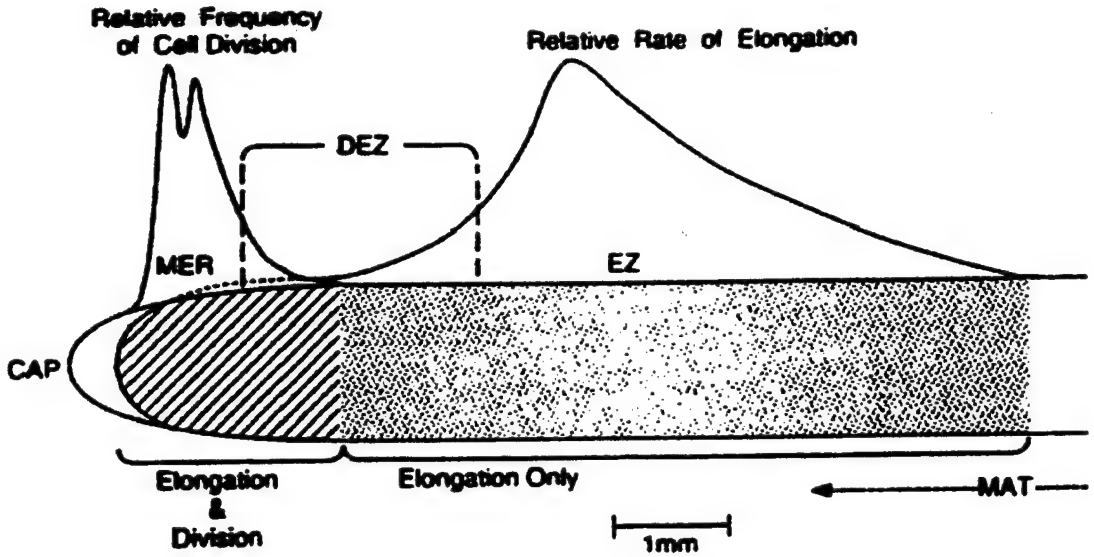

Figure 2.9 - Specialized Zones of Root Development
Relative rates of cell division and cell elongation are shown from the root cap (CAP), through the meristem region (MER), into the elongation zone (EZ), and, finally, into the maturation zone (MAT). The distal elongation zone (DEZ) is shown as a continuum between the meristem and elongation zones. Scale is appropriate for a typical root of maize. (Ishikawa & Evans, 1995)

In 1991, Ishikawa *et al.* used computer-based digitized video to analyze the gravitropic response in maize roots. The study found that a major factor causing the downward curvature during graviresponse is the induction of a very rapid elongation of cells in the DEZ on the top side of the root. The rate of elongation in these cells prior to gravistimulation is low with the majority of elongation occurring in the more basal portions of the elongation zone. In contrast, the rate of elongation of cells in this main portion of the elongation zone is inhibited by gravistimulation, especially in those cells on the bottom portion of the root (Ishikawa *et al.*, 1991). It is clear that the growth response occurs in specialized cells of the elongation zone and not the entire elongation region.

In 1992, Sievers and Zieschang provided a quantitative analysis of the validity of the Cholodny-Went theory. They found that the root graviresponses of both *Lepidium* and of *Phleum* show a characteristic curving process in four phases:

1. After the root has been placed horizontally, during the first 1-1.5 hrs, the relative elemental rates of elongation (RELELs) on the physical upper side increase compared to those of a vertically growing root, the RELELs of the lower side decrease.
2. A transient equality of RELELs follows on both sides.
3. After 2-3 hrs, the growth gradient inverts. Now the RELELs on the lower side are higher than those on the upper side.
4. After completion of the graviresponse, the RELELs on both sides are equal again.

After 15-20 min., the graviresponse begins, and at this time, a small region of maximal curvature is visible. Later on, this region extends and exhibits two local maximal values of curvature after 2-2.5 hrs of horizontal stimulation. Thus, there exist two maxima of curvature but only one RELEL maximum is found. In all the roots examined, the RELEL maximum is positioned basal to the apical maximum of curvature. Thus, the maxima of RELEL and curvature do not coincide. For Sievers and Zieschang it was obvious that the curving process began in a region 480-680 μm basal to the tip, where the cells are already on an average five times longer than the meristematic cells. This region of first visible curvature is represented by only six rhizodermal cells on both the upper and the lower flanks. These results gave rise to three main questions which suggest a modification to the classic Cholodny-Went theory (Sievers & Zieschang, 1992):

1. How is it possible that in a horizontal root a gradient first develops in one direction, and then 2 hrs later, without any obvious variation in conditions of gravity, a gradient in the opposite direction?

2. Which mechanisms are able first to produce only one maximum of curvature, later two maxima, then even transform the apical maximum to a minimum later on?

3. Why does a region of six rhizodermal cells, which is not situated directly at the beginning of the elongation zone but 100-130 μm nearer to the base, respond first to a signal coming from the root cap? In which properties do these cells differ from other cells?

Konings (Konings, 1995) also reviewed the different elongation behavior of the DEZ from that of the main elongation zone. He noted that the bending response does begin closer to the tip, in the region between the meristem and the elongation zone (the DEZ). He also noted that the cells most involved with a differential elongation were closer to the tip on the upper side of the root while those on the bottom side (those with more suppressed elongation) are farther from the tip. In *Phleum pratense*, the greatest proton efflux occurs in the DEZ of the upper-side of a gravistimulated root. These data indicate that the DEZ plays a role in the growth response portion of the control system, but it is also proposed that the DEZ has a role in the sensing of gravity.

Ishikawa and Evans (Ishikawa & Evans, 1990) examined gravity-induced changes in intracellular potentials in primary roots of 2-day-old mung bean (*Vigna mungo* L.) seedlings. Gravistimulation caused intracellular potential changes in cortical

cells of the elongation zone. The data suggest that the change in intracellular potential in the elongation zone is an early transduction event of the gravitropic response system. Ishikawa and Evans point out that there are at least two possible ways that these electrical changes within the elongation zone might occur:

1. An electrical signal induced by gravity detection within the root cap might move rapidly to the elongation zone; or
2. Cells in the elongation zone might be capable of sensing gravity directly.

These data suggest that the classic Cholodny-Went hypothesis of gravitropism, while still intact, requires a modification of its simplistic cause-and-effect chain of events from sensor, through transduction, and finally the growth response. The sensor may not be simply composed of a single statolith, but a combination of mechanisms working in parallel. The complex growth response within the elongation zone also indicates that the transduction may not simply result from a hormonal gradient within the elongation zone of the root and that the growth response is not uniform within the entire elongation zone, but is temporally and spatially specialized.

2.4.3 Transduction

This section is divided into three subsections. The first subsection examines the role of the auxins, principally the plant hormone IAA. The second subsection examines the role of the primary ion considered to be crucial in gravitropism, calcium. The final subsection examines the nature of membrane potentials, currents, and mucilage and their possible role in the gravitropic mechanism.

2.4.3.1 The Role of Auxin

Whether animal or plant, cells require communication between themselves to regulate and coordinate growth, metabolism, and other functions. Higher plants are dependent on signals from one part of the plant to another. In the last century, this was not an obvious concept. A German botanist, Julius von Sachs, proposed that chemical messengers were responsible for the formation and growth of various plant organs (Taiz & Zeiger, 1991). He also proposed that external factors such as temperature, gravity, and mechanical forces could affect the distribution of these chemical messengers. Sachs' work led to the eventual discoveries of the five classes of plant hormones: auxins, gibberellins, cytokinins, ethylene, and abscisic acid. These hormones aid in intercellular communication by interacting with specific protein receptors. All of the plant hormones are relatively small molecules, ranging from the small ethylene molecule (28 Da) to the largest molecule, gibberellin (346 Da). To date, findings indicate that these hormones are effective in very low concentrations such as 10^{-6} to 10^{-8} M. The first of the plant hormones to be discovered are the auxins. This class of hormones was found to play a major role in the regulation of plant elongation and in various growth responses known as tropisms. This hormone was the first to be linked with the gravitropic response as early as the initial theory of Cholodny and Went. Auxin is held to be the most important regulator of growth in plants. At a microscopic level, the auxins create membrane hyperpolarization and by stimulating the plasma membrane's H^+ ATPase, creates cell wall acidification. This brings about cell wall loosening and promotes elongation growth in these tissues

(Millner, 1995). The principal auxin in higher plants was identified in the mid-1930s as indole-3-acetic acid (IAA). The term auxin applies to a chemical substance that stimulates elongation in coleoptiles and stems, but IAA is by far the most important, naturally occurring auxin (Taiz & Zeiger, 1991). Figure 2.10 displays the chemical structure of IAA. In neutral pH, IAA has a strong negative charge separated from a weaker positive charge on the ring structure. This separation is on the order of about 0.055 nm. The charge separation is the likely requirement for auxin's activity. The weak positive charge on the indole ring is on the nitrogen atom while the negative charge arises from the dissociation of the proton from the carboxyl group.

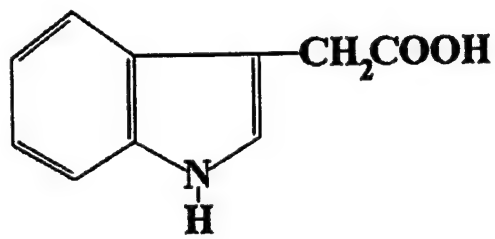

Figure 2.10 - Indole-3-Acetic Acid (IAA)

The classic Cholodny-Went hypothesis proposed that the differential growth response of gravitropism (and other tropisms) is the result of an auxin gradient between the upper and lower sides of the root. Few specifics were given as shown in this excerpt from Went's 1937 book on phytohormones:

> Growth curvatures, whether induced by internal or by external factors, are due to an unequal distribution of auxin between the two sides of the curving organ. In the tropisms induced by light and gravity, the unequal auxin distribution is brought about by a transverse polarization of the cells, which results in lateral transport of the auxin (Went & Thimann, 1937).

Not only does this statement leave room for the mechanism for auxin redistribution, but of the various auxins present in the root, it was unknown as to which auxin(s) were responsible for the curvatures. Various auxins were investigated over the century. Early work was accomplished with externally applied auxins in an attempt to replicate the gravicurvatures. By the end of the 1970's it seemed that abscisic acid was the inhibitor that created the bending response, but was later found to occur in extremely low concentrations; too low to create the known responses. Now, idole-3-acetic acid (IAA) is the best candidate for the auxin of Cholodny-Went (C-W) (Salisbury & Ross, 1992b). A 1991 review by Evans elucidates the evidence for IAA as the gravitropic effector. Evans pointed out that arguments against the C-W hypothesis were based primarily on concerns over the timing and magnitude of hormone asymmetry. He feels that recent evidence shows such asymmetry develops early and is sufficiently large to account for curvature. He concluded that although the C-W hypothesis is fundamentally valid, recent comparative studies of the kinetics of curvature and the timing of the development of hormone asymmetry indicate that this hypothesis alone cannot account for the intricacies of the gravitropic response. It appears that time-dependent gravity-induced changes in hormone sensitivity as well as changes in sensitivity of the gravity receptor play important roles in the response (Evans, 1991). A brief list of all the evidence pointing to IAA as the growth response effector:

1. An asymmetric external application of auxin produces growth curvatures in both shoots and roots similar to gravicurvature responses (Evans *et al.*, 1986).

2. When inhibitors of auxin transport are applied to a gravistimulated plant, gravitropic curvature is inhibited in both shoots and roots (Lee *et al.*, 1984).

3. Radiolabeled IAA applied to shoots or roots accumulates along the lower side of these organs following gravistimulation [Young, 1990 #94]. This also provides evidence in support of the importance of the auxin transport mechanisms in gravitropism.

4. The altered growth of cucumber hypocotyls during gravitropism appears to be attributable to change in the wall relaxation process, a process thought to be controlled by auxin (Cosgrove, 1990).

5. Within the coleoptile of maize, auxin controls the orientation of cortical microtubules in the outer walls of the outer epidermis, and the change in the orientation pattern of these microtubules in gravistimulated coleoptiles is consistent with the development of a gradient of auxin or auxin activity across the coleoptile (Nick *et al.*, 1990).

6. Following gravistimulation, free IAA in maize shoots becomes rapidly redistributed [Bandurski, 1984 #98].

7. Following gravistimulation of soybean hypocotyls, an asymmetry of auxin-regulated RNAs develops rapidly. Auxin-induced RNAs predominate along the lower side (McClure & Guilfoyle, 1989).

Evans found that auxin asymmetry develops prior to curvature in dicotyledonous as well as monocotyledonous plants. The asymmetries are moderate and it is clear that the auxin dose/response curve in shoots is arithmetic not

logarithmic. There are auxin-sensitivity mutants in which root growth is resistant to inhibition by high levels of IAA. When barley roots are made agravitropic through chemical treatment, those roots are also an order of magnitude less sensitive than normal roots to growth inhibition by IAA. (Evans, 1991). Therefore, a very slight gradient of auxin is sufficient to induce curvature in shoots. Some of Evans' work on maize showed interesting kinetics within the gravitropic growth response that is displayed in Figure 2.2 earlier in this chapter. During the first hour following stimulation the growth rate for the side of the root producing the outer side of the curve increased nearly **threefold** in some regions in comparison with the rate prior to stimulation. During this time, the rate along the side of the root producing the inner side of the curve dropped nearly to zero. The roots curved downward during this time period. Later in the response, the growth rates on the two sides of the root became equal. This occurred because the growth rate along the upper side decreased somewhat while the rate along the lower side increased. This new rate of elongation was greater than that prior to gravistimulation. Still later in the response, the growth gradient was reversed, with a portion of the root along the inner side of the curve growing rapidly while the growth rate along the outer side of the curve dropped to zero. This occurred **before** the root reached vertical (Evans, 1991). These facts infer that a change in cellular sensitivity to auxin and/or a change in statolith sensitivity is occurring in the response mechanisms.

Modeling of the growth response portion of the gravitropic control system will require data that relate auxin levels with growth rates within the elongation zone.

Such data is found in the work of Pilet in 1989. In gravistimulated maize roots, he found that the IAA content in the upper and lower parts were 27.8 ± 0.9 ng/g and 35.1 ± 1.1 ng/g, respectively. At the same time, the fresh mass was similar and the IAA taken from opposing sides within vertical controls was identical (Pilet, 1989). The IAA gradient was significant, but could it account for the differential growth? A later study by the team of Meuwly and Pilet showed that gravicurvature in maize produced a mean bending rate of 21 degrees/hour which corresponds to a growth rate of 0.67 ± 0.04 mm/hour on the upper side and 0.19 ± 0.03 mm/hour on the lower side. Enhanced growth was found between 2.5 and 3.5 mm from the root tip while inhibited growth was found between 2 and 5 mm from the tip (Meuwly & Pilet, 1991). This led the team to conclude that the slight IAA redistributions found in the earlier study could explain the differential elongations. Dose-response data have been found that indicate an inverse linear relationship between root elongation rate and IAA level within the elongation zone. Roots elongating at 0.2 mm/hour contain 5.5 ± 0.4 ng of IAA (total amount within 50 segments) while those roots elongating at 1.2 mm/hour contain 1.8 ± 0.2 ng of IAA within 50 segments analyzed (Pilet, 1992). This finding is in agreement with Evans' earlier assertion that the IAA effect on elongation is arithmetic not logarithmic. This and later data on the relationship of IAA to elongation rates and curvature is summarized in Table 2.6.

Table 2.6 - Elongation Rates and Level of IAA

Level of IAA	Growth Rate	Curvature Rate	Comments
27.8 ± 0.9 ng/g	0.67 ± 0.04 mm/hr	21 degrees/hour	12 samples of 100 segments (1-5 mm from the tip)
35.1 ± 1.1 ng/g	0.19 ± 0.03 mm/hr		
1.8 ± 0.2 ng/50 segments	1.2 mm/hr	-	segments taken as 2.5-5 mm from tip
5.5 ± 0.4 ng/50 segments	0.2 mm/hr		

Some have suggested that the transport of auxin out of the root cap may not require active processes within the cells of the cap, but instead may involve an apoplastic pathway within the mucilage. Evidence exists that does point to the necessity of the root cap mucilage in transducing the gravity signal. In 1989, Moore characterized the plasmodesmata linking the root cap and root in primary roots *Zea mays*. He found that they are restricted to approximately 200 protodermal cells bordering approximately 110000 square microns of the calyptrogen of the root cap. This area is less than 10% of the cross-sectional area of the root-tip at the cap junction (Moore & McClelen, 1989). The obvious conclusion is that gravitropic effectors moving from the root cap to the root can move symplastically only through a relatively small area in the center of the root. Decapped roots are non-responsive to gravity. However, decapped roots whose caps are replaced immediately after decapping are strongly graviresponsive. Thus, gravicurvature occurs only when the root cap contacts the root, and symplastic continuity between the cap and root is not required for gravicurvature. Most interestingly, after complete removal of mucilage from the root tip, the root is non-responsive to gravity. Taken together, Moore's data suggests that gravitropic effectors move apoplastically through mucilage from the cap to the

root. Even more convincing data was accomplished a year later in the same lab. Work was accomplished on the primary root of the mutant 'Ageotropic' cultivar of *Zea mays* which is non-responsive to gravity. The mutant root caps secrete little or no mucilage and touch the root only at the extreme apex. A gap separates the cap and root at the periphery of the cap. Applying mucilage from normal roots or substances with a consistency similar to that of mucilage to tips of mutant roots caused these roots to become strongly graviresponsive. Gravicurvature stops when these substances are removed. Caps of some mutants secrete small amounts of mucilage and are graviresponsive. Moore believed that these results indicate (1) the lack of graviresponsiveness in the mutant results from disrupting the transport pathway between the cap and root, (2) movement of the growth-modifying signal from the cap to the root occurs via an apoplastic pathway, and (3) mucilage is necessary for normal communication between the root cap and the root in this cultivar (Moore *et al.*, 1990).

2.4.3.2 The Role of Calcium

Research over the last decade has indicated a crucial role for calcium ions (Ca^{2+}) in the mechanism of root gravitropism. Calcium's role within the entire gravitropic control system may encompass all three subdivisions; the sensor, signal transduction, and the growth response. The majority of experimental evidence indicates that Ca^{2+} is necessary, but not necessarily sufficient, to the transduction mechanism and some findings indicate that Ca^{2+} may play a role within the growth response itself. Some of the results pointing to calcium's role in transduction are as follows:

1. Ca^{2+} movement across the root tip (meristem and root cap) is found to be at least 20 times greater than movement across the elongation zone. The rapid movement of Ca^{2+} across the tip is severely inhibited in roots from which the root cap had been removed. Gravistimulation has no effect on Ca^{2+} movement across the elongation zone, but causes a strong asymmetry in the pattern of Ca^{2+} movement across the tip; inducing polar movement of Ca^{2+} toward the lower side of the root cap (Lee *et al.*, 1983) (Zieschang & Sievers, 1994).

2. The application of calcium-chelating agents to the tips of maize and cress roots cause a loss of gravitropic sensitivity (Lee *et al.*, 1983) (Wendt & Sievers, 1989).

3. Treatment of maize or pea roots with inhibitors of auxin transport (morphactin, naphthylphthalamic acid, 2,3,5-tri;odobenzoic acid) prevents both gravitropism and gravity-induced polar movement of calcium across the root tip. This result indicates that calcium movement and auxin movement are closely linked in roots and that gravity-induced redistribution of calcium across the root cap may play an important role in the development of gravitropic curvature (Lee *et al.*, 1984).

4. The decreased graviresponsiveness of primary roots of the maize mutant cultivar, Amylomaize, correlates positively with a reduced movement of Ca^{2+} across its root tip. The ratio of Ca^{2+} in the receiver block on bottom to Ca^{2+} in the receiver block on top after 1 hour in the wild-type cultivar is 53% greater than that for gravistimulated roots of Amylomaize seedlings. This more pronounced movement of

the Ca^{2+} after 1 hour correlates positively with their roots having curved significantly more than those of Amylomaize (Moore, 1986).

5. Ca^{2+} accumulates along the lower side of caps of horizontally-oriented roots, especially concentrated in the mucilage (2.5-3 times that on the upper side). No significant difference in the concentrations of Ca^{2+} is found in the central cytoplasm of columella cells along the upper and lower sides of caps of horizontally-oriented roots. Ca^{2+} also accumulates (largely in the mucilage; 6 times that on the upper side) along the lower side of the elongating zone of these roots (Moore *et al.*, 1987).

6. Calmodulin activity per mm of root tissue was about 4-fold higher in the apical mm (including the root cap) than in the subtending 3 mm of positively gravitropic cultivars of maize. However, calmodulin activity is very low in the apical mm of roots of dark-grown seedlings of the Merit (agravitropic) cultivar. Upon illumination, the calmodulin activity in the apical mm increased to a level comparable to that of gravitropic seedlings and the roots became positively gravitropic (Stinemetz *et al.*, 1987).

7. Maize roots, which are agravitropic in the dark, release more Ca^{2+} in their root caps and become graviresponsive when illuminated. Diagravitropic maize roots in the dark contain much less Ca^{2+} in their root caps than their graviresponsive, illuminated counterparts (Suzuki *et al.*, 1994) (Leopold & Wettlaufer, 1988).

8. Auxin transport in the apical region of intact *Zea mays* roots is preferentially basipetal, with a polarity (basipetal transport divided by acropetal transport) of 6.3. Application of calcium to the root cap enhanced basipetal

movement of auxin, increasing polarity from 6.3 to 7.6. One conclusion to this finding is that transport of auxin is dependent upon Ca^{++}-dependent auxin pumps. Application of a calcium chelator greatly decreased basipetal auxin movement, reducing polarity from 6.3 to 3.7 (Hasenstein & Evans, 1988).

9. External Ca^{2+} is required for normal graviresponsiveness and a normal ratio of downward to upward cytoplasmic streaming velocities within the characean alga *Nitellopsis obtusa*. The Ca^{2+} concentration of the medium determines the polarity of cytoplasmic streaming. Less than 1 μM Ca^{2+} resulted in a ratio<1 and agravitropism while greater than 1 μM Ca^{2+} resulted in a ratio>1 and a normal gravity response (Wayne *et al.*, 1990).

10. When agar containing calcium chloride is applied to one side of the DEZ, the root curves toward the side of application. This response could not be induced by plain agar indicating that the reaction was not from thigmotropism, but from direct calcium-induced inhibition of growth (Ishikawa & Evans, 1992).

11. The return of positive gravitropism following the decapping of maize roots correlates with the development of a downward gradient of Ca^{2+} within the apoplast (mucilage). Binding of the apoplastic Ca^{2+} by EDTA prevents the return of positive gravitropism (Bjorkman & Cleland, 1991).

These findings provide for a solid argument that Ca^{2+} is an essential messenger in the gravitropic transduction mechanism. Whether Ca^{2+} is a primary or secondary messenger in the process is still open for debate. In 1992, Scott proposed a series of

questions that need to be answered to place Ca^{2+} in its proper position within the gravitropic model:

> Is a lateral redistribution of Ca^{2+} in the root cap responsible for triggering the gravitropic response? Is Ca^{2+} a second messenger or perhaps a different type of chemical primary messenger? Does Ca^{2+}, through activation of other chemical effectors or electrical polarity, cause a lateral asymmetry of one or more hormones in the zone of elongation and does this result in overall growth stimulation or inhibition in the horizontal root? Does a hormonal asymmetry come about because of lateral transport or is it due to basipetal movement from the tip along the bottom of the root to the zone of elongation (Scott, 1992)?

Clearly, auxin and calcium are involved in the gravitropic transduction mechanism. Which gradient forms first in the chain of transduction events is still unknown. As Roux points out in 1992, textbooks offer a naive view indicating that the auxin gradient occurs as a final step and then differential growth occurs (Roux, 1992). Experimental evidence indicates a much more complex interaction between auxin and Ca^{2+}. Ca^{2+} may be involved with both the auxin transport, but also auxin's effect on cell elongation:

1. In studies investigating the interaction of Ca^{2+} and auxin on root elongation in seedlings of *Zea mays* L., seedlings raised in either high or intermediate concentrations of Ca^{2+} and subjected to auxin concentrations from 0.1 to 10 micromolar showed strong inhibition of downward unidirectional elongation. However, in roots of seedlings raised in low concentrations of Ca^{2+}, auxin concentrations as high as 10 micromolar caused only slight inhibition of elongation. The data indicate that Ca^{2+} may be necessary for the growth-regulating action of auxin (Hasenstein & Evans, 1986).

2. Results indicate that both the number of auxin binding sites and their ability to interact with auxin were strongly affected by gravistimulation with the lower cells of the elongation zone more sensitive than the upper cells (Salisbury, 1992a).

3. Kinetics of graviresponding roots strongly indicate that auxin sensitivities are modulated (Evans, 1991) (Evans, 1992).

4. EGTA, a Ca^{2+}-chelator interferes with the transport of IAA across the root cap of maize (Hasenstein & Evans, 1988).

5. In the root cap of maize, lateral distribution of IAA is promoted by Ca^{2+} (Young & Evans, 1994).

Various conclusions can be derived from these data. Ca^{2+} could sensitize the cells of the elongation zone to the effects of IAA. In this case, an immediate auxin gradient may not be required for the differential response or a smaller gradient than originally conceived may be possible when factoring in the effects of Ca^{2+}. Secondly, the Ca^{2+} may create a sink for auxin either for the transport process or within the elongation zone itself (Konings, 1995).

2.4.3.3 Significance of Changes in Membrane Potential

When attempting to identify the mechanisms responsible for the transduction of the gravity signal in the plant root. The dynamics of the transduction mechanism must fit the growth response timing data. If a hormone gradient, proposed as the transduction mechanism, actually takes 30 minutes to occur but the growth response occurs in 10 minutes, the transduction mechanism requires refinement. Therefore the dynamics of all reactions detectable within the plant root following gravistimulation

must be considered when determining the transduction mechanism models. One of these reactions, root potential changes, appears to provide very stringent time period limitations for the transduction model.

Behrens (Behrens *et al.*, 1982) suspected a close connection between the current and the transduction of information from the root cap to the elongation zone following graviperception in the cap after an experiment where he examined the naturally occurring currents around *Lepidium sativum* L.. A more or less symmetrical pattern of current was found around vertically oriented, downward growing roots. Current entered the root at the root cap, the meristem, and the beginning of the elongation zone and left the root along most of the elongation zone and in the root hair zone. After the root was tilted to a horizontal position, they observed current flowing acropetally at the upper side of the root cap and basipetally at the lower side within about 30 seconds in most cases. The relatively fast change of 30 seconds gives us insight into the time response of characteristics of the transduction mechanism. Later experiments would confirm this short response period.

Instead of currents, Behrens also measured membrane potentials in the putative statocytes of *Lepidium sativum* three years later. Vertically growing roots showed a stable resting potential of -118+-5.9 mV without spontaneous fluctuations. After tilting the root 45° from the vertical, an electrical asymmetry was observed. Statocytes on the physically lower side of the root depolarized by approximately 25 mV (an absolute potential of -93 mV, a change of 21% from the vertical root). This depolarization occurred after only 8 seconds and reached minimum (approx. -93 mV)

after 170 sec. This depolarization was the earliest event in graviperception ever recorded at the time and remains so today (Behrens *et al.*, 1985). Obviously, any model of gravity sensing and transduction must take this data into account. After depolarizing, the cell repolarized within 60 sec to a potential only approximately 10 mV more positive than the original vertical root (approx. -108 mV). Statocytes on the upper flank showed a slow hyperpolarization ($t_{1/2h}$- half time for hyperpolarization = 168 sec) reaching a final, stable potential at a level 10 mV more negative (approx. -128 mV). These effects of gravistimulation were tissue-specific, since cells in the cortex and rhizodermis showed no similar effects.

Experiments on the electrical characteristics of roots following gravistimulation have continued to the present day. Various species and methodologies have been used and results appear to consistently indicate a rapid time response in the gravity perception and transduction mechanisms of the plant root. Table 2.6 (next page) summarizes the current research efforts in this area.

Table 2.6 - Examination of the Electrical Properties of Gravistimulated Roots

NAME	YEAR	SPECIES	Findings Following Gravistimulation
Behrens	1982	*Lepidium sativum*	Within 30 sec, current flowed acropetally on the top and basipetally on the bottom (Behrens *et al.*, 1982)
Behrens	1985	*Lepidium sativum*	Bottom membrane depolarized within 8 sec while the top hyperpolarized (Behrens *et al.*, 1985)
Bjorkman	1987	*Zea mays*	Current shifted within 3-4 min to a predominant outward current in the columella region. Current density remained constant distal of the columella region (Bjorkman & Leopold, 1987)
Ishikawa	1990	*Vigna mungo* L.	Top cortical cells of the elongation zone hyperpolarized within 30 sec while bottom cells depolarized. Maturation zone showed no changes. Failed to measure root cap (Ishikawa & Evans, 1990)
Weisenseel	1992	*Lepidium sativum*	Current symmetry changes in the root cap and meristem. Current leaves upper side and enters lower side. Roots treated with low calcium showed no gravitropism and no current changes on gravistimulation (Weisenseel *et al.*, 1992)
Ishikawa	1994	*Zea mays* & *Vigna mungo*	Upper DEZ hyperpolarize within 30 sec along with rapid potassium uptake from the stele (Ishikawa & Evans, 1994)
Schatz	1994	-	Applied Gouy-Debye-Huckel (GCDH) theory to model membrane changes due to gravitational stresses. Showed that surface potential varies by layer deformations at horizontally oriented membranes (Schatz *et al.*, 1994)
Momonoki	1997	*Zea mays*	Showed the existence of acetylcholinesterase between the stele and cortex. The enzyme was found to have higher hydrolytic capability on the bottom of a horizontal plant (Momonoki, 1997)

2.5 Summary and Conclusions

The gravitropic reaction has been studied for over one hundred years, but much work remains to be accomplished to fully understand this plant movement. Analysis of gravitropism from the approach of control theory and system identification is only in its beginning stages with even the most basic quantification of time response characteristics not fully documented. Various attempts have been accomplished to describe the gravitropic response through mathematical descriptions that imitate the response, but little has been done to apply system engineering tools to the biological processes that make up the gravitropic response other than to break the overall system into the smaller mechanisms: sensor, transduction, and differential growth.

The putative sensors for the gravitropic system are the amyloplasts within the central columella cells of the root cap. Although sedimenting plastids may not be the unique gravity sensor in all species of the plant kingdom, the evidence appears to indicate that in the higher plants, such as maize, these amyloplasts are necessary and sufficient for gravity perception. The actual curvature in the root tip is created nearly 3 mm basal (for maize) to the point of perception and appears to be caused by a differential in elongation rates between the top and bottom side of the gravistimulated root. This differential elongation rate appears to be mediated by IAA, calcium, and other possible factors. Transduction is the series of mechanisms that take the gravity signal, sensed at the distal end of the root, to the actual cells that display the differential elongation. Cellular potentials and electric currents monitored across the

root appear to indicate a more immediate transduction mechanism than simply cellular transport of the IAA hormone.

CHAPTER 3

THE GRAVITROPIC SENSOR

3.1 Introduction

For any mechanism to act as a sensor of a given stimulus, the mechanism must both be susceptible to and perceive changes in the given stimulus. The plant root, a typical biological system, is complex in both its structure and biochemistry. To single out a specific organelle as the one and only gravity sensor, or statolith, seems presumptuous at the outset. Obviously, gravity acts upon every cell, organelle, and apoplastic structure in the plant root, but the real question is whether the structure produces a "signal" based on changes in the gravity vector. One intriguing idea in this area is the model that the entire cell or collection of cells perceives gravity through altered distributions of tensions along the plasma membrane mediated by the cytoskeletal network (Ding & Pickard, 1993; Pickard & Ping Ding, 1993; Pickard, 1994). This model of perception proposes the cell as a whole as the gravity sensor since altering the cell's orientation to gravity would cause alteration in the tensions in the plasma membrane and thereby cause an altered distribution of mechano-sensitive channel opening along the membrane. Though intriguing, this model cannot account for the substantial evidence that points to the truly specialized, amyloplast sedimentation as the single gravity sensor in the plant root. This is not to say that several different gravity-sensing mechanisms cannot exist across the range of prokaryotes and eukaryotes. Various categories of cell-environment interactions obviously exist that allow for differing gravity sensing mechanisms (Todd & Klaus,

1996). Since this thesis concentrates simply on the higher-plant root gravitropic response, the numerous gravity-mediated plant reactions such as gravimorphism, reaction-wood formation, lignin-cellulose ratios, cytoplasmic streaming, and gravitaxis are placed aside in response to the substantial evidence that the amyloplasts of the columella cell are the unique gravity sensor of the higher-plant root.

Compelling evidence as to the unique nature of sedimenting amyloplasts as the plant root gravity sensors has been compiled over the last one hundred years. Section 2.4.1 (and subsections) of this thesis details this evidence. In arguing for the columella cell-as-the-statocyte hypothesis, four general observations stand out concerning the columella's unique ability as a gravity sensor and two recent experiments stand out as truly pointing to the columella as the necessary and sufficient sensor for gravitropism. The general observations include the fact that the columella location is highly specialized. Since the purpose of the gravitropic motion is to orient the root tip in response to gravity, the sensor should be placed on the platform that is to be oriented. If a robot arm were being designed, the sensor that detects the position of the arm would be designed into the arm not into the "head" of the robot. Likewise, the location of the columella is at the core of the root cap at the very tip of the root and is protected by layers of outer peripheral cells and a mucilage coat. Additionally, these columella cells favor sedimentation of the amyloplasts like no other cell in the entire plant. This sedimentation creates the "susceptibility" characteristic for a gravity sensor. The columella cell is only a single step in the differentiation of the root cap cells. From creation in the root cap meristem region near the cap-root junction, the cell begins with small amyloplasts, a relatively central nucleus, random endoplasmic

reticulum (ER), and a typically large vacuole. As differentiation continues, the nucleus moves basally, the amyloplasts become larger and sediment distally, the ER concentrates peripherally, and the vacuole decreases in size. The basal movement of the nucleus and small vacuole is crucial for unobstructed sedimentation of the plastids. This mature columella cell continues to differentiate into a peripheral cell by once again producing a large vacuole, mobilizing starch from the amyloplasts (decreasing their size), and depositing large amounts of mucilage in Golgi vesicles which is later deposited into the apoplast coating the root cap. This differentiation sequence has been observed to cover 36-48 hours. Both the morphologically and temporally specialized form of the columella cell strongly validates its purpose as a gravity sensor. Thirdly, sedimentation of the statolith correlates with positive gravitropic competence in every wild-type plant (Sack, 1997). The final general observation that favors the unique statocyte is the reduced gravitropic sensitivity found in starchless and intermediate starch mutants described in section 2.4.1.3 of this thesis.

Two recent experiments truly indicate the role of the columella cell as the plant root's statocyte. Kuznetsov and Hasenstein (Kuznetsov & Hasenstein, 1996) established the diamagnetic properties of the starch-filled amyloplasts in 1996 and then placed the root tip into a high gradient magnetic field. The repulsion of the amyloplasts was shown both *in vitro* and *in vivo*. The movement of the amyloplasts away from the magnetic field produced a curvature response commensurate with that of a graviresponse following sedimentation of the amyloplasts due to gravity. Applied magnetic fields to any region of the root tip other than the columella region produced no such response. These data significantly point to the necessary and sufficient nature

of the columella cells as the statocytes. The second experiment (Blancaflor *et al.*, 1998) used laser ablation techniques to remove specific columella cells in *Arabidopsis thaliana*. Following ablation, the group analyzed the plant root's response to gravity including time-course of curvature, presentation time, and steady-state angle achieved. Ablation of peripheral cells or meristematic cells of the root cap caused no change to gravitropic behavior. Ablation of any columella cell inhibited the gravitropic behavior with the most significant inhibition caused by ablation of the innermost columella cell of the second storey. A six-fold increase in presentation times with significant increase in steady-state angles was identified with destruction of the innermost, second-story columella cells.

With the four categories of circumstantial evidence and the two very recent experiments providing functional confirmation for the role of columella cells as the plant root statocytes, this thesis assumes the sensor for the plant root gravitropic mechanism is the root cap columella cell and provides the groundwork for modeling of the dynamics of the columella cell.

3.2 Objective

The objective of this chapter is to develop a mathematical model of the physical principles governing the plant root's putative sensor, the columella cell or statocyte. This development requires both mathematical modeling and experimental data acquisition. The information required includes the characteristics of the the columella cell. Modeling begins with verification of the mathematical feasibility of the statolith perceiving gravity in the presence of the cell's background noise. The

amyloplast is the only cell organelle that is witnessed to sediment in response to a change in the gravity input vector, but is this sedimentation sufficient to perceive gravity? This inquiry into feasibility establishes whether amyloplast sedimentation provides the work or energy required to perceive gravity over background thermal noise in the cytoplasm and provide the energy required to initiate the cascade of transduction events within the plasma membrane.

After establishing the amyloplast as a feasible statolith, the following section creates a force balance model using the free-body diagram shown in Figure 3.1. Viscosity and elastic forces created by the actin network are values that need to be refined through experimentation. The actin fibers provide a force on the amyloplast analogous to a spring while viscosity, through Stokes' drag, provides a force analogous to a damper. This model essentially applies the principles of the classic spring-mass-damper system to the columella cell.

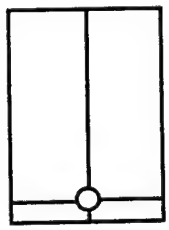

Figure 3.1 - Statolith Model

To develop a more accurate picture of the interactions between the statoliths and the cytoskeletal network inside the columella cell, viable columella cells were examined in order to analyze the amyloplast sedimentation dynamics. Velocity profiles of the sedimenting amyloplasts were constructed for both normal maize columella cells

and those treated with cytochalasin D. The experiment, described in section 3.4.1 of this chapter, was used to gather data that would aid in choosing a model set for the statolith-cytoskeletal interaction within the columella cell. Some possible model sets for this interaction are shown in Figure 3.2.

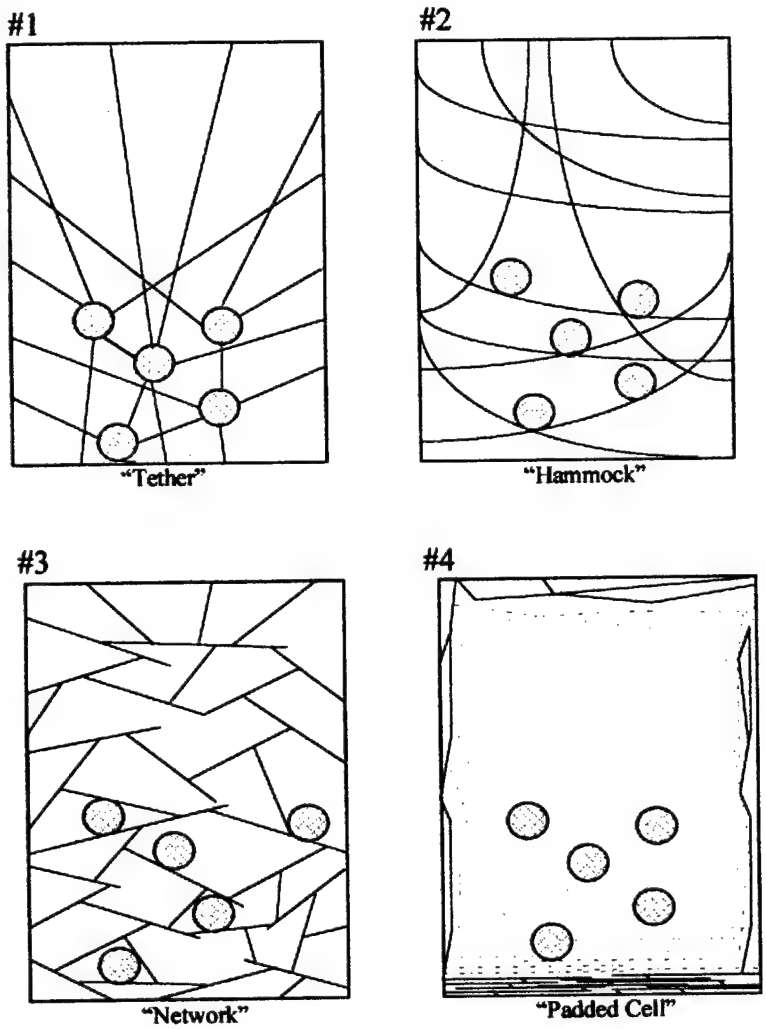

Figure 3.2 - Possible Models of Statolith-Cytoskeletal Interaction
Model #1 is the classic, "textbook" model of interaction where actin is tethered directly to the statoliths. Model #3 is a random network or mesh of interconnecting actin fibers while Model #2 is a slight alteration with fibers running side-to-side with a higher density near the distal cell wall. Model #4 is a model set where the actin fibers are in greatest concentration near the cell periphery, but the elastic forces are derived from not only actin, but microtubule and endoplasmic-reticulum interaction also.

Once the sedimentation dynamics are analyzed, this information refines the mathematical model for the columella cell equations of motion. A computer model is built where the viscosity and number of actin attachments can be adjusted until the simulated velocity and acceleration profiles of sedimenting amyloplasts is equivalent to

the experimental results. As further confirmation on the sensor model, the results of the 1990-1991 TEXUS rocket experiments can be used to verify the predicted movement of the amyloplasts upon introduction to microgravity. Figure 3.3 summarizes and flowcharts the methodology for accomplishing this chapter's objective.

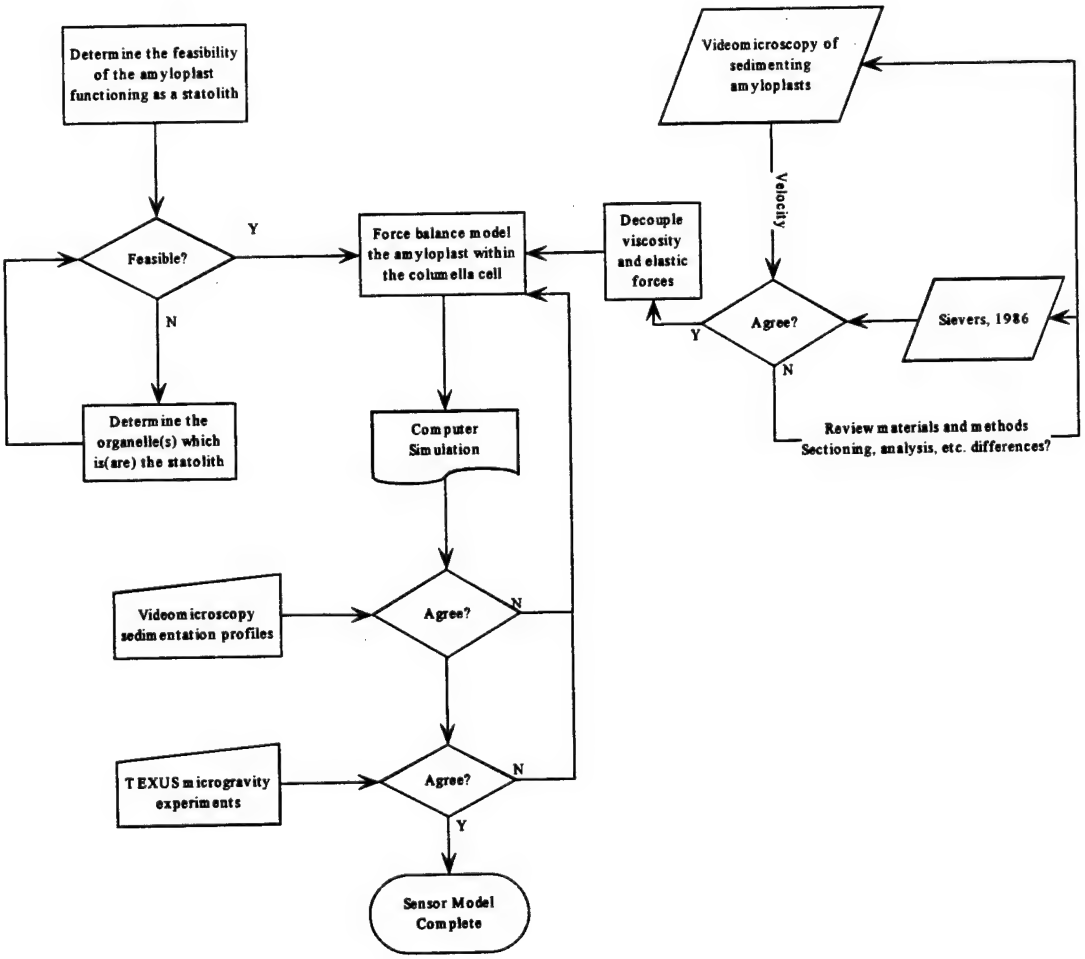

Figure 3.3 - Flowchart for Objective #1 Accomplishment

3.3 Theory Development

As shown in the flowchart of Figure 3.3, the first step of sensor modeling requires an analysis of the feasibility of the putative statolith actually perceiving gravity. After feasibility is established, further modeling is accomplished. The following subsections explore these two theoretical developments.

3.3.1 Development of Statolith Feasibility

The first step in quantifying the feasibility of the amyloplast as a statolith in the columella cell of a maize root is to examine the relative effect gravity has on the plastid as compared to that of diffusion. The buoyant weight (W_b) of the amyloplast in 1 g, its weight minus the buoyant force of displaced cytoplasm, is given by:

$$W_b = V_{amyl}\left[\rho_{starch} \cdot s + \rho_{stroma}(1-s) - \rho_{cyto}\right]g \qquad (3\text{-}1)$$

The values for amyloplast volume (V_{amyl}), starch density (ρ_{starch}), fraction of starch in the amyloplast (s), stroma density (ρ_{stroma}), and cytoplasmic density (ρ_{cyto}) are all found in Table 1-1 in Chapter 1 of this thesis. This buoyant weight for the typical maize amyloplast in a 1 g environment is:

$$W_b = 9.59\text{x}10^{-9}\,\frac{g \cdot cm}{s^2} \equiv 9.59 \text{ nanodynes} \equiv 9.59\text{x}10^{-14}\,N \qquad (3\text{-}2)$$

This is an extremely small weight indeed, but the real question is whether this small force due to gravity is greater or smaller than those forces directing "Brownian" motion. If so, then the sedimentation of the amyloplast due to gravity is dominant over the thermal background, and the "susceptibility" of the plastid to gravity would be demonstrated, a requirement to be a gravity sensor. The Peclet number (Pe), which

represents the ratio between a body's linear movement versus its random-walk movement due to "Brownian" motion, is given by:

$$Pe = (\text{velocity})(\text{distance}) / D \qquad (3-3)$$

Where D is the diffusion coefficient for the body that undergoes a linear movement for a given distance under a terminal velocity. Peclet numbers greater than approximately 10 indicate predominance of the linear forces (gravity in this case) while Peclet numbers less than 0.1 indicate dominance of diffusion. The diffusion coefficient for the amyloplast (roughly spherical in structure) can be approximated by the Stokes-Einstein Equation for the diffusion of spheres:

$$D = \frac{kT}{6\pi\eta r_{amyl}} \qquad (3-4)$$

Where the diffusion coefficient (D) is found using Boltzman's constant ($k=1.38\times10^{-23}$ J/^{0} K), the Kelvin temperature ($T=25^0C\equiv77^0F\equiv298.15^0K$), the cytoplasmic viscosity (η), and the radius of the amyloplast (r_{amyl}). Using a lowest value for viscosity from Table 1-1 in Chapter 1 and the size of the maize amyloplast from Table 1-2, the diffusion coefficient for a maize amyloplast is $D_{maize}=1.16\times10^{-9}$ cm^2/s. This is a slightly higher value than that of a typical bacterium ($\approx10^{-10}$ cm^2/s) which is considered the organism at the border between domination by gravity or diffusion. This value is also conservative since the lowest estimate of cytoplasmic viscosity is used (1 cp). Higher viscosity would have decreased the diffusion coefficient. The highest estimated cytoplasmic viscosity (20 cp) creates $D=5.8\times10^{-11}$ cm^2/s while the midrange (11 cp) creates $D=1.05\times10^{-10}$ cm^2/s. The smaller D-values appear the most reasonable because

of the relatively large size of the amyloplast and as Section 3.5.3 will present, the actual viscosity does appear to be greater than originally assumed.

The low value for a maize amyloplast's diffusion coefficient immediately indicates a "non-Brownian" dominance of forces, but with such a small buoyant weight the two effects still need comparison. The Einstein Random Walk equation predicts the distance (x) from the starting point of a particle undergoing diffusion:

$$< x >^2 = 2Dt \qquad (3-5)$$

For the maize amyloplast, 20 minutes of time (t) would produce a mean distance of diffusion (x) equal to 3.7 μm < x < 16.7 μm (range of values due to the range in estimate of cytoplasmic viscosity). In other words, 20 minutes of time would produce only an average movement of approximately 10 microns due to diffusion while observation shows us that a sedimenting amyloplast moves the width of the cell (≈23 μm) in 20 minutes. This produces a Peclet number on the order of 2, but could range anywhere from 7 down to 1.3 indicating that a dominance by gravity induced sedimentation exists, but is not a large dominance. In conclusion, the amyloplast is "susceptible" to gravity.

While examining effect ratios, the Reynolds' number (Re) associated with the amyloplast and its environment should be examined. The Reynolds' number provides a ratio of dominance between inertial forces and viscous forces. If Re is found to be <<1 then viscous forces dominate and Stokes' drag applies while high Reynolds' numbers indicate dominance of the inertial forces. Reynolds' number is given by:

$$Re = \frac{2r_{amyl}\rho_{amyl}\,\text{velocity}}{\eta} \qquad (3-6)$$

All the values from equation 7-6 are again found in the tables of Chapter 1 and for the sake of consistency, the conservative, observed value of sedimentation velocity (≈1 μm/min.) is used for velocity. Again the range of cytoplasmic viscosity (η) is significant here, so the range in Re is determined as: $4.28\text{x}10^{-9} < Re < 8.57\text{x}10^{-8}$. This result shows that the amyloplast motion through the columella produces extremely low Reynolds' numbers (viscous forces are very dominant) and therefore, Stokes' drag law can be used to analyze the motion.

With the relatively dominant effect of gravity-induced sedimentation established, the issue of amyloplast susceptibility to gravity is established, but is this susceptibility precise enough to perceive the gravity signal with the known sensitivity? Bjorkman established the high end of the plant root's sensitivity as detecting 10^{-3} g's (Bjorkman, 1988). For 10^{-3} g's to be sensed by the statolith, the energy from its sedimentation must be greater than 1000 times the background noise. The energy of thermal noise is given by:

$$H = \frac{1}{2}kT \qquad (3-8)$$

Thermal noise in the columella cell would then be dependent on the room temperature (298.15^0 K) and the Boltzman constant. Initially, the ability of the maize amyloplast to produce 1000 times this energy in its sedimentation can be viewed simply from an aspect of the potential energy given up as it accomplishes the work of sedimentation. With work being simply a (force * distance) construct, the minimum sedimentation

distance required to produce 1000 times the background thermal noise can be found as follows:

$$d_{sed} = \frac{1000kT}{2W_b} \tag{3-9}$$

Therefore, the minimum sedimentation distance (d_{sed}) required to produce the equivalent energy as 1000 times the thermal noise is:

$$d_{sed} = 21.5\ \mu m$$

or, when averaged over 29 amyloplasts per average maize columella cell:

$$d_{sed_avg} = 0.74\ \mu m \text{ per amyloplast}$$

Since, the requirement on a single amyloplast is on the order of the entire width of the cell, the single plastid cannot reasonably be expected to serve as the statolith. However, the entire collection of amyloplasts per columella cell can produce 1000 times the energy of the background noise while only sedimenting less than 1 micron. This finding shows that the collection of amyloplasts can quite feasibly create a functional statocyte with the observed sensitivity.

Extending the analysis of feasibility, tension produced within the cytoskeletal network during sedimentation is considered instead of simply the potential energy of sedimentation. If gravity acts upon the amyloplasts and, therefore, upon the cytoskeletal network they are embedded within, tensions in the network could open stretch-sensitive channels as a first step in transducing the gravity signal. Tensions required to open a stretch-activated channel are overestimated because of the nature of the experimental techniques used to determine the figures (i.e. patch-clamp techniques). Guharay and Sachs found in 1984 that a patch-clamp pressure of 5 cm

Hg could open a channel 22% of the time (Guharay & Sachs, 1984). More recent work has brought these initial figures down by a third (Falke *et al.*, 1986; Edwards & Pickard, 1987; Ding & Pickard, 1993). The tension (t) on the plasma membrane in a patch-clamp is determined by the following formula:

$$t = p_{clamp} d_{sphere}/4 \qquad (3\text{-}10)$$

Where the pressure on the clamp (p_{clamp}=1.7 cm Hg≡2.3 kPa≡2.3×10^{-4} dyne/μm^2) and the diameter of the membrane sphere (d_{sphere}≈2 μm) formed inside the clamp determine the tension on the membrane. Of course, this is a very conservative estimate of what tension is applied to an individual channel since there could be many channels existing within the clamped patch. The conservative estimate of tension is therefore; t = 1.15×10^{-4} dyne/μm. Assuming a 6 nm (60 Angstrom) diameter calcium channel; t = 6.9×10^{-6} dyne/channel or 6.9×10^{3} nanodynes/channel. Since the buoyant weight of an amyloplast is 9.59 nanodynes, these patch-clamp findings indicate tensions on the order of 720 times the buoyant weight of a single amyloplast, but only 25 times the buoyant weight of all amyloplasts in the cell. However, because of the large overestimation of the tensions found by present patch-clamp findings and the fact that the amyloplast collection is within an order of magnitude of producing these tensions, this analysis also attests to the feasibility of the columella as a statocyte by imparting tensions upon channels in the cell membrane and thereby initiating a cascade of transduction events. Not only tensions can be analyzed for proper magnitude to open a channel, but the energy to open a channel can also be analyzed for feasibility.

The energy required to open a typical calcium cation channel is found within the hydrolysis of a single molecule of ATP. Since typical models for such channels

include the hydrolysis of an ATP molecule to open the channel, the question becomes whether the sedimentation of the amyloplasts can produce an equivalent energy. Since the change in Gibbs free energy (ΔG) is 10 kcal/mole of hydrolyzed ATP and there is 4.184 Joules/cal and 6×10^{23} molecules/mole, the energy associated with this reaction is 6.97×10^{-20} J/molecule of ATP. Given the buoyant weight of a single amyloplast undergoing work of sedimentation, the distance required for a single amyloplast to produce an equivalent amount of energy is given by:

$$\begin{aligned} \text{Work}_{\text{sedimentation}} &= \text{Energy of a hydrolyzed ATP molecule} \\ (W_b)(d_{sed}) &= 6.97 \times 10^{-20}\ \text{J} \\ d_{sed} &= 0.73\ \mu\text{m} \end{aligned}$$

average for 29 amyloplasts:

$$d_{sed} = 0.025\ \mu\text{m}$$

Therefore, all the plastids sedimenting a distance of 2.5 μm is equivalent to the energy required to open 100 channels. This result also validates the feasibility of the amyloplasts as sensors of the gravity signal.

Feasibility as a gravity sensor has now been demonstrated in a variety of ways. With the amyloplast now assumed to provide the necessary work or energy needed to sense a gravity vector, development of a force balance model begins. The immediate use of this work is to either confirm or deny the applicability of the classical, "tether" model set shown in Figure 3.2(#1).

3.3.2 Development of a Force Balance Model

A model of the amyloplast within the columella cell based on a balance of forces acting upon the plastid is now developed. The statolith model assumes four forces acting on the statolith (amyloplast); weight, drag, buoyancy, and elastic force. Figure 3.3 shows the directions that these forces act upon the amyloplast. The weight (F_g) is simply the mass of the amyloplast multiplied by the local acceleration due to gravity which is assumed to be a constant of 9.81 m/sec^2, the value of gravity at sea-level. The force of drag (F_d) is directly proportional, but in opposition to the velocity that the statolith has within the cytoplasm. The value for drag not only depends on the shape and size of the amyloplast, but the physical characteristics of the cytoplasm and amyloplast. With the low Reynolds' number determined in the previous section, Stokes' drag relationships are assumed to apply. Buoyancy (F_b) is dependent on the amount of cytoplasm displaced by the amyloplast and the difference in density between the cytoplasm and the plastid. Elastic force (F_e) is the force imposed on the statolith by any cytoskeletal elements in contact with the plastid. Quantitative measure of this force requires both a knowledge of the structural properties of the interacting filaments and assumptions as to the scheme of interaction, such as whether the plastid is directly connected to a dozen actin filaments attached to the basal wall versus the plastid resting in a network of actin filaments connected to the lateral walls.

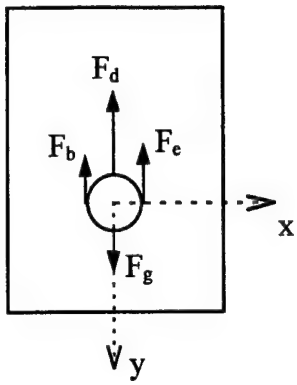

Figure 3.4 - The Balance of Forces Acting on the Amyloplast

$$\sum F = ma_y$$

$$F_g - F_d - F_b - F_e = ma_y \qquad (3\text{-}11)$$

where, $F_g = m_{amyl} g \equiv V_{amyl} \rho_{amyl} g$

$F_d \equiv$ Stokes' drag $= 6\pi r_{amyl} \eta v$

$F_b = V_{amyl} \rho_{cyto} g$

$F_e = E \varepsilon A_{cs}$

m_{amyl} = amyloplast mass {kg}

V_{amyl} = amyloplast volume {μm^3}

ρ_{amyl} = amyloplast density {$kg / \mu m^3$}

r_{amyl} = amyloplast radius {μm}

g = acceleration due to gravity (9.81 m / s^2 at sea - level)

η = cytoplasmic viscosity {cp or Pa - s or kg / μm - s}

ρ_{cyto} = cytoplasmic density {$kg / \mu m^3$}

v = velocity of the sedimenting amyloplast {$\mu m / s$}

E = Young's Modulus for actin {Pa}

ε = strain (Δlength / length) on the actin filament

A_{cs} = cross - sectional area of the actin filament {μm^2}

The dynamics of the amyloplast under various conditions can now be predicted using this force balance model. Two such conditions that have been studied experimentally are the amyloplast under a constant, or terminal, velocity, and the

amyloplast subjected to microgravity conditions. Under a condition of terminal velocity, a_y equals zero. The terminal velocity, v_{term} is then developed:

$$F_g - F_d - F_b - F_e = 0$$

$$m_{amyl}g - 6\pi r_{amyl}\eta v - V_{amyl}\rho_{cyto}g - E\varepsilon A_{cs} = 0$$

$$V_{amyl}\rho_{amyl}g - V_{amyl}\rho_{cyto}g - E\varepsilon A_{cs} = 6\pi r_{amyl}\eta v$$

$$V_{amyl}g(\rho_{amyl} - \rho_{cyto}) - E\varepsilon A_{cs} = 6\pi r_{amyl}\eta v$$

assume amyloplast is a sphere: $V_{amyl} \equiv \frac{4}{3}\pi r_{amyl}{}^3$

$$\frac{4r^2 g}{18\eta}(\rho_{amyl} - \rho_{cyto}) - \frac{E\varepsilon r_{amyl}}{6\eta} = v_{term}$$

$$\frac{4r^2 g(\rho_{amyl} - \rho_{cyto}) - 3r_{amyl}E\varepsilon}{18\eta} = v_{term} \qquad (3\text{-}12)$$

Equation 3-12 is as previously published (Todd, 1994), but with cytoskeletal forces explicitly included. Predicted terminal velocity of a sedimenting amyloplast can now be compared to observed values and an appropriate model of cytoskeletal interaction can be inferred because of the ($E\varepsilon$) term. Likewise, motion in microgravity conditions can be calculated. Under microgravity conditions, $g \approx 0$ and the velocity of an amyloplast under these conditions is caused purely by any elastic force imposed on the plastid:

$$F_g - F_d - F_b - F_e = m_{amyl}a_y$$

$$0 - F_d - 0 - F_e = m_{amyl}a_y$$

$$-(6\pi r_{amyl}\eta v + E\varepsilon A_{cs}) = m_{amyl}a_y$$

for motion in one direction, $v \rightarrow \dot{y}$ and $a_y \rightarrow \ddot{y}$:

$$\therefore\ \ddot{y} + \frac{6\pi r_{amyl}\eta}{m_{amyl}}\dot{y} + \frac{E\varepsilon A_{cs}}{m_{amyl}} = 0 \qquad (3\text{-}13)$$

Therefore, Equation 3-13 is the 2nd-order Equation of Motion (EOM) for an amyloplast acted upon by viscous drag and cytoskeletal elastic forces, but not gravity. After steady-state conditions are achieved ($\ddot{y}$=0), velocity ($\dot{y}$) becomes terminal velocity (v_{term}).

$$\frac{6\pi r_{amyl}\eta}{m_{amyl}}v_{term} + \frac{E\varepsilon A_{cs}}{m_{amyl}} = 0$$

$$v_{term} \approx \frac{-E\varepsilon A_{cs}}{6\pi r_{amyl}\eta}$$

for elliptical microfilament cross-section inserting values from Table 1.3 gives

$$v_{term} \approx \frac{-E\varepsilon(\pi r_a r_b)}{6\pi r_{amyl}\eta} \qquad (3\text{-}14a)$$

$$\approx -0.124\frac{m}{s} * \varepsilon \qquad (3\text{-}14b)$$

$$\approx -4.43\text{x}10^{-11}\frac{m}{s}\frac{m^2}{N} * E\varepsilon \qquad (3\text{-}14c)$$

The derivation leading to Equations 3-14 assumes steady conditions, no accelerations, which is not quite true since the plastid undergoes changing elastic forces with all movement, but because of the highly viscous environment (the very low Reynolds' number), this derivation produces a useful approximation for plastid velocity at a given strain condition for a relatively instantaneous period of time. Using the value for E-modulus in Table 1.3 (Chapter 1), Equation 3-14b shows, with a middle range estimate of viscosity (12cp), the resulting velocity due to elastic forces from actin can be quite high. For example, a very small value of strain (ε=0.01 or 1%) would

produce an initial velocity of approximately 1239 μm/sec. which is well over (10^3-fold) than ever witnessed experimentally. However, since the value assumed for E-modulus has a great effect on the outcome, Equation 3-14c is the more appropriate in developing a better value for E-modulus from experimental data of sedimentation velocities.

When developing a visco-elastic model for the amyloplast falling within the columella cell, the actin interactions should be kept within reasonable limits. With a columella cellular volume of 17900 μm^3 and actin elliptical cross-sectional area ($\pi r_a r_b$) of 1.885×10^{-5} μm^2 and a persistent length of approximately 10 μm. The volume of an actin fiber comes to 1.885×10^{-4} μm^3. Therefore, a single, straight-length actin fiber is 1.05×10^{-6} % by volume of the cell. In muscle cells, this protein can take up over 20% of the cell while most cells have at least 5% taken up by actin (Alberts *et al.*, 1994). Therefore, for actin to constitute 1% of the columella cell, approximately 1×10^6 actin fibers lengths would be found in the cell. This appears as a good starting place for the proposed number of fibers that could provide interaction with the statoliths.

3.3.3 Development of a Second Order, Linear Equation of Motion

The single amyloplast sedimenting within the viscous cytoplasm of the columella cell has the mechanical analog of the spring-mass-damper system shown in Figure 3.5. The cytoskeletal tensions placed on the amyloplast are analogous to the spring constant (k) which produces an opposing force proportional to position. The viscous nature of the cytoplasm is analogous to the dashpot constant (b) which produces an opposing force proportional to velocity.

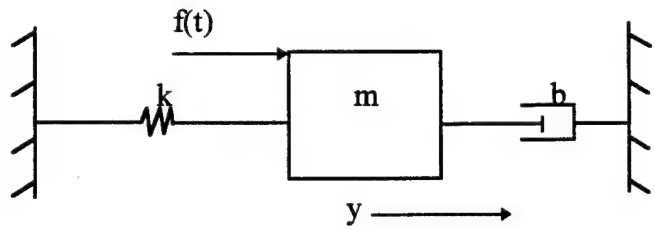

Figure 3.5 - Spring-Mass-Damper System

To produce a simplified EOM for amyloplast sedimentation dynamics, the motion in the direction of gravity (see Figure 3.4) is assumed uncoupled from motion along the x-axis. Therefore, neglecting forces along x, the EOM along y is developed as shown in Figure 3.4.

$$\sum F_y = m\ddot{y}$$

$$F_{gravity} + F_{buoyancy} + F_{drag} + F_{elastic} = m_{amyl}\ddot{y}$$

$$V_{amyl}\rho_{amyl}g_y - V_{amyl}\rho_{cyto}g_y - 6\pi r_{amyl}\eta\dot{y} - F_{actin} = m_{amyl}\ddot{y}$$

$$V_{amyl}g_y(\rho_{amyl} - \rho_{cyto}) - 6\pi r_{amyl}\eta\dot{y} - F_{actin} = m_{amyl}\ddot{y}$$

$$\therefore \quad \ddot{y} + \frac{6\pi r_{amyl}\eta}{m_{amyl}}\dot{y} + \frac{F_{actin}}{m_{amyl}} = \frac{V_{amyl}g_y\Delta\rho}{m_{amyl}} \qquad (3\text{-}15)$$

Where V_{amyl}, ρ_{amyl}, r_{amyl}, and m_{amyl} are the volume, density, radius, and mass, respectively, of the amyloplast. The component of the gravity acceleration in the y-axis (g_y), the cytoplasmic viscosity (η), and the density of the cytoplasm (ρ_{cyto}) are also depicted. The difference in density between the amyloplast and the displaced cytoplasm ($\Delta\rho$) contributes to the EOM forcing function which is the difference between the amyloplast's weight and buoyancy. The elastic forces due to cytoskeletal interaction (F_{actin}) can be represented in various ways. This interaction model can be simplified to a simple, linear tether on the amyloplast where F_{actin} is proportional to the

y-position, or the model can be a complex, nonlinear interaction between numerous actin filaments and the falling amyloplast.

For a simple, linear model for F_{actin}, the cytoskeletal interaction is assumed to act similar to a marble on a rubber band where the elastic force increases with the stretch of the rubber band.

$$F_{actin} = (\text{stress})(\text{cross-sectional area of actin})$$
$$F_{actin} = (E_{actin}\varepsilon)(A_{cs})$$
$$F_{actin} = E_{actin}\, A_{cs}\, \Delta l/l$$

Where ε is strain or $\Delta l/l$ on an actin fiber, E_{actin} the elastic modulus, and the cross-sectional area for a single actin filament can be computed as in Table 1.3 of Chapter 1. If Δl is assumed to be equivalent to the motion along the y-axis (the plastid begins sedimentation at y=0 under no elastic strain) then $y=\Delta l$ and F_{actin} is derived as proportional to motion along the y-axis, and the EOM is as follows:

$$\therefore\ \ddot{y} + \frac{6\pi r_{amyl}\eta}{m_{amyl}}\dot{y} + \frac{E_{actin}A_{cs}/l_{actin}}{m_{amyl}}y = \frac{V_{amyl}g_y\Delta\rho}{m_{amyl}} \qquad (3\text{-}16)$$

In terms of the spring-mass-damper system:

$$\ddot{y} + b\dot{y} + ky = f(t)g_y$$

$$\text{where,} \quad b = \frac{6\pi r_{amyl}\eta}{m_{amyl}}$$

$$k = \frac{E_{actin}A_{cs}/l_{actin}}{m_{amyl}}$$

$$f(t) \equiv f = \frac{V_{amyl}\Delta\rho}{m_{amyl}}$$

The forcing function, f(t), is assumed constant since the change in gravity is negligible over the small sedimentation distance within the columella cell.

In terms of a state space representation where the states x_1, x_2, x_3, and x_4 are, respectively, x-position, y-position, x-velocity, and y-velocity:

$$\dot{\bar{x}} = \begin{bmatrix} 0 & 0 & 1 & 0 \\ 0 & 0 & 0 & 1 \\ -F_{actin}(x_1) & -F_{actin}(x_2) & -b & 0 \\ -F_{actin}(x_1) & -F_{actin}(x_2) & 0 & -b \end{bmatrix} \bar{x} + \begin{bmatrix} 0 & 0 \\ 0 & 0 \\ f & 0 \\ 0 & f \end{bmatrix} \begin{bmatrix} g_x \\ g_y \end{bmatrix}$$

$$\text{where, } \bar{x} = \begin{bmatrix} x_1 \\ x_2 \\ x_3 \\ x_4 \end{bmatrix} \quad \text{and} \quad F_{actin} = \frac{E_{actin} A_{actin} \Delta l}{l} / m_{amyl} \tag{3-17}$$

When F_{actin} is uncoupled between x and y motion (attachments are only colinear or perpendicular with motion), is treated as a linear force dependent on position only, and the original actin fiber length is assumed to be approximately half the cell width (≈10 μm):

$$\dot{x}_3 \equiv \ddot{x}_1 = T_r - T_l - b\dot{x}_1 + fg_x$$
$$\dot{x}_4 \equiv \ddot{x}_2 = T_d - T_b - b\dot{x}_2 + fg_y$$

$$\text{tension directed positive - x (right)} \equiv T_r = \frac{E_{actin} A_{actin} (-x_1)}{\text{cell width} / 2} / m$$

$$\text{tension directed negative - x (left)} \equiv T_l = \frac{E_{actin} A_{actin} (+x_1)}{\text{cell width} / 2} / m$$

$$\text{tension directed positive - y (distal)} \equiv T_d = \frac{E_{actin} A_{actin} (-x_2)}{\text{cell height} / 2} / m$$

$$\text{tension directed negative - y (basal)} \equiv T_b = \frac{E_{actin} A_{actin} (-x_2)}{\text{cell height} / 2} / m$$

For a linearized system with zero initial conditions assumed on the amyloplast position and velocity, a closed-form solution can also be worked out using partial fraction expansion of the system's Laplace Transform. This solution is used to

provide insight into the system's dynamics prior to solution using a numerical technique.

$$\ddot{y} + b\dot{y} + ky = fg_y$$

For g_y a step input: $$Y(s)(s^2 + bs + k) = \frac{fg}{s}$$

$$Y(s) = \frac{fg}{s(s^2 + bs + k)}$$

by Partial Fraction Expansion: $$Y(s) = \frac{Res1}{s} + \frac{Res2}{s + pole2} + \frac{Res3}{s + pole3}$$

The poles provide the information as to the dynamics of the system (speed, stability, etc.) while the residues provide the general weighting of each pole's contribution to the overall response.

One final issue of importance to the dynamics of the amyloplast is the concept of group sedimentation versus single plastid sedimentation. For particles in a viscous fluid, the particle sedimentation can be treated as sedimentation of the entire group (flocculation) if the diffusion coefficient is sufficiently low or the particles are physically connected in some manner (Mason, 1976; Smith, 1996). Through both the calculations shown earlier in section 3.3.1 and recent findings as to the actual diffusion and association of amyloplasts to each other (Bjorkman, 1988; Sievers & Hejnowicz, 1992), both of these conditions certainly apply to the amyloplasts within the columella cells of corn. Therefore, all the amyloplasts can be examined as a single droplet or "floc" containing all the individual plastids and the density of the whole is given by:

$$\rho_{floc} = \rho_{cyto} + \frac{r_{amyl}^{\ 3}}{r_{floc}^{\ 3}} N(\rho_{amyl} - \rho_{cyto}) \qquad (3\text{-}18)$$

Where the density of the floc (ρ_{floc}) is found given the number of amyloplasts (N), the difference between amyloplast and cytoplasmic densities (ρ_{amyl}-ρ_{cyto}), and the effective radius of the floc (r_{floc}). Once this floc density is computed, the buoyant weight of the floc is attained and the dynamics of the entire floc can be predicted using the models developed earlier. The radius of the floc is the only remaining value to be developed.

Development of the floc radius requires quantitative determination of the amyloplast grouping under 1-g conditions for this purpose. If it is assumed that gravity packs the plastids together as closely as possible, then the fractional void volume for a hexagonal close packing formation of spheres is known as ε=0.31. The volume of the floc can then be computed if the sum volume of all amyloplasts (V_{all_amyl}) is known:

$$V_{floc} = \frac{V_{all_amyl}}{(1-\varepsilon)}$$

assuming roughly spherical shape of floc:

$$\frac{4}{3}\pi r_{floc}^{\ 3} = \frac{V_{all_amyl}}{(1-\varepsilon)}$$

$$\therefore \qquad r_{floc} = \sqrt[3]{\frac{3V_{all_amyl}}{4\pi(1-\varepsilon)}} \qquad (3\text{-}19)$$

With all the quantitative data given in Table 1.1 of Chapter 1, the floc radius (r_{floc}) computes to a value of: r_{floc}=6.55 μm. This value, which is approximately 5 times greater than the individual amyloplast radius, will surely produce higher Stokes' drag in the analysis of the velocity of the sedimenting floc. An adjusted version of Equation 3-1 is required to compute the floc's buoyant weight:

$$W_{b_floc} = V_{floc}\left[\{\rho_{starch}\cdot s+\rho_{stroma}(1-s)\}\cdot(1-\varepsilon)+\rho_{cyto}\cdot\varepsilon-\rho_{cyto}\right]g \qquad (3\text{-}20)$$

The adjustment to this equation is in the form of the void volume (ε) so that the starch-stroma densities only apply to that part of the floc which is actually amyloplast and applies the density of the cytoplasm (ρ_{cyto}) to the void volume of the floc. The buoyant weight of the floc (W_{b_floc}) is found to be 2.78×10^{-7} dynes $\equiv$ 278 nanodynes $\equiv$ 2.78×10^{-12} N. As expected, this is about 29 times the single amyloplast buoyant weight.

With the development of these equations describing the dynamics of the amyloplast sedimentation, observational data are required to compare the predicted sedimentation to actual sedimentation. The observational data provided a means to choose the form of the columella model so that the predicted dynamics of sedimentation more closely matched that witnessed in nature. To obtain the observational data, videomicroscopy was used to witness first-hand the sedimentation of the corn amyloplasts.

3.4 Experimental and Mathematical Procedures

Both experimental and computational techniques were used to accomplish the objective of this chapter. Laboratory materials and methods along with computational software developed to visualize and analyze empirical data are discussed in the following subsections.

3.4.1 Experimental Methods

Seeds of Yellow Dent corn (*Zea mays* L. cv. Yellow Dent) were obtained from the East Texas Seed Company (Tyler, Texas, {800}888-1371). Seeds were disinfected and washed for 6 minutes using 5.25% NaOCl and 1.0% Triton X-100

solution (100 μl of Triton per 10 ml of commercial bleach) by continuously agitating the seeds in solution. Following the wash, the seeds were rinsed using 6, 2-minute washes of sterilized, distilled water (dH_2O) under a sterile hood. Six seeds were imbibed between 2 sheets of filter paper (90mm Whatman Qualitative #1) in a 100mm x 15mm Petri dish using 5 ml of sterilized, ultra-filtered water. The filter paper, dH_2O, and ultra-filtered water were sterilized by autoclave using a 10 minute wet-cycle. Petri dishes were sealed with Parafilm™ sheets and placed in a vertical position. This method of imbibing produced less than one fungal contamination per 100 petri dishes (600 seeds). At six seeds per Petri dish, the germinated corn seedlings grew vigorously for approximately 5 days, after which arrested growth rate and atrophied root caps became evident. Experimentation designed to extend this 5 day limit using various salt solutions such as Hoagland's No. 2 (Hoagland & Arnon, 1950) proved unsuccessful. The limiting factor appears to be gases (CO_2 and O_2) versus moisture and nutrients. Therefore, with 6 seeds per Petri dish, all subject seedlings were used within 5 days of germination. The vertical Petri dishes were kept at 25 ± 1.5^0C. Germinating seeds of Yellow Dent remained in darkness. Germination occurred at approximately the 36 hour point after imbibing. Vertically growing, primary roots in three different length categories were selected for study. The three categories were 20-29 mm lengths, 30-39 mm lengths, and 40-55 mm lengths.

The distal 5 mm of the root tips of these roots were sectioned using a vibratome (Leica VT1000M). Procedures were very similar to those conducted by Sack, *et al.* with the Merit cultivar. (Sack *et al.*, 1986) Section thickness ranged from 50 μm to 60 μm, with the goal of leaving 1-2 layers of intact columella cells within the

section. Sections containing greater than 1 layer of mature columella cells created reduced contrast and clarity for both viewing and analyzing the motion of individual amyloplasts. Vibratome buffer solution consisted of 0.5 mM KCl, 0.1 mM $CaCl_2$, 0.1 mM $MgCl_2$, 0.5 mM NaCl, and 1.0 mM MES buffer at pH 6.8. The 5 mm tip of the corn root was secured to the vibratome specimen mount using a very thin layer of super glue (Ross Super Gel). Cover slips were mounted with Vaseline petroleum jelly. In order to increase the clarity and contrast of individual amyloplasts, various stains were investigated for this procedure. Iodine-Potassium Iodide (IKI_2) at 2 g of KI_2 with 100 ml H_2O and 0.2 g of iodine was the weakest solution that significantly improved visualization of the amyloplasts. However, control sections of coleoptile cells showed a loss of cytoplasmic streaming at even this low concentration. It was concluded that columella cells would not remain viable under this stain. A 0.33% solution of Neutral Red (Sigma) allowed the cells to remain viable and significantly demonstrated the cell walls, but actually decreased the contrast between individual amyloplasts. Therefore, only the vibratome buffer solution (with no stain) was used under the cover slips. For sections investigating the effect of Cytochalasin D (CD), a 100 μM solution of CD was made in 1.0% DiMethylSulfOxide (DMSO - $\{CH_3\}_2SO$).

Sections were placed on glass slides and mounted with respect to gravity in such a way as to ensure proper initial sedimentation locations. Video-microscopy aimed at examining the kinetics of amyloplast sedimentation from the distal end to either a lateral side or the basal end required initial mounting of the root section in a vertical orientation, while video examining side to side kinetics required that the section be mounted horizontally on the glass slide. Videomicroscopy was conducted

with a Zeiss Standard 14 light microscope (400x/1000x) fitted with a Edmund Scientific video relay lens/C-mount and a Dage-DGI, Inc Series 68 video camera. Universal Imaging Corporation's MetaMorph (ver. 3.0) imaging software was used to control and capture the video images. The entire microscope, specimen stage, and video camera were mounted on a platform constructed to allow rotation and adjustment in 3 dimensions. This platform allowed the section, microscope, and camera to be rotated as a unit, placing the columella cells within the section at various angles with respect to gravity. Figure 3.6 shows the mechanical drawings for this microscope mount.

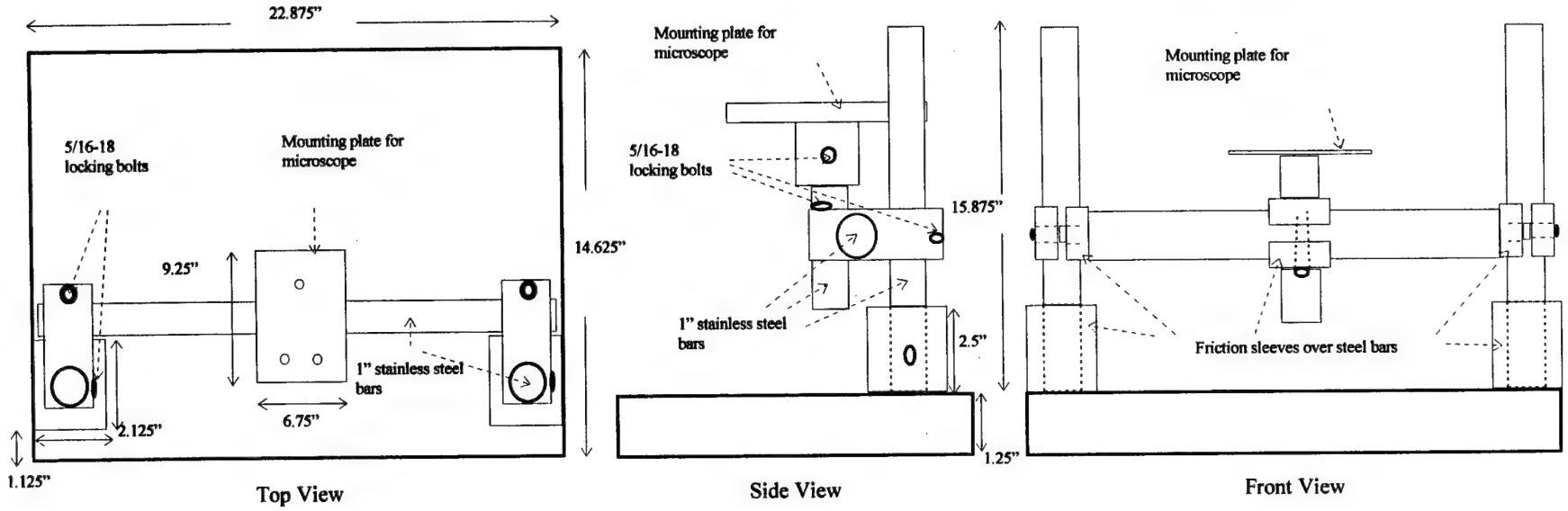

Figure 3.6 - Microscope Mount
The posts on either side of the aluminum base provide mounting for two vertical stainless steel bars that mount 90 degree post clamps to fix and allow rotation of the horizontal stainless steel bar. The microscope is mounted on the mounting plate. The mounting plate is fixed on the top of a shorter stainless steel bar which connects to the horizontal bar through another 90 degree post clamp. The post clamp allows the mounting plate and therefore the microscope, to rotate and be adjusted into or away from the horizontal bar for balance.

Three sedimentation profiles were investigated for each of the three length categories. The sedimentation profiles included distal-to-lateral side sedimentation, distal-to-basal end sedimentation, and side-to-side sedimentation. Additionally, the same length categories and sedimentation profiles were investigated for sections treated with CD. Since cytoplasmic streaming was not witnessed in columella cells, coleoptile sections and elongating cells of the root cortical region were examined to determine the amount of CD needed to halt streaming in the section thicknesses made for this experiment. Following sectioning on the vibratome, the sections were bathed in the CD solution while under the coverslip for a period of 30 minutes prior to examination. A 100 μM concentration of CD in 1% DMSO was found to halt cytoplasmic streaming in the coleoptile and root cortical cells. Therefore, this same concentration was used to treat the root columella sections.

Initial investigation showed that the sedimentation kinetics showed negligible positional changes in less than 20 seconds, therefore, 20 to 30 second interval still images were acquired for digital processing. Horizontal and vertical coordinates over time on individual amyloplast centers were processed using NIH Image (ver. 1.67) software. For sedimentation kinetics analysis the y-axis was selected to always point toward the gravity vector, and the x-axis was chosen to complete a right-handed coordinate system with the positive z-axis pointed toward the video camera. See Figure 3.7 for details.

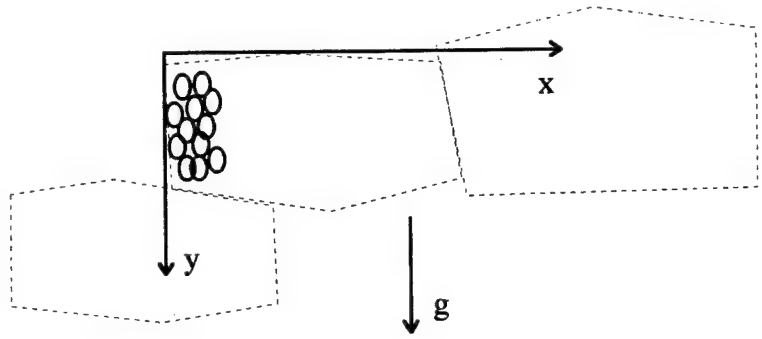

Figure 3.7 - Coordinate System Used for Amyloplast Sedimentation Kinetics
The y-axis is parallel with the gravity vector. The x-axis, chosen to parallel the side of the columella opposite and perpendicular to the gravity vector, creates a right-handed coordinate system with the z-axis (not shown) into the columella cells. By drawing the coordinate system tangent with the outermost cell wall of the columella cell, the coordinate axes approximate the upper and lateral physical boundaries of the simplified rectangular cell.

3.4.2 Computational Techniques

Using NIH Image software, data files were acquired for each amyloplast's sedimentation profile. The first data file simply lists the time between frames of each of the selected video captures. These data identify the time periods between all of the corresponding x-y coordinate data. The second data file consists of x-y coordinates plotting the sedimentation kinetics. Initial data in this file consist of a choice of two precise reference points (such as striking cell wall intersections) visible on each frame in the sequence and a recording of the x-y coordinates of these points throughout the frame sequence. This sequence of points serves as reference to any object drift due to movement of the specimen stage. This is used to subtract any global movement from the movement noted in the sedimenting amyloplasts. Following a "0 0" entered as a visual break in data, the sedimentation profile of individual amyloplasts is recorded by first recording the columella cell's x- and y-axis dimensions, thus providing a set of

approximate boundary conditions to the sedimentation. Then the x-y coordinates of the center of selected amyloplasts is recorded from frame to frame of the sedimentation profile. Another data marker of "0 0" identifies another x-y coordinate set to follow for an amyloplast within the same columella cell. A double marker ("0 0" on two sequential rows) identifies a shift to another columella cell and begins with the cell's x- and y-axis dimensions and then the x-y coordinates of the first amyloplast plotted in that cell. This sequence of data collection is followed until all amyloplasts that are traceable on that video capture are reduced to x-y coordinate data.

These coordinate-time data were processed and graphically visualized using MATLAB software. A script file (AMYLFALL.M) was programmed for use with MATLAB and is found in Appendix I of this thesis. Complete documentation of the variables assigned and code execution is found in this appendix. AMYLFALL.M basically opens a data file in the format described in the preceding paragraph and executes the following tasks in order.

(1) Stores the reference points over time.

(2) Stores the x-y axis information for the columella cell.

(3) Stores the amyloplast raw x-y coordinate data over time.

(4) Removes any drift calculated from the reference point time history from the amyloplast x-y coordinate data.

(5) Normalizes each amyloplast's x-y coordinate data to its columella cell's x-y axes and origin.

(6) Plots the amyloplast sedimentation positions within each reconstructed columella cell.

(7) Back computes the velocity of each amyloplast for its motion since the last recorded position.

(8) Computes and plots numerous velocity statistics based on Step (7).

(9) Computes and plots quantifications of channeling and group behavior.

(10) Computes and plots a trajectory plot containing velocity (magnitude and direction) of each amyloplast within a columella.

MATLAB was also used to compute the time-history of amyloplast sedimentation given a specific model of statolith-cytoskeletal interaction. The computational technique required a parent program (SEDIMENT.M) that sets the parameters for the simulation while the EOM's are found in a second function (STATE.M). Both of these script files are found in Appendix II.

3.5 Results

Results are divided into four subsections. The first subsection details the analytical results obtained using the EOM derived earlier in sections 3.3.2 and 3.3.3. The second examines the results obtained from the empirical amyloplast sedimentation study. The third examines results of viscosity and diffusion analysis. The final subsection presents the analytical results of the EOM derived in section 3.3.3 after adjustment with the empirical results from the plastid sedimentation study. It is this final subsection that presents and introduces the appropriate model set that the data appear to indicate.

3.5.1 Analytical Results of the Force Balance Model

The homogeneous form for the amyloplast equation of motion (Equations 3-12 and 3-16) is presented again here.

$$\ddot{y} + \frac{6\pi r_{amyl}\eta}{m_{amyl}}\dot{y} + \frac{EA_{cs}/l_{actin}}{m_{amyl}}y = 0$$

$$\text{where, } b \equiv \frac{6\pi r_{amyl}\eta}{m_{amyl}} = 1.1158\text{x}10^{9} \ \ / \min$$

$$k \equiv \frac{EA_{cs}/l_{actin}}{m_{amyl}} = 4.9608\text{x}10^{14} \ \ / \min^{2}$$

Values for constants were introduced in Tables 1.1, 1.2, and 1.3 in Chapter 1 of this thesis. The highest value from the range of viscosity (adjusted to units in minutes) was used in computing the damping constant, b. Figure 3.8 shows the dynamic response based on this EOM of an amyloplast under the "tethered" plastid/cytoskeletal interaction shown in Figure 3.2(#1). The amyloplast is simulated in microgravity (no forcing function) and initially displaced to the bottom of the cell, 10 microns from a proposed equilibrium position approximately 1/3 of the way from the cell bottom (Smith, 1996). At time zero, the amyloplast is released and the simulated dynamics are witnessed as the plastid moves back toward equilibrium (y=0) under the modeled viscous and elastic forces.

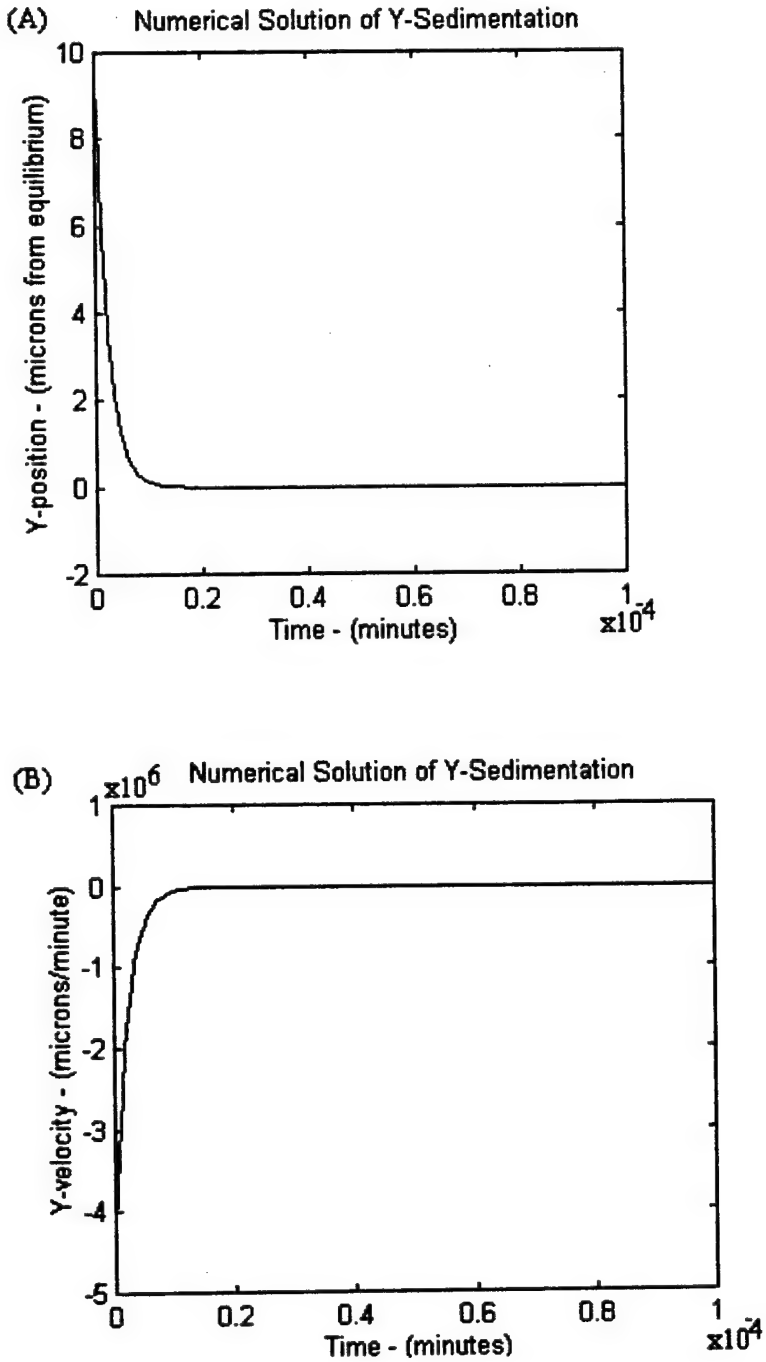

Figure 3.8 - Simulated Amyloplast Dynamics - Initial Displacement Only
(A) shows the position of the plastid. Note the initial displacement of 10 microns and the rapid response of the dynamics. (B) shows the velocity which peaks at -4 meters/minute; a rather large value. Note that the return to equilibrium occurs within approximately 10 micro-minutes.

Obviously, these dynamics have a time constant that is much too small. The maximum velocity ever documented for an amyloplast (see section 2.4.1) is 19 μm/minute; those simulated above, some 4 meters/min., are much too large. Therefore, the "tethered" model set used to derive the force balance model and/or the model parameters (e.g. the actin elastic modulus, the viscosity, etc.) are likely to be in error. Specifically, in this case of motion that "springs" the plastid back toward equilibrium, the spring constant (a function of actin) appears far too large, possibly as much as 10^6-fold. One piece of empirical evidence exists to compare against these findings; namely the TEXUS rocket experiment discussed in section 2.4.1.4.

The TEXUS rocket experiment placed the amyloplasts of cress and *Chara* under the conditions simulated in Figure 3.8. Under 1+ g of rocket propulsion, the statoliths were all forced to the distal end of the cell. At rocket cutoff, microgravity conditions existed, and the statoliths were free to "spring" back basally toward their new equilibrium positions in the cell. The basic analysis of the data presented from this experiment (Volkmann *et al.*, 1991) provides the following information. The experiment lasted for only 6 minutes. Storey II statoliths moved approximately 3.6 μm while storey III statoliths moved 3.2 μm. The average statolith velocities in the first 6 minutes of microgravity were 0.6 μm/min. for storey II statoliths and 0.53 μm/min. for storey III statoliths. The average statolith velocities undergoing inversion gravity or 1-g toward the cell basal end were 1.1 μm/min. for storey II and 1.4 μm/min. for storey III. The simulation model requires a change in certain physical parameters in order to accurately model the cress statocytes. Specifically, the cress amyloplast radius is 2.1 μm, the volume is 38.8 μm^3, and the amyloplast mass is

6.2×10^{-14} kg. This causes an increase in the drag-damping coefficient and a slight decrease in the spring constant as compared to maize. Figure 3.9 shows the results of a simulation of the TEXUS low-gravity rocket experiment. In this simulation, the values of the spring constant k and drag-damping coefficient b were altered until the results approximately matched those from the TEXUS experiments (i.e. sedimentation velocity on the order of 1 μm/min. and statolith movement of 3.6 μm in approximately 6 minutes).

In order to achieve agreement with the simulation results in Figure 3.9, the spring constant (actin properties) was altered by a factor of 10^{-6}. The time response shows results comparable to those found on the TEXUS flights; the average velocity is 0.7 μm/min. with a maximum of 1.4 μm/min., and the plastid moves approximately 3.5 μm within the 6 minute period. Altering the spring constant by only a 10^{-5} factor produces velocity in the 15 μm/min. range and dynamics are complete in less than 2 minutes while an applied factor of 10^{-7} produces extremely small velocities and very little plastid movement during the 6 minute period. It should be noted that the simulation model presently executes with a single actin attachment assumed, so this 10^{-6} factor is a multiplicative factor of actual actin property change and not the number of actin attachments simulated. As an example, a 10^{-6} factor applied to presumed E_{actin} values could produce these results so that a 10^{-8} factor would have to be applied to presumed E_{actin} if 100 actin attachments were assumed as a means of producing these results. Either way, the correction factor required for the spring constant itself is on the order of 10^{-6} and is further evidence that the spring constant chosen above is in error. Before examining the source of error, forced sedimentation is explored.

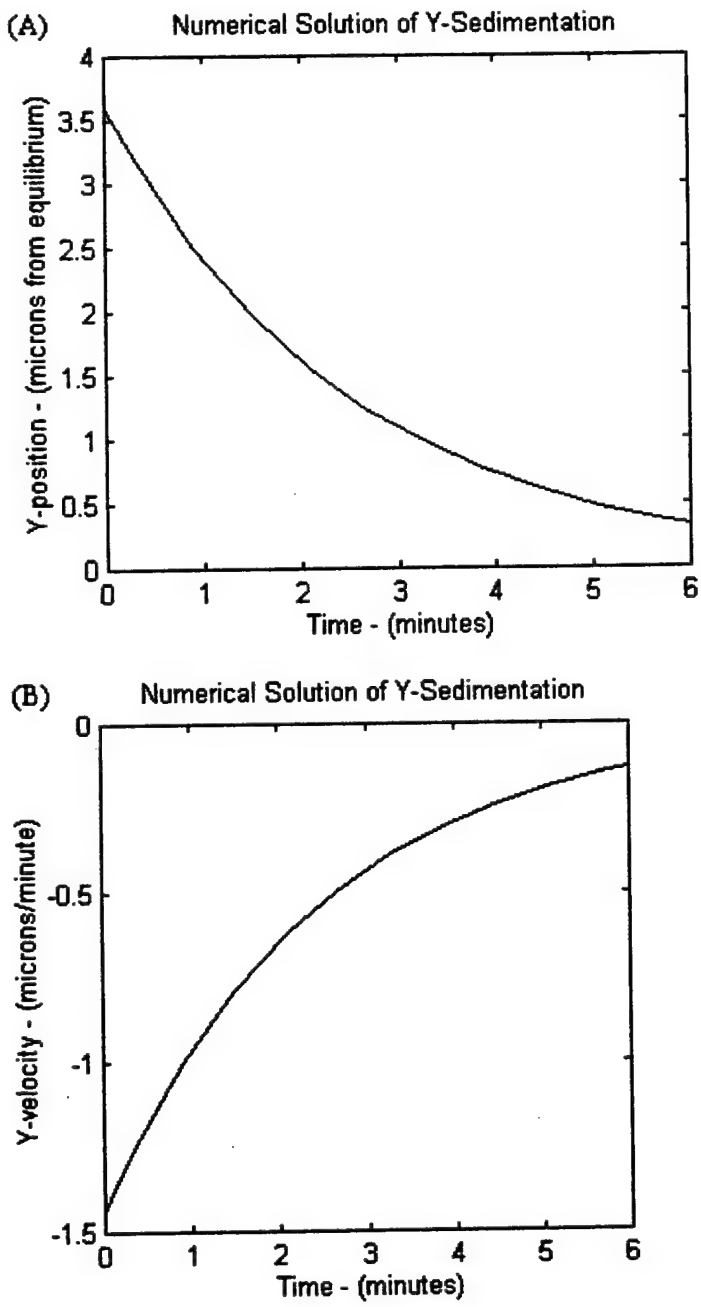

Figure 3.9 - Simulated Amyloplast Dynamics - TEXUS Experiment
(A) shows the amyloplast position over time, while (B) shows the plastid's velocity as it undergoes a return to equilibrium position during microgravity conditions.

As opposed to simulating a plastid "springing" back toward equilibrium, Figure 3.10 shows the results if gravity-induced sedimentation is simulated. In this case, initial conditions are zero; the plastid is at equilibrium with any elastic forces (1/3 distance up from the distal cell wall) and at zero velocity. A 1-g gravity forcing function is introduced to the EOM to determine if the high spring constant problem witnessed in the last section is also evident under these conditions. The extremely small sedimentation displayed by this model ($<2\times10^{-5}$ microns) again appears to signify that the actin spring constant is too large. The maximum (initial) sedimentation velocity of 6-7 μm/min. (affected predominantly by the drag or damping coefficient) appears within the boundaries of historical literature and therefore means that the physical parameters for the plastid and the viscosity used for the cytoplasm are close to correct. To rule out that the error lies in the operation of the numerical integrator, results were also attained using the closed form solution as derived in Section 3.3.3 earlier in this chapter. Thus the simulation procedure is not the source of the disagreement in the damping coefficient.

Using partial fraction expansion techniques, a closed-form solution to the non-homogeneous EOM, forced by gravity, with zero initial conditions was used to verify the results coming from the numerical integrator model of the amyloplast. The closed-form solution produced identical time responses as those seen in Figure 3.10. Additionally, the poles were determined to be located at -1.12×10^{9} and -4.45×10^{5}. These poles are extremely fast, confirming the dynamics witnessed in the simulation. The closed form solution (Equation 3-21) serves to explain and confirm the numerical

integrator results, but applies only to the gravity-forced, zero-initial condition case.

$$y(t) = 7.27\text{x}10^{-9} e^{-1.12\text{x}10^{9}} - 1.82\text{x}10^{-5} e^{-4.45\text{x}10^{5}} + 1.82\text{x}10^{-5} \quad \{\text{microns}\} \tag{3-21}$$

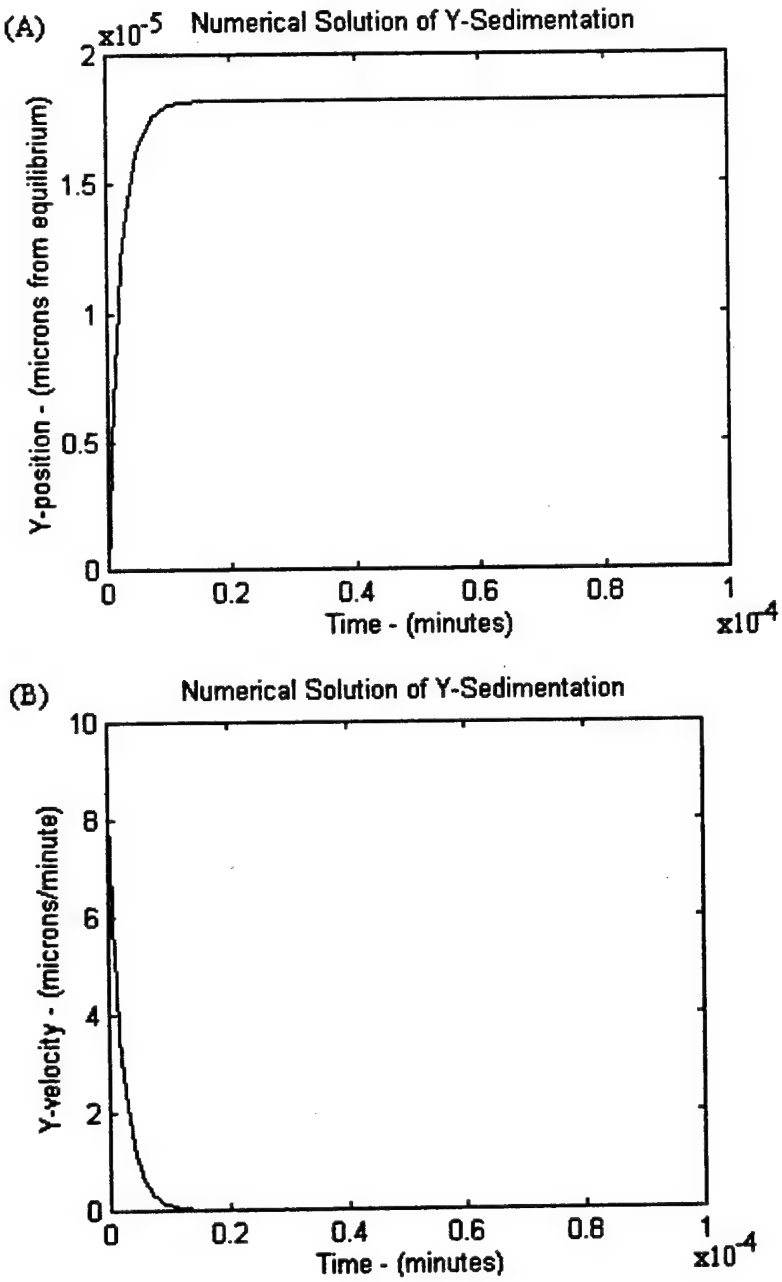

Figure 3.10 - Simulated Amyloplast Dynamics - 1-g Gravity Only
(A) shows the amyloplast position over time, while (B) shows the plastid's velocity as it undergoes gravity sedimentation from an equilibrium position. Note that a maximum velocity of 8 μm/min. is achieved very rapidly and the dynamics are complete in less than 2 milli-minutes.

The preceding model simulations show that the state-space model programmed into MATLAB (Appendix II) is producing results verified by alternative means and that those results demand a change in either the assumed actin properties, the amyloplast-cytoskeletal interaction model set, or both. Because the correction factor (10^{-6}) appears extremely large, the techniques used to develop the actin properties appear quite rigorous, the value for E_{actin} is within an order of magnitude of other common elastomers such as polystyrene and PVC, and the evaluation of actin structural properties is beyond the scope of this thesis, the conclusion must be that the "tethered" amyloplast-cytoskeletal interaction model set is incorrect. Alternatively, modeled sedimentation velocities appear to be within those found empirically in the literature and therefore indicate proper modeling of the amyloplast morphology and the cytoplasmic viscosity. Therefore, further work was intended to shed light on a proper interaction model set.

3.5.2 Observed Maize Amyloplast Sedimentation Dynamics

Amyloplast sedimentation events were recorded in columella cells from 3 different root length groupings (20-29, 30-39, and 40-55 mm) and during 3 different sedimentation profiles (distal-to-side, side-to-side, and distal-to-basal). Processed data produced by the AMYLFALL.M routine (Appendix I) enabled the determination of both the position and velocity characteristics of the sedimenting amyloplast. Various formulations were used to quantify the characteristics of the falling statoliths. Therefore, this section is divided into three parts. The first subsection presents the various raw position and velocity presentations accomplished by the analysis routine.

The second subsection introduces the various graphics that were formulated to quantify the behaviors seen in the sedimentation process. The final subsection presents the statistical findings for all amyloplasts studied.

3.5.2.1 Amyloplast Sedimentation Position and Velocity Profiles

Figures 3.11, 3.12, and 3.13 present examples of distal-to-side, side-to-side, and distal-to-basal sedimentation profiles, respectively. Each amyloplast within the columella cell is assigned a different color or shape of plotting symbol.

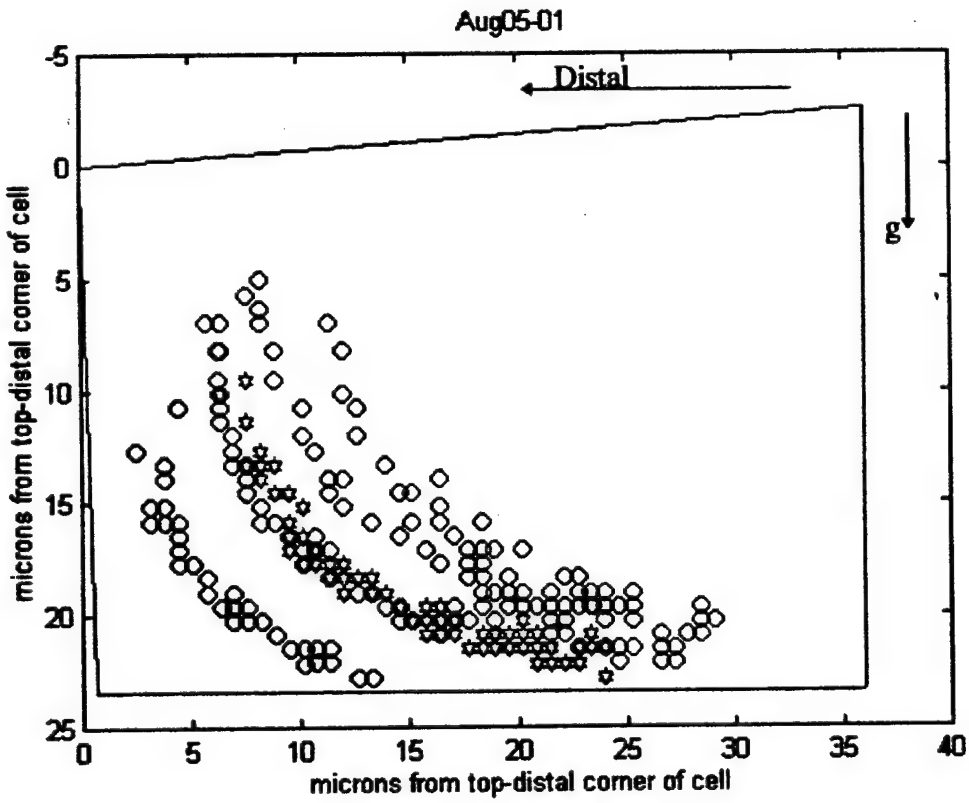

Figure 3.11 - Distal-to-Side Sedimentation Profile of 7 Plastids

The gravity vector is down in each presentation. The blue outline is a rough approximation of the location of the columella cell walls. The length of the blue outline is accurate only on the axes, therefore providing an accurate location only for

the upper-right, upper-left, and lower-left corners of the columella cell. As shown earlier in Figure 3.7, the axis origin is on the distal wall side with y in the down direction and x along the length of the columella, perpendicular to gravity. Plot titles indicate the video identification date and the columella cell number within that sequence.

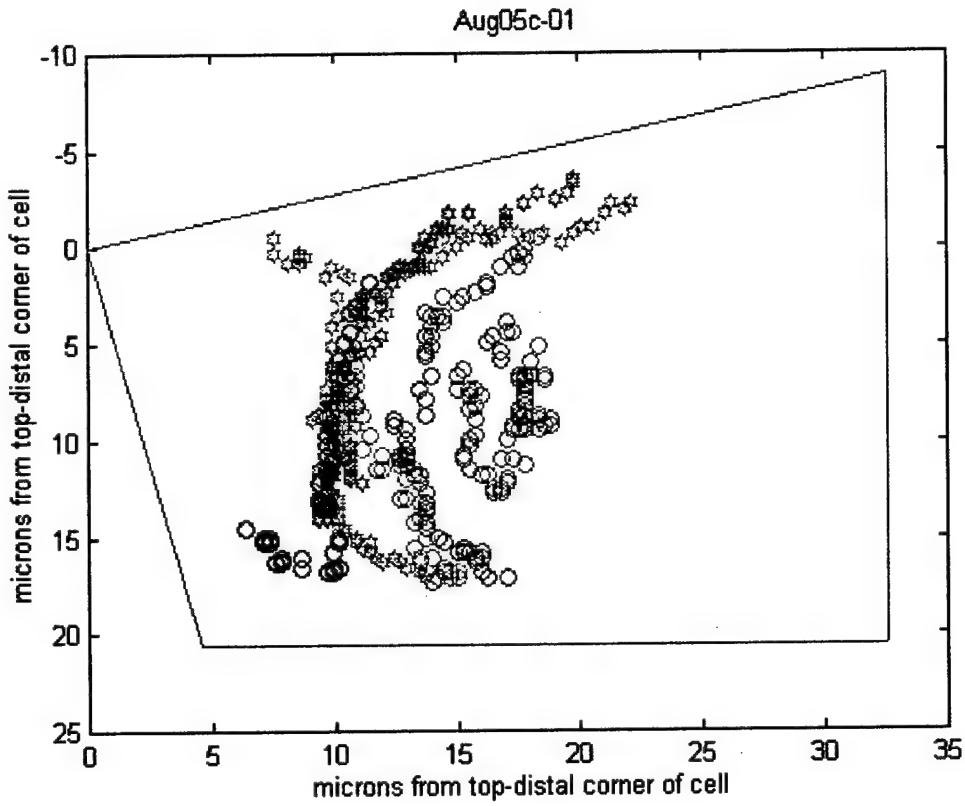

Figure 3.12 - Side-to-Side Sedimentation Profile of 9 Plastids

The side-to-side sedimentation profile presents an anomalous motion entitled "channeling." This channeling is apparent in every side-to-side and distal-to-basal sedimentation profile and thus occurs any time the plastid must transverse the columella's central region. This motion spurred the creation of numerous data formulations in order to quantify and localize the channeling.

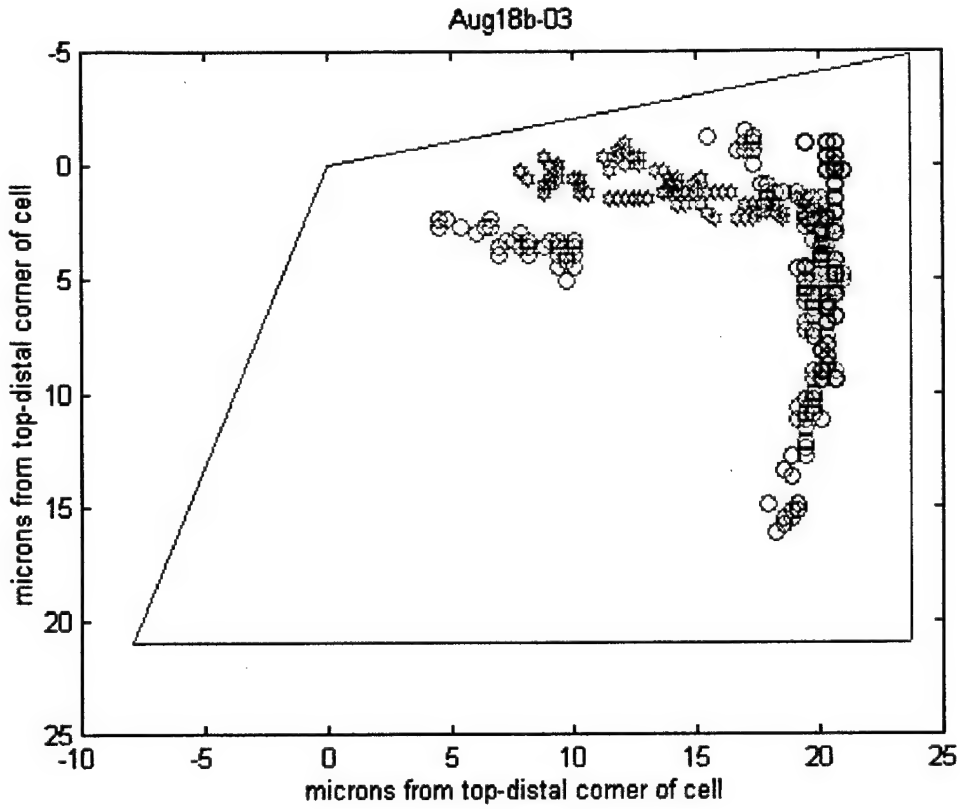

Figure 3.13 - Distal-to-Basal Sedimentation Profile of 7 Plastids

Velocity during the sedimentation is also profiled. Figures 3.14, 3.15, and 3.16 present the velocity profiles for the same columella cells found in the preceding three figures. The profile uses the same axis system as the previous figures except no columella cell boundary is displayed, and the aspect ratios are slightly dissimilar. The colormap provides velocity as the third dimension in the plot. The position of the isosceles triangles are position coordinates of an amyloplast at a given time while the long-axis orientation of the triangle points to the next position of that same amyloplast as it sediments. Velocity is post-processed as the average velocity required for the plastid to move from its PRIOR position to its current position.

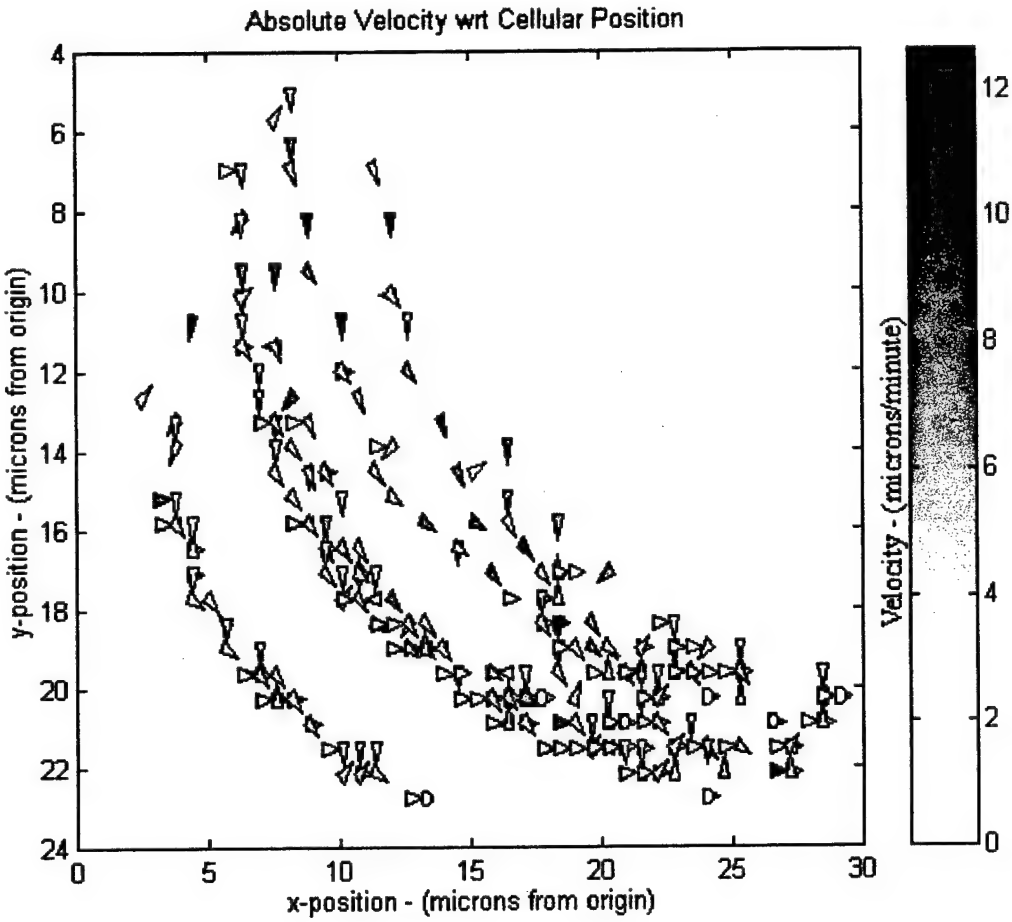

Figure 3.14 - Distal-to-Side Velocity Profile
This is the same cell as shown in Figure 3.11. The apex of each triangle points in the direction of motion and its color (using the color scale on the right) represents instantaneous velocity computed from the previous position.

Each individual plastid's starting position is marked with a white triangle (since velocity is post-processed) and the final position is marked with a circle (with appropriate velocity color). It is readily noted that some statoliths appear to oppose gravity (velocity upward) at various times. This motion is witnessed frequently on a small scale and appears to be diffusion related. Motions such as these demanded a statistical approach to mapping the velocities within the cell in order to get the general trends and characteristics of the velocity.

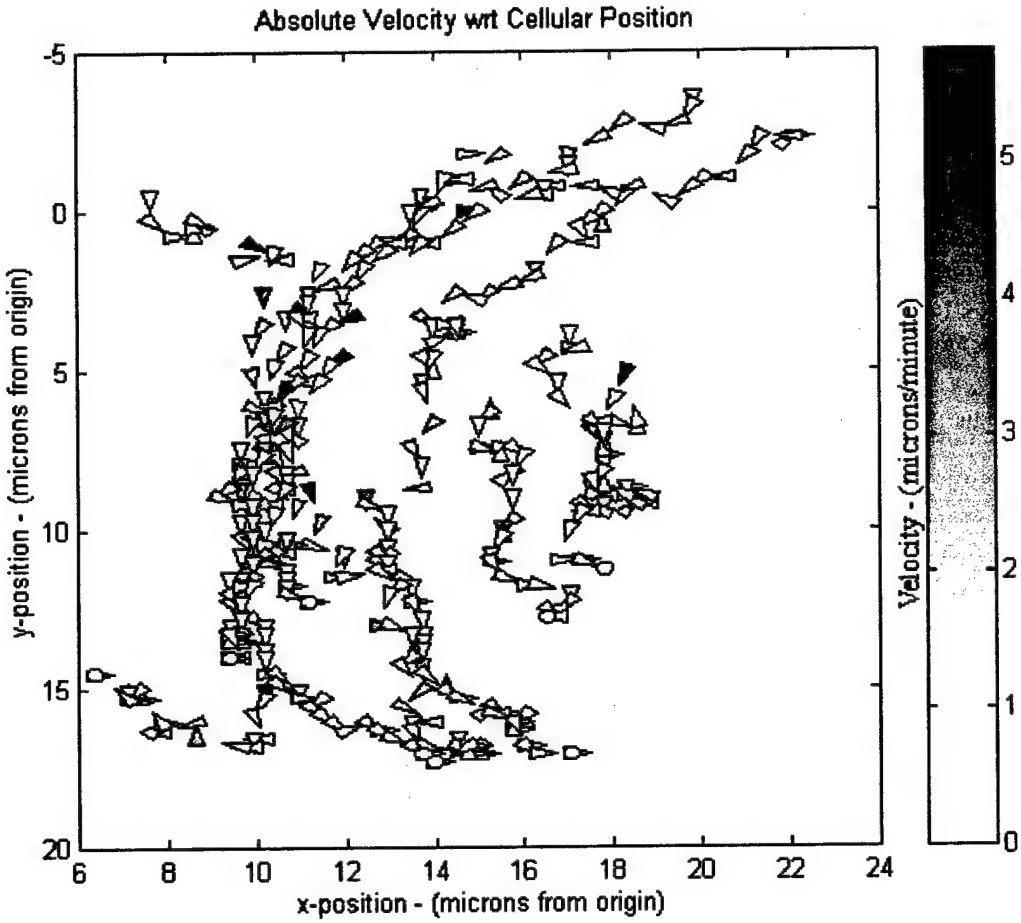

Figure 3.15 - Side-to-Side Velocity Profile
This is the same cell as shown in Figure 3.12.

Velocity in side-to-side and distal-to-basal profiles appears to increase as the plastid moves through the channel. As expected, velocities at the end of the sedimentation are low, but not zero because of diffusion. However, the velocity at the start of sedimentation appears lower than expected, with the higher speeds appearing to occur within the central region of the cell, as channeled movement occurs. However, quantification in a statistical manner is required to achieve the full picture of

velocity. This quantification is accomplished using the data formulations and statistical analysis of the following sections.

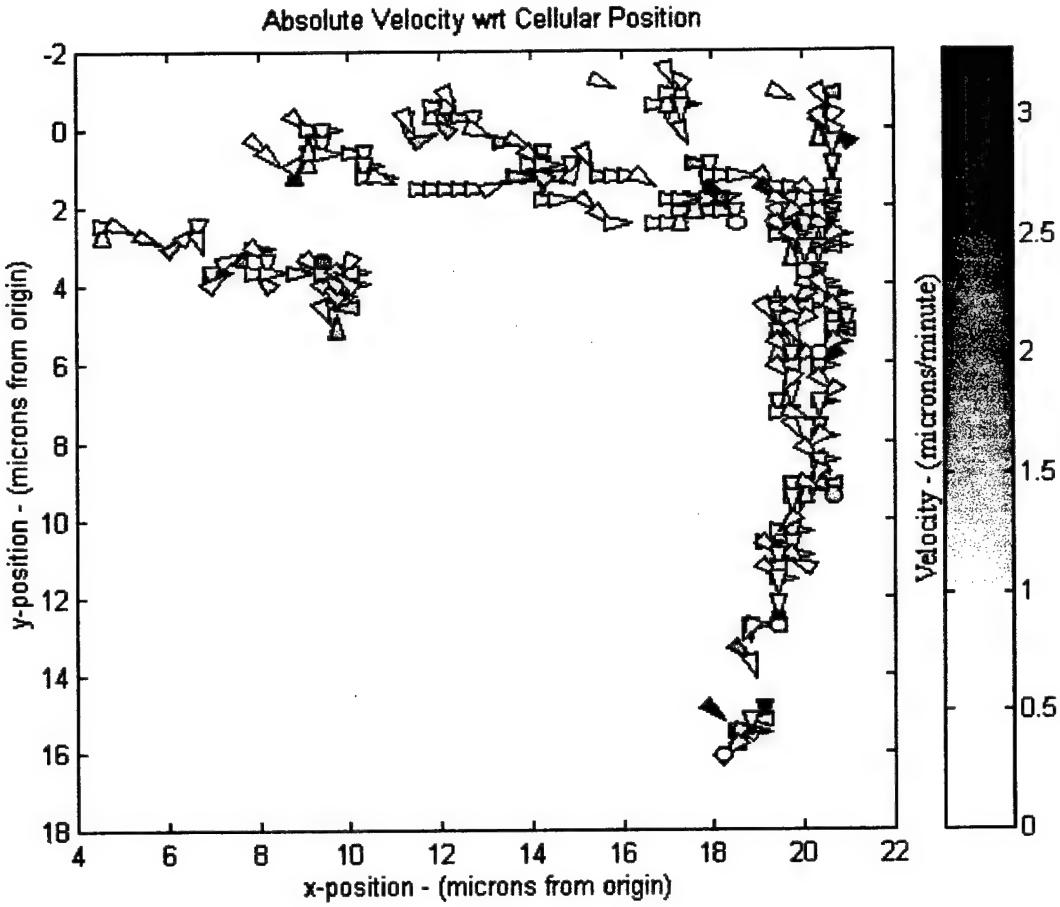

Figure 3.16 - Distal-to-Basal Velocity Profile
This is the same cell as shown in Figure 3.13.

3.5.2.2 Quantification of Sedimentation Dynamics

Various data formulations were created to analyze and quantify the sedimentation behaviors witnessed in the amyloplasts. These formulations were in three different categories: the channeling behavior, group movement behavior, and velocity correlation with cellular position.

Channeling behavior, introduced in the previous section, becomes apparent in both side-to-side and distal-to-basal profiles. The channeling behavior of the statoliths (see Figures 3.12 or 3.13) appears in practically every side-to-side or distal-to-basal profile. If the statoliths are unobstructed, sedimentation profiles should show near-vertical trajectories with little x-velocity. The actual profiles do not exhibit this, but instead, demonstrate significant deflection of the statoliths around what appears to be a central obstacle. Morphology of the maize columella indicates that this significant deflection is probably not attributable to a central vacuole or other organelle (Barlow & Sargent, 1978; Moore, 1983; Moore & McClelen, 1983; Moore & McClelen, 1983; Moore & Pasieniuk, 1984; Moore *et al.*, 1987). Future experiments suggested in Chapter 8 are intended to confirm this assumption. If this lateral motion is not an artifact of collision with a central organelle, it appears that channeling is a result of the amyloplast-cytoskeletal interaction. The location, size, and overall effects of interaction with the cytoskeletal barrier is the goal of formulating the raw sedimentation data into quantifications of channeling. Figure 3.17 shows the first of the formulations; the Channeling Coefficient. This coefficient is a measure of the variance in position of each statolith along the x-axis as a function of y-position, normalized to the starting variance at the top of the cell. The vertical range of amyloplast coordinates throughout the entire course of sedimentation are equally divided into 9 separate bins for analysis. The Correlation Coefficient (CC) is defined mathematically in Equation 3-22.

$$CC = \frac{\sum_{i=1}^{n}(x_i - \overline{x})^2}{n-1} \Big/ CC_{top} \qquad (3-22)$$

where CC_{top} is the x-position variance in the top vertical bin, x_i is the x-position of an amyloplast within a specific bin, $\overline{x}$ is the mean x-position of all amyloplast coordinates within the bin, and n is the total number of amyloplast coordinate points within the bin. As statoliths approach a channel, their x-axis spread becomes narrower, and the Channeling Coefficient increases. Note that even though a Channeling Coefficient of 3 is reached, this value is mediated by other plastids within the profile that do not approach the channel. For the profile shown in Figure 3.17, these plastids are amyloplasts #5 and #6 (blue circle and green pentagon). A variation to the AMYLFALL.M program, found at the end of Appendix I, allows only certain plastids to be included for analysis. Figure 3.18 shows how analyzing the behavior of only specific amyloplasts strengthens the argument for channeling.

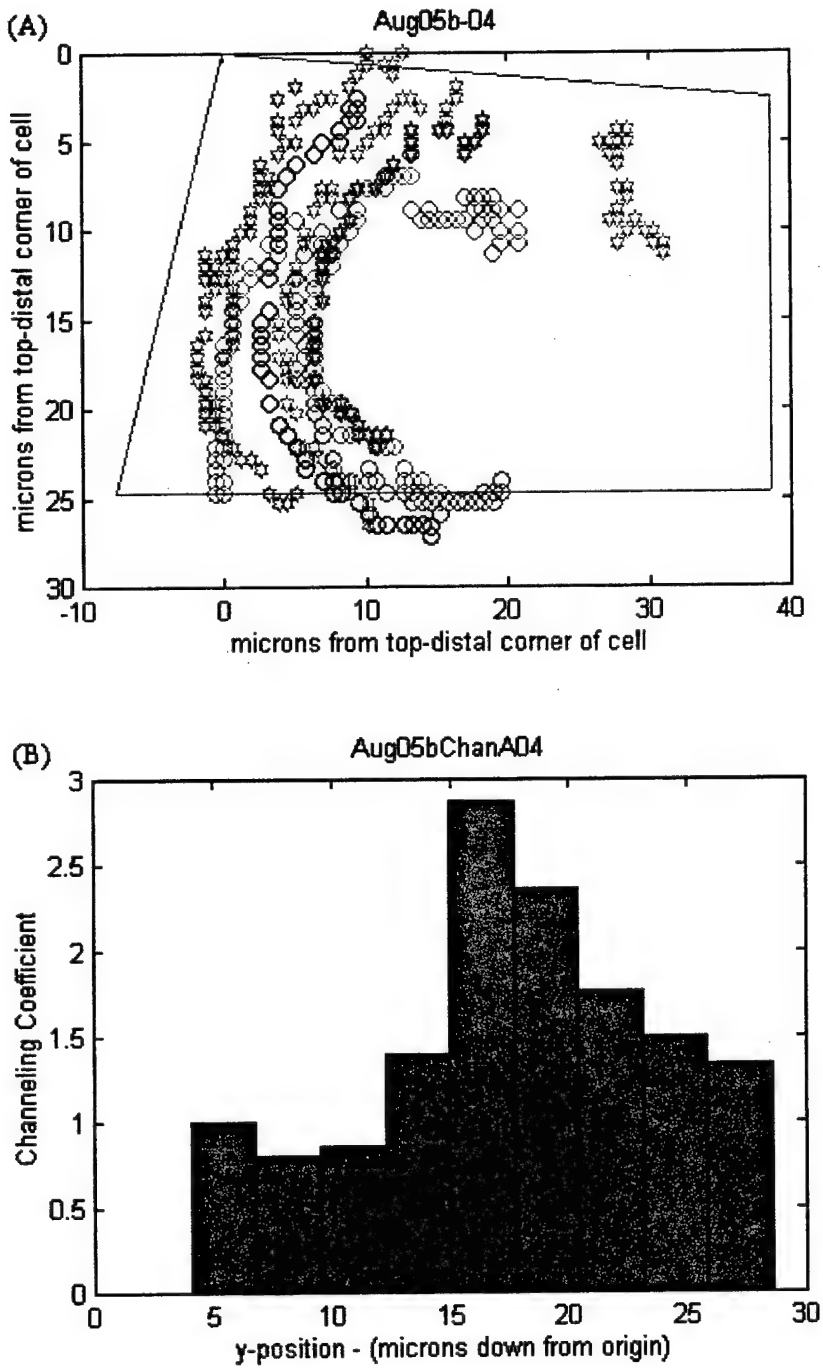

Figure 3.17 - Channeling Behavior Formulation #1
(A) shows the sedimentation profile, while (B) quantifies the channeling behavior that is witnessed. Note that approximately half way down the cell, a maximum of approximately 3 is achieved which signifies that the statoliths approach 1/3 of their starting variance along the x-axis. Equation 3-22 calculates the CC for each bin of the histogram.

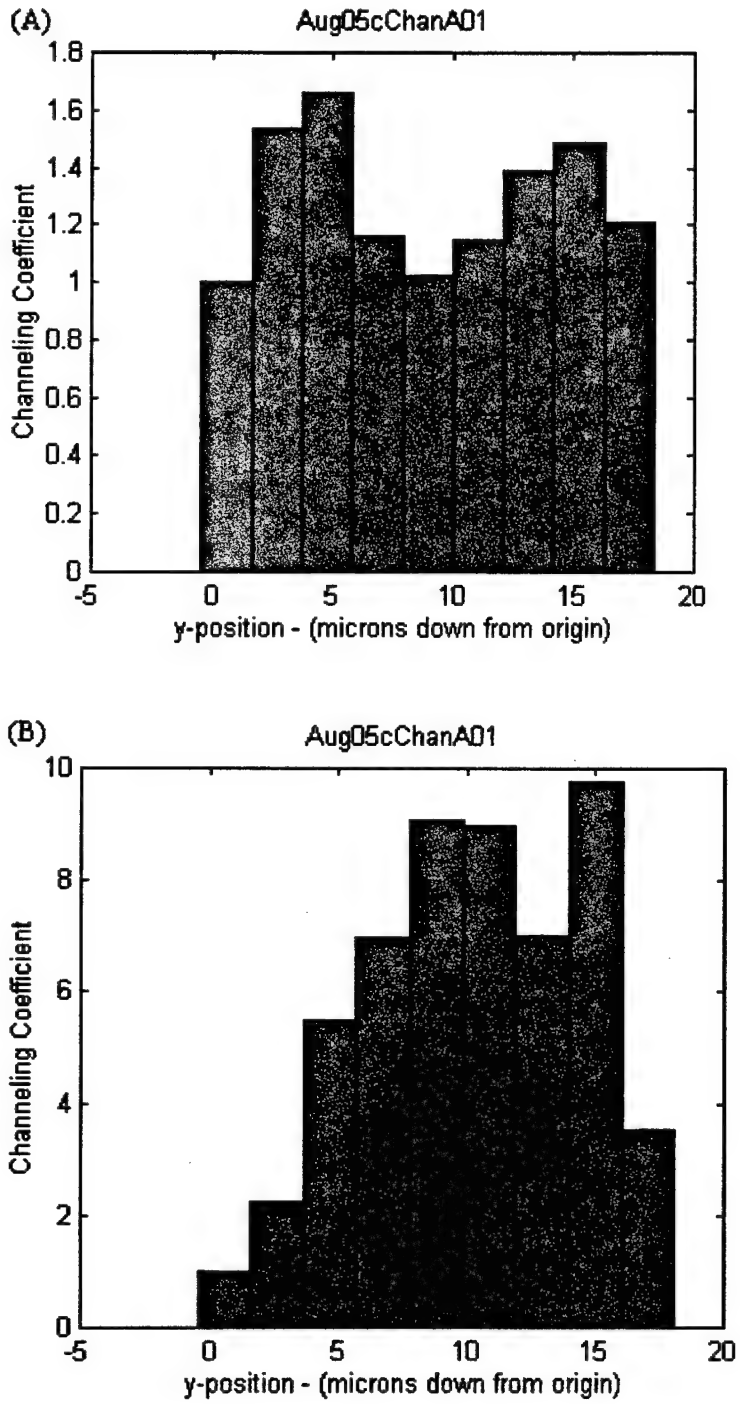

Figure 3.18 - Channeling Coefficient with Specificity
(A) shows the channeling coefficients for the sedimentation profile shown in Figure 3.12. This formulation is mediated by amyloplasts (green and blue circles in Figure 3.12) not approaching the main channel. (B) is the channeling coefficients for only the last four amyloplasts plotted (green, red, magenta, and black pentagons).

The program which produces analysis for specific statolith groups (AMYLFALL_SPEC.M) is executed following the AMYLFALL.M script and the user enters the specific cell and amyloplasts that should be included in the coefficient calculations. Figure 3.18 compares the overall channeling of the sedimentation profile shown earlier in Figure 3.12 and the channeling of only the last 4 amyloplasts initially spread out across the top of the cell (green, red, magenta, and black pentagons). The figure strongly confirms the existence of a central obstruction (approximately 10 μm down from the cell wall) that opposes free sedimentation through the cell central region. Another formulation was developed to quantify the channeling behavior and is based on the observation that the channeling plastids must move laterally (along the x-axis) in order to approach a channel.

The second formulation of channeling behavior entailed examination of the x-velocities along the x-axis. Statoliths approaching the channel move with x-velocity when obstructed from free, downward motion. Once inside a channel, x-velocity reaches a minimum, or zero if complete unobstructed motion existed in that region. Figure 3.19 shows an example of this second channel formulation. This formulation confirms channel existence, confirms a central "obstruction," and provides kinetics data on the velocity profiles upon approaching a channel. In the example of Figure 3.19, the channel at approximately 14 μm along the x-axis is flanked by areas of rapid x-velocities as the amyloplast is drawn into the unobstructed region. The non-zero x-velocities found even within this relatively significant channel can be attributed to inter-plastid collisions, diffusion, and noise in the data.

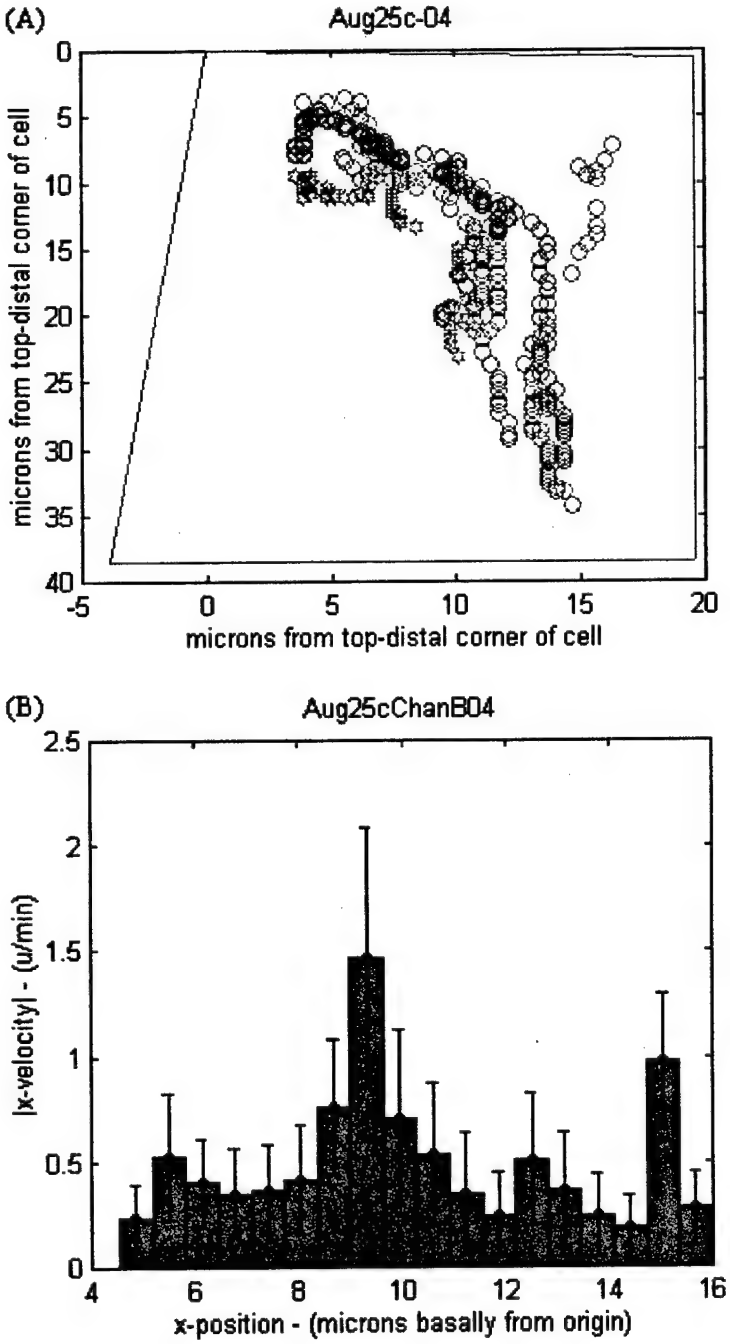

Figure 3.19 - Channeling Behavior Formulation #2
(A) shows the sedimentation profile, while (B) shows where, along the x-axis, the x-velocity approaches its minima and maxima. Minimum of approximately 0.2 μm/min. occurs at the 14 μm point along the x-axis (confirmed visually in (A) as a channel) while a maximum of 1.5 μm/min. occurs at the 9 μm point (rapid lateral movement approaching the channel).

The second category of data formulations attempts to measure any indications of group movement between the amyloplasts. The goal of the analysis is to determine if the statoliths are acting individually or as a group. As with channeling behavior, two separate formulations were developed to analyze the group behavior. The first formulation is a plot of the y-velocities over time for all amyloplasts tracked within the cell. This plot provides a visual means to analyze correlation in velocity between the amyloplasts, but finding the correlation coefficients between each amyloplast also provides a quantitative means of measuring a tendency toward group behavior. The correlation coefficient is the covariance of a set of random variables normalized by the standard deviations of each random variable (Montgomery & Runger, 1994). In this case, the random variables are each amyloplast's velocity. The coefficient can range from -1 to 1 and is a measure of the linear association. Figure 3.20 shows an example of this group behavior formulation for a cell with 7 amyloplasts. Because of data collection noise and diffusion of the statoliths, these correlations are not very high. A maximum correlation of 0.5228 is seen between amyloplasts #3 and #6 which signifies some linear association but not significant. Since this formulation, how velocity changes over time, is essentially a matching of acceleration and this is inherently a noisy environment. The second group-behavior formulation looks at how y-position changes over time are correlated.

(A)

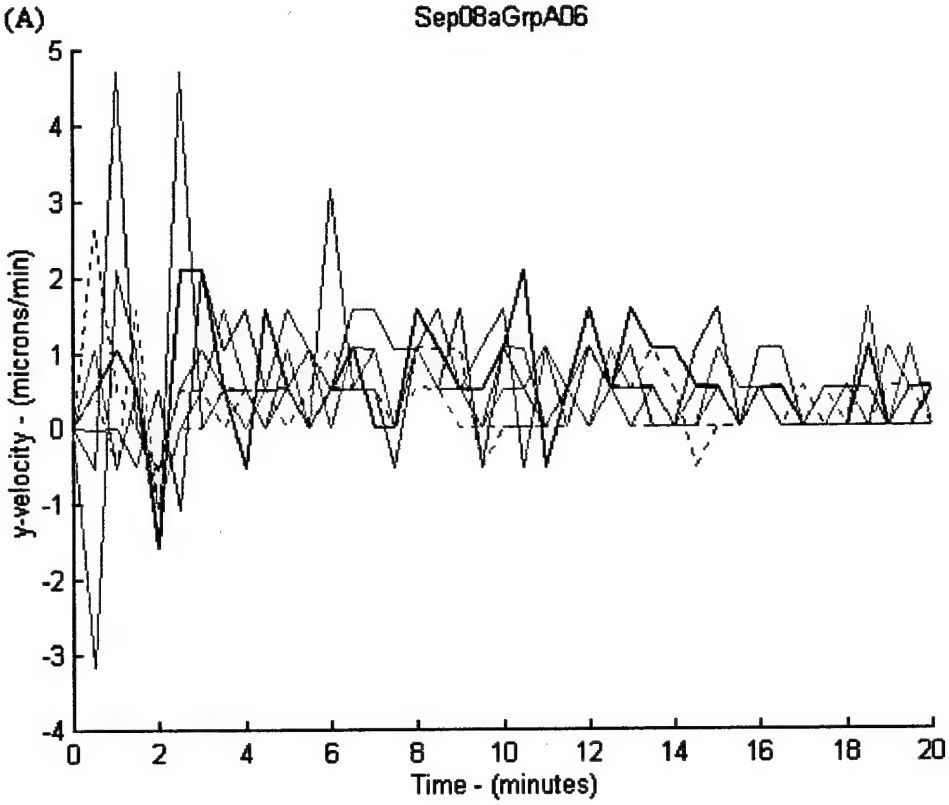

(B)

1.0000	-0.1918	-0.0766	0.4770	0.4034	0.0731	-0.1259
-0.1918	1.0000	0.2646	0.0641	-0.0009	-0.0269	0.0451
-0.0766	0.2646	1.0000	0.0980	-0.0739	0.5228	0.2424
0.4770	0.0641	0.0980	1.0000	0.2192	0.1050	0.3212
0.4034	-0.0009	-0.0739	0.2192	1.0000	-0.1332	0.0855
0.0731	-0.0269	0.5228	0.1050	-0.1332	1.0000	0.2117
-0.1259	0.0451	0.2424	0.3212	0.0855	0.2117	1.0000

Figure 3.20 - Group Behavior Test Formulation #1
(A) shows the y-velocity over time of every amyloplast within the cell; note the visual difficulty in correlating the motion. Amyloplast numbers (1-7) are depicted in order with green, red, magenta, black, and blue lines (first 5 solid lines with remaining color scheme repeating with dashed lines). (B) shows the correlation coefficient matrix for these velocities. For example, the correlation between amyloplast #1 (row 1) and itself (column 1) is 1.0, while the correlation between amyloplast #1 (row 1) and amyloplast #4 (column 4) is 0.477.

The second group behavior formulation is very similar to the first in that a visual plot of y-positions over time for each amyloplast is accomplished, followed by a correlation analysis. Figure 3.21 shows the results using the same columella cell analyzed in the preceding figure.

(A)

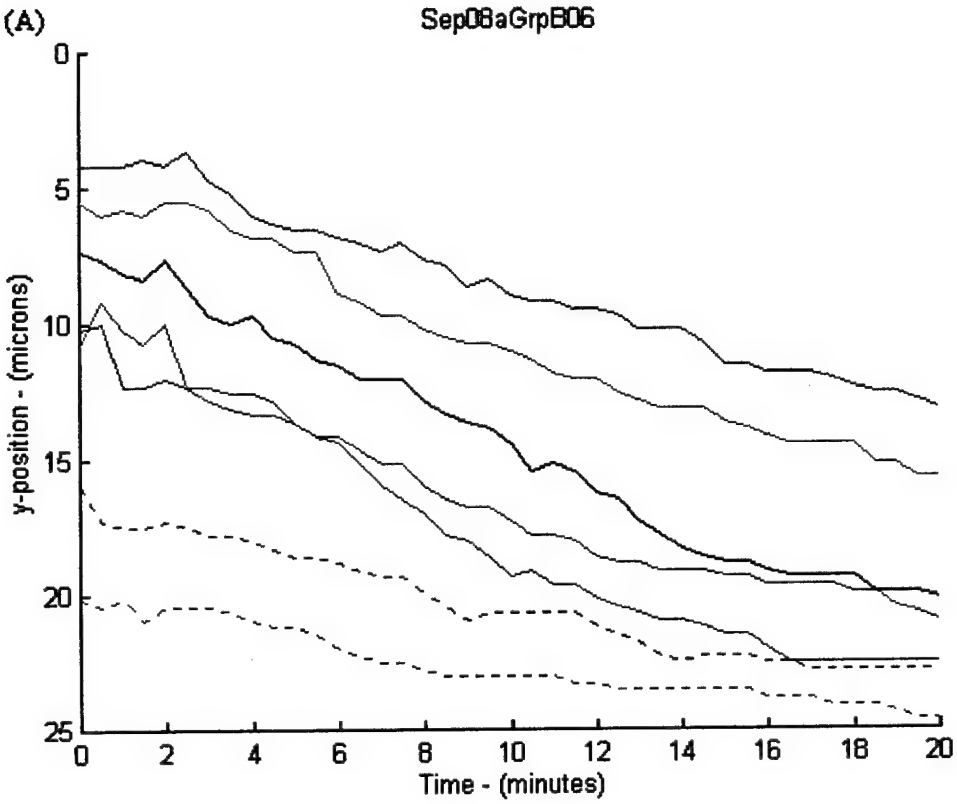

(B)

1.0000	0.9729	0.9784	0.9802	0.9871	0.9785	0.9773
0.9729	1.0000	0.9894	0.9898	0.9763	0.9660	0.9781
0.9784	0.9894	1.0000	0.9873	0.9847	0.9842	0.9838
0.9802	0.9898	0.9873	1.0000	0.9856	0.9607	0.9883
0.9871	0.9763	0.9847	0.9856	1.0000	0.9758	0.9899
0.9785	0.9660	0.9842	0.9607	0.9758	1.0000	0.9726
0.9773	0.9781	0.9838	0.9883	0.9899	0.9726	1.0000

Figure 3.21 - Group Behavior Formulation #2
(A) plots the y-positions over time for each amyloplast (color-code same as in previous figure), while (B) displays the correlation matrix for these statoliths.

The graphical formulation of group behavior in Figure 3.21(A) readily leads the viewer to appreciate the common motion among the plastids. Note the leveling off and upward motion common to all but one plastid (#7, dashed red line) around 2 minutes into the sedimentation. The correlation matrix confirms this visual interpretation by showing strong correlation between all pairs of plastids. Again, a following subsection will present the statistical results of these two, group movement data formulations, however, one final data formulation category is presented in this subsection; measurements of velocity versus cellular position.

In an attempt to quantify the extent and location of significant cytoskeletal interaction with the sedimenting amyloplasts, one further data formulation was accomplished. This formulation is a map of the velocities witnessed by the 2 μm probes (amyloplasts) as they move to different regions of the columella cell. If the mapping shows domains of distinctly different velocities, inferences can be made about the cytoskeletal densities experienced within that domain and therefore it may become possible to determine the final amyloplast-cytoskeletal interaction model set. Figure 3.22 shows an example of this formulation. This one example leads us to infer that the upper, starting point for the amyloplast sedimentation does not produce the fastest velocities; the center region does. Again, this example leads us to the conclusion that an obtrusive cytoskeletal interaction in the center region dampens initial sedimentation velocity, but once a channel is found, the velocity reaches maximum during movement through the channel. Statistical trends with this formulation along with appropriate conclusions are examined in the following subsection.

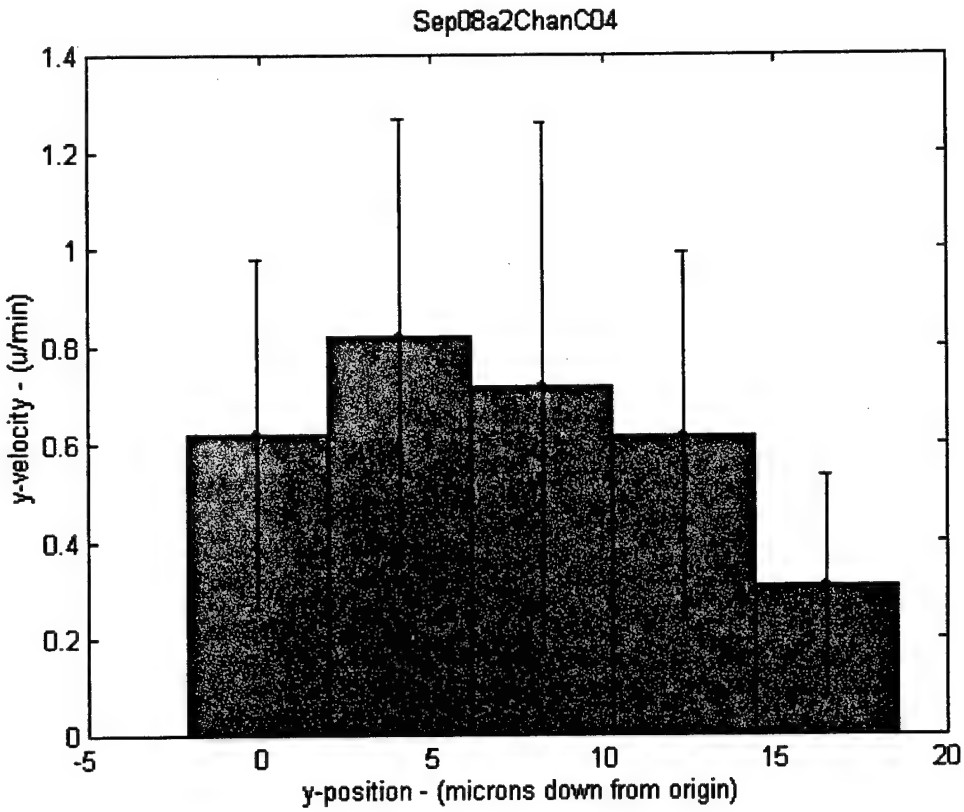

Figure 3.22 - Vertical Velocity as a Function of Vertical Position

3.5.2.3 Statistical Inferences from Sedimentation Studies

This section presents the statistical analysis of the various data formulations described in the previous section. As review, there are 5 data formulations designed to characterize 3 different types of behavior in the sedimenting amyloplasts. The behaviors of interest are channeling, group action, and velocity within different vertical cellular domains. Two data formulations describe the channeling behavior, two describe group action behavior, and one describes the velocity within the different vertical regions. Presentation of the statistical analysis and discussion follows the same order as that in which the formulations were introduced in the previous section; channeling formulations 1 and 2, group action formulations 1 and 2, and, finally,

velocity as a function of vertical position. Initially an analysis of sensor dynamics as a function of root size/age is discussed. The root size categories were 20-29 mm, 30-39 mm, and 40-55 mm. Statolith velocities were averaged over the first, second, and third thirds of total sedimentation time. Sedimentation profiles included distal-to-side, side-to-side, and distal-to-basal amyloplast movements. This analysis scheme produces a 3x3x3 matrix of average velocities that is analyzed and discussed. Table 3.1 summarizes an analysis of the various velocities of statoliths in the three categories of root lengths during the first and second thirds of sedimentation times. The final third of total sedimentation time was omitted from the analysis because many plastids complete their sedimentation during this time period and therefore would systematically skew the data. Of interest is the higher velocities found for statoliths undergoing sedimentation in distal-to-side direction as compared to those sedimenting through the cell's central region. This velocity difference appears to confirm the presence of the putative central cytoskeletal obstruction. The x-velocities cannot be compared because the distal-to-side sedimentation creates x-velocity as the statolith collides with other plastids and the distal cell interior surface, causing a predominantly positive x-migration of the amyloplasts.

Table 3.1 - Summary of Statolith Velocity

Description	1st Total x - Velocity	-Third Time y - Velocity	of (μm/min) Abs. - Velocity	2nd Total x - Velocity	-Third Time y - Velocity	of (μm/min) Abs. - Velocity
distal-to-side profiles, 20-29 mm lengths (n=15)				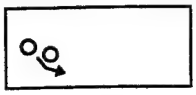		
mean:	0.87	1.90	3.27	0.70	0.80	2.40
standard deviation:	2.05	2.18	1.84	2.07	1.51	1.56
30-39 mm lengths (n=19)						
mean:	0.33	0.67	1.50	0.47	0.43	0.90
standard deviation:	0.96	1.16	1.15	0.63	0.48	0.65
side-to-side/distal-to-basal profiles, 20-29 mm lengths (n=82)	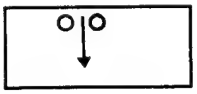 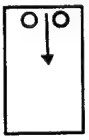			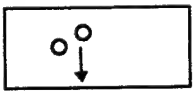 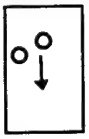		
mean:	0.28	0.83	1.93	0.12	0.77	1.53
standard deviation:	1.68	1.63	1.74	1.18	1.37	1.44
30-39 mm lengths (n=75)						
mean:	-0.04	0.32	0.91	0.09	0.47	0.90
standard deviation:	0.67	0.81	0.71	0.68	0.90	0.84
40-55 mm lengths (n=83)						
mean:	-0.09	0.58	1.16	-0.06	0.46	1.03
standard deviation:	0.71	0.96	0.78	0.62	0.88	0.70

Table 3.2 summarizes the t-test analysis accomplished between compared pairs among the various categories in order to determine any statistically significant differences (P-value ≤ 0.05 for the Student's t-test) in their mean values. No mean x-velocities differed significantly among the root-length categories or time partitions. This is expected since x-velocity is created by diffusion or interplastid collisions. Any difference here would have meant a significant morphological difference among the columella cells, and this has not been noticed elsewhere. Additionally, only one out of

six t-tests indicated a statistical difference in the mean y-velocity. This occurred between the 2nd and 3rd length category in the 1st time partition. This might indicate some difference in the amyloplast-cytoskeletal interaction between cells of roots in these two length categories, but because the significance is not witnessed in the 2nd time partition (a time when the statoliths are still to complete their sedimentation), this significance may only be a data anomaly. On the other hand, five out of the six t-tests performed on absolute-velocity means showed significant differences among the mean velocities from the three root-length categories. This is witnessed in both time partitions. Since the significant differences are witnessed in absolute velocity and are not directional, it appears that the length categories may have different cytoplasmic viscosities inherent to their central columella cells with the younger, short roots having the lowest viscosities (highest velocity), progressing to higher viscosities (lower velocity) in the 30-39 mm length group, and then beginning to decrease again into the final group. To confirm the lack of evidence for cytoskeletal differences between the length categories, they are compared again with respect to the channeling behaviors in the following paragraphs.

Table 3.2 - Summary of t-Testing on Statolith Velocities

Tested Values	1st Third Time Test Statistic	Degrees of Freedom	P-Value	2nd Third Time Test Statistic	Degrees of Freedom	P-Value
x - velocity *distal-to-side profiles*						
between 20-29 mm and 30-39 mm lengths:	0.94	20	0.38	0.42	16	0.65
side-to-side/distal-to-basal profiles						
between 20-29 mm and 30-39 mm lengths:	1.59	109	0.12	0.20	133	>0.8
between 30-39 mm and 40-55 mm lengths:	0.46	158	0.65	1.44	152	0.15
y - velocity *distal-to-side profiles*						
between 20-29 mm and 30-39 mm lengths:	1.98	21	0.06	0.91	17	0.35
side-to-side/distal-to-basal profiles						
between 20-29 mm and 30-39 mm lengths:	2.51	122	**0.001**	1.63	143	0.10
between 30-39 mm and 40-55 mm lengths:	-1.85	157	0.07	0.07	156	>>0.8
Abs. - velocity *distal-to-side profiles*						
between 20-29 mm and 30-39 mm lengths:	3.26	23	**0.004**	3.49	18	**0.003**
side-to-side/distal-to-basal profiles						
between 20-29 mm and 30-39 mm lengths:	4.88	110	**<0.001**	3.38	134	**0.001**
between 30-39 mm and 40-55 mm lengths:	-2.11	158	**0.035**	-1.05	146	0.32

Table 3.3 summarizes the statistical results concerning the first formulation for channeling behavior; the channeling coefficient. This analysis was performed only on side-to-side and distal-to-basal sedimentation profiles since channeling is not witnessed

in distal-to-side profiles. Note that maximum channeling occurs at approximately 12 μm from the top of the cell which, on the average, is the vertical middle of the cell. The large deviation in minimum location is due to the fact that the starting positions for the statoliths is somewhat random in relation to the y-axis origin since only those plastids that are clearly in view throughout the sedimentation are included in the study. As mentioned previously, all tracked plastids are included in the calculation of the cell's channeling coefficient and therefore the "maximum" shown here is quite conservative, with many statoliths displaying significantly more channeling behavior. Even with this caveat in mind, a maximum of approximately 2 signifies motion that channels plastids to half of their initial distribution; a significant effect. Table 3.4 summarizes the t-test results accomplished to any determine statistically significant differences in the population means. Note that those roots treated with cytochalasin D (CD) have a significantly lower (Student's t-test, α=0.05) maximum channeling coefficient. This is consistent with the belief that the channeling behavior is caused by a centrally higher gradient of amyloplast-cytoskeletal interaction. The amount of actin cytoskeleton and, therefore, the extent of this interaction is decreased (but not eliminated) upon introduction of the CD. Significant differences were not found in the minimum channeling values or the location of the maximum or minimum channeling. Results of t-tests between the maxima of the three root length categories are provided. The 40-55 mm length group is found to be significantly different from the 30-39 mm group with just barely the required level of significance (0.05), but the 20-29 mm group is not found to be significantly different by an equally small margin. This

information along with the previous length category discussion allows the conclusion that sensor dynamics are not significantly dependent upon the length/age of the root and therefore these groupings are not analyzed in further sections. However, this dependency cannot be ruled out and could be a topic of further research.

Table 3.3 - Summary of the Channeling Coefficient

Description	Minimum	Location (y - μm)	Maximum	Location (y - μm)
No CD, all lengths (n=31)				
mean:	0.86	7.35	2.28	11.45
standard deviation:	0.22	5.71	1.87	6.64
With CD, all lengths (n=25)				
mean:	0.90	4.96	1.27	12.76
standard deviation:	0.17	5.31	0.78	6.17
No CD, length 20-29 mm (n=10)				
mean:	0.89	7.20	3.31	12.20
standard deviation:	0.13	4.85	2.43	4.47
No CD, length 30-39 mm (n=9)				
mean:	0.73	10.22	1.16	9.00
standard deviation:	0.30	7.82	0.29	8.85
No CD, length 40-55 mm (n=12)				
mean:	5.33	5.33	2.26	12.67
standard deviation:	0.16	3.37	1.65	6.31

Table 3.4 - Summary of t-Testing on Channeling Coefficient

Tested Values	Test Statistic	Degrees of Freedom	P-Value
maxima, between those wo/CD and w/CD	2.73	43	**0.01**
maxima, wo/CD, between 20-29 mm and 30-39 mm lengths	2.25	9	0.06
maxima, wo/CD, between 30-39 mm and 40-55 mm lengths	-2.26	12	0.051

Table 3.5 summarizes the statistical results concerning the second formulation for channeling behavior; the x-velocity as a function of x-position. As with the previous study, this analysis was only accomplished for side-to-side and distal-to-basal sedimentation profiles since channeling is not witnessed in distal-side profiles. Note that the location of minima and maxima are statistically insignificant (P-value ≈ 0.4). This is understandable since examining the individual histograms (see Figure 3.19) shows that in almost every case the area of minimum x-velocity is bordered by the area of maximum x-velocity. Interpretation is that the plastid moves laterally (x-velocity) most rapidly as it approaches the vertical channel. Both the minimum and maximum were found to differ insignificantly (P-values of 0.06 and 0.24, respectively) between normal roots and those treated with CD. The difference between maximum and minimum is statistically significant (P-value <0.001) again confirming the presence of a channel where x-velocity is significantly lower as the statolith falls in a nearly vertical manner as compared with motion prior to the channel.

Table 3.5 - Summary of the |x-Velocity| as a Function of x-Position

Description	Minimum (μm/min)	Location (x - μm)	Maximum (μm/min)	Location (x - μm)
No CD, all lengths (n=31)				
mean:	0.33	9.35	1.13	10.39
standard deviation:	0.22	4.93	0.53	4.77
With CD, all lengths (n=25)				
mean:	0.24	9.10	0.97	14.04
standard deviation:	0.12	4.01	0.46	5.10

The following summaries deal with the formulations of statolith group behavior as presented in Figures 3.20 and 3.21. Table 3.6 summarizes both the first formulation

(correlations of y-velocities over time) and the second formulation (correlations of y-positions over time) for all statoliths. Recall, that the AMYLFALL.M routine that compiles these formulations, finds the minimum, maximum, mean, and standard deviation of the correlation coefficients between all statoliths in a single cell. The means and standard deviations computed in Table 3.6 reflect the averaging of these data for all columella cells in a particular group. Note that the correlation between statolith y-velocities is always lower than the correlation between statolith y-positions. This is expected since y-velocity over time is subject to more noise from both data acquisition technique and diffusion than is y-position over time. With this in mind, the existence of a mean maximum correlation found in cells on the order of 0.5-0.7 is significant. This appears to indicate that some plastids (at a minimum) are acting as a group, even while under the obstructive influences established in the side-to-side and distal-to-basal sedimentation profiles. Confirming this is the second formulation summary; the statolith y-position correlations. If the plastids fall unobstructed, similar to marbles in a can, this correlation would be close to 1.0, but if falling within an environment of significant cytoskeletal interaction (argued in previous sections as the case here), this value should be much lower if the plastids are not under a grouping influence such as actual attachments or mutual influence by the nature of the cytoskeletal interaction. The summary shows that y-position is highly correlated between the statoliths within a cell. Significant to note is the higher correlations between those amyloplasts sedimenting in the distal-side profiles from those sedimenting in profiles that must transit the center cellular regions (P-value=0.015).

Again this confirms, the existence of a central region of higher amyloplast-cytoskeletal interaction. This and other t-test analyses are summarized in Table 3.7. Another significant finding from this analysis is the statistically significant difference found between y-velocity correlations from normal roots and those treated with CD as they traverse the central region in side-to-side or distal-to-basal sedimentation profiles (P-value=0.0024). The significantly higher correlation in those treated with CD appears to validate the central region obstruction being composed of actin cytoskeleton. The insignificant differences found between all the tests accomplished on the second group behavior formulation (y-position over time) can be partially attributed to the consistently high value this correlation achieves in all groupings. As the channeling formulations indicate the creation of channels through a central obstruction, the group behavior formulations have indicated the presence of group behavior. In the presence of cytoskeletal interactions and interference with other plastids, the amyloplasts display highly correlated changes in y-position and higher than expected correlation in changes to y-velocity. These correlations and their mediation by cytoskeletal changes (CD introduction) strongly indicate some mechanism of group interaction. Further research is necessary to establish whether this interaction is through physical attachment or as a result of the channeling nature of a distorted actin network.

Table 3.6 - Summary of Group Behavior Formulations

Description	Correlation Coefficients			
	Minimum	Maximum	Mean	Std. Dev.
y-velocity correlated over time, wo/CD, *distal-to-side profiles* (n=6)				
mean:	0.19	0.73	0.50	0.15
standard deviation:	0.26	0.11	0.11	0.07
side-to-side & distal-to-basal profiles (n=31)				
mean:	-0.05	0.51	0.24	0.13
standard deviation:	0.14	0.12	0.07	0.03
y-velocity correlated over time, w/CD, *distal-to-side profiles* (n=13)				
mean:	0.08	0.64	0.39	0.16
standard deviation:	0.26	0.10	0.15	0.03
side-to-side & distal-to-basal profiles (n=35)				
mean:	0.01	0.61	0.32	0.15
standard deviation:	0.16	0.12	0.10	0.04
y-position correlated over time, wo/CD, *distal-to-side profiles* (n=6)				
mean:	0.51	0.99	0.91	0.08
standard deviation:	0.66	0.01	0.08	0.07
side-to-side & distal-to-basal profiles (n=31)				
mean:	0.58	0.98	0.88	0.10
standard deviation:	0.46	0.03	0.10	0.09
y-position correlated over time, w/CD *distal-to-side profiles* (n=13)				
mean:	0.80	0.99	0.92	0.07
standard deviation:	0.24	0.01	0.07	0.08
side-to-side & distal-to-basal profiles (n=25)				
mean:	0.71	0.99	0.91	0.08
standard deviation:	0.23	0.01	0.06	0.07

Table 3.7 - Summary of t-Testing on Group Behavior Statistics

Tested Values	Test Statistic	Degrees of Freedom	P-Value
y-velocity correlated over time, wo/CD, between distal-to-side and side-to-side/distal-to-basal profiles:	5.58	6	**0.015**
y-velocity correlated over time, *distal-side profiles,* between those wo/CD and w/CD:	1.8	16	0.09
y-velocity correlated over time, *side-to-side/distal-basal profiles,* between those wo/CD and w/CD:	-3.39	43	**0.0024**
y-position correlated over time, wo/CD, between distal-to-side and side-to-side/distal-to-basal profiles:	0.8	10	0.46
y-position correlated over time, *distal-side profiles,* between those wo/CD and w/CD:	-0.26	10	0.80
y-position correlated over time, *side-to-side/distal-to-basal profiles,* between those wo/CD and w/CD:	-1.39	52	0.17

The velocity of the amyloplast as a function of its vertical position in the cell was examined (see Figure 3.22). Table 3.8 summarizes the findings with the sedimentation study divided into 2 categories, with and without cytochalasin D (CD), and 2 subcategories (distal-side profiles and side-to-side (or distal-basal) profiles).

Table 3.8 - Summary of Velocity (μm/min.) as a Function of Vertical Position

Description	Top Sector	Sector #2	Sector #3	Sector #4	Bottom Sector
wo/CD (n=274)					
distal-side (n=34): mean	1.73	1.71	1.34	1.18	0.68
standard deviation	0.70	0.96	0.76	0.63	0.32
side-to-side (n=240): mean	0.77	0.82	0.96	0.86	0.68
standard deviation	0.36	0.37	0.45	0.37	0.23
w/CD (n=292)					
distal-side (n=77): mean	0.70	0.87	0.62	0.53	0.36
standard deviation	0.23	0.43	0.16	0.10	0.10
side-to-side (n=215): mean	0.69	0.91	0.94	0.70	0.47
standard deviation	0.19	0.26	0.33	0.16	0.14

Examination of these values immediately shows a significant difference between the distal-side profile velocities and those of the side-to-side (or distal-basal) profiles. The velocities are higher in the 1st four sectors (upper 4/5) of the cell during distal-to-side sedimentations. It appears that the central obstruction is manifesting itself in this data also, slowing the plastid during transit of the central regions of the cell which only occurs during side-to-side or distal-to-basal sedimentation profiles. Other significant differences (Student's t-test, α=0.05), include velocities between the top and 3rd sectors (top and middle of the cell). Table 3.9 summarizes the t-test findings for various situations. The P-value of 0.035 for the distal-side velocities at the top versus those in the 3rd sector indicates a significant difference between the starting and middle velocities of the sedimenting plastid in this profile, but not the progression of velocity from Table 3.8 above. In the distal-to-side profile the plastid obviously begins with its highest velocity and slows as sedimentation continues (approaching the bottom and other plastids fairly rapidly). As a contrast to this the

side-to-side profiles show P-values <0.001 when comparing their top and 3rd sector velocities. This higher level of significant difference is enhanced by the observation that the plastids in these profiles also begin sedimenting at lower velocities and actually increase in speed to a maximum occurring in this middle or 3rd sector. Note also that side-to-side profiles produce middle (3rd) sector velocities insignificantly different between normal roots and those treated with CD. On the other hand, the difference is significant in the 2nd sector, the sector where the central obstruction appears to begin to effect the amyloplasts. These findings provide further evidence of a central region of the cell containing a higher gradient of amyloplast-cytoskeletal interactions which obstruct and slow the plastid as it sediments, once a channel is found, the plastid increases in speed as it falls through the central region.

Table 3.9 - Summary of t-Testing on Sector Velocities

Tested Values	Test Statistic	Degrees of Freedom	P-Value
wo/CD, distal-to-side profiles, top and 3rd sectors	2.20	67	**0.035**
wo/CD, side-to-side profiles, top and 3rd sectors	-4.76	397	**<0.001**
w/CD, side-to-side profiles, top and 3rd sectors	-9.60	343	**<0.001**
side-to-side profiles, w/CD and wo/CD 3rd sectors	0.52	381	>0.8
side-to-side profiles, w/CD and wo/CD 2nd sectors	-2.89	372	**0.005**

3.5.3 Viscosity Analysis and Diffusion Effects

This section documents the results of procedures used to refine the value for columella cytoplasmic viscosity and presents the results of analysis on diffusion effects

of the statoliths. Since the range of assumed cytoplasmic viscosity appears very large (see Table 1.1 of Chapter 1), a procedure was accomplished to refine the value specifically for the *Zea mays* L. cv. Yellow Dent columella cell under study. The following methodology was used to compute the viscosity value. Using the AMYFALL.M sedimentation analysis routine detailed in previous sections, the y-velocity was plotted against the absolute velocity of the same amyloplast over time. A search was accomplished for those moments where the statolith's y-velocity was equal to its absolute-velocity (i.e. falling unobstructed in a purely vertical direction) AND these velocities were at their maximum for the time course. It is assumed that this condition exists when the statolith is more or less at a terminal velocity, unimpeded by any cytoskeletal interaction. These amyloplasts were identified and re-examined on the original video frames where their diameters were measured. Using the following equation (a modification of Equation 3-12 derived earlier), the viscosity was calculated. Equation 3-23 assumes terminal velocity is reached (a good assumption based on the low Reynolds' number derived in section 3.3.1) and the only forces acting on the statolith at that moment are drag and gravity.

$$\ddot{y} + b\dot{y} + ky = f(t)g_y$$

where, $$b = \frac{6\pi r_{amyl}\eta}{m_{amyl}}$$

$$k \Rightarrow 0 \text{ (no actin interaction)}$$

$$f(t) \equiv f = \frac{V_{amyl}\Delta\rho}{m_{amyl}}$$

$$\ddot{y} \Rightarrow 0 \text{ (terminal velocity)}$$

$$V_{amyl} = \frac{4}{3}\pi r_{amyl}^{3}$$

$$\therefore \; b\dot{y}_{terminal} = fg_y$$

$$\frac{6\pi r_{amyl}\eta}{m_{amyl}}\dot{y}_{terminal} = \frac{V_{amyl}\Delta\rho}{m_{amyl}}g_y$$

$$\eta = \frac{g_y V_{amyl}\Delta\rho}{\dot{y}_{terminal}\, 6\pi r_{amyl}} = \frac{2g_y r_{amyl}^{2}\Delta\rho}{9\dot{y}_{terminal}} \qquad (3\text{-}23)$$

An example of the plots used to identify freely falling statoliths is found in Figure 3.23. The identified plastids are amyloplasts #3 and #5 at 8.5 minutes into the sedimentation profile.

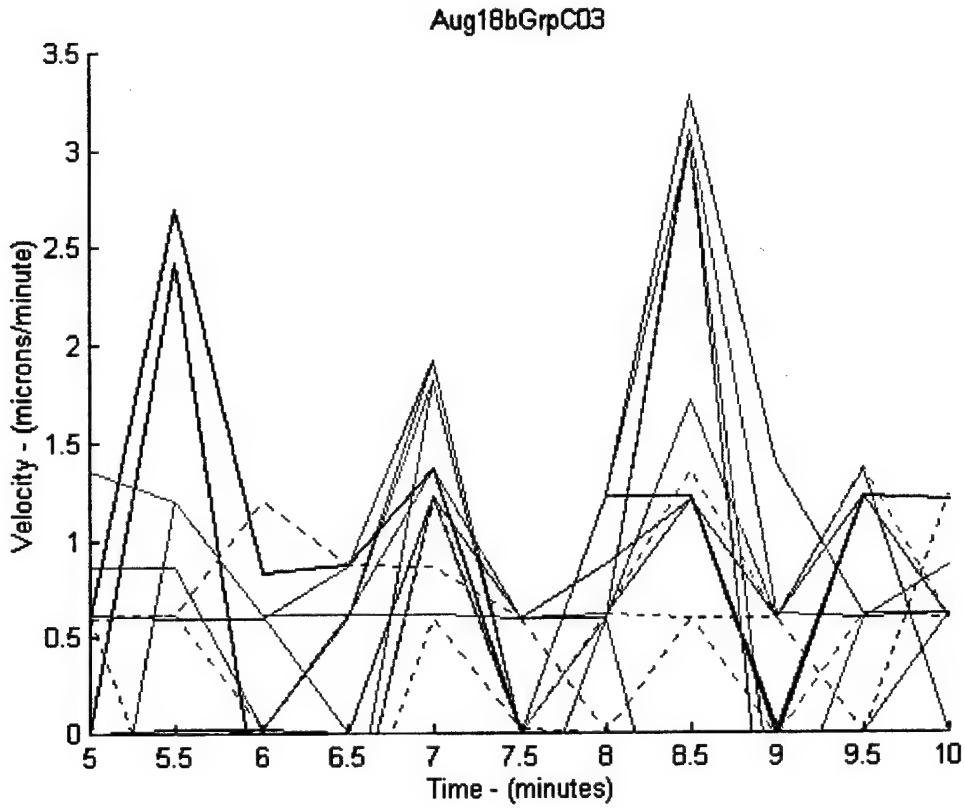

Figure 3.23 - Identifying an Unobstructed Statolith during Sedimentation
The y-velocity and absolute velocity over time is plotted for each amyloplast within this columella cell. The two velocities are the same color-code so a search is accomplished for a point where the two are identical. Amyloplasts #3 (magenta) and #5 (blue) are equal and at a global maximum at 8.5 minutes into the sedimentation. As before, statolith identification follows the same green, red, magenta, black, and blue (first solid line then dashed lines) color-code scheme. In this example, only amyloplast #3 (magenta) is chosen since it displays close to purely vertical velocity, while amyloplast #5 (blue) still displays a noticeable difference between its y-velocity and absolute-velocity.

Of a total of 274 amyloplasts (292 amyloplasts treated with CD) examined, only 21 (15 treated with CD) reached a global maximum velocity at the same moment as purely vertical velocity. A maximum of one amyloplast per cell was found to display the proper velocity characteristics. Table 3.10 summarizes the results of the study. The final viscosity, used in further modeling, is 34 cp. This value is 70% higher

than the high end of the range described from the literature in Chapter 2 and the table of assumptions in Chapter 1 (5-20 cp). Note that no significant difference exists in the viscosity calculation between normal amyloplasts and those treated with CD.

Table 3.10 - Viscosity Analysis Summary

Number of Columella Cells	Number of Amyloplasts	Viscosity (kg/μm-min) Mean	Sigma	95% CI Error
wo/CD: 21	21	34.10	8.91	3.81
w/CD: 15	15	34.57	8.62	4.36

A number of columella cells were studied under steady-state conditions with the amyloplasts fully sedimented on the distal floor of the cell. Their recorded motions in the x-direction, unforced by gravity, can be attributed to diffusion effects. As predicted by the Peclet number derivations in section 3.3.1 of this thesis, the diffusive motions of the amyloplasts are not insignificant. Table 3.11 documents the results. The x-velocity was obtained by averaging the second channeling formulation histograms produced by the AMYLFALL routine (refer back to Figure 3.19). Because of the number of amyloplasts examined the 95% Confidence Interval (CI) expected error is small (0.1 μm/min.).

Table 3.11 - Diffusion Kinetics of the Maize Amyloplast

Number of Columella Cells	Number of Amyloplasts	Diffusion induced X-Velocity (μm/min) Mean	Sigma	95% CI Error	<x> (μm)	Time Interval (seconds)
6	20	1.01	0.5	0.1	0.34	20

Since the AMYLFALL routine computes velocity as μm/min. based on the motion observed across the previous time interval and, during these video segments,

that interval was 20 seconds, this velocity equates to an average movement of 0.34 μm (<x>) during the 20 seconds (t). These values in Equation 3-5 produce a value for D (diffusion coefficient) of 0.0029 μm^2/second. This result is on the high-end of those predicted earlier in Section 3.3.1, but now it is possible to estimate the cytoplasmic viscosity inferred by these diffusion results. Using Equation 3-4, the viscosity is $4x10^{-8}$ kg/μm-sec (40 cp) with a range due to the 95% CI error of 33-50 cp. This finding compares well with the viscosity finding (34 cp) using the vertical velocity matching techniques. Calculations of diffusion coefficient, Reynolds' Number, and Peclet Number are now possible with this more precise value for viscosity:

From Equation 3-4: $D=3.41x10^{-11}$ cm^2/s - comparable to larger bacterium

From Equation 3-6: $Re=2.52x10^{-9}$

From Equation 3-5 (and discussion): $Pe \approx 10$

One final investigation concerning diffusive motions of the amyloplasts was explored. Circumnutation effects are documented in Section 4.4.5 of this thesis. The amplitude of this oscillatory plant root movement is approximately 10^0 and this curvature creates a "noise" over which gravitropic curvature stimulated by small stimulation angles ($\approx 10^0$) cannot be witnessed. A resulting question is whether the "noise" is on the growth side (circumnutational differential growth masking gravitropic differential growth) or on the sensor side (sensor noise leading to circumnutational effects masking gravitropic sensing by the statoliths). The video-sedimentation study accomplished a short analysis of the second possibility. The diffusion results of the last paragraph were compared to results from the same root sections gravistimulated

by 10 degrees to determine if the amyloplast sedimentations would produce significantly different results. Table 3.12 summarizes the results. In summary, the vertical and 10 degree stimulated statoliths showed equivalent motions with no significant (to a P-Value of 0.85) difference in the y-motion of the statoliths. The conclusion is that at 10^0 of gravistimulation, the diffusive movements within the sensor are as dominant as those forced by gravity and the stimulus for circumnutation is consistent with the diffusive motions of the statoliths. Chapter 8 discusses further research areas along this avenue.

Table 3.12 - Vertical versus 10^0 Gravity Stimulated Statolith Movement

	Number of Cells	Number of Amyloplasts	Statolith Y - Motion (μm) Mean	Standard Dev.
Vertical:	6	20	$\mu_v = 0.44$	1.0
10 Deg.:	4	23	$\mu_{10} = 0.39$	0.43
t-Test:	-	-	$\mu_v = \mu_{10}$	P-value: 0.85

3.5.4 Final EOM and Sensor Model Results

The results and discussion in the previous sections appear to indicate a model set that involves an actin-modulated network similar to that introduced in Figure 3.2(#3), the "network." The cytoplasmic viscosity arrived at in the previous section (34 cp) produces a terminal velocity (from Equation 3-23) of 4.8 μm/min. and although velocities to this magnitude have been noted in various instances, the mean velocity within various cell spatial-sectors and sedimentation time-sectors are much lower (≈1-2 μm/min.). This indicates that some actin-amyloplast interaction must be occurring throughout the sedimentation. Additionally, since significantly lower

velocities are noted during side-to-side sedimentation profiles than in distal-to-side profiles, the actin-amyloplast interaction appears greater within the central region of the cell, producing a more "privileged zone" of movement around the cell periphery. We model this actin-plastid interaction scheme by making the following assumptions:

1. The columella cell is assumed to be cylindrical with actin fibers having evenly distributed attachment points along the cell surface.

2. Each actin fiber stretches the length (or width) of the cell with its opposite end attached at point on the opposing surface.

3. All parameters are documented in Tables 1.1, 1.2, and 1.3 of Chapter 1, except for the recently improved value for viscosity (34 cp).

The model set is diagrammed in Figure 3.23. The total surface area for actin attachment points is the sum of the lateral surface area and the surface area of the cylinder ends. Lateral surface area is $\pi*d*h$, where d is the cell diameter and h is the cell height. End surface area is $2*\pi*(d/2)^2$. For the values given in Table 1.1, the total columella cell surface area is approximately 3250 μm^2. Actin fibers attached evenly across this surface area create a grid network with openings ("pores") becoming smaller in the central region of the cell. Near the cell periphery, the pore is assumed to be square in shape, but is truly a trapezoid with the long-side directed toward the cell's lateral surface. The algorithm to approximate the spring acceleration imparted on a plastid during contact with the actin grid is documented in the STATE.M file of Appendix II and begins with the entering a desired volume fraction (total actin volume/total cell volume) for actin.

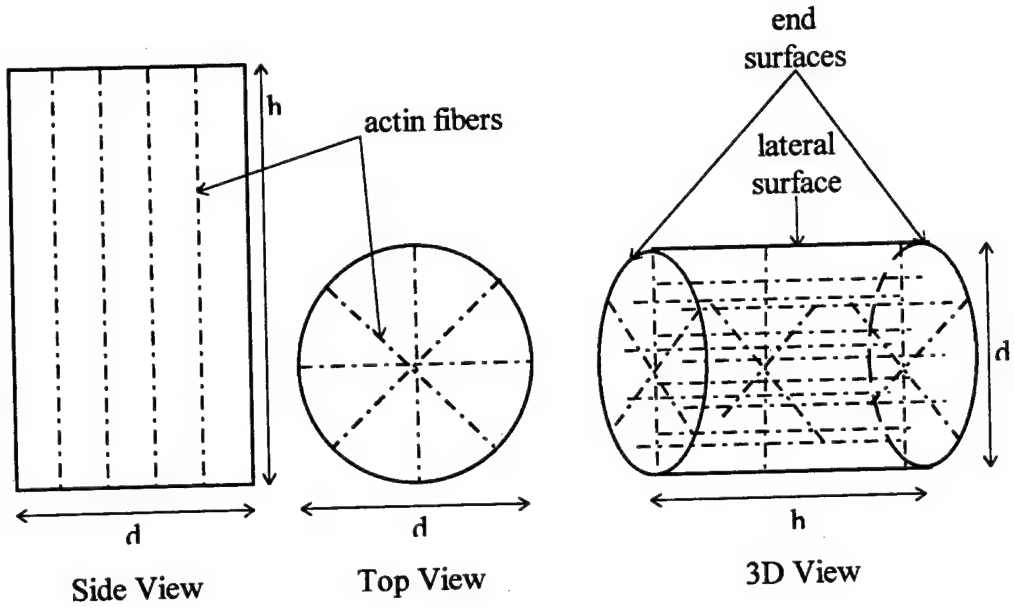

Figure 3.23 - Network Model Set
d represents the cell diameter (cell width in Table 1.1) while h is the cell height.

The algorithm approximating the acceleration imparted on a plastid by contact with the actin grid follows the general steps shown below:

1. The lateral, end, and total surface areas of the cell are calculated.

2. Taking into account that fibers running the height of the cell are of greater length, and therefore, greater volume than fibers running laterally, the number of longer fibers, shorter fibers, and total fibers are calculated to meet the desired volume fraction for actin in the cell.

3. Since each fiber takes 2 attachment points, the total surface area is divided by twice the total fiber number to obtain the area that each evenly distributed fiber attachment point can occupy.

4. Concerned only with the grid characteristics near the cell periphery, the area found in the last step is the pore-size with a square shape.

5. An amyloplast in contact with the center of the grid is diagrammed in Figure 3.24. The Δr is the amount an actin fiber must be deformed laterally to allow passage of the plastid. This Δr must be modified with a $1/\mathrm{Cos}(\theta)$ term since the lateral deformation is only a component of the radial deformation (Δr_{radial}) that the plastid must accomplish.

6. The load (W) required to produce the Δr_{radial} deflection is shown in Equation 3-24. This equation is for deflection of a flexible beam of length, L, and attached at both ends with the load approximately centered and a flexural rigidity of EI (Eshbach & Souders, 1975). Equation 3-25 is for the same configuration except when the load is not centered but a distance, a, from the farthest attachment point and distance, b, from the closest.

$$\Delta r_{radial} = \frac{\Delta r}{\cos\theta} = \frac{WL^3}{192EI} \qquad (3\text{-}24)$$

$$= \frac{2Wa^3b^2}{3EI(3a+b)^2} \qquad (3\text{-}25)$$

7. Finally, the load, W, is multiplied by 4 (4 fibers comprising the grid), 8, or 12 depending on the relationship between the pore-size and the amyloplast radius (how many fibers are in contact at a given instant) and this value is adjusted with a $\mathrm{Sin}(\theta)$ term for the vertical component of the force. This vertical force is then included with the other forces acting on the plastid and the numerical solution to the equation of motion is computed.

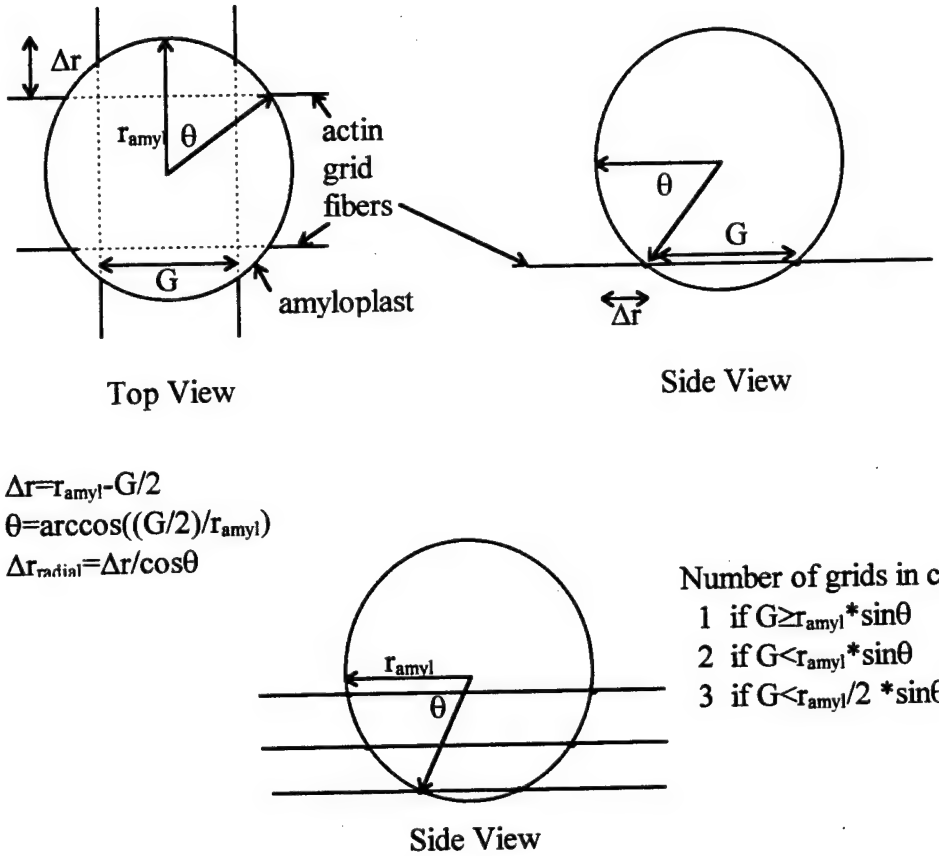

Figure 3.24 - Actin Grid Forces

This algorithm was used to analyze the general effect of such a grid network on a single amyloplast in the vertical (y) direction. The goal was to increase the actin volume fraction until the velocity of the simulated amyloplast was comparable to those found for untreated cells during initial times of distal-to-side sedimentation (≈1.9 μm/min., see Table 3.1) and for top sector y-velocity (≈1.7 μm/min., see Table 3.8). The resulting simulation produces 3726 actin fibers in the cell producing a pore-size of 0.863 μm^2 and a total of volume fraction was 0.03; 3% of the columella cell would need to be actin fibers to duplicate the empirical findings. This figure is quite

interesting since the majority of cells contain 5% or greater of their cell volume in actin (Alberts *et al.*, 1994) and from the material reviewed in Chapter 2 we know that the columella cell is unusually devoid of typical actin concentrations. This model with its low actin concentration and the nature of the grid interaction with the amyloplast could explain both the deficit of total actin historically found within columella cells and the highest concentration being identified as occurring in an "envelope" around the amyloplasts (Sievers *et al.*, 1989). Figure 3.26 shows the y-velocity profile of the simulated amyloplast under this model.

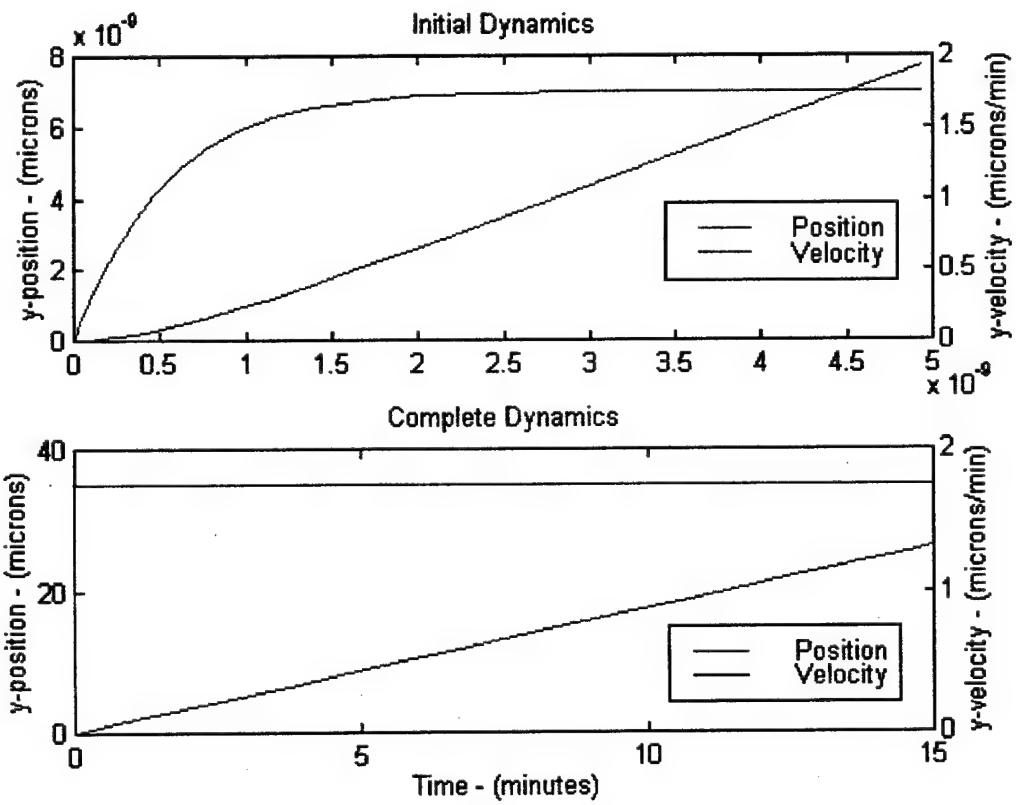

Figure 3.26 - Network Model Dynamics with 3% Actin by Volume

The only proper way to examine the network model is through finite-element models and software designed to explore their resulting dynamics. The finite-element approach allows the inclusion of boundary conditions and actin-applied forces in all three dimensions. Toward this end a graduate-student independent study project was undertaken by Balaji Agoram (Agoram, 1998). Similar to the actin-grid model described in the previous paragraph, his model requires opposing actin attachment points to be on the cell boundary with no interconnections between fibers. Contrasting with the cylindrical cell and evenly distributed actin of the actin-grid model, his model used a rectangular-shaped columella cell with a randomly distributed actin fiber distribution. The number of actin fibers was also altered between 0 and 25,000 within the cell. Figure 3.26 shows an example of three amyloplasts falling within this actin network. Note the lateral deviations caused by interaction with the actin fibers as the plastid falls. Further refinements are necessary in this model to produce quantitative measurements such as actin fiber tensions during sedimentation, grid pore-size gradients, and boundary effects.

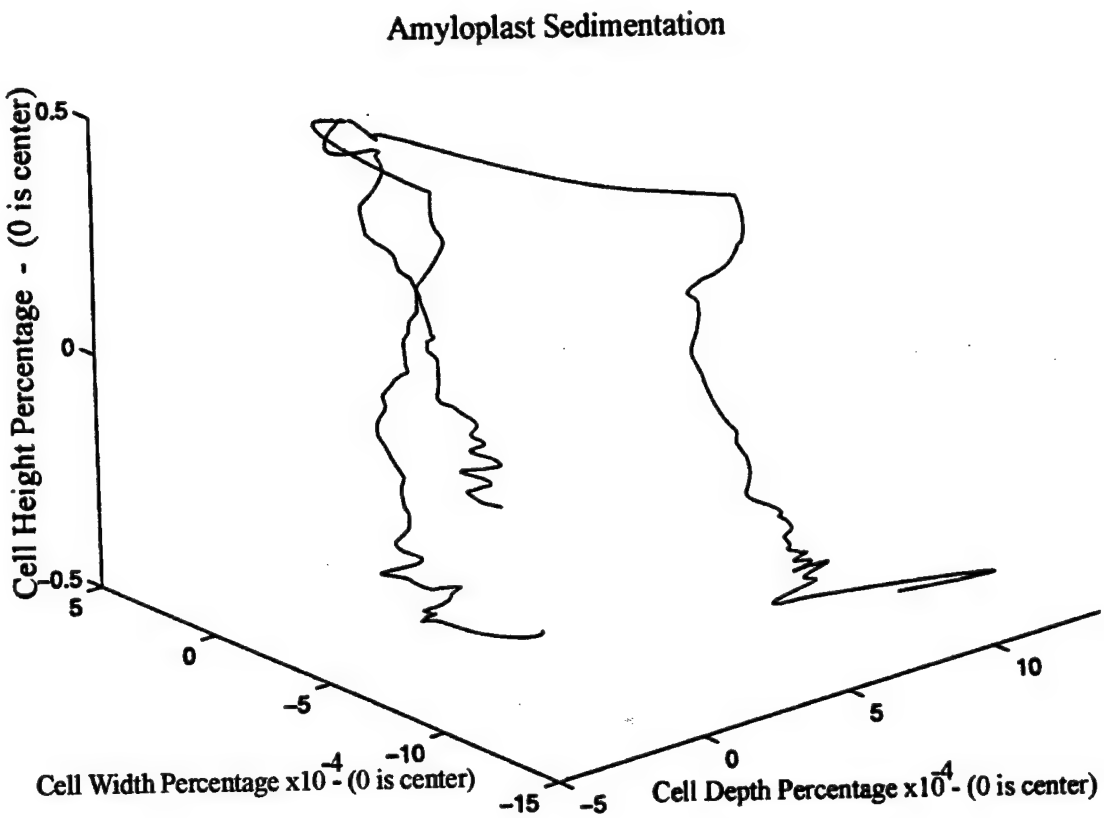

Figure 3.26 - Finite-element Model of Falling Amyloplasts

A linear, s-domain model for either the finite-element model or the simplified, cylindrical actin-grid model is problematic. The empirical study described early has illustrated the complex nature of the amyloplast's sedimentation dynamics. Describing the complex, nonlinear interaction between the amyloplasts and the actin grid in a linear form will lower the model's resolution beyond the level of usefulness. However, if instead of attempting to describe the sedimentation dynamics of the amyloplasts, we describe a putative distribution of tension applied by the sedimenting amyloplasts, a useful s-domain model is attained. See Figure 3.27 for an illustration of the proposed overall effect.

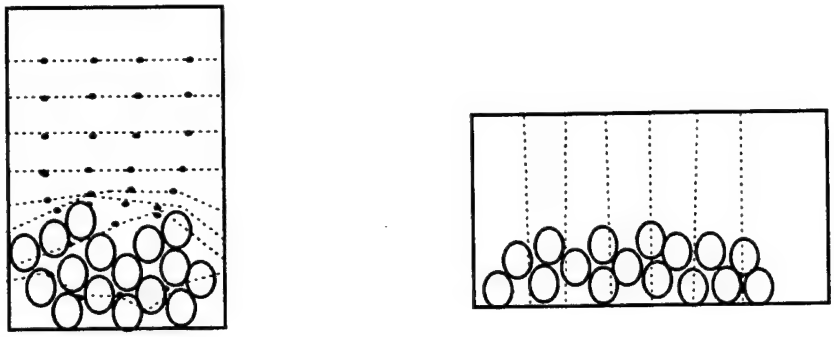

Figure 3.27 - Amyloplast Group Effect on the Actin-Grid Model

Remember that the cylindrical, actin-grid model attempts to explain the higher density, central actin concentration that produces the channeling effect seen in the empirical models and the higher amyloplast velocities seen during distal-side sedimentation where the plastids remain near the cell periphery. One implication of this model is that during vertical orientation, with the plastids at the distal end of the cell, the "pile" of plastids would create a upward deformation of this central, actin concentration. This is because of the smaller pore-sizes within the grid of the central region. This upward deformation has two implications. First, tensions in the actin network would be directed laterally across the cell. Secondly, these tensions would have the effect of dampening the diffusive movements of the plastids in the vertical direction, thereby lowering the background noise on the sensor; "increasing the gain" on the statolith function. As the cell was turned toward the horizontal, the plastid movement toward the lateral side would have the immediate effect of releasing the lateral tension in the actin network. Upon being turned horizontally, the original tension would serve to keep the plastids from cascading basally over themselves, but

instead display a motion that is characterized by vertical motion followed by an even extension across the lateral wall of the cell. It is precisely this motion that is witnessed in distal-to-side sedimentation profiles. If a density gradient also existed in those actin fibers running from the distal to basal ends of the cell (longitudinally), then the original lateral tensions in the network would be substituted by predominately longitudinal tensions when gravistimulated by 90^0. This exchange in tension orientation could then serve as the first step in the transduction mechanism of gravitropism. Figure 3.28 shows the step response (vertical to horizontal rotation of the root) of a simple, 1st-order s-domain model for the above mechanism. Based on the empirical data (see Table 3.1) concerning distal-to-side sedimentation velocities in the beginning, middle, and final thirds of the total sedimentation time, the σ value for this model was selected to be 0.01, providing a nearly complete transfer of tensions from lateral to longitudinal within approximately 5 minutes which corresponds to a significant decrease in sedimentation velocity in the empirical trials. This is only a rough approximation of the dynamics of tension redistribution and further work should proceed to refine this model.

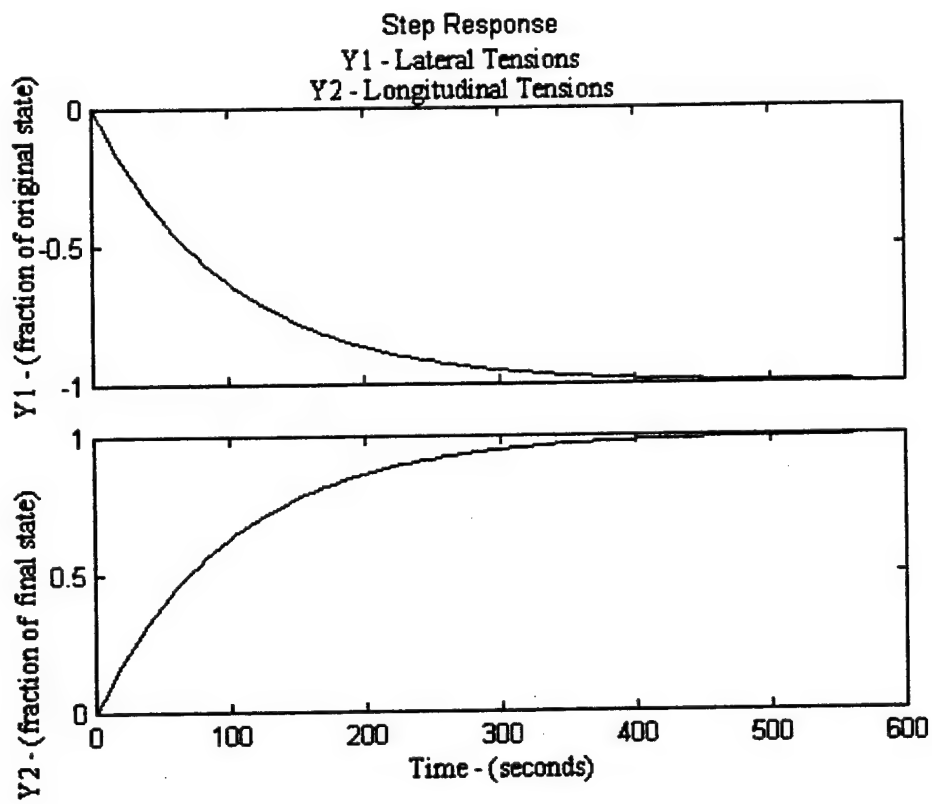

Figure 3.28 - 1st-Order, s-Domain Model for Tension Redistribution

3.6 Discussion

This chapter has shown the development of a model for the plant root gravitropic sensor. Three separate mathematical approaches were used to validate the feasibility of the amyloplast as a gravity sensor. The amyloplast within its environment was found to be a feasible sensor, creating signals on the order of or higher than that of various background noise sources. Further mathematical and computer modeling was accomplished and analyzed to test and explore the various model sets describing the amyloplast within the columella cell. Initially, the classical "tethered" model of amyloplast-cytoskeletal interaction was shown to be invalid with assumed values for actin structural properties. With this invalidation, the goal was to find a more

appropriate model set that modeled the general amyloplast interaction with the columella cell's cytoskeleton.

Extensive exploration of the dynamic properties of the columella cell interior was accomplished by using the cell amyloplasts as 2 μm probes and recording the kinetics of their sedimentation through the columella cell. Three general sedimentation profiles were examined including the distal-to-side profile (naturally seen in the plant by vertical to horizontal root tip stimulation), the side-to-side profile, and the distal-to-basal profile. Intriguing movements were seen in the amyloplasts during the side-to-side and distal-to-basal profiles; each time plastids were forced to sediment through the cell's central region. These movements create a "channeling" effect that causes the plastids to approach each other while still at the top of the cell, vertically drop as a column, and, once reaching the cell bottom, spread back out in an even distribution. This channeling is witnessed, in varying degrees of magnitude, in every side-to-side and distal-to-basal profile of untreated roots, but is absent in a few roots treated with cytochalasin D. Efforts to quantify the channeling appear to indicate that the channeling reaches a maximum near cell center, coincident with maximum y-velocities, and is significantly lessened by the introduction of cytochalasin D. Minimum velocities coincide with the start of sedimentation in these profiles. These findings appear to indicate a central region of the cell with a higher gradient of amyloplast-cytoskeletal interaction. The amyloplasts appear to congregate toward a localized channel or create the channel by group action on a weaker area of the cytoskeletal obstruction. The higher velocities witnessed in distal-to-side profiles coupled with higher

correlation found between the velocities of these plastids is further evidence that this obstructive region is found more central to the columella cell; leaving the distal end of the cell a "privileged" zone.

The AMYLFALL.M routine is an extensive MATLAB script file that can be used to analyze any future probing of the cellular interiors. The raw x,y-coordinate data over time is transformed into velocity profiles, graphical formulations of channeling and group behavior, statistical analysis for 3 time partitions, and may be modified for any number of applications. The statistical correlations produced by the program appear to indicate that the amyloplasts act as a group and not as separate plastids. Further research is necessary in this area since this correlation could indicate physical connection through cytoskeletal attachments or that the amyloplasts are under the mutual influence of a deformed network of cytoskeleton channeling their movements. The analysis of the MATLAB routine also led to some interesting findings in the area of diffusion and viscosity.

Amyloplasts were identified which attain a global maximum velocity for the entire sedimentation profile coinciding with that velocity being purely in the vertical (y) direction (i.e. absolute velocity = y-velocity). This velocity was then assumed to be that plastid's terminal velocity, unhampered by any cytoskeletal or collision forces, accelerated only by of gravity. This allowed an estimation of cytoplasmic viscosity which was compared to a few video runs that examined only diffusive movements. The diffusive velocities and motions produced a viscosity on the order of 30-50 cp

while the velocity matching technique produced a viscosity of 34 cp. A final model was designed based upon these findings.

The final model is in the form of a general model set that attempts to explain the channeling a group behaviors of the amyloplasts by designing a cylindrical model of the cell with actin fibers running radially through the longitudinal axis. This model produces a higher concentration of actin fibers near the cell center. Modeling of this "actin-grid" model shows that actin fibers should only make up approximately 3% of the cell volume for the model's velocity to match the empirical findings. This low percentage is consistent with historical actin analysis within columella cells. Finally, it is proposed that the amyloplasts, reacting as a whole congregate, cause a shift in tension within this actin-grid from predominately lateral- to longitudinal-oriented as the statoliths move from the distal side to the lateral side of the cell following gravistimulation. This shift in tension polarity becomes the initial mechanism within the transduction process. Although cytoskeletal tension shifts are a common theme in transduction literature, this thesis appears unique in the use of the specific inductive reasoning based on experimental results and the specific form and polarity of the cytoskeletal tension gradients.

3.7 Conclusions

The chosen sensor model set is a random network (Figure 3.2 - #3), but with a higher gradient of network approaching the center. The model can be visualized as a slightly denser region of visco-elasticity, a "gel," within the central region of the columella cell. One can speculate that this design increases the signal-to-noise ratio of

the sensor by "compressing" the statoliths onto the distal end of the cell, thereby lessening their tendency to diffuse and increasing their flocculation effect. During gravitropic movement, even stimulations as large as 90^0, this central "gel" still allows free movement of the statoliths from their distal positions toward the side, because the cell periphery appears as a "privileged" zone of motion.

More studies of sedimentation using the amyloplast as a 2 μm probe can refine this model and provide further insight as to group movement correlation. Chapter 8 covers many ideas for future research along these lines. Additionally, in order to confirm the model, finite-element modeling techniques might provide more precise quantitative estimates of various mechanical parameters that may be compared with empirical data.

CHAPTER 4

CURVATURE BY DIFFERENTIAL ELONGATION

4.1 Introduction and Objective

The final mechanism in the gravitropic response path is the curvature of the root tip. The universally accepted cause for this curvature is a growth differential between those cells on the top versus those cells on the bottom of the gravistimulated root. This curvature brings the root back to either the vertical or a point near to vertical which corresponds to an altered gravitropic setpoint. The curvature of the root tip, therefore, serves to return the root tip to growth along its gravitropic setpoint, thereby completing the gravitropic response. Refer to section 2.4.2 of Chapter 2, for a complete review of the current literature concerning the growth response. To thoroughly model the growth and curvature of the root tip, both elastic (temporary and reversible) curvature and plastic (irreversible) curvature should be examined as contributors to the overall curvature. In order to provide the proper variable to feedback into the remainder of the gravitropic model, the growth/curvature model output should be the angle of the root cap from vertical. The choice of inputs into this growth/curvature model is extensive, but to simplify the model development, this chapter will consider only gravity as the elastic model input and changes in growth factors (growth rates, distribution, etc.) as the plastic model input. Chapter 6 will cover the transduction mechanisms and propose appropriate links between the changes in growth factors and changes in growth effectors. The specific objective of this chapter is to develop a mathematical model of the plant root's differential elongation

and curvature by exploring the contribution to curvature by elastic and plastic mechanisms.

4.2 Theory Development

A mechanical system analogous to the bending portion of the root gravitropic mechanism is the curvature of a bimetallic metal. This structure provides the framework, or model set, for accomplishing this chapter's objective. Temperature fluctuations produce a change in length (ΔL) in one metal, but less ΔL in the other metal. The differential change in length in one metal relative to the other produces an internal shear stress, creating an internal moment, resulting in a curvature in the structure. Figure 4.1 shows this system applied to the elongation zone of the plant root.

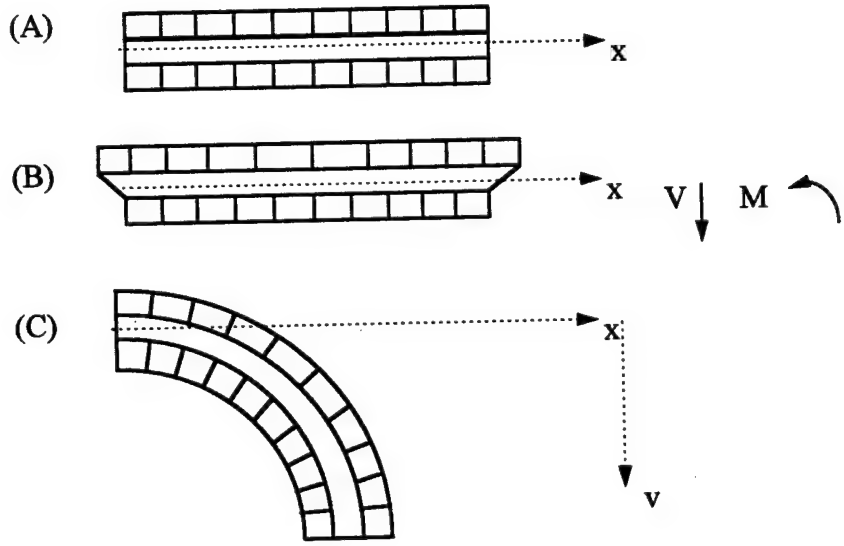

Figure 4.1 - Differential Elongation Produces Curvature of the Plant Root
A section of the root's elongation zone is shown in (A) with the morphology simplified to an exterior cortical region surrounding an interior, non-elongating vascular region. This section undergoes a differential elongation in (B) with the upper side cells growing faster. This creates an internal shear stress between the layers, producing an interior moment that results in an elastic curvature in the section (C).

The following model of the resultant curvature in the root is developed by exploring the contribution to curvature by both elastic and plastic mechanisms. Elastic curvature is simply the reversible curvature created in the tissues by the application of stress placed on the cantilevered root. This contribution is explored with both mathematical derivation of the forces acting on the root while gravistimulated and with published experimental observations as to the bending caused directly by gravity. Plastic curvature is the irreversible curvature caused by actual changes in the length of the cells making up the length of the root's elongation zone. This curvature is attained to minimize the stress in the interior of the root and seeks to create an equivalent curvature on both the upper and lower side of the root. Figure 4.2 flowcharts the logic used to accomplish this modeling.

The elastic investigation (the left-side pathway in Figure 4.2) initially examines the stress relationships on the plant material placed horizontal to the gravity vector and then analyzes experimental data of maize root bending immediately after being placed horizontal. If significant elastic curvature is created by only the cantilevered weight of the root itself, then further experimentation would be required to develop a value for flexural rigidity (EI) for the maize root elongation zone. As the data shows in the results section of this chapter, this is not the case, as the elastic curvature contribution to the overall curvature is found to be negligible.

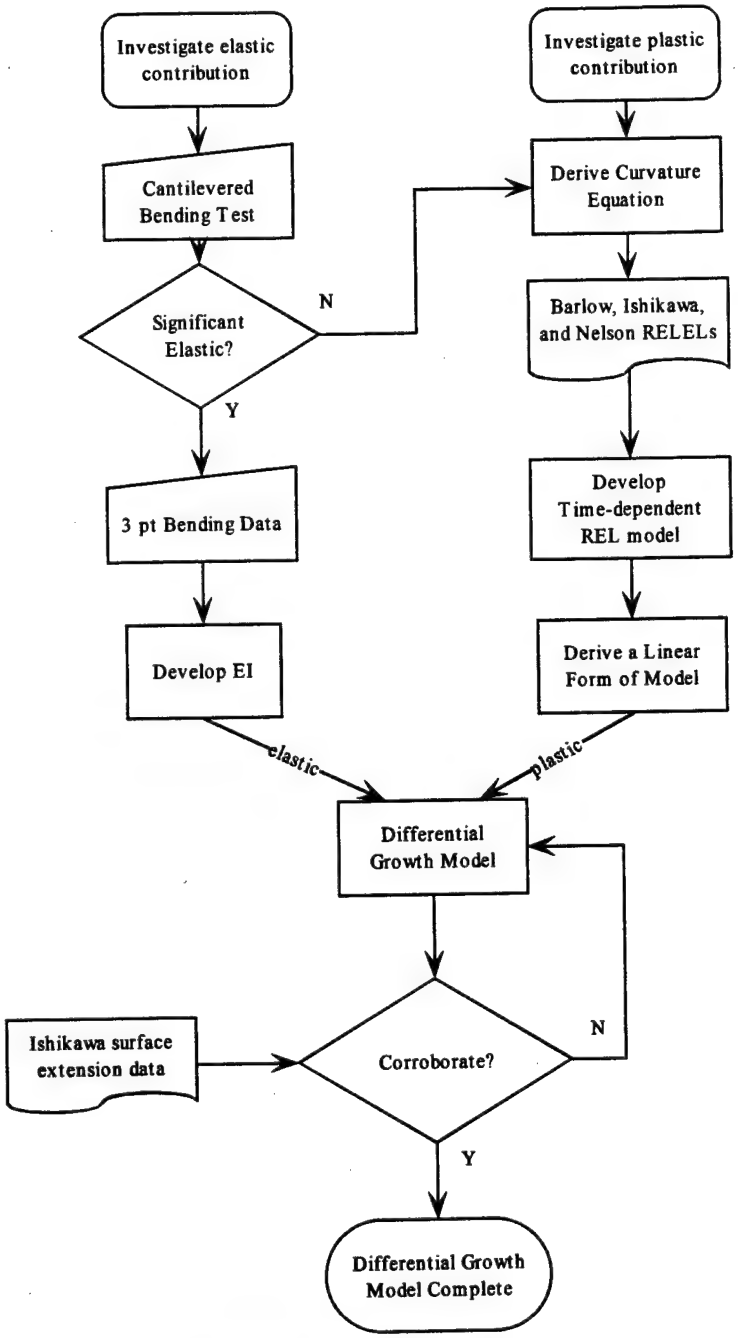

Figure 4.2 - Flowchart for Chapter Four Objective

The plastic investigation (the right-side pathway of Figure 4.2) applies the bimetallic bending model set to the differential elongation of individual cells along the elongation zone. Historical data is then used to develop a picture of the actual distribution of elongation rates on the top and bottom sides of the root. Since the use

of Relative Elemental Elongation (RELEL) rates (described in section 2.4.2) creates a complex, nonlinear, and time-varying model of elongation rates in various cells of the elongation zone, this model is then simplified to provide a transfer function that can be used to operate on the overall gravitropic model developed in Chapter 5.

4.2.1 Development of Elastic Curvature

Elastic curves produce the relationship,

$$\frac{M}{EI} \cong \frac{d^2v}{dx^2} \tag{4-1}$$

where EI is flexural rigidity, M is the internal moment, v is the vertical deflection, and x is the horizontal axis along the root after placing it horizontally. If EI is assumed constant along the length of the elongation zone, the following relationships exist:

$$\begin{aligned} V(x) &= EI\frac{d^3v}{dx^3} \\ M(x) &= EI\frac{d^2v}{dx^2} \\ \theta(x) &= \frac{dv}{dx} \end{aligned} \tag{4-2}$$

Therefore, if the flexural rigidity is known or estimated, V (shear stress, as calculated through the forces acting on the cantilevered root) can lead to a calculation for M (moment) and finally, the curvature angle, θ. Appendix III derives the elastic curvature for the cantilevered root. The resulting equation that describes the curvature of a cantilevered root under the influence of its distributed weight (dg; density*gravity) as a function of distance from the cantilever (x) is shown in Equation 4-3.

$$\theta(x) = \frac{dg}{2EI}(-L^2x + Lx^2 - \frac{x^3}{3}) \qquad (4-3)$$

4.2.2 Development of Plastic Curvature

Elastic bending does not accurately model the curvature dynamics within the elongation zone since the plant undergoes a plastic phase of growth during this tropic reaction. This occurs through an acidification process within the cell wall that loosens the wall to relax the buildup of stresses caused by increased turgor pressure within the cell (Hager *et al.*, 1991; Alberts *et al.*, 1994). The stress is relaxed with an inelastic or plastic stretching of the cell wall. If the elongation growth of cells on opposing sides of the root does not equate, a curvature in the root is created. This curvature is modeled through a radius of curvature matching between the upper cells and the lower cells of the bending section, analogous to the chosen model set; bimetallic expansion. Appendix V derives the angle of curvature produced when two arc sections maintain a radius of curvature differing only by the separation between the two sections. This derivation assumes that the separation between the two sections remains constant, which is true for the case of the root since the root diameter remains relatively constant during this response (Ishikawa & Evans, 1994; Ishikawa & Evans, 1995). Equation 4-4 below summarizes the results.

$$\theta = \frac{\Delta L}{d}, \text{where d is the separation between the sections} \qquad (4\text{-}4)$$

The value for ΔL in Equation 4-4 is the difference in elongation between the top and bottom of the growing root. If growth is calculated as simply additive across all the cells on the top versus all those on the bottom, then this would produce a smooth curve, with equal radius of curvature across the entire length of root as shown in Figure 4.3 (A), but if the resolution on growth is increased, comparing specific regions of the top versus those on the bottom, then varying curvature is localized at those root zones which show comparatively high regions of differential growth as shown in Figure 4.3 (B). These figures indicate that the finer the resolution, the more precise the growth response model becomes. Taking this resolution to its logical limit, the elongation of each and every cell on the top, bottom, and all parts of the circumference in between should be taken into account in order to accurately model the curvature along the graviresponding root. Numerous experiments by many researchers have measured the differential growth response, but only a few have recorded the cellular elongation close to this level of resolution, allowing development of a type of "finite element" model.

(A)

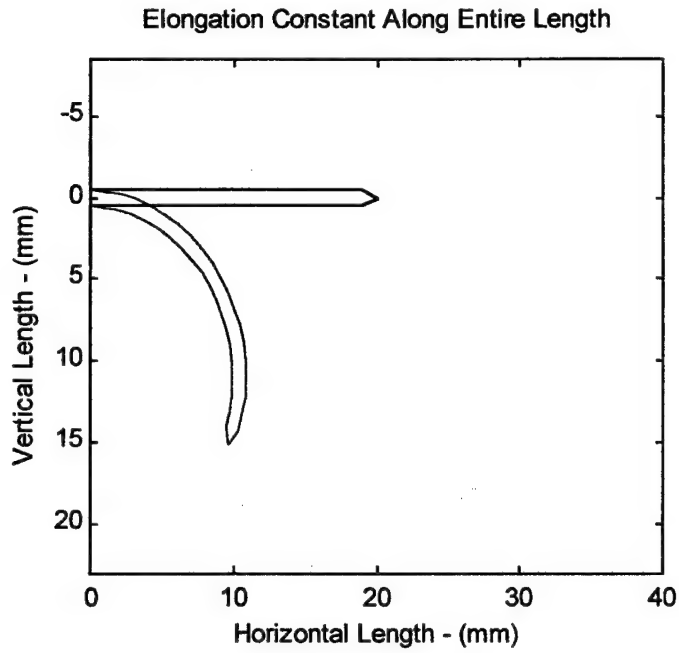

(B)

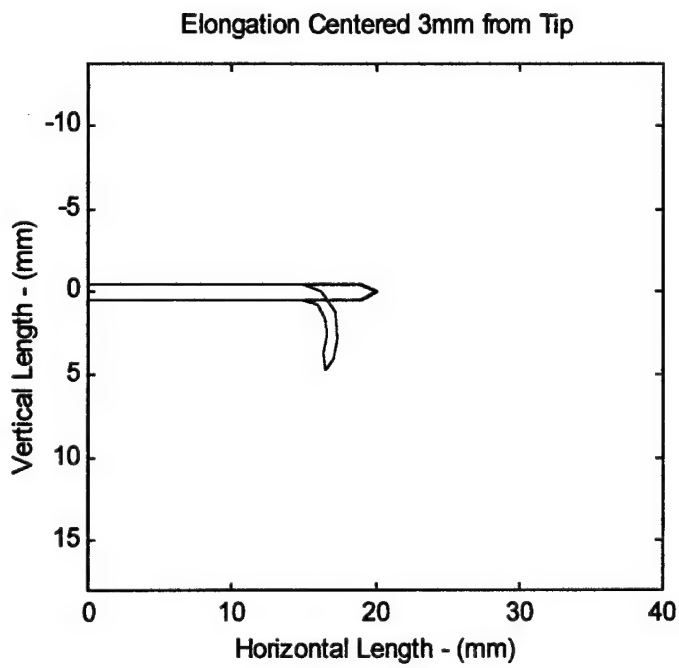

Figure 4.3 - Changes in Curvature with Model Resolution
Figure (A) shows a root section where the difference in growth between the top and bottom (ΔL=2 mm) is assumed to occur as a total across the entire length of the root, while Figure (B) shows the same ΔL isolated in a specific region.

The growth of any section of the root or of any individual cell can be described as a percent elongation over time. This "RELEL" or Relative Elemental Elongation is defined in Equation 4-5 (Erickson & Sax, 1956; Zieschang & Sievers, 1994). Lengths are of any elemental segment chosen, but for highest resolution should be the distance between the distal and basal cell walls of a given cell. Note that the RELEL is normalized to the average length achieved during the time interval and not the starting length.

$$\text{RELEL} = \frac{L_2 - L_1}{t_2 - t_1} \Big/ \frac{L_1 + L_2}{2} \quad ; \text{ where } L_1, \text{ is length at } t_1, \text{ time 1} \qquad (4\text{-}5)$$

$$L_2, \text{ is length at } t_2, \text{ time 2}$$

Table 4.1 summarizes some of the data concerning RELELs in the literature. One problem that has been witnessed throughout the literature is the use of various methods to record growth. The RELEL method described above provides high resolution, but requires meticulous work where noisy data and temperature variations can significantly alter the findings for various segments of the root. Other groups use a relative growth rate developed by Green (Green, 1976) which relates extensions of small surface regions over short time periods to exponential bacterial growth models and, therefore, defines the RELEL with natural logarithms. At small values for RELEL (e.g. 0.4 %/min.), the two techniques produce similar results. Temperature effect on RELELs is not thoroughly documented and, therefore, two research groups accomplishing RELEL distribution experiments at two different temperatures show quite different results for otherwise identical root conditions. However, while developing a model of growth based on historical RELEL data requires integrating the entire collection of data into one coherent model, overall elongation (mm/hr) data

exist that is used to confirm the coherent construct. Such data is summarized in Table 4.2.

Placing RELEL data into simple look-up tables that can be used to compute growth rates for specific regions would be one possible application into the model, but this would create lengthy program execution, heavy user intervention to substitute new data, and discontinuities between the discrete RELEL information published in the literature. Advantageous to modeling, the RELEL is found to display a characteristic Gaussian-shaped curve along the length of the root (Barlow *et al.*, 1989). RELEL reaches a maximum at some distance from the root tip (in the elongation zone) which is defined as the mean position (μ) for the Gaussian curve and the RELEL declines to a value of 0.607 of maximum RELEL at a distance of 1σ both distal and basal to the maximum position. Examination of numerous RELEL data confirms that, although far from perfect bell-curves, the data can accurately be approximated by the Gaussian function show below.

$$\text{RELEL} = \text{RELEL}_{max} * e^{\frac{-(s-\mu)^2}{2\sigma^2}} \qquad (4-6)$$

where, μ is the location from the root tip of RELEL_{max}, σ is the distance of 1 standard deviation from μ (the point where RELEL drops to $0.607*\text{RELEL}_{max}$), and s is the independent variable of distance along the root from the root tip. This allows the creation of a model that is both continuous along the root length and only has three parameters to: (1) RELEL_{max}, (2) μ, and (3) σ. Only the pre-gravistimulation values of these parameters along with 3 mathematical descriptions of how they are perturbed during a graviresponse are required to enter into the model's computer code.

Table 4.1 - RELEL Information

Category	Findings	Reference
Maize Vertical Growth	RELEL ranges from 0.6%/hr at quiescent center to a maximum of 40%/hr at 4mm and finally zero at 10 mm Also: 0.40%/min at 4mm, σ=1.5mm	(Barlow & Rathfelder, 1985)
"	max RELEL of 43%/hr at 2.5mm with a σ=1mm.	(Nelson & Evans, 1986)**
"	max RELEL=17%/hr at 4mm, σ=1.5mm	(Versel & Pilet, 1986)
Maize Gravistimulated Growth	At 46 min; Upper side: max=0.67%/min with no change in position, σ=1mm Bottom side: max=0.23%/min at 5.3mm, σ=2mm	(Barlow & Rathfelder, 1985)
"	Over 2 hrs; Upper-side: max RELEL=32%/hr at distance of 4.5mm and σ=2mm Bottom-side: max RELEL=20%/hr at 3.5 mm and σ=1.5mm	(Nelson & Evans, 1986)**
"	averaged over 1-3 hours: Upper-side: max RELEL=22%/hr at 3mm, σ=1mm Bottom-side: max RELEL=6%/hr at 4.5 mm, σ=1.5 mm	(Versel & Pilet, 1986)
Vertical Circumnutation	+0.05%/min decrease by 0.5mm to a -0.1%/min increase by 1mm with no sigma changes	(Barlow & Rathfelder, 1985)

** found to compute RELEL in a non-standard manner $((\ln L_2-\ln L_1)/(t_2-t_1))$

Table 4.2 - Elongation Rate Information

Category	Findings	Reference
Vertical Maize Elongation	0.18 mm/hr	(Pilet & Ney, 1981)
"	0.5 mm/hr	(Ishikawa *et al.*, 1991)
"	1.2 mm/hr	(Barlow & Rathfelder, 1985)
Horizontal Maize Elongation	see Figure 4.4(A)	(Pilet & Ney, 1981) (Pilet, 1989)
"	see Figure 4.4(B)	(Ishikawa *et al.*, 1991)
Vertical Circumnutation	approx. 1 hour period with mean growth rate=0.18mm/hr with ±0.0036mm/hr oscillations	(Pilet & Ney, 1981)

(A)

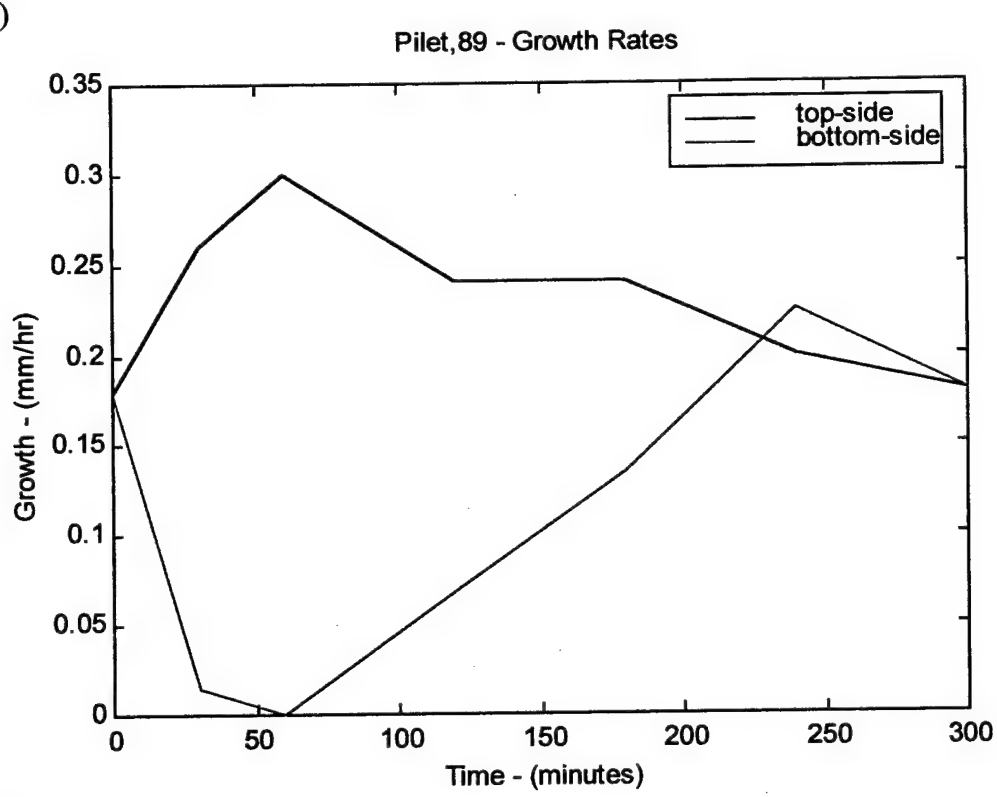

(B)

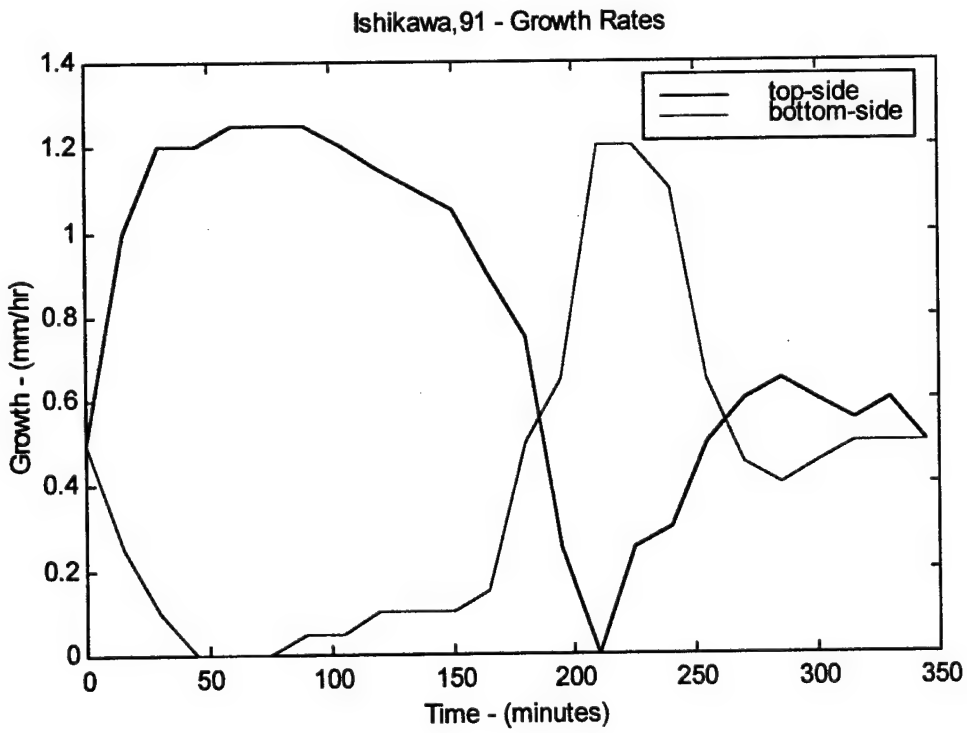

Figure 4.4 - Overall Elongation Rates on the Top and Bottom of the Maize Root
Linear interpolation between actual data points every 30 minutes for (A)(Pilet, 1989) and every 15 minutes for (B)(Ishikawa *et al.*, 1991).

4.3 Experimental and Mathematical Procedures

Modeling the differential growth of the plant root elongation required both experimental and computational procedures.

4.3.1 Experimental Methods

A simple laboratory procedure was used to record the elastic deflections of the root when placed perpendicular to the gravity vector. Seeds of maize (*Zea mays* L. cv. Yellow Dent) were germinated using the same procedure outlined in the first paragraph of section 3.3 of this thesis. Since gravitropic curvature occurs within the elongation zone of the maize root (2-6 mm from the tip), seedlings of length 20-30 mm were selected so that the cantilever location could be the seed itself, just basal to the elongation zone, therefore, testing the elastic properties of the root's elongation zone and not its maturation zone. The seedlings were placed on a microscope slide using modeling clay above a graduated reticle with a precision of 0.5 mm. The horizontal microscope diagrammed in Figure 3.XX of Chapter 3 was used to turn the specimen horizontal to the gravity vector and the reticule was used to measure the immediate vertical (elastic) displacement of the root-tip within 3 seconds.

4.3.2 Computational Techniques

The second procedure accomplished toward the objective of this chapter is the use of MATLAB computational software to compute, analyze, and visualize the actual elongation rates and curvature angles produced by various historical RELEL data when integrated along the length of the typical maize root. The fully documented script files for use in MATLAB are found in Appendix VI. One script file

(GROWTH.M) provides the main framework for the calculations while the second and third (RELEL.M and RELEL_VERT.M) are the functions that contain the RELEL data defined with circumferential and root length dependence. The script files, taken as a whole, are referred to as the Differential Growth and Curvature (DG/C) routine. The general scheme of calculation begins by breaking up the initial root length into individual length increments (elements). The length of the elements on the upper- and lower-sides along with their growth rates at that time frame are stored in the first column of a matrix. Additional columns of the matrix are filled with the same data at each progressive time frame. The element's growth rate at each time frame is found by integrating the RELEL function for that time and the element's position along the root length. Therefore, each incremental length element is increased (or decreased) into the next time frame by propagating with its growth rate. This data matrix is then converted to x-y coordinates, where y is parallel with the gravity vector and x is perpendicular to gravity (refer back to Figure 4.3). The origin of the x-y system lies at the base and center of the root. This conversion to x-y coordinates involves Equation 4-4 and allows the visualization of how the root should appear as it undergoes the differential growth.

The RELEL function is programmed into the functions, RELEL.M and RELEL_VERT. Equation 4-6 is used to describe the RELEL as a function of position along the root length. Therefore, the user must program only $RELEL_{max}$, μ, and σ and how these three parameters change over the circumference of the root. For the purposes of this study, this circumferencial change is assumed to occur smoothly (as a sine function) between the upper and lower sides with the front and back facing sides

of the root (positions 0^0 and 180^0) maintaining pre-gravistimulated growth conditions. The RELEL_VERT.M function contains the vertical, steady-state RELEL parameters and any circumnutational perturbations that the user wishes to program. The RELEL.M function contains any gravitropic perturbations from steady-state conditions that the user wishes to program. As an example, a simple, non-circumnutating root that doubles all its parameters on the upper-side and all bottom-side parameters fall to zero following gravistimulation, would have the following program assignments. RELEL_VERT.M would include $RELEL_{max}$, u, and σ both assigned constant, time-invariant values that did not change circumferentially around the root while RELEL.M would program the perturbations as $+RELEL_{max}*\sin(c)$, $+u*\sin(c)$, and $+\sigma*\sin(c)$, where C is circumferential position (90^0 on top and 270^0 on bottom). Any time-variance would also require factoring into the functions.

Nine plots are created during execution of this program. The first four plots include a 3-dimensional surface plot of the chosen RELEL function over root length and circumferential position. This surface plot is created for the vertical, steady-state RELEL conditions and also 1/4, 1/2, and 3/4 of the way through the gravistimulation time period. Plots five and six are surface plots of the vertical RELEL parameters with the circumnutational effect applied in plot six. If plot five and plot one are not identical, the vertical RELEL conditions are not consistent between RELEL.M and RELEL_VERT.M. The seventh plot is the visualization of the root undergoing the growth and curvature. Ongoing time points are plotted as different colors (repeating order of black, blue, green, red, cyan, magenta, and yellow). The eighth plot shows the overall upper- and lower-side elongation rates and root tip angle from vertical as a

function of time. The final plot shows the root tip angle from vertical as a function of time. A datafile is produced that contains length, growth rates, curvature angle, curvature rates, and location of maximum curvature for each time point of the execution.

The input parameters for the DG/C routine that the user must specify include the total time period to run the root growth simulation, time until gravistimulation occurs, incremental time period, initial root length, length increments, root diameter, and increment size around the root's circumference. The final computational procedure used in this chapter includes the development of a transfer function that imitates the complex, RELEL-based growth rates developed in the previous procedure.

One final computational technique was applied for this modeling effort. This technique involved the use of the system identification features of MATLAB including the Controls Toolbox and the Signal Processing Toolbox. The following time responses were analyzed to compute s-domain response functions for each: root tip angle, angular rate, upper-side length, lower-side length, upper-side growth rate, and lower-side growth rate. This produced six response functions. Chapter 6 will discuss the form of the input to convert these response functions (output for a given input) to transfer functions (output to input ratios), but for now, the input is assumed to be a generic "RELEL stimulus factor." The parametric modeling technique used to convert the time responses of each variable into a z-domain filter is Prony's method for time-domain filter design. This technique produces a numerator and denominator in the z-domain. Processing this information with the Controls Toolbox included creating a

transfer function model and converting to the s-domain by providing the sampling time (the DG/C routines time increment variable). To verify the accuracy of the s-domain models, the impulse responses of the results are used to compare against the empirical results from the DG/C routine.

4.4 Results

4.4.1 Elastic Curvature: Experimental Results

Table 4.3 summarizes the results of the root elastic bending experiments. As expected, this experiment shows that insignificant curvature occurs due to simple, elastic deflection induced by a distributed load on a cantilevered root. Roots of longer length, being of greater weight, bend significantly just distal to the cantilever point (in the maturation zone), but this bending is uncharacteristic of the gravitropic bend occurring much nearer the tip. If the longer root is secured (cantilevered) just basal to the elongation zone, no significant deflection is witnessed prior to the start of gravitropic curvature. Therefore, the "3-point bending data" step and further steps along the "elastic" path of the flowchart in Figure 4.2 were omitted and research proceeded directly to development of the right or "plastic" path of the flowchart.

Table 4.3 - Deflection and Curvature on Cantilevered Roots

N	Deflection Mean (mm)	Deflection Std.Dev.(mm)	Curvature Mean (deg. from vertical)	t-Test P-Value for Deflection = 0.1mm
31	0.18	0.275	89.6	0.064

The computerized simulation produces results dependent upon the specific RELEL function programmed into the simulation. These results are presented in four groups: (1) vertical growth, (2) time-invariant, gravistimulated growth, (3) time-variant, gravistimulated growth, and (4) the inclusion of circumnutation effects.

4.4.2 Vertical Growth

The first example of results obtained from the Differential Growth and Curvature (DG/C) routine are shown in Figure 4.5. The data used to construct a RELEL comes from Barlow and Rathfelder's 1985 work on maize (Barlow & Rathfelder, 1985). The simulation runs for two hours and shows the incremental growth at each of 30 minute intervals. Initial root length of 20 mm. Note that the RELEL function is constant, time-invariant around the circumference of the root. This invariance over circumference leads to equal growth along all sides of the root and, therefore, symmetric downward growth.

(A)

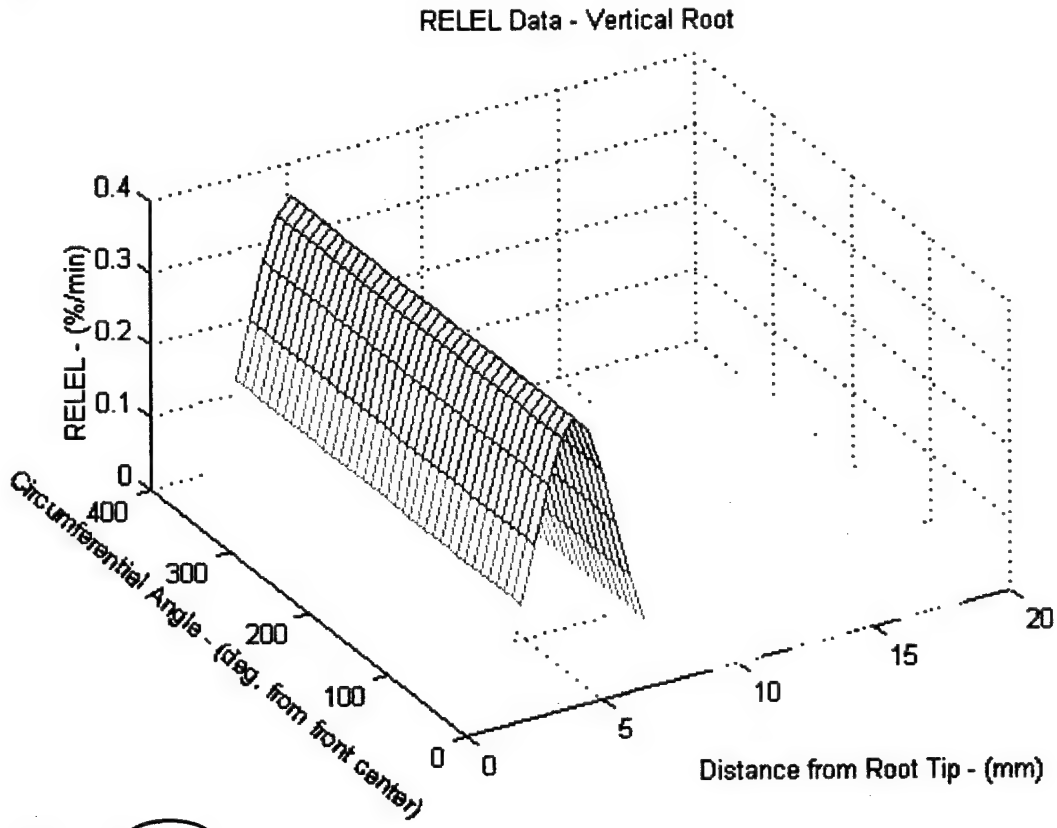

(B)

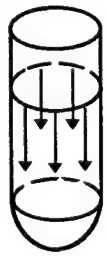

- growth vector (all equal, constant magnitude/direction)

Figure 4.5 - Vertical Growth RELEL Model
(A) shows the surface plot of the RELEL function variability along both the root length and the circumference position while (B) shows a simplified view of the variability of the RELEL as a vector around the circumference of the root.

Figure 4.6 shows the effect of this RELEL integrated over the two hour period over the entire length of the root.

(A)

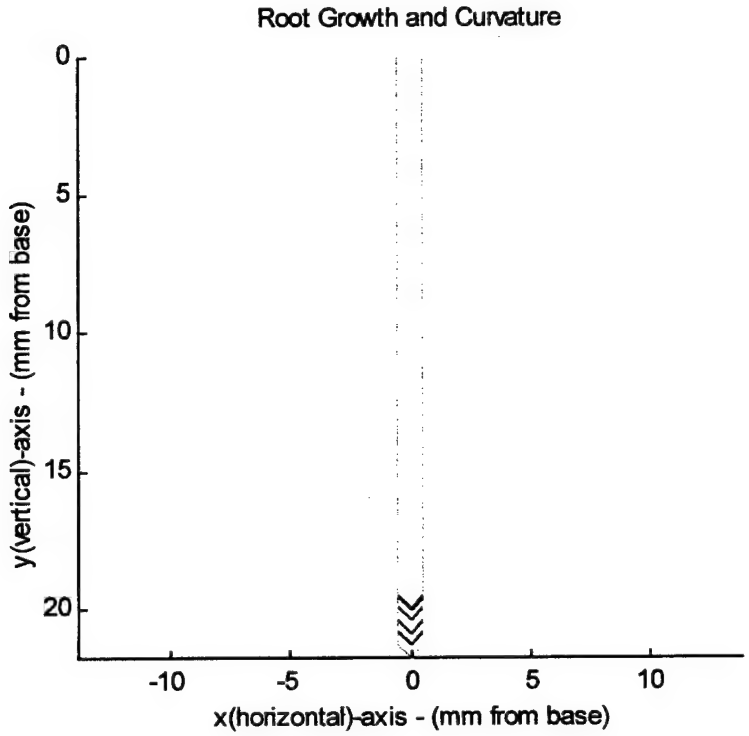

(B)

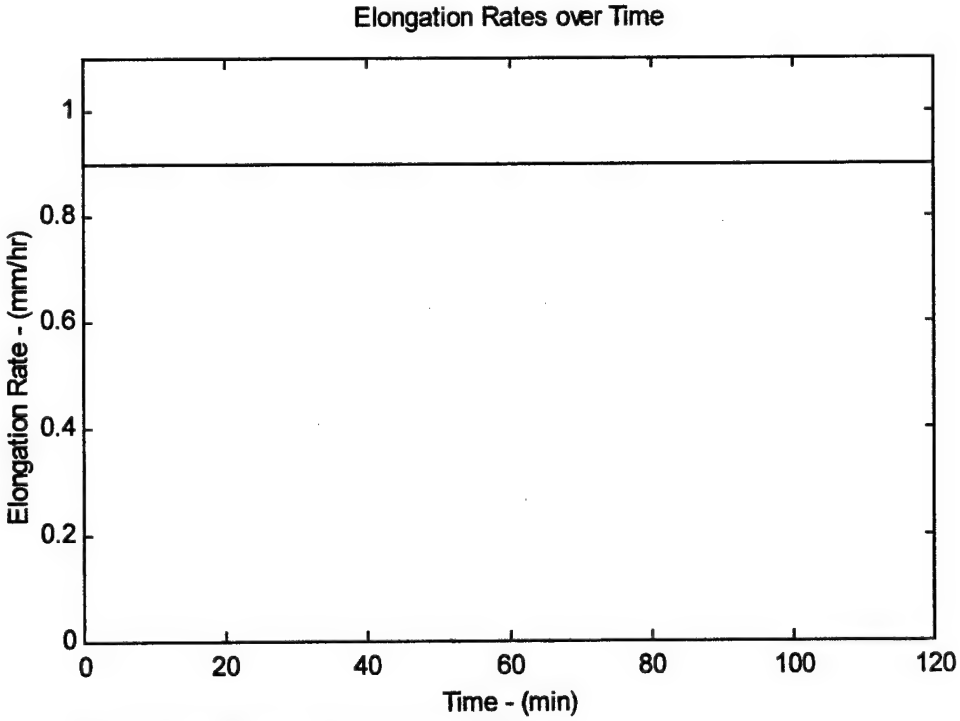

Figure 4.6 - Vertical Root Growth Simulation
(A) shows the visualization of root growth/curvature for the time-invariant RELEL data and (B) shows the elongation rates achieved by both the left and right sides of the root.

4.4.3 Time-invariant, Gravistimulated Growth

As presented earlier in Tables 4.1 and 4.2, historical research has recorded various values for RELEL data. In order to employ and examine the effects of each of these data, this subsection presents the results in three categories: (1) a model based upon the average between Barlow's 1985 data and Versel's 1986 data, both with similar materials and methods, (2) a sensitivity analysis of RELEL parameters, and (3) a model based upon the weighted averages of all research data presented in Table 4.1.

4.4.3.1 Model Based on Two Averaged Data Sets

The data from Barlow (Barlow & Rathfelder, 1985) and Versel (Versel & Pilet, 1986) as shown in Table 4.1 were averaged, smoothed, and programmed into the RELEL function. Table 4.4 shows the averaging and smoothing of all three RELEL parameters for both data sets before and after gravistimulation. Smoothing is an average between the upper and lower side changes so that the change in the RELEL data occurs evenly between the upper and lower sides, allowing for mathematical modeling of RELEL as a function of circumferential position with continuous first derivatives. The first row of each RELEL parameter (e.g. $RELEL_{max}$) contains the steady-state, vertical growth values from each researcher. The following two rows show the perturbation from vertical values detected by each researcher for the upper and lower sides. The percent change from the vertical is calculated for each perturbation, these percent changes are averaged in the fourth column, and the overall perturbation is then found from the averaged vertical parameter.

Table 4.4 - Barlow and Versel RELEL Data Processed for Simulation

Parameter	Barlow	Versel	Averaged	Smoothed
$RELEL_{max}$ vertical	0.4 %/min	0.28 %/min	0.34 %/min	n/a
upper-side	+0.27 / +67%	+0.09 / +32%	+50% / +0.17	+0.2 %/min
lower-side	-0.17 / -43%	-0.18 / -64%	-53% / -0.18	-0.2 %/min
μ vertical	4 mm	4 mm	4 mm	n/a
upper-side	0 / 0%	-1 / -25%	-12.5% / -0.5	-0.7 mm
lower-side	+1.3 / +33%	+0.5 / +13%	+23% / 0.9	+0.7 mm
σ vertical	1.5 mm	1.5 mm	1.5 mm	n/a
upper-side	-0.5 / -33%	-0.5 / -33%	-33% / -0.5	-0.4 mm
lower-side	+0.5 / +33%	0 / 0%	+17% / +0.3	+0.4 mm

The averaged vertical parameters from Table 4.4 are programmed as the initial growth conditions along the root prior to gravistimulation while the smoothed values are used to model the perturbations experienced by the upper and lower sides following gravistimulation. This model produces the RELEL surface plots shown in Figures 4.7 and 4.8. Note that the higher RELEL, centered at 90^0 from the front center (the upper side), is slightly closer to the root tip, while the lowest RELEL, centered at 270^0 (the lower side), is slightly farther from the root tip.

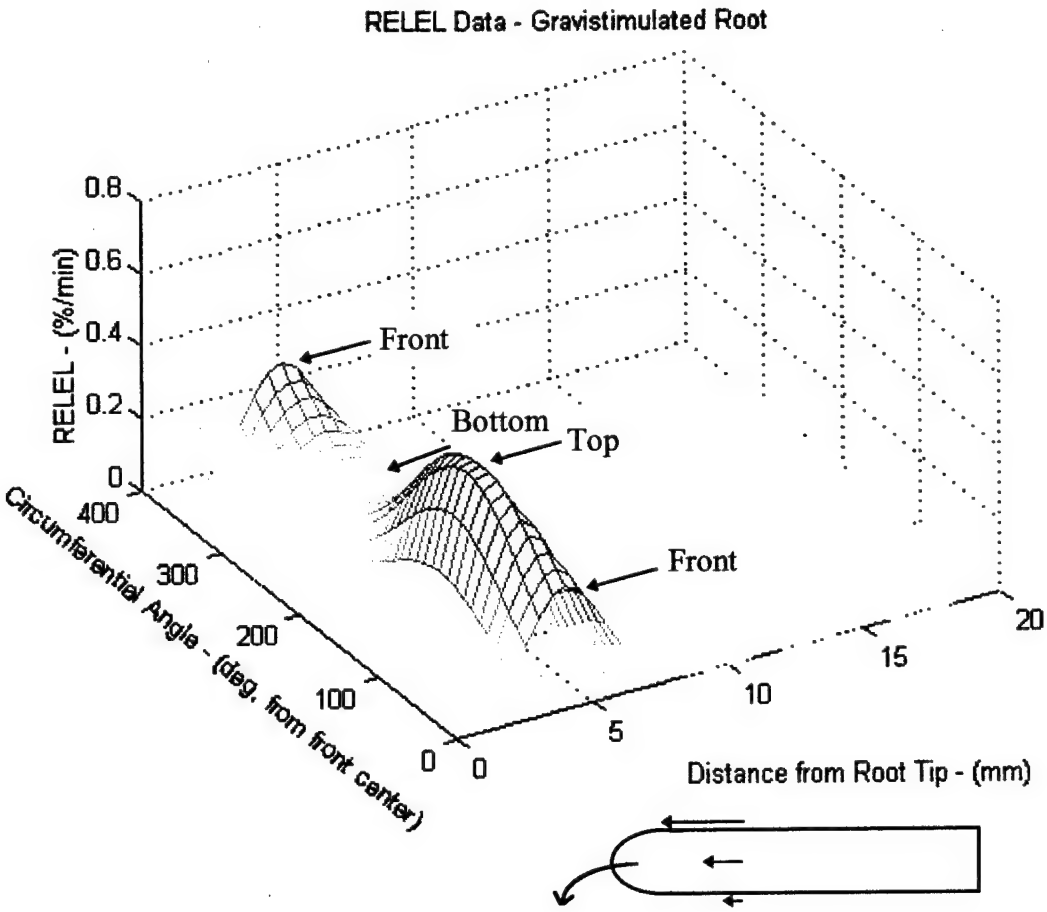

Figure 4.7 - A Gravistimulated RELEL with Two Averaged Data Sets

This RELEL is time-invariant, but provides a good approximation of the growth and curvature effects of gravitropism for short time periods (1-3 hours). Figures 4.8 and 4.9 show the RELEL at various viewpoints and provides further interpretation of the surface plot along with verification of the accuracy of the simulation.

(A)

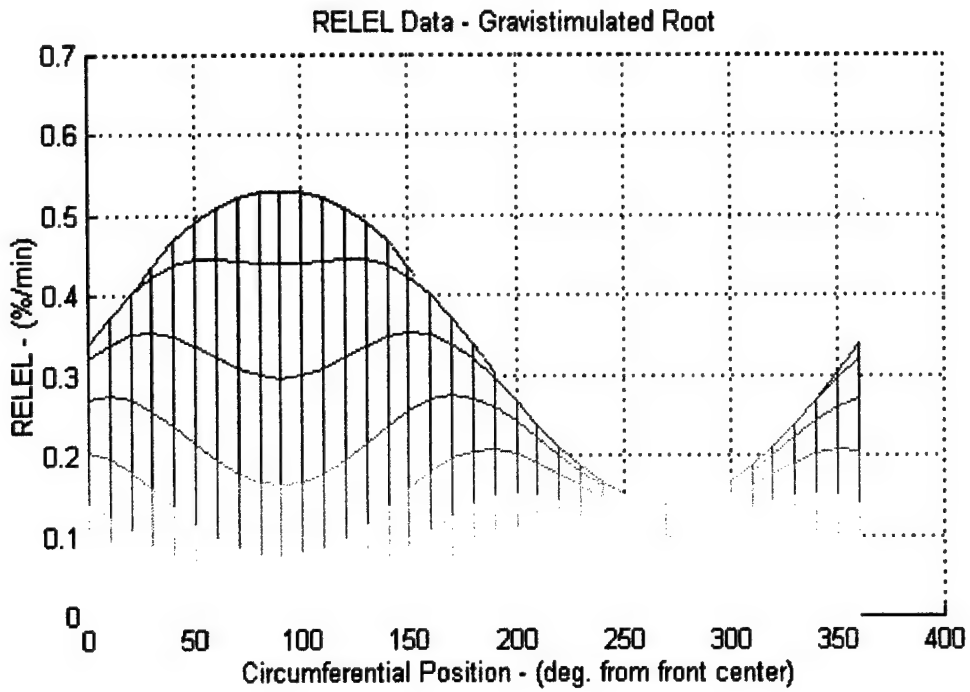

(B)

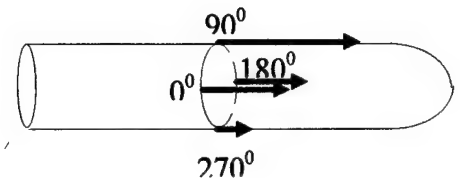

Figure 4.8 - The RELEL Surface Curve Interpreted
(A) shows the RELEL from Figure 4.7 as viewed from the left at no elevation angle. Note that the RELEL at the front and back sides(0^0 and 180^0) are the same as ungravistimulated RELEL values. The upper and lower sides are ±0.2 %/min. from this value. (B) shows the RELEL along the circumferential direction as the magnitude of a growth vector on the root as it is growing horizontally. The front and back of the root (0^0 and 180^0) are equal at ungravistimulated growth, while the upper- and lower-sides are respectively increased and decreased.

(A)

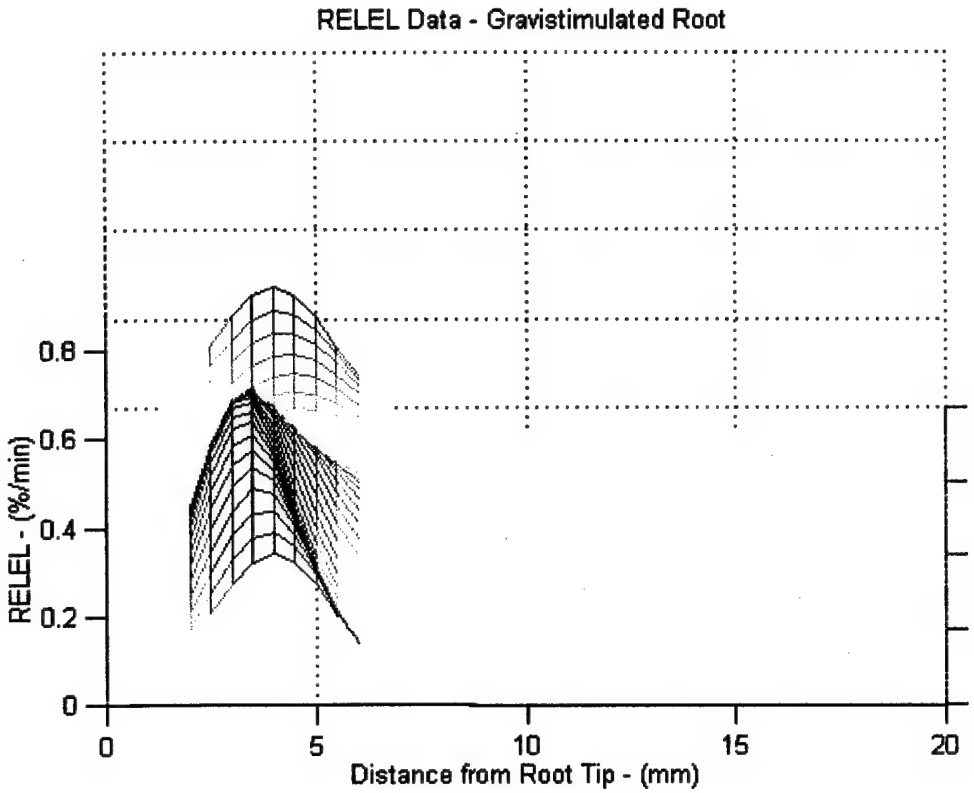

(B)

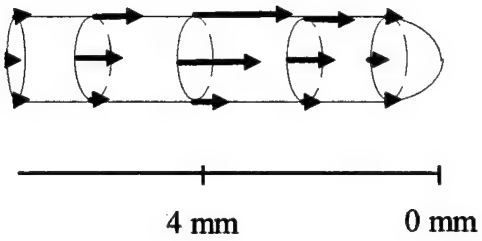

Figure 4.9 - Further Interpretation of the RELEL Surface Curve
(A) shows the RELEL curve with the abscissa as the distance from the root tip, while (B) shows growth vectors as a function of this distance along the length of the root, with the maximum reached at 4 mm basal from the tip.

The time period for this model was increased to 3 hours (180 minutes) with time increments of 10 minutes. Figure 4.10 shows the root growth and curvature incurred by the root experiencing this RELEL model. Note the significant "S-shape" created in the root. This effect occurs when the mean position of maximum RELEL on the lower-side shifts basally in relation to the position on the upper-side, but the decrease in lower-side $RELEL_{max}$ is not enough to compensate for the offset growth patterns, therefore producing slightly more growth on the bottom-side in this region and creating a slight upward curvature. Figure 4.11 characterizes this effect.

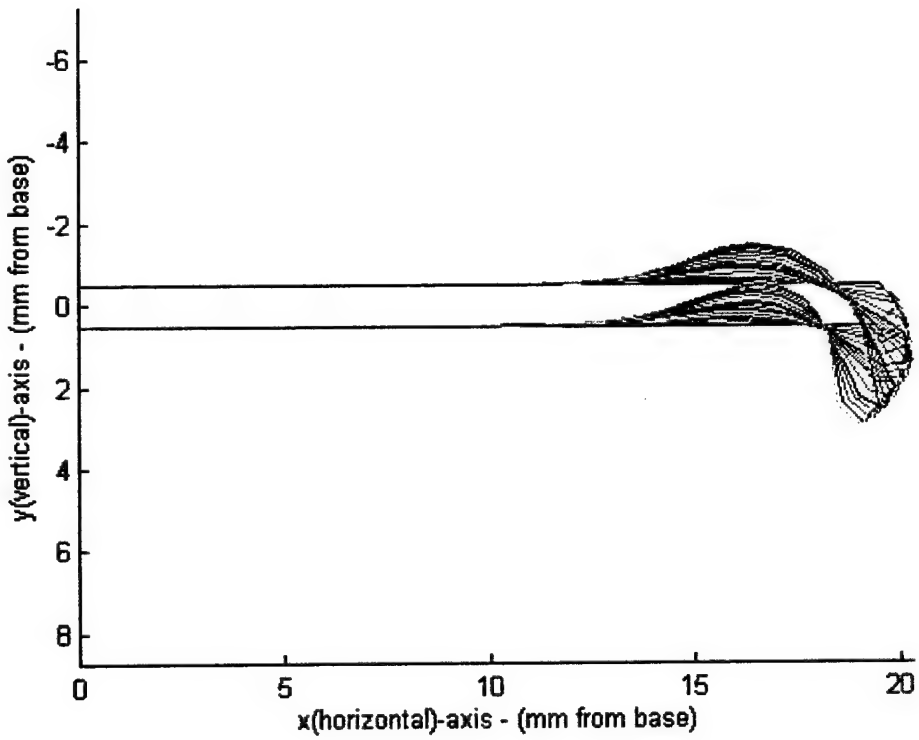

Figure 4.10 - Root Curvature for Two Averaged Data Sets
Total growth rate achieved is 0.64 mm/hr with a total length of 21.9 mm at the end of 3 hours and a tip angle of 4.95 degrees from vertical.

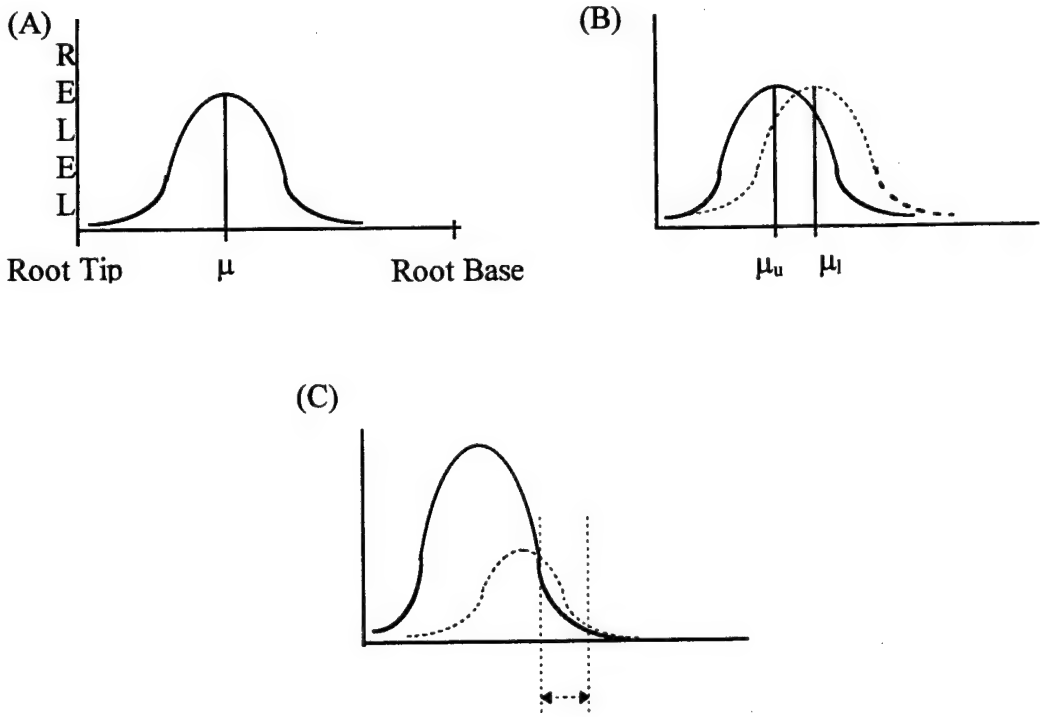

Figure 4.11 - Explanation of the S-shape Curvature Effect
(A) shows the nongravistimulated root where the upper- and lower-sides both experience equivalent growth parameters. (B) shows the effect of one gravitropic RELEL parameter change: the distal movement of the upper-side μ (μ_u) and the basal movement of the lower-side μ (μ_l). Without any further changes, this would create a large, basal region of higher growth on the lower side, producing large upward curvatures, but (C) shows that when compensated by smaller, lower-side RELEL magnitudes, this region can be reduced and possibly eliminated. If not completely eliminated, an S-shaped curvature will result as shown in Figure 4.10. Changes in the growth curve's σ parameter can also affect the outcome.

4.4.3.2 Sensitivity Analysis of RELEL Parameters

The results from the previous subsection bring to mind the question of just how sensitive is the actual growth curvature to the RELEL parameters. This subsection is designed to create an appreciation of this sensitivity. Using the model created from the two averaged data sets in the previous subsection, the gravitropic perturbation to the RELEL parameters of that model were individually altered by 5% and the effects noted and then all parameters are altered by 5 % and the cumulative

effects noted. Table 4.5 notes the original parameters and their altered values as applied to the Differential Growth and Curvature routine.

Table 4.5 - Parameters Used in the Sensitivity Study

Parameter		Original	+5 % Alteration	-5 % Alteration
$RELEL_{max}$	vertical	0.34 %/min	0.36	0.32
	upper-side	+0.2 %/min	+0.21	+0.19
	lower-side	-0.2 %/min	-0.21	-0.19
μ	vertical	4 mm	4.2	3.8
	upper-side	-0.7 mm	-0.74	-0.66
	lower-side	+0.7 mm	+0.74	+0.66
σ	vertical	1.5 mm	1.58	1.42
	upper-side	-0.4 mm	-.42	-0.38
	lower-side	+0.4 mm	+.42	+0.38

Table 4.6 documents the changes in growth rate, total growth, and curvature attained after 3 hours. It must be remembered that this is a simple, time-invariant model and no oscillating property occurs in the growth pattern. Initially, the steady-state, vertical parameter values ($RELEL_{max}$, μ, and σ) were altered, then the gravitropic perturbations were altered, followed by combinations of the two. This was accomplished for each of the three RELEL parameters ($RELEL_{max}$, μ, and σ) individually and, finally, they were altered in groups. The extreme effect on final tip angle effected by almost every single altered parameter is noteworthy. Although the control (the averaged two-data-set model) final angle was small (4.95^0) and, therefore, small angles produce large percentage change, these percentage changes are large, equating up to 23^0. As expected, the largest growth and curvature effects occur when $RELEL_{max}$ and σ values are altered, and the largest effect on the peculiar S-shape occurs when μ is altered.

Table 4.6 - Results of Sensitivity Study

Altered Parameter (s):						Resulting Change in: (%)			
$RELEL_{max}$ vertical	$RELEL_{max}$ perturbation	μ vertical	μ perturbation	σ vertical	σ perturbation	Growth Rate	Total Growth	Curvature	S-Shape Altered?
+5 %						+8	+1	+82	< -less
-5 %						-6	-1	-82	≈ -equal
	+5 %					0	0	-156	<
	-5 %					+1	0	+156	> -more
+5%	+5 %					+6	+1	-73	<
-5 %	-5 %					-5	-1	+74	>≈
-5%	+5%					-8	-1	-238	<≈
		+5 %				+1	0	+1	≈
		-5 %				0	0	0	≈
			+5 %			0	0	+1	>
			-5 %			0	0	0	<
		+5 %	-5 %			+1	0	0	<
				+5 %		+6	+1	-166	≈
				-5 %		-6	-1	+167	<≈
					+5 %	0	0	+69	≈
					-5 %	0	0	-69	≈
				+5 %	-5 %	+8	+1	-235	<
-5 %	+5 %	+5 %	-5 %			-8	-1	-239	-40
-5 %	+5 %			+5 %	-5 %	0	0	-477	-45
-5 %	+5 %	+5 %	-5 %	+5 %	-5 %	0	0	-479	-55

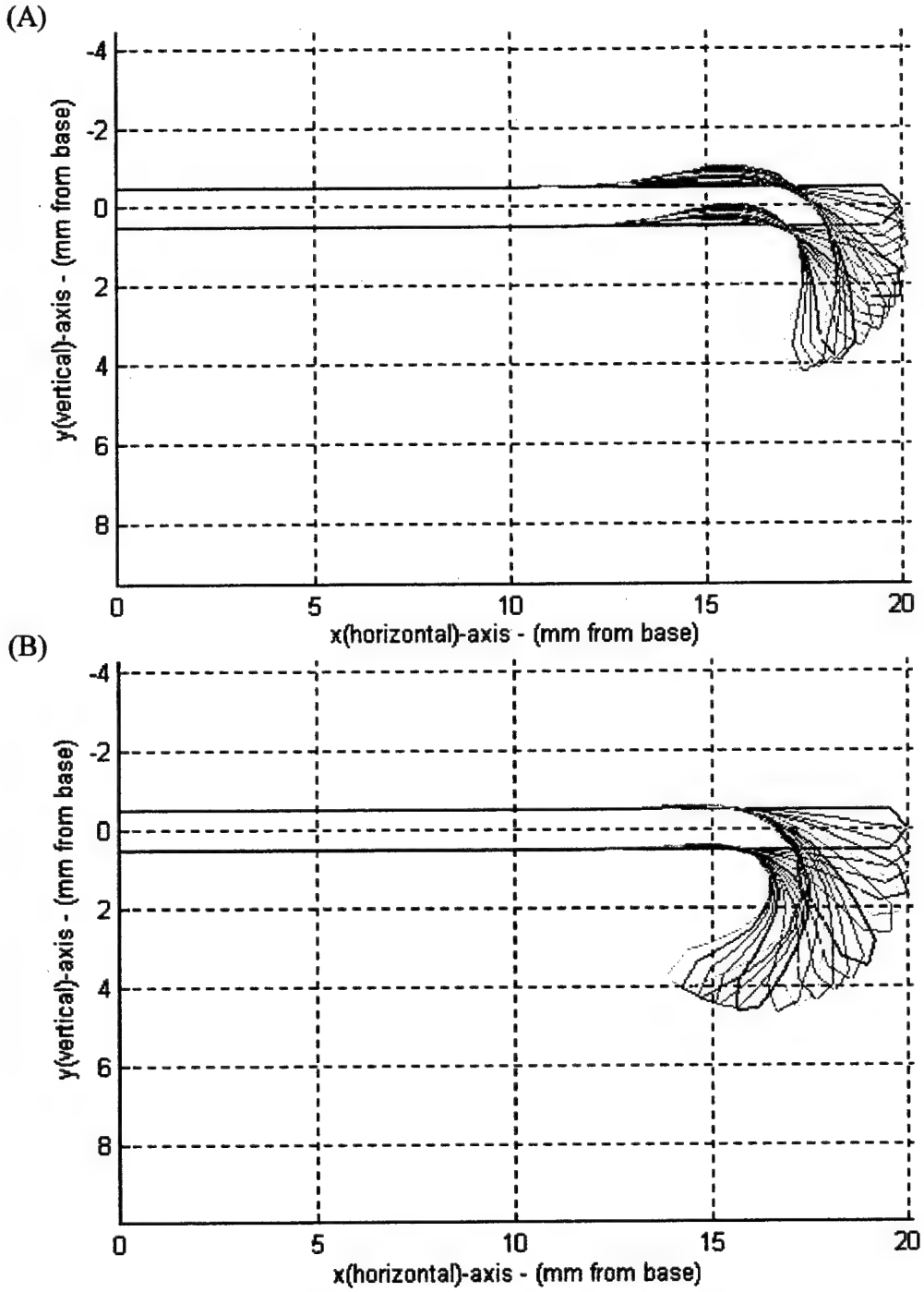

Figure 4.12 - Eliminating the S-shaped Growth Characteristic
(A) shows the significantly less S-shape (as compared with Figure 4.10) when the final combination of 5% changes (last row of Table 4.6) are incorporated into the model. (B) shows complete elimination of the S-shape by only increasing the $RELEL_{max}$ gravitropic perturbation to 0.25 %/min., a difference of only 25%, with other researchers documenting even larger perturbations to this parameter (Nelson & Evans, 1986; Versel & Pilet, 1986; Ishikawa *et al.*, 1991).

4.4.3.3 Model Based on Weighted Average of Selected RELEL Data

The previous subsection showed that the root's growth and curvature is remarkably sensitive to small changes in RELEL parameters. Therefore, accurate RELEL data must be used within the Differential Growth and Curvature routine. To encorporate even more historical data into the model, the weighted averages of the three main sources of detailed RELEL data, using similar materials and methods, are now used to create the model. These three sources, introduced in Table 4.1, were the most detailed, time-invariant RELEL data sets found in the literature in which similar materials and methods were used, but even these differ slightly in the techniques used to record the data. Because of these differences, a weighted averaging scheme was used to integrate all three data sets into a coherent RELEL model. The (Barlow, 1985) data serves as the benchmark by using the classic RELEL definition along with temperature control and root length choices similar to the materials and methods used in accomplishing gravitropic responses for this thesis. Any deviation from the Barlow materials and methods serves to decrease the weight factor applied to those data. Table 4.7 documents the procedure. As before, "smoothing" serves to ensure that the RELEL data are distributed evenly between the upper and lower sides and without any discontinuities in the data's first derivatives.

Table 4.7 - RELEL Parameters Obtained Through Weighted Average

Parameter	Barlow	Versel	Nelson	Weighted Average	Smoothed
$RELEL_{max}$	(%/min)	(%/min)	(%/min)	(%/min)	
vertical	0.4	0.28	0.72	0.4	n/a
upper-side	+67%	+32%	-26%	+45% / +0.18	+0.2 %/min
lower-side	-43%	-64%	-54%	-51% / -0.2	-0.2 %/min
μ	(mm)	(mm)	(mm)	(mm)	
vertical	4	4	2.5	3.8	n/a
upper-side	0%	-25%	+80%	+0.56% / +.02	-0.5 mm
lower-side	+33%	+13%	+40%	+27% / +1.03	+0.5 mm
σ	(mm)	(mm)	(mm)	(mm)	
vertical	1.5	1.5	1.0	1.4	n/a
upper-side	-33%	-33%	+100%	-18% / -0.25	-0.3 mm
lower-side	+33%	0%	+50%	+24% / +0.34	+0.3 mm
Cultivar	LG11	LG11	MO		
Temp.(^{0}C)	21-25	22	28		
Length (mm)	10-30	15	25		
RELEL type	classic	classic	log		
Time Period	1 hr	1-3 hrs	0-2 hrs		
Weight Factor	5	3	1		

Figure 4.13 shows the resulting growth and curvature of the simulated root using the weighted average RELEL data over a 3 hour period. The RELEL surface curves are not shown for this simulation as they are very similar to the previous model with only minor deviations. To further enhance the usefulness of the simulation, time variability must now be brought into the model; a difficult modification to achieve since little detailed work on time variability of RELEL data (a meticulous endeavor) has been published.

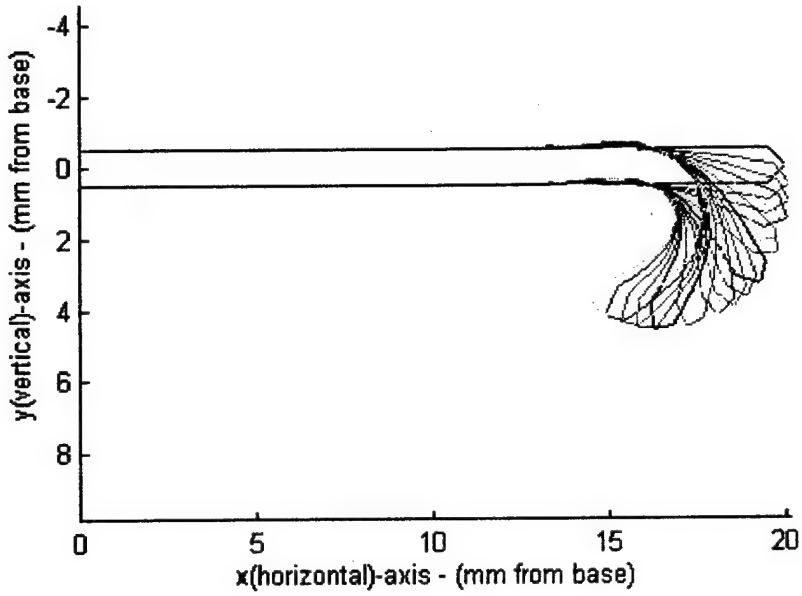

Figure 4.13 - Root Curvature for Weighted Average Data Sets

4.4.4 Time-variant, Gravistimulated Growth

The Ishikawa and Evans work documented in Figure 4.4(B) of this chapter provides an insight into the time-dependent nature of the differential growth mechanism. The data covered approximately 7 hours and shows a damped period (w_d) of approximately 300 minutes that damps to steady-state, vertical growth parameters at the end of 7 hours. Since an exponential decay approaches zero after approximately 4-5 time constants (T_c), the initial time-variable model will use the weighted average vertical, steady-state parameters with the gravitropic perturbations applied with a decayed, sinusoidal time coefficient (TC):

$$TC = Ae^{\frac{-t}{T_c}} \sin(\frac{2\pi}{w_d} t) \qquad (4-7)$$

where, the coefficient, A, adjusts the magnitude of the time-variable term, the time constant (T_c) equals 100 minutes, the damped period (w_d) equals 300 minutes, and

time (t) is variable. Figure 4.14 displays the results of this model which is simulated for a time period of 420 minutes in 10 minute increments with the root redrawn every 30 minutes. Figure 4.15 displays the RELEL surface plots for times 0, 105, 210, and 315 minutes.

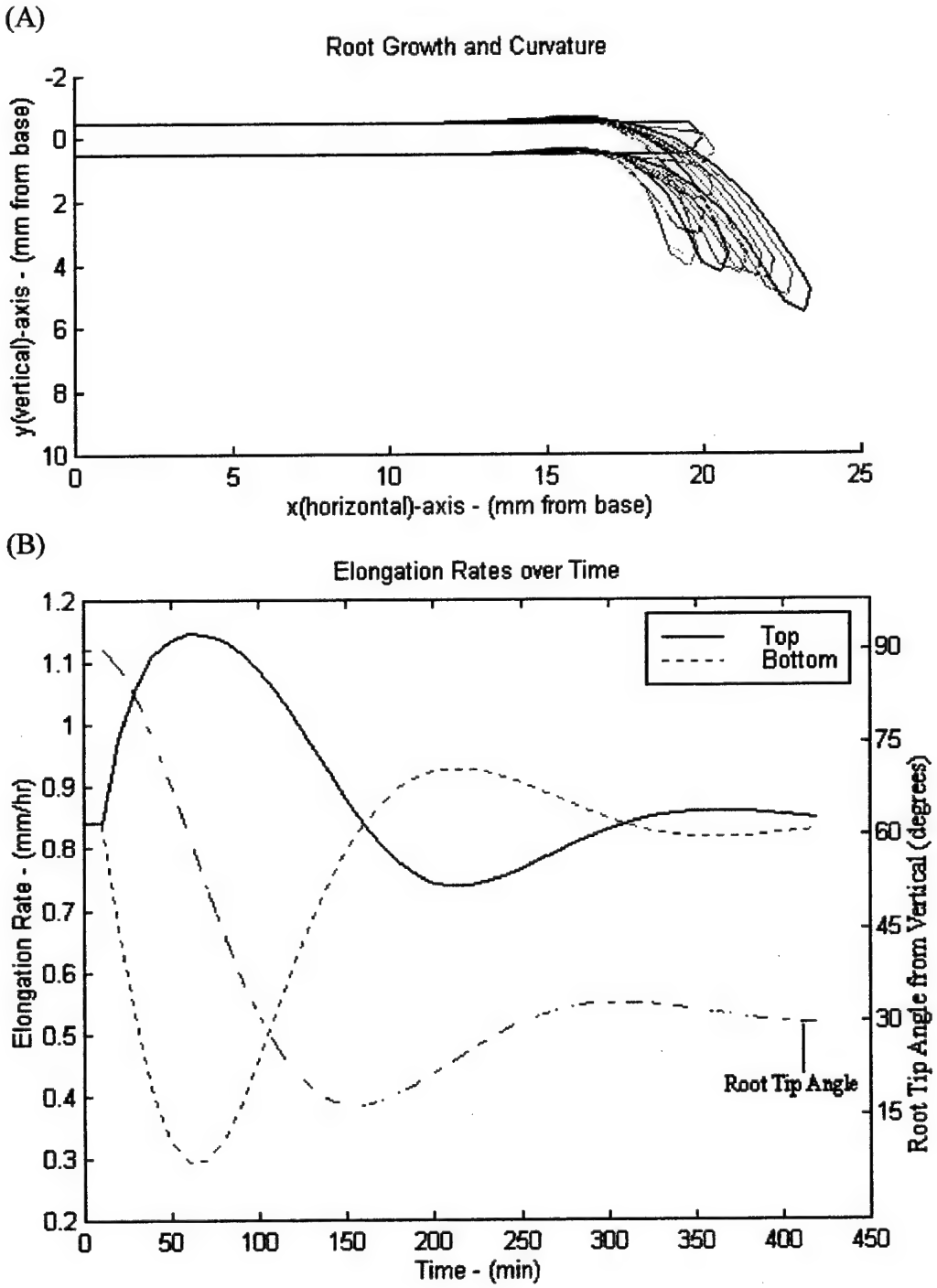

Figure 4.14 - Root Curvature for Time-variant, Weighted Average Data Sets (A) shows the time-lapse simulation for every 30 minutes; progressive black, blue, green, red, cyan, magenta, yellow is the time-ordered color scheme. (B) shows both the top- and bottom-side elongation rates and the root-tip angle over time. Final conditions include a length (integral of rate) of 25.7 mm and a curvature angle of 29 degrees.

(A) RELEL Data - Time-variant, Weighted Average Model (0 minutes)

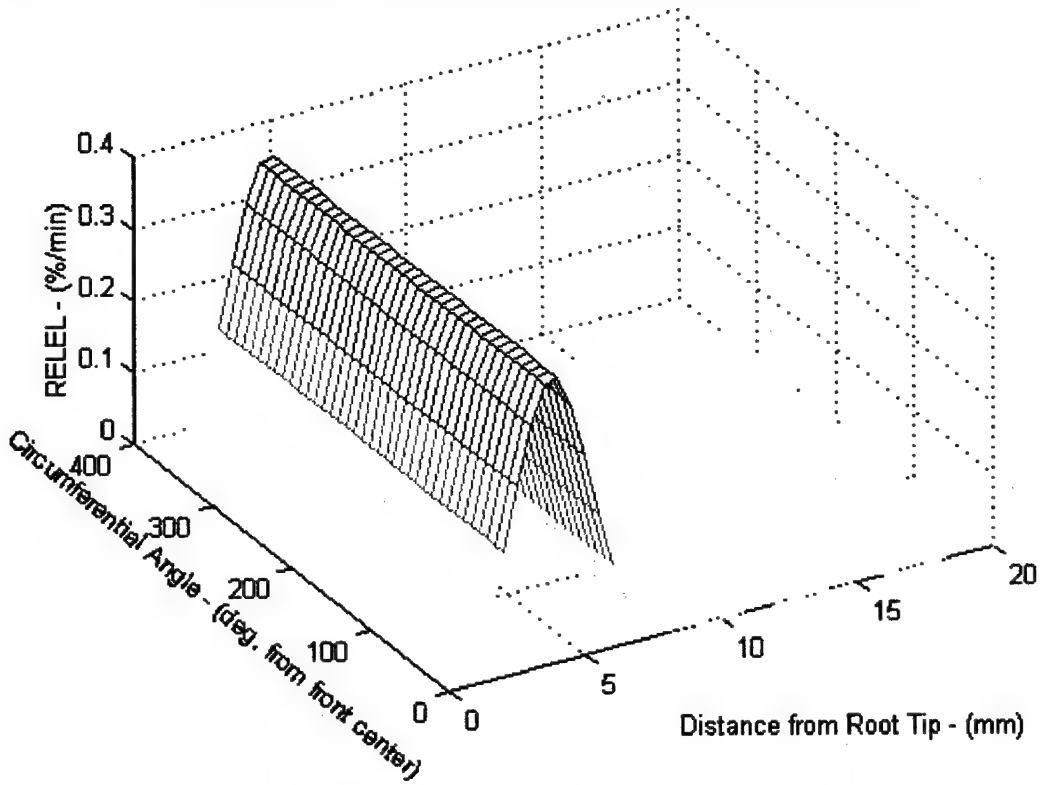

(B) RELEL Data - Time-variant, Weighted Average Model (105 minutes)

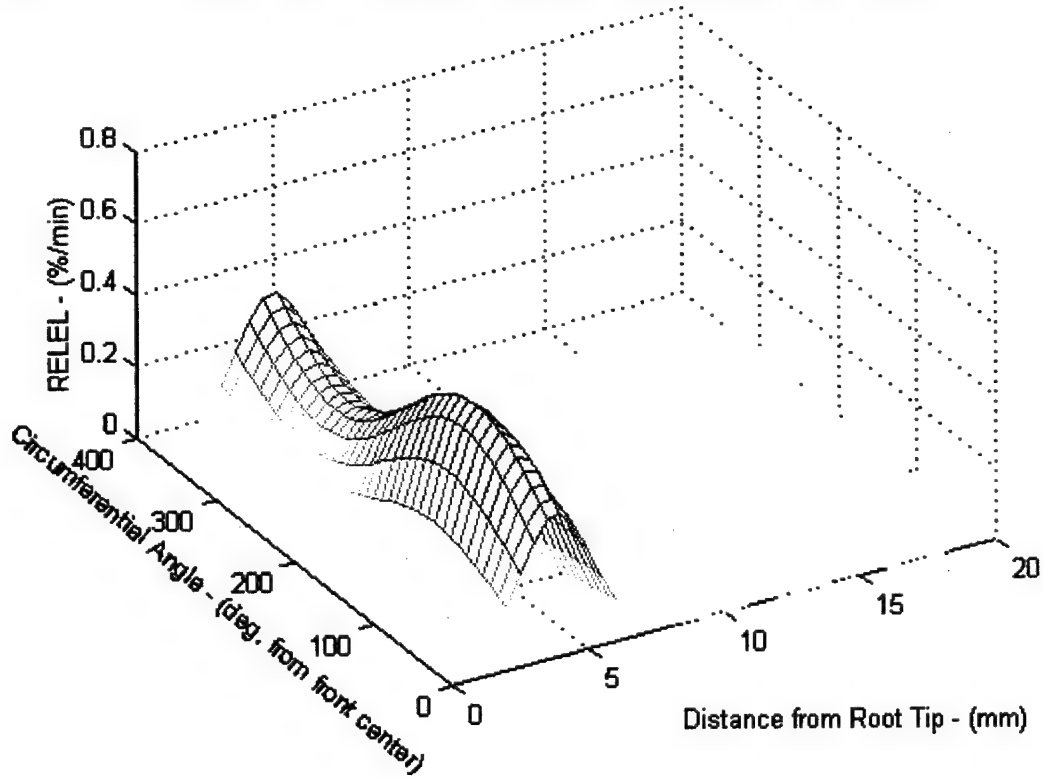

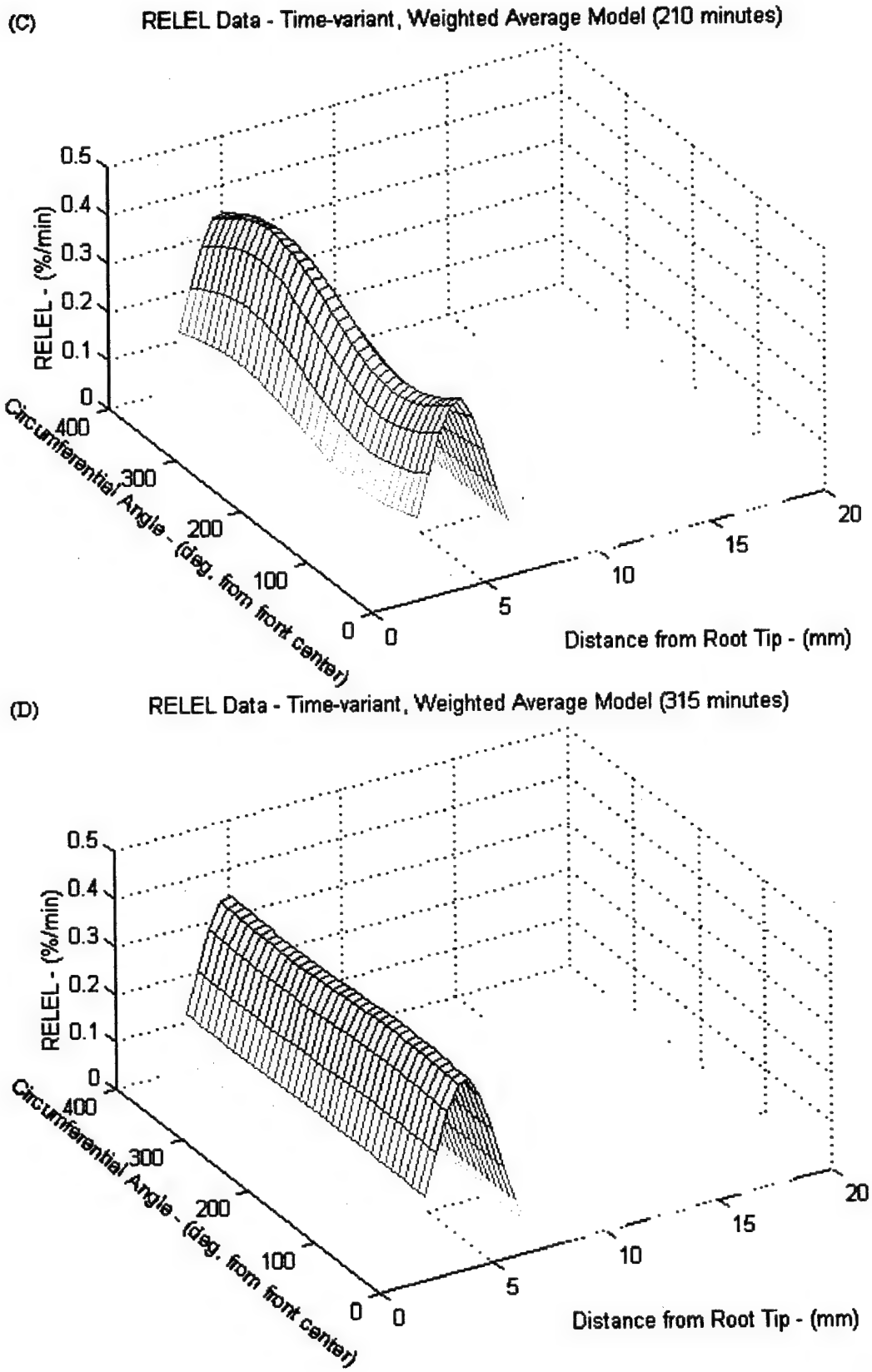

Figure 4.15 - RELEL Surface Plots for Selected Times of Time-variant Model

When comparing these results to the Ishikawa data displayed in Figure 4.4(B), the latest, smoothed model based on exponentially decayed sinusoidal perturbations to vertical RELEL parameters appears very close to actual experimental results. Closer comparison would result if Ishikawa's RELEL data could be adapted into the model. Therefore, one final model set was constructed using Ishikawa's RELEL data which was provided for 6 discrete periods over a 7-hour time frame. These data were "smoothed" in order to model the RELEL state in the root continuously between the discrete times over which the data were originally averaged. Time histories of the three RELEL parameters are displayed in Figures 4.16 through 4.18. The resultant programming of these time-dependent parameters is found in the documentation of the Differential Growth and Curvature routine in Appendix VI. This model, more empirical than the others, required that the RELEL parameters detailed for 6 specific times be approximated by 5th order polynomial functions and the polynomials used to define the time-dependent RELEL parameters. The RELEL surface curve for 120 and 240 minutes are produced in Figure 4.19 and the elongation/curvature graphics (now run over 480 minutes) are found in Figure 4.20.

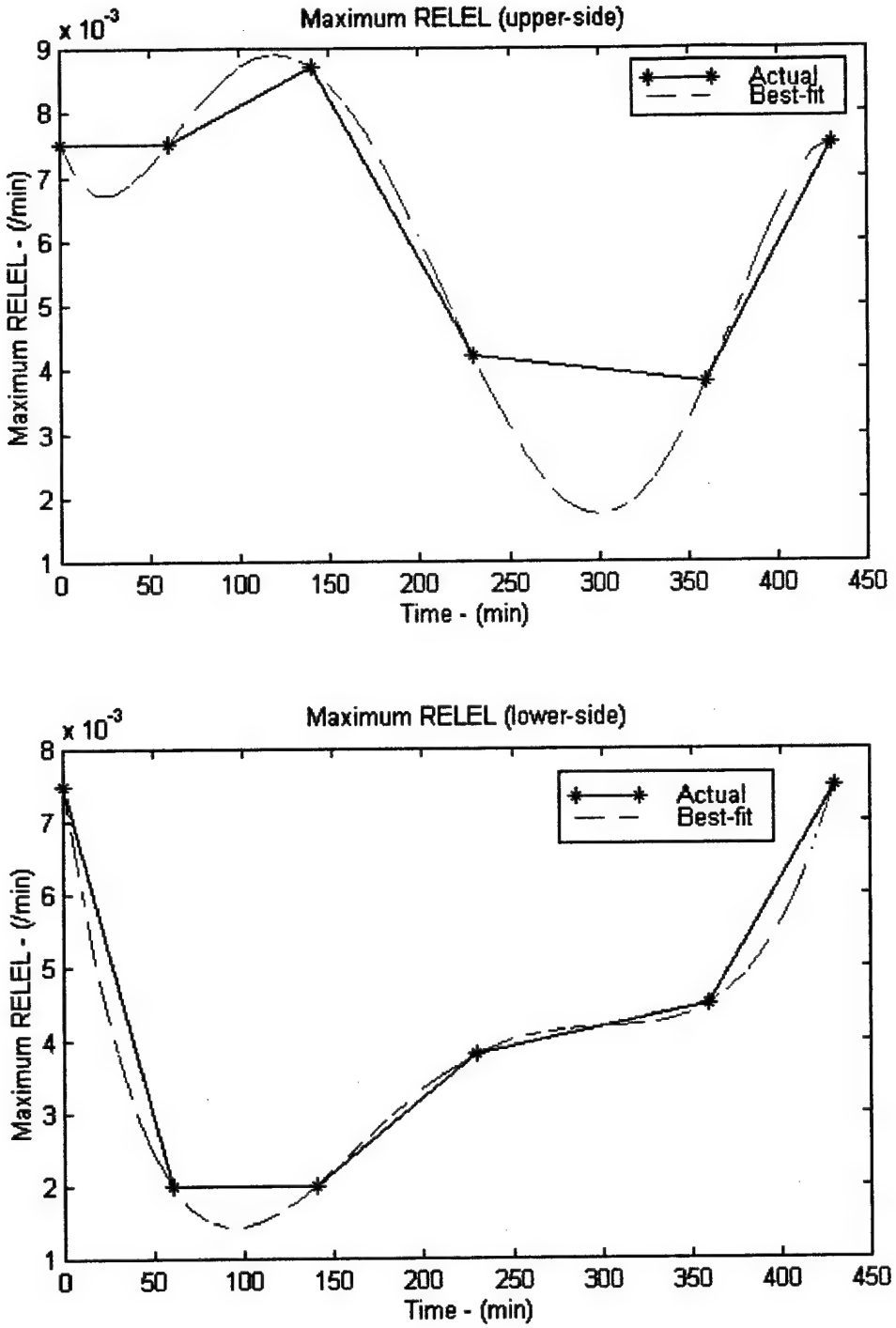

Figure 4.16 - RELEL Maximum ($RELEL_{max}$) Time History
Data obtained from (Ishikawa and Evans, 1991). The original data were averaged to discrete times and polynomial functions were applied (method of least-squares) to provide a continuous function to represent the data. Best-fit polynomial is 5th order.

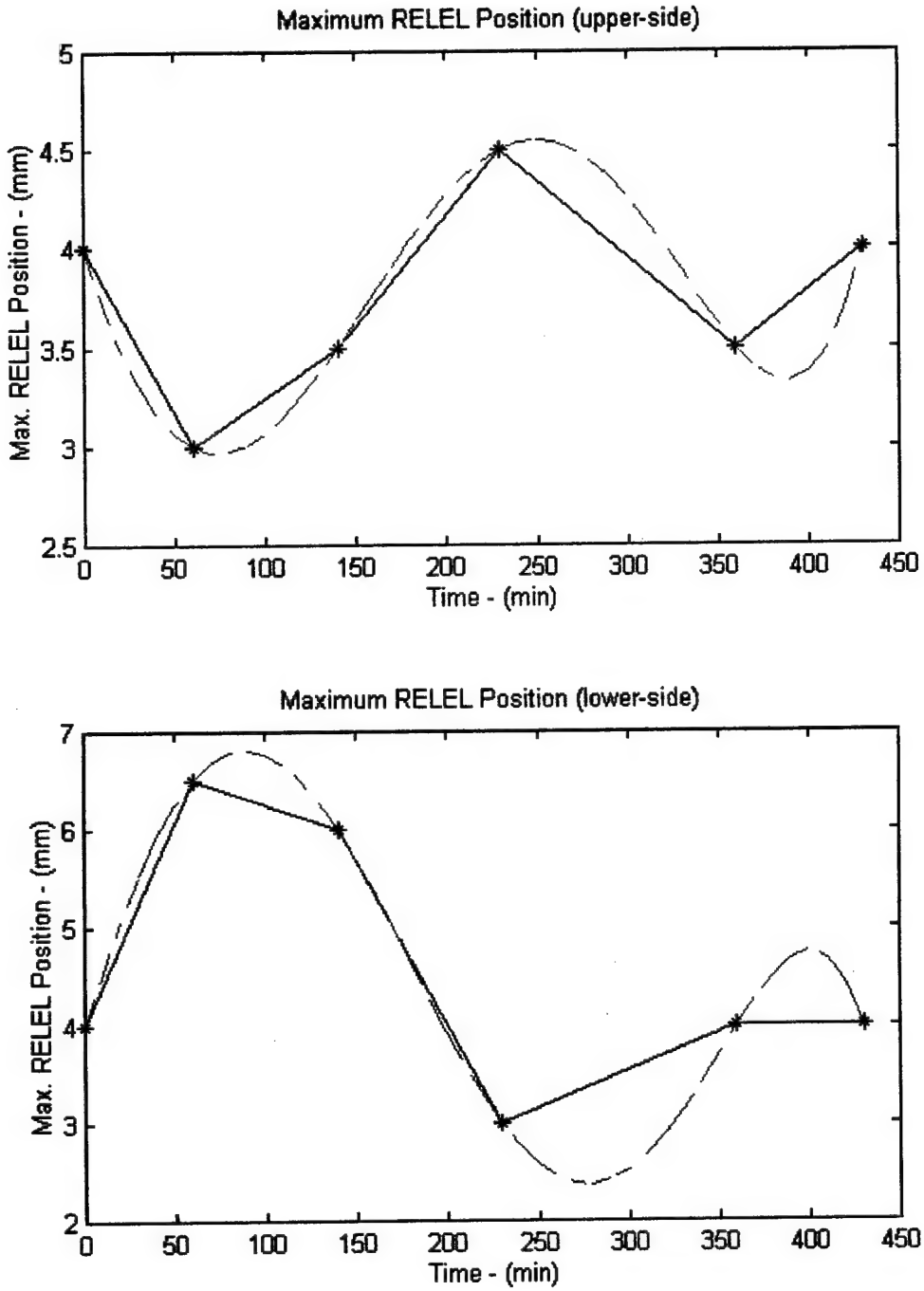

Figure 4.17 - RELEL Position (μ) Time History
Data obtained from (Ishikawa and Evans, 1991). The original data were averaged to discrete times and polynomial functions were applied (method of least-squares) to provide a continuous function to represent the data. Best-fit polynomial is 5th order.

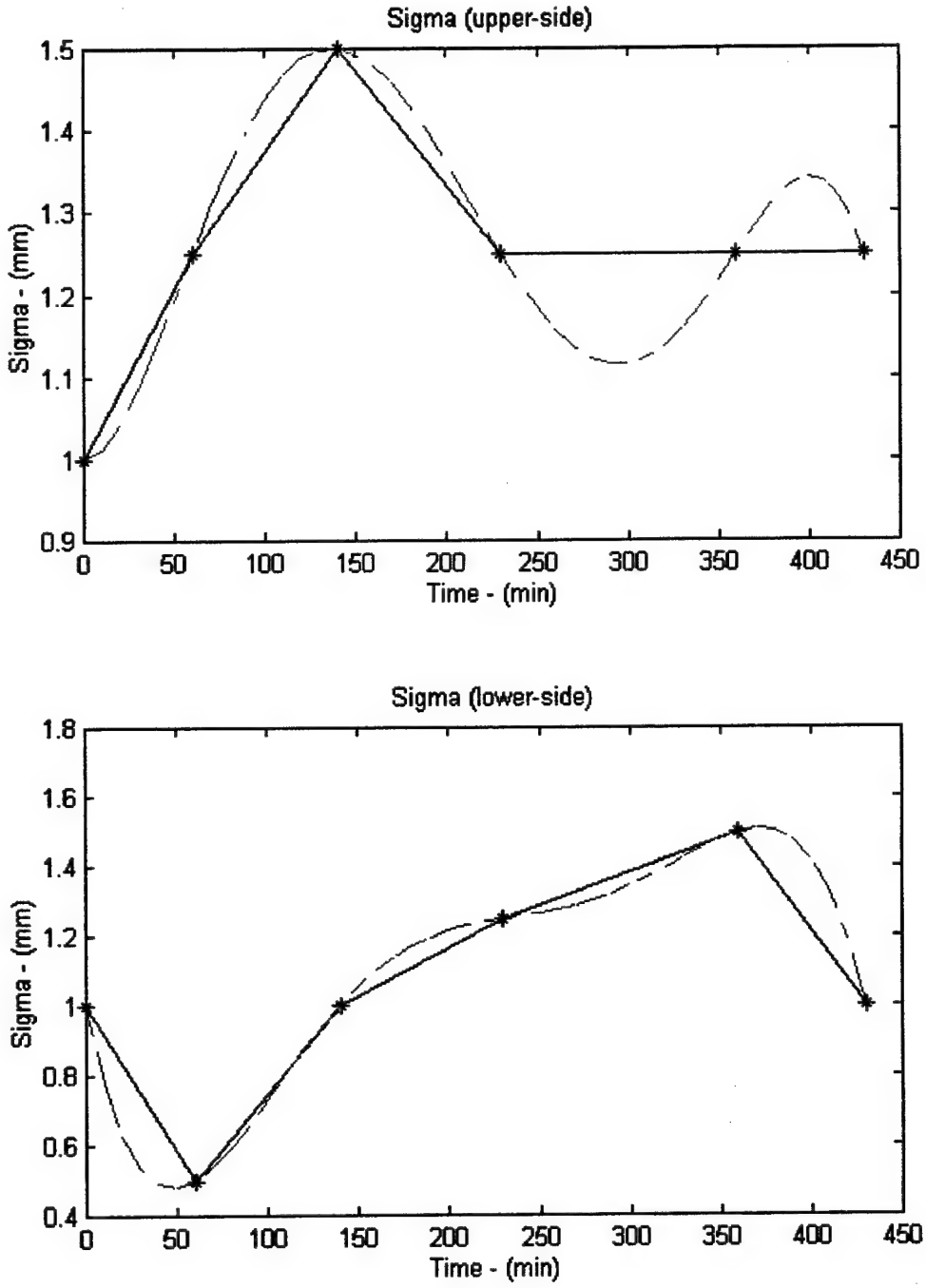

Figure 4.18 - RELEL Standard Deviation (σ) Time History
Data obtained from (Ishikawa and Evans, 1991). The original data were averaged to discrete times and polynomial functions were applied (method of least-squares) to provide a continuous function to represent the data. Best-fit polynomial is 5th order.

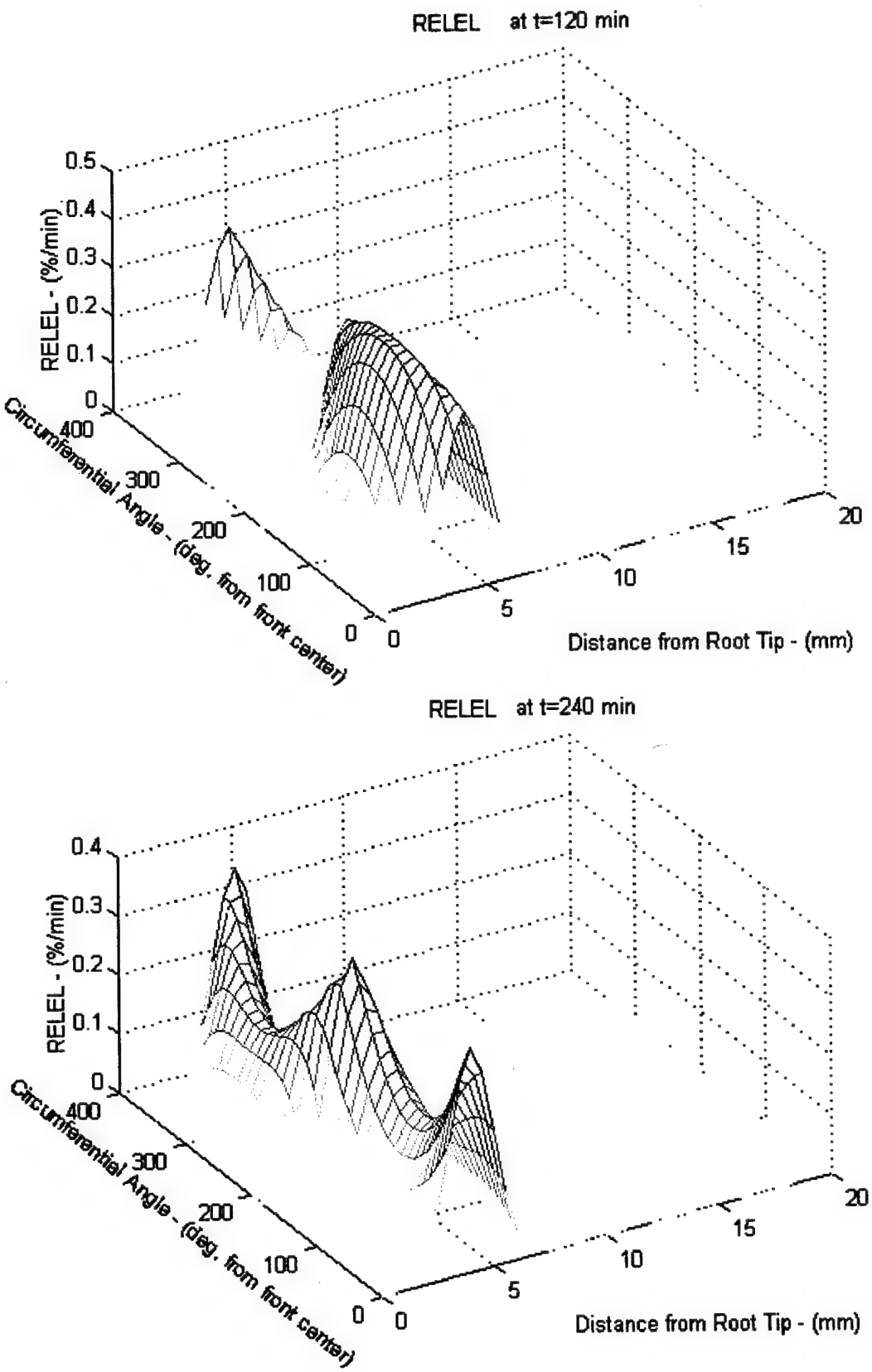

Figure 4.19 - RELEL Surface Plots for Selected Times of Empirical Model

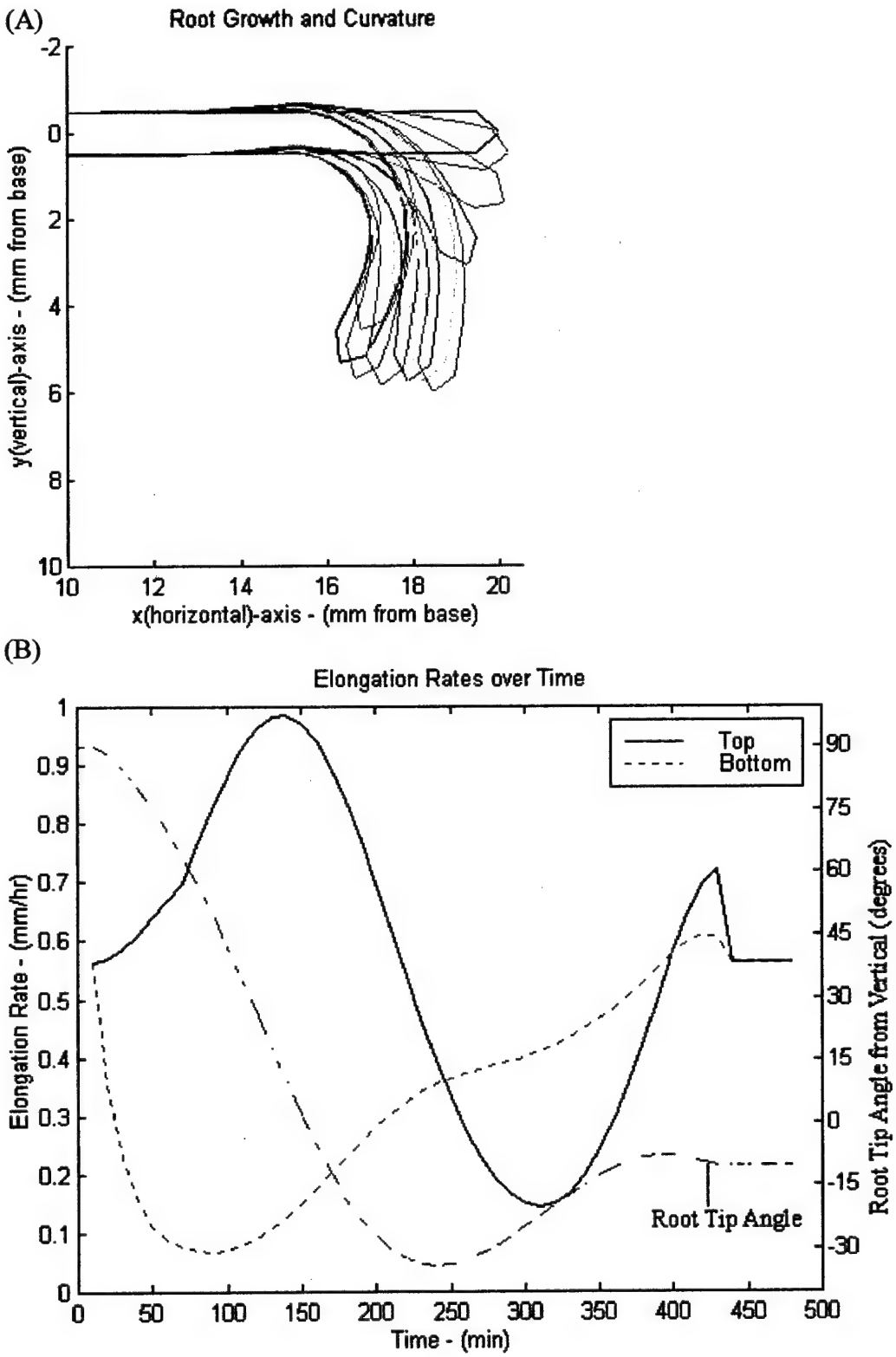

Figure 4.20 - Root Curvature for Time-variant, Empirical Model
(A) shows the time-lapse for this model, while (B) displays the elongation rates for the top and bottom sides. Curvature approached -34^0 before reversing to a final -9^0.

4.4.5 Model of Circumnutation Effects

To include circumnutational effects into the model and simulation, additional data was acquired from historical research and an alteration was made to the structure of Differential Growth and Curvature routine. Table 4.1 highlighted some circumnutational RELEL data, but quantitative literature as to the time-variant nature of this tropism is lacking. Periods and amplitudes of oscillation are the most necessary quantitative data to accurately model the circumnutation effects. Table 4.8 highlights some of the historical findings in this area. Therefore, a starting model for circumnutational effects includes the RELEL perturbations found in Table 4.1, desiring an ultimate amplitude resulting from these perturbations to achieve approximately 5^0, with a time period of 1 hour.

Table 4.8 - Circumnutation Parameters

Parameter	Species	Value	Reference
period	maize	1 hour	(Barlow *et al.*, 1993)
amplitude	maize	10 degrees	(Barlow *et al.*, 1993)
period	maize	50-125 minutes	(Kryder & Evans, 1990)
amplitude	maize	5 degrees	(Kryder & Evans, 1990)
period	maize	approx. 1 hour	(Pilet & Ney, 1981)
period	pea	50 minutes	(Yang & Tepper, 1996)

The alteration made to the DG/C routine involved splitting the RELEL functions into two different files; one for steady-state, vertical RELEL and circumnutational perturbations and one for gravitropic perturbations (refer back to

section 4.3.2). An input parameter was added that specifies the time into the simulation to gravistimulate the root, thereby allowing visualization of circumnutational movements prior to gravistimulation. This allows analysis of how circumnutational movement is correlated with gravitropic movement. Figure 4.21 shows the results of the weighted average model (section 4.4.4.3) under only circumnutational effects. Note that the period and amplitude are both at the target values of approximately 1 hour and $\pm 5^0$, respectively; a successful model of circumnutation.

Note two important results. The difference in the right- and left-side elongation rates are close to 60% of that experienced by a fully graviresponding root. The RELEL parameter perturbations are also close to 60% of those experienced by graviresponding roots. Therefore, the RELEL perturbations witnessed in circumnutations are similiar in magnitude to those witnessed in gravitropism, with the gravitropic perturbations having a much longer period and, therefore, having a much more cumulative effect on root elongation. With circumnutations, these perturbations are applied at higher frequency and, therefore, create much smaller curvature motions ($\pm 5^0$).

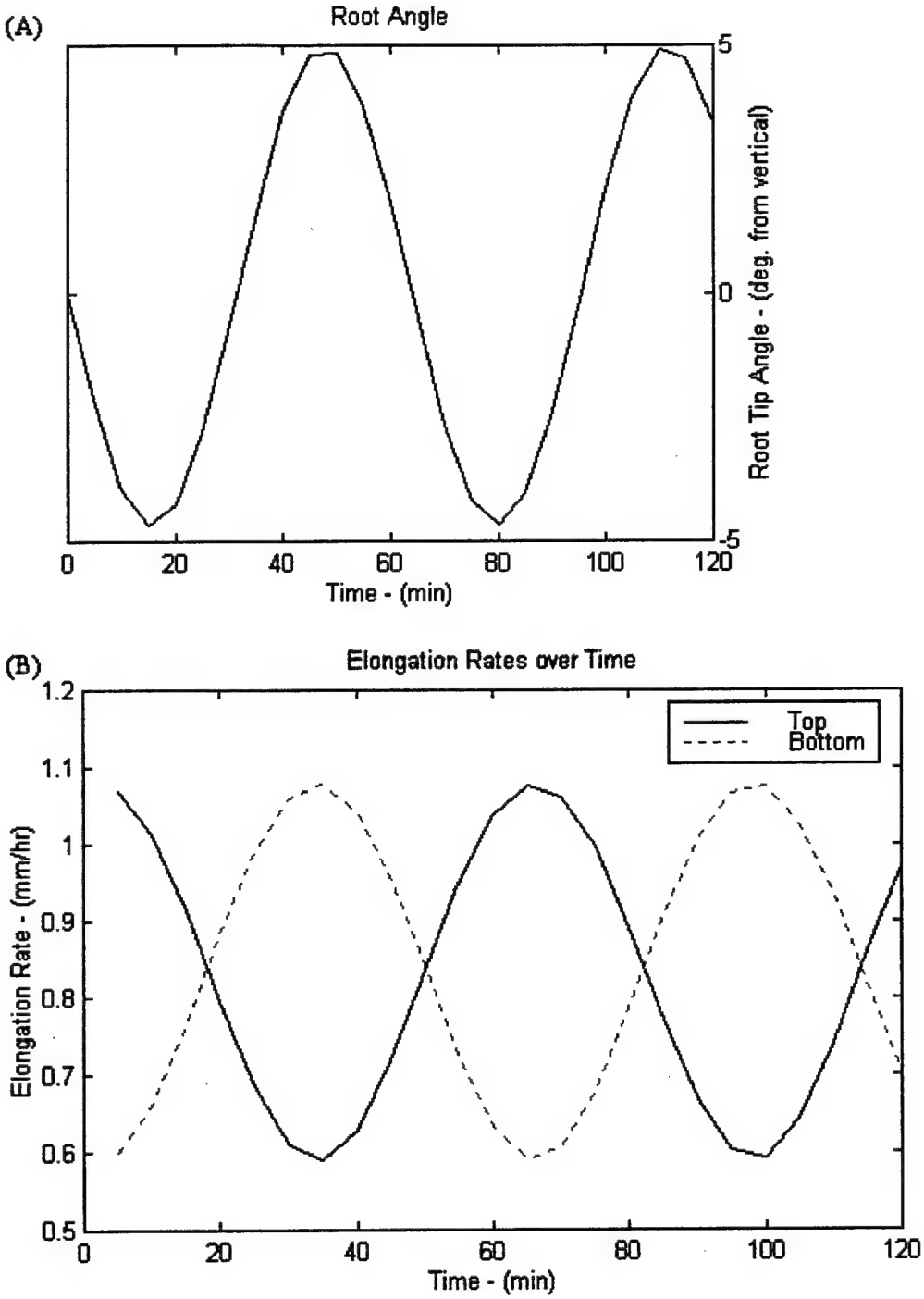

Figure 4.21 - Circumnutations on a Vertical Root
(A) shows the root tip angle from vertical over time. (B) shows the elongation rates over time of the opposing sides (top equates to right-side and bottom equates to left-side).

Figures 4.22 and 4.23 show the results when the circumnutation model is applied to the gravistimulation model whose results were displayed in Figure 4.14. The root remained vertical for 90 minutes following the beginning of the simulation and then gravistimulated by turning it 90^0. Note the time-course of circumnutation prior to the gravistimulation and its effect on the form of the initial graviresponse. At the time of gravistimulation, circumnutation was reaching a peak of left-side differential growth over the right-side. Therefore, an "apparent" negative gravitropic reaction is seen in the opening stages of the graviresponse. Also note the emergence of the circumnutational dynamics following the initial time-course (first 100 minutes) of the graviresponse.

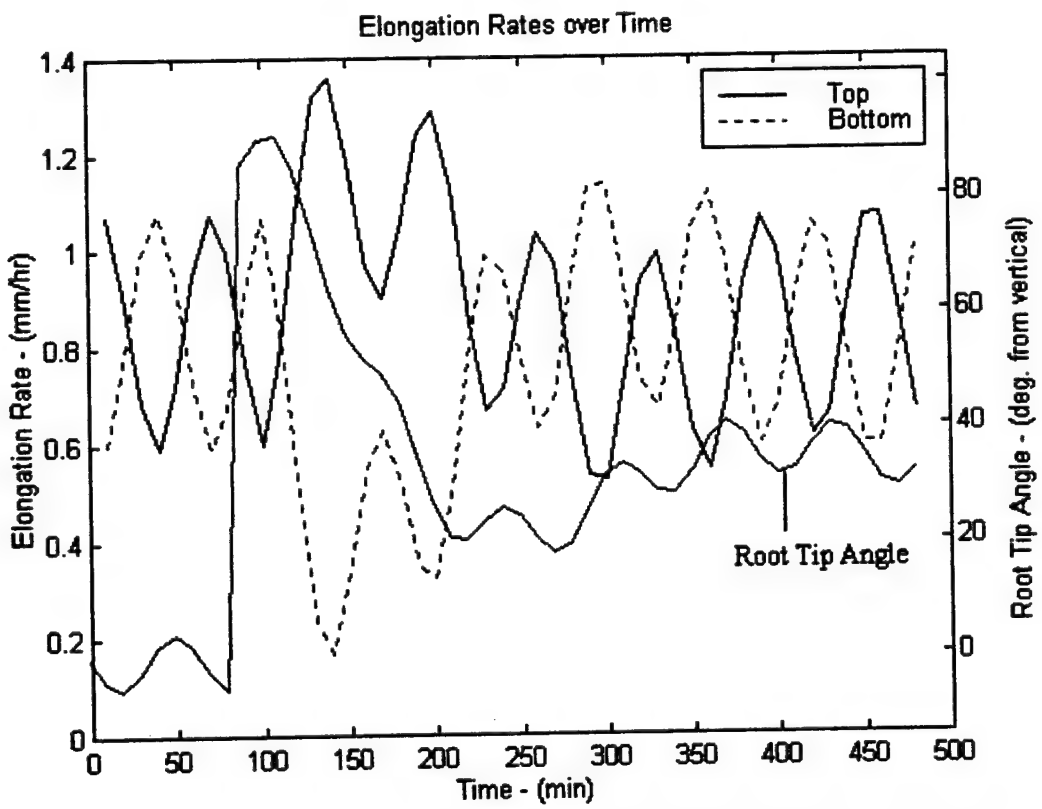

Figure 4.22 - Circumnutating Gravitropic Response Rates and Curvature

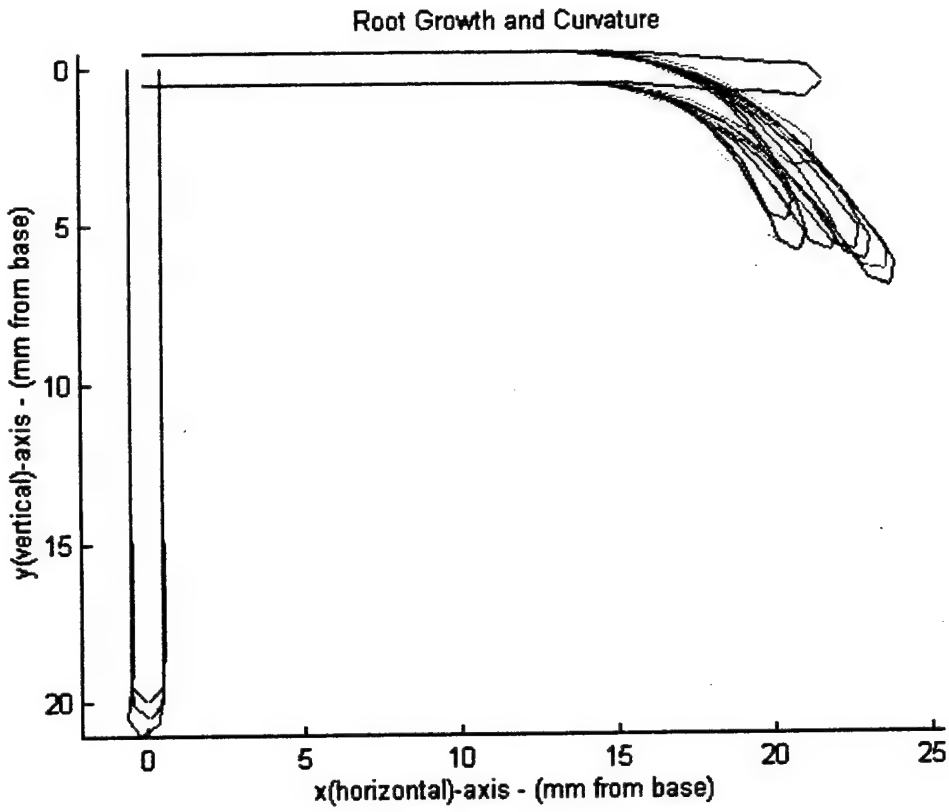

Figure 4.23 - Circumnutating Gravitropic Root

As seen from these results, the circumnutation overlay model produces circumnutation characteristics comparable to that found in the literature. The curvatures caused by circumnutational movements occur concurrently with and not separate from gravitropic responses. The temporal phase of circumnutation impacts the beginning response form of the gravitropic reaction. However, if sampling is done at too large a time-step, these circumnutational effects will not be witnessed in the time-averaged data of gravitropic response curves. This topic is covered in further depth in Chapter 5 of this thesis.

4.4.6 Transfer Function Model

The DG/C routine includes a flag near the end of the routine so that the user, when ready, can produce response function models in the s-domain from the simulation. The impulse responses can verify the accuracy of the models. Figure 4.24 shows the impulse response for a circumnutating, vertical root and Figure 4.25 shows the impulse response for a graviresponding root. These figures, when compared with the simulation raw data from Figures 4.21 and 4.14, respectively, verify the accuracy of the s-domain, simplified models. The s-domain models are listed following the figures.

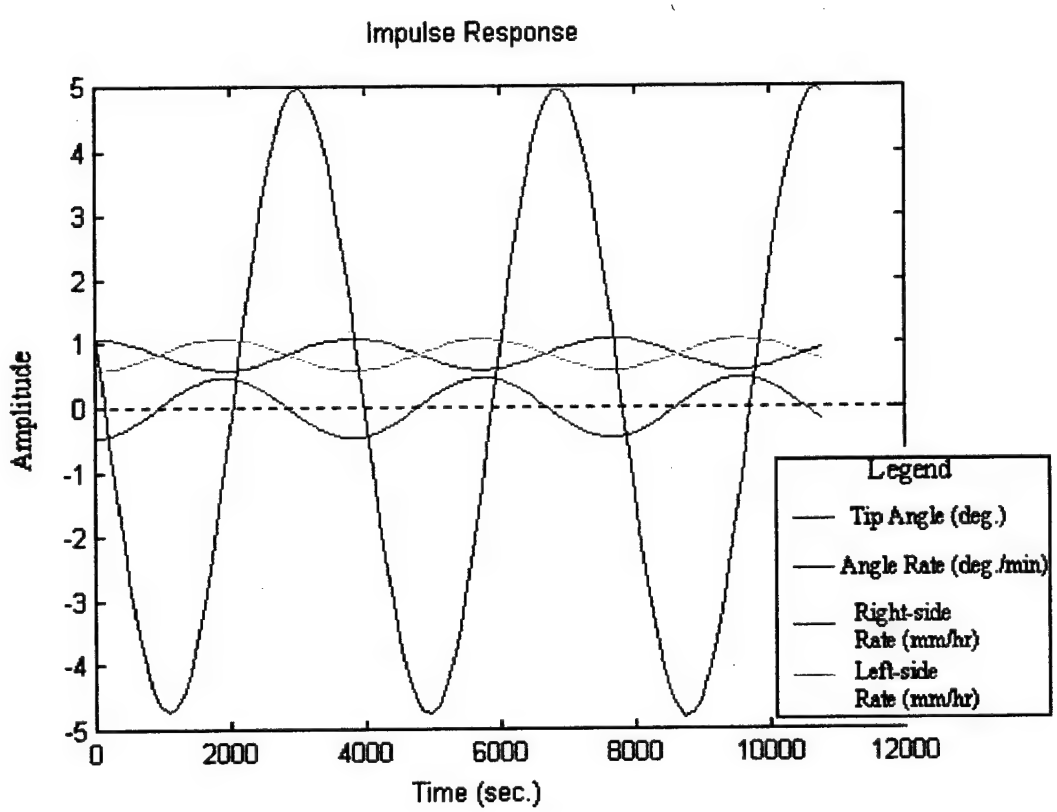

Figure 4.24 - S-domain Model of Circumnutating, Vertical Root

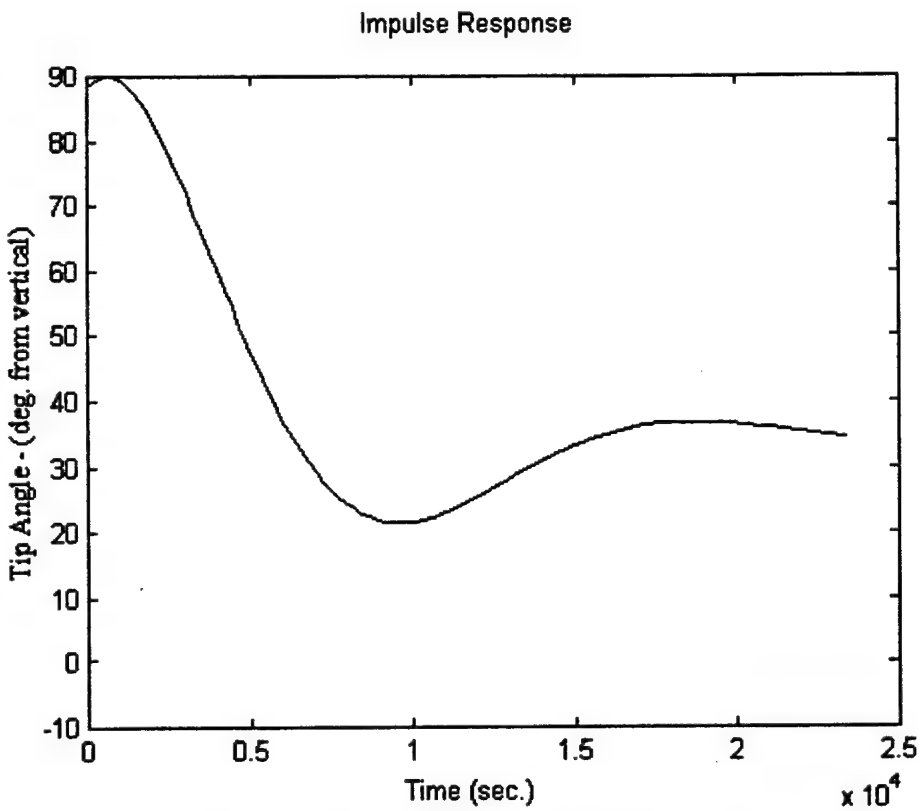

Figure 4.25 - S-domain Model of Graviresponding Root
Only the tip angle is plotted in this figure since the growth and angular rates were too small in magnitude to appear with this scale.

The transfer functions for the root tip angle, angular rate, upper-side length, lower-side length, upper-side growth rate, and lower-side growth rate are numbered #1 through #6, respectively. For the vertical, circumnutation model only:

$$\#1: \frac{1.181\, s^2 - 0.007685\, s - 9.852e\text{-}008}{s^3 + 5.54e\text{-}005\, s^2 + 2.679e\text{-}006\, s + 1.538e\text{-}010}$$

$$\#2: \frac{-0.4597\, s^2 - 0.003186\, s + 1.684e\text{-}007}{s^3 + 0.006923\, s^2 + 2.67e\text{-}006\, s + 1.854e\text{-}008}$$

$$\#3: \frac{19.99\, s^2 + 0.0008421\, s + 5.189e\text{-}005}{s^3 + 2.726e\text{-}005\, s^2 + 2.594e\text{-}006\, s - 2.834e\text{-}011}$$

$$\#4: \frac{20.01\, s^2 - 0.0005967\, s + 5.28e\text{-}005}{s^3 - 3.786e\text{-}005\, s^2 + 2.64e\text{-}006\, s - 2.881e\text{-}011}$$

$$\#5: \frac{1.079\, s^2 - 1.709e\text{-}006\, s + 2.248e\text{-}006}{s^3 - 6.671e\text{-}007\, s^2 + 2.697e\text{-}006\, s + 4.898e\text{-}013}$$

$$\#6: \frac{0.5798\, s^2 + 1.885e\text{-}005\, s + 2.215e\text{-}006}{s^3 + 8.154e\text{-}006\, s^2 + 2.664e\text{-}006\, s + 4.799e\text{-}012}$$

For the graviresponse model:

$$\#1: \frac{88.5\, s^2 + 0.03495\, s + 5.081e\text{-}006}{s^3 + 0.0003336\, s^2 + 1.496e\text{-}007\, s - 6.463e\text{-}015}$$

$$\#2: \frac{0.1553\, s^2 - 0.0004261\, s - 2.332e\text{-}007}{s^3 + 0.0008018\, s^2 + 3.055e\text{-}007\, s + 7.003e\text{-}011}$$

$$\#3: \frac{20.02\, s\text{^}2 + 0.008509\, s + 2.401e\text{-}006}{s^3 + 0.0004156\, s^2 + 1.114e\text{-}007\, s - 1.075e\text{-}012}$$

$$\#4: \frac{20.02\, s^2 + 0.005771\, s + 3.745e\text{-}006}{s^3 + 0.0002741\, s^2 + 1.874e\text{-}007\, s - 1.9e\text{-}012}$$

$$\#5: \frac{0.7637\, s^2 + 0.0006934\, s + 3.697e\text{-}008}{s^3 + 0.0004966\, s^2 + 7.249e\text{-}008\, s - 8.661e\text{-}013}$$

$$\#6: \frac{0.924\, s^2 - 1.092e\text{-}006\, s + 1.551e\text{-}007}{s^3 + 0.0002955\, s^2 + 2.434e\text{-}007\, s - 2.554e\text{-}012}$$

If both the circumnutational and gravitropic simulations are modeled, the DG/C routine user must alter the model order requested in the final lines of the GROWTH.M script file. Usually, a 2nd-order numerator and 3rd-order denominator

are satisfactory for the Prony Method, but if seeking a model of the combined responses, the user must change the request to 5th-order numerator and 6th-order denominator. Figure 4.26 shows the s-domain model results alongside the actual tip angle response from the simulation. Residuals are less than 2 degrees per simulation time point (every 10 minutes).

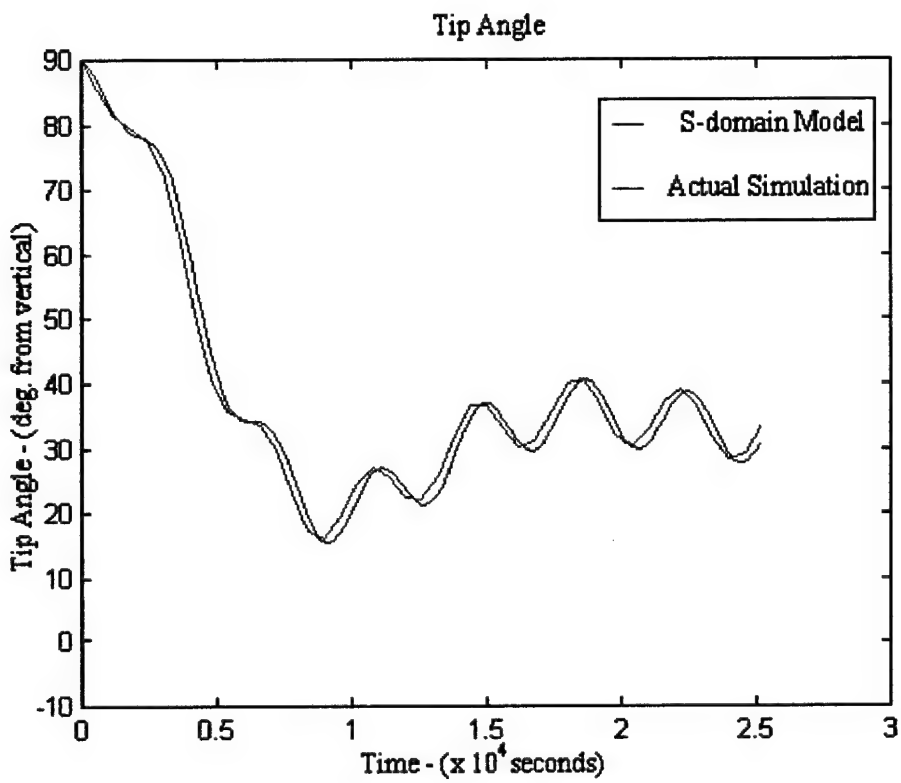

Figure 4.26 - S-domain Model of Both Circumnutation and Gravitropism

The response functions are as follows:

#1:

$$\frac{90s^6 + 0.03435s^5 + 0.002705s^4 + 8.972e\text{-}7s^3 + 6.472e\text{-}9s^2 + 2.483e\text{-}12s + 3.591e\text{-}16}{s^7 + 0.0003935s^6 + 3.026e\text{-}5s^5 + 1.018e\text{-}8s^4 + 7.795e\text{-}11s^3 + 2.443e\text{-}14s^2 + 1.097e\text{-}17s + 2.079e\text{-}25}$$

#2:

$$\frac{-0.31s^5 - 0.0008071s^4 - 8.268e\text{-}6s^3 - 2.313e\text{-}8s^2 + 7.503e\text{-}12s - 3.603e\text{-}14}{s^6 + 0.0003934s^5 + 3.026e\text{-}5s^4 + 1.018e\text{-}8s^3 + 7.795e\text{-}11s^2 + 2.443e\text{-}14s + 1.097e\text{-}17}$$

#3:

$$\frac{19.99s^4 + 0.01255s^3 + 5.635e\text{-}5s^2 + 3.299e\text{-}8s + 7.082e\text{-}12}{s^5 + 0.000616s^4 + 2.802e\text{-}6s^3 + 1.624e\text{-}9s^2 + 3.237e\text{-}13s - 3.075e\text{-}18}$$

#4:

$$\frac{20.07s^4 + 0.008022s^3 + 5.751e\text{-}5s^2 + 2.151e\text{-}8s + 1.006e\text{-}11}{s^5 + 0.0003886s^4 + 2.87e\text{-}6s^3 + 1.034e\text{-}9s^2 + 5.005e\text{-}13s - 5.046e\text{-}18}$$

#5:

$$\frac{0.9635s^5 + 0.00606s^4 + 4.036e\text{-}5s^3 + 4.578e\text{-}8s^2 + 7.893e\text{-}11s + 6.645e\text{-}14}{s^6 + 0.005881s^5 + 4.021e\text{-}5s^4 + 3.576e\text{-}8s^3 + 1.011e\text{-}10s^2 + 5.273e\text{-}14s + 1.409e\text{-}18}$$

#6:

$$\frac{1.1s^4 + 0.004799s^3 + 3.497e\text{-}6s^2 + 1.782e\text{-}8s + 1.833e\text{-}12}{s^5 + 0.005106s^4 + 4.69e\text{-}6s^3 + 1.359e\text{-}8s^2 + 5.421e\text{-}12s - 8.119e\text{-}17}$$

4.5 Discussion

This chapter has explored the effects of both elastic and plastic curvature of the root tip undergoing gravitropism. Indications are that little to no elastic contribution exists to root curvature during gravitropic responses. Practically all curvature is from the differential growth of cells between the upper-side of the root as compared to those on the lower-side of the root. Therefore, no further work was accomplished toward elastic modeling and all modeling efforts were directed toward differential growth with the analogous model set chosen as bimetallic bending, or differential expansion of metals with dissimilar thermal expansion coefficients.

The differential expansion of two layers separated by a constant distance produces Equation 4-4 as the defining relationship of the differential growth to curvature produced along the layers. This model set applies well to the plant root since the diameter remains constant while elongation rates differ between the upper- and lower-sides during gravitropism. During gravitropic curvature, the root does not curve equally along its entire length as it seeks to realign its tip with the vertical. Instead, localized curvature is created in the elongation zone (4-6 mm basal from the tip) while the meristem and maturation zones show little to no curvature. Therefore, appropriate resolution of the curvature must include growth data for specific regions of cells, while data on individual cell layers would provide the best possible resolution. Some historical data was gathered that appeared detailed enough to provide such resolution, allowing a more exact simulation of the distribution of curvature along the entire root.

The modeling effort used RELEL data which records the growth along specific regions of the root in the form of percentage growth over time, where the percentage is based on that section's length. This data format lends itself well to modeling in a "finite-element" fashion. The root can be divided up into discrete length segments and the RELEL data is approximated as a Gaussian distribution with a maximum ($RELEL_{max}$), maximum location from the root tip (μ), and a standard deviation or "spread" of data (σ) as the 3 parameters that define the distribution of growth. The RELEL curve, a 3-dimensional surface plot dependent upon both distance from the root tip and circumferential position around the root cylinder, is then integrated for a

specific discrete length segment to determine that segment's growth rate. Growth of each segment is propagated in this fashion by the use of a Differential Growth and Curvature (DG/C) routine in MATLAB.

The results of the RELEL modeling and the simulations of the DG/C routine were tested and analyzed for vertical and gravistimulated conditions and RELELs based on a single researcher along with simple averages and weighted averages of various historical data. The DG/C routine produces curvature profiles very comparable to those witnessed with actual roots. Even peculiar variations, such as S-shaped curvatures, can be duplicated by fine-tuning the RELEL models within the DG/C routine. The results give an extreme appreciation for the sensitivity of the root's curvature profile to the RELEL parameters. Very small changes in one or extremely small changes in multiple parameters ($RELEL_{max}$, μ, or σ) can greatly affect the subsequent curvature appearance of the root.

Time-variability was introduced into the model both by applying a exponentially decaying, sinusoidal variant and by directly programming the empirical results from the only laboratory found that produced a time history of RELEL-style information. Both gave comparable results with the simulated differential growth rates and curvature history of the empirical model nearly duplicating the empirical data for these parameters. The success of this model and its dependence on detailed RELEL data calls for further research to increase the RELEL resolution. As is outlined in Chapter 8 of this thesis, more elemental growth data, for specific temperatures, humidities, and growth media must be obtained. The temporal and spatial resolution

of the data must be as fine as possible allowing more precision in the RELEL model. The need for varying the environmental conditions will allow the formulation of "Growth Coefficients" that quantify the effect of each environmental factor and allow modeling of such factors.

Circumnutational effects were added to the model by creating a second RELEL function that provides vertical, steady-state parameters and the circumnutation perturbations experienced by the RELEL curve. Gravitropic changes to the RELEL curve are also treated as perturbations to the vertical, steady-state conditions. The modeling and simulation results exposed two points of interest. The effect of circumnutational perturbations was found to have nearly 60% of the effect on both RELEL and elongation rates as does the gravitropic perturbations. Therefore, circumnutation produces similar changes in elongation rates as to those witnessed during gravitropism. The only reason that similiarly large curvatures are not witnessed in circumnutation is that the period of the circumnutation is a half to a third as compared to the gravitropic reaction. This higher frequency prevents large curvatures from accumulating under circumnutation. The similiarity in RELEL perturbations and differential elongation rates highlights a need to re-examine the relationship between circumnutation and gravitropism.

Finally, in order for the differential growth model to be included and compared with the other mechanisms of the overall gravitropic response, the RELEL model and DG/C simulation results were reduced and simplified in order to create a transfer function model that can represent the differential growth mechanism with curvature as

its output. The time responses of the six outputs (tip angle, angle rate, upper-side length, lower-side length, upper-side growth rate, and lower-side growth rate) are reduced to a z-domain response function using Prony's Method. This z-domain filter is converted to s-domain using the time increment as the sampling period. Examination of the impulse responses of this simplified, linear, time-invariant (LTI) models confirms their accuracy in modeling the RELEL-based simulation. These transfer functions are examined again in Chapter 6.

4.6 Conclusions

The RELEL-based model produces results with relatively high resolution. The data produced by the simulation compares favorably with both historical summaries and empirical data. The visual aesthetics of the output provide the user with both an immediate spacial representation of a bending root and root parameter time response data such as angular rate and elongation rates. However, since any model is only as good as the data upon which the model is constructed, further RELEL refinement and quantification is highly desireable. Additionally, such RELEL quantification should include an attempt to correlate RELEL data with environmental conditions such as temperature, humidity, ionic content, and nutrient content. This would provide an additional link between the differential growth mechanism and the transduction mechanisms in the overall gravitropic model.

CHAPTER 5

THE OVERALL GRAVITROPIC RESPONSE

5.1 Introduction

The gravitropic response in its entirety can be divided into an infinite number of subsystems or described in an equal number of methods. One possible method is to develop a sequence of mathematical equations which duplicates the root's gravitropic time response. This "imitative" approach provides a good model with which to predict the response of the imitated plant root. As with all models, these imitative models are of various complexity. Equation 5-1 simulates gravitropic curvatures that return the root to vertical (0^0) or the shoot to vertical (180^0) while Equation 5-2 adds the possibility of the root (or shoot) curving to an liminal angle other than vertical thereby simulating a change in the plant's gravitropic set-point (Stockus, 1994).

$$\ddot{\alpha} = k * \sin[\alpha(t-\tau)] * g(t-\tau) - k_d * \dot{\alpha} \qquad (5\text{-}1)$$

$$\ddot{\alpha} = (k_1 * \sin[\alpha(t-\tau)] + k_2 * \cos[\alpha(t-\tau)]) * g(t-\tau) - k_d * \dot{\alpha} \qquad (5\text{-}2)$$

where: k & k_1 are coefficients weighting the positive-gravitropic component, k_2 weights the non-gravitropic component, τ is the time-delay prior to curvature, $g(t-\tau)$ is the gravitational force at time $(t-\tau)$, and k_d is a diffusion coefficient which represents a loss of physiological bending signal (damping). The root cap angle from vertical (α) is solved numerically based on the above parameters and those parameters are altered until the simulated curvatures approximate actual empirical data. The parameters can be found by various parameter finding techniques such as least squares

approximations. For example, with k=-535, τ=20 minutes, and k_d=3.21, Equation 5-1 produces the result shown in Figure 5.1.

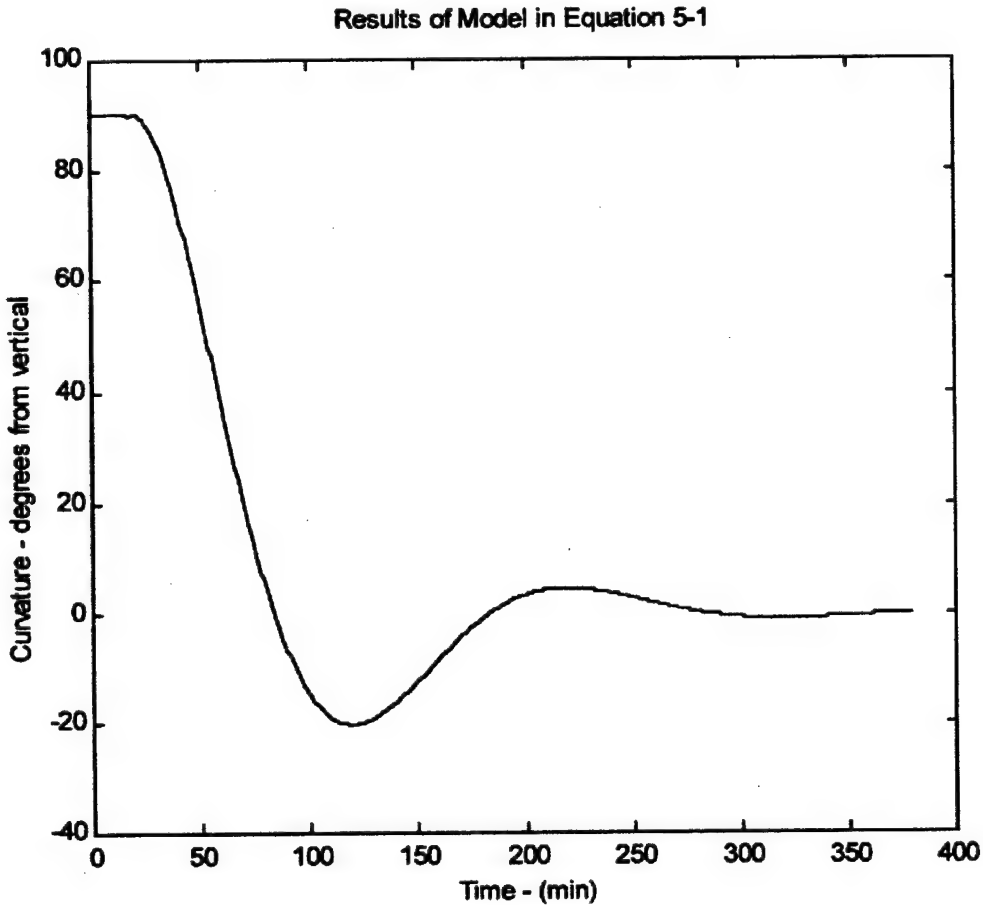

Figure 5.1 - Simple Imitative Model Time-Response Curve

This type of modeling can accurately duplicate and predict a plant root graviresponse, but provides a low level of insight into the actual physical parameters of the system. For example, the value for k_d is found and this represents a loss of a physiological signal during rapid curvature rates, but we do not know what that signal physically is or what mechanism creates this damping. More insight might be attained by breaking the entire response into smaller subsystems, or blocks, that can be more easily described.

For many decades the entire gravitropic system has been viewed as consisting of three separate parts; the perception of gravity (the sensor), the transduction of this signal, and the actual differential growth response. This thesis accepts and adopts this classic formulation. Often times, perception is further broken into susception and perception, where susception is the actual work of gravity on the sensor that the sensor can then perceive. Continuing on an imitative approach to the model, but dividing the imitative model into smaller parts could lead to further insight into the mechanisms at work during gravitropism. The model in Equation 5-1 can be divided into four mechanisms; susception, perception, transduction, and growth response. Each of these parts produces its own physiological signal that may or may not be physical present in the actual root, but serves as a means to imitate the overall response (Stockus & Moore, 1996).

$$\begin{aligned}
\text{Susception:}\quad & y_s = k_s * g(t) \\
\text{Perception:}\quad & y_p = k_p * \sin[\alpha(t)] * y_s \\
\text{Transduction:}\quad & y_t = k_t * y_p(t-\tau) \\
\text{Response:}\quad & \ddot{\alpha} = k_r * y_t - k_d * \dot{\alpha} \\
\text{Overall:}\quad & \ddot{\alpha} = k_r * k_t * k_p * k_s * \sin[\alpha(t-\tau)] * g(t-\tau) - k_d * \dot{\alpha} \qquad (5\text{-}3)
\end{aligned}$$

Note that Equation 5-3 is equivalent to Equation 5-1 where the original coefficient, k, has now been divided into four coefficients, each associated with the individual mechanism. Again, even though this technique provides more resolution, it is still imitative in nature. The gravitropic response is still treated as a "black box" where we know only what is put in and what comes out. Even though the "black box" has been divided into four parts, those parts are arbitrary in nature and the output of each part may or may not actually represent a true physical mechanism in the plant.

Although the complexity of the entire gravitropic process is so great that this "black box" technique is necessary, there is some knowledge of the gravitropic process and its internal order of events that can refine the black box closer to what may physically be present within the root. That is the goal of this thesis. This chapter's goal, although relying heavily upon "black box" approaches, attempts to provide a more specific general structure (model set) to the root's overall gravitropic response.

5.2 Objective

The objective of this chapter is to develop an empirical model of the plant root's overall gravitropic response. This development requires both mathematical modeling and experimental data acquisition. The information required includes the time response data and characteristics of the plant root's graviresponse. An extensive database of historical research exists on the gravitropic responses of various species of plants. Quantitative response data sets are available from numerous researchers on *Zea mays* (Moore, 1987; Ishikawa *et al.*, 1991; Barlow *et al.*, 1993; Evans & Ishikawa, 1997). Using MATLAB's System Identification and Control System Toolboxes, models were developed that fit these historical data. Although some responses can be adequately modeled using a first order system, most response data show second-order characteristics. Higher order models obtain the lowest residuals (difference between model and empirical results).

To further refine and develop the model, new gravitropic responses were acquired. *Zea mays* (maize) seedlings in various stages of growth (age) were investigated. Still photography, taken at 5-10 minute intervals over 6 hours, recorded

the responses. Photographs were scanned and analyzed using NIH Image software. Various second-order response specifications such as time constant, rise time, settling time, and steady-state error were correlated with the specimen age. Figure 5.2 diagrams the process followed to complete this, the third objective of the thesis.

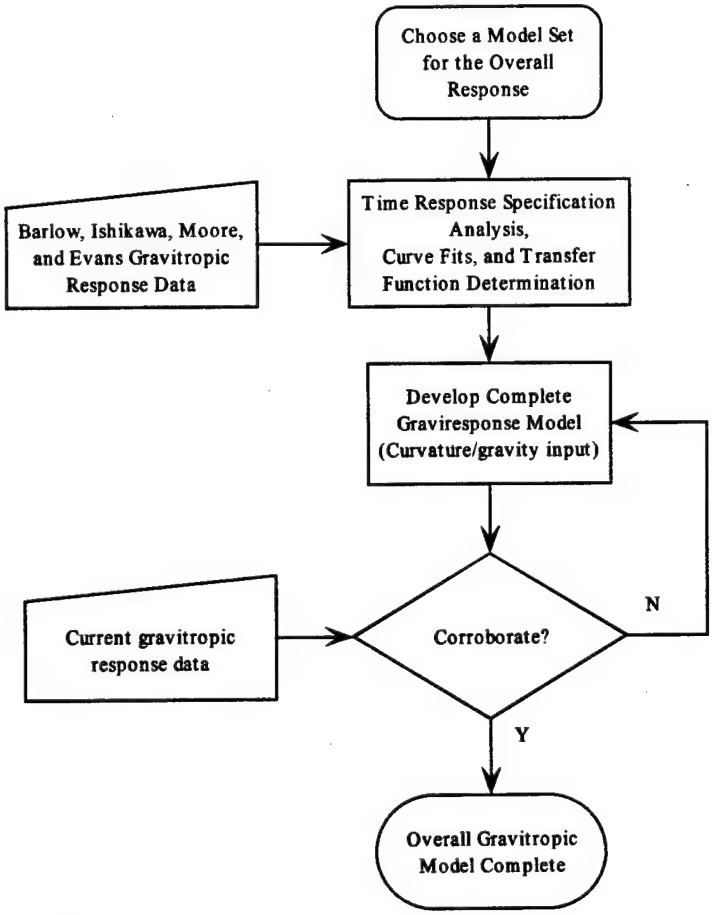

Figure 5.2 - Flowchart for Objective 3

5.3 Theory Development

A model of the root's graviresponse can be built using one of two possible approaches. Most attempts to model the plant root's gravitropic response have been accomplished by using mathematical imitations of the root's curvature-over-time response characteristics. This approach produces an imitational model of the

graviresponse that ignores, or, at least, relegates as superfluous the physical parameters of the system such as hormone concentrations, cellular elongation rates, sensor output, and other physical parameters making up the complete gravitropic response. Instead, the imitational approach focuses on the end-state of segments of the response and the information those segments produce that may be used by the following segment. This information is developed independently of any real physical processes occurring within the plant root. This approach can duplicate and predict the graviresponses of the root without going into detail on how the response occurs, but it can give little or no insight into the mechanisms at work in accomplishing the response.

In the second approach, a systems engineering approach, specific characteristics of various mechanisms of the overall response system are developed and analyzed as specific model parameters. Although more complex, these techniques can provide insight into the underlying physical mechanisms at work within the overall graviresponse system. The first approach, known as a "black box," relies little on physical insight and knowledge of the involved mechanisms and seeks to reconcile the model's input-output relationships to those known to occur with actual roots under gravitropism. The second approach, known as a "white box," begins with the selection of a "model set," or a general design as to the structure and interconnections of the system(Schoukens & Pintelon, 1991). This general design is then matured by choosing subsystem designs of varying structure, order, and interconnection to the whole. A beginning form of model set is obtained from the initial proposals as to the chain of events involved in the response.

Based on earlier observations by Charles Darwin, Haberlandt proposed that the starch-filled amyloplasts of the central root cap served as statoliths (Haberlandt, 1900) and the Cholodny-Went Theory connected this perception of gravity to an auxin differential and differential growth in the root's elongation zone causing the bending toward gravity (Went & Thimann, 1937). This leads to a simple model set shown in Figure 5.3.

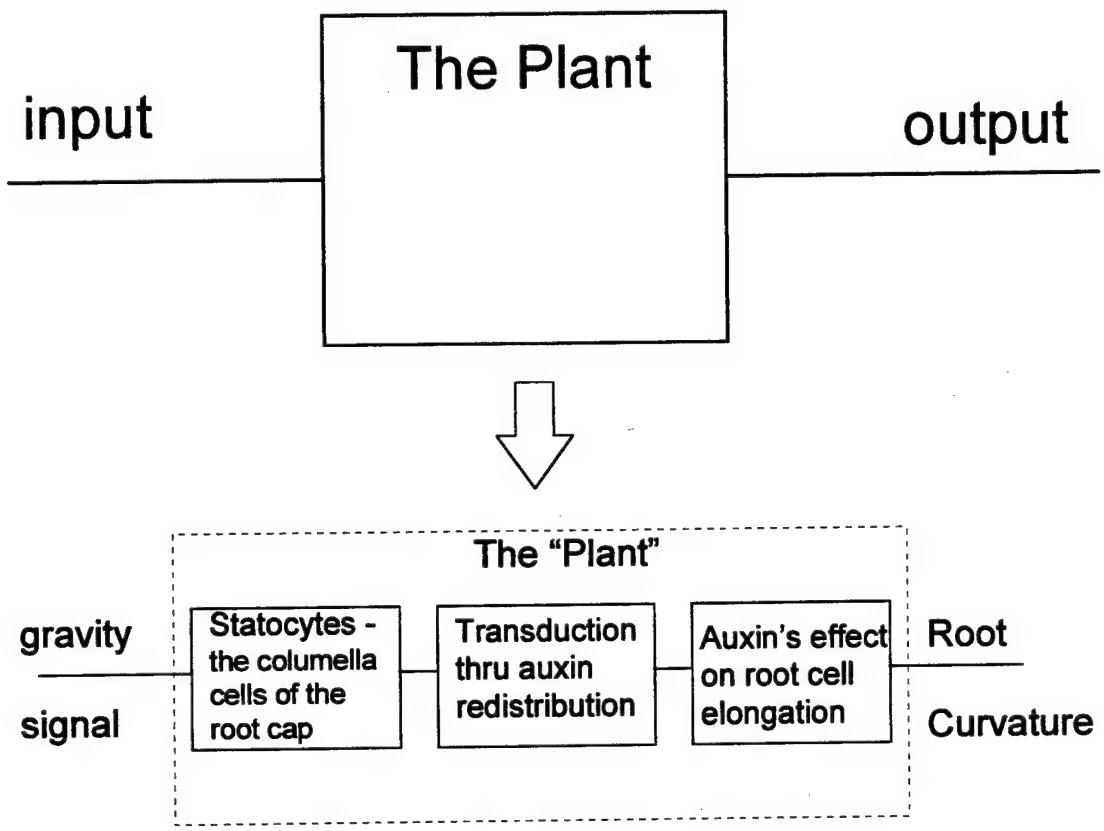

Figure 5.3 - Simple Model Set for Gravitropism

Evidence that was outlined in Section 2.4.1 of this thesis leads to modifications of this initial model set. The existence of cytoskeletal interaction with the statoliths within the columella cell seems very likely given the evidence shown in Chapters 2 and 3. Even though this interaction appears likely, the effect of this interaction, which

begins the sequence of transduction, is less known. One possible chain of events that could result from the movement of amyloplasts in response to gravity is pictured in Figure 5.4, a further modification of the initial model set. Although this represents only one of numerous possibilities, it shows the progress (and complexity) that results with further refinement of the model set.

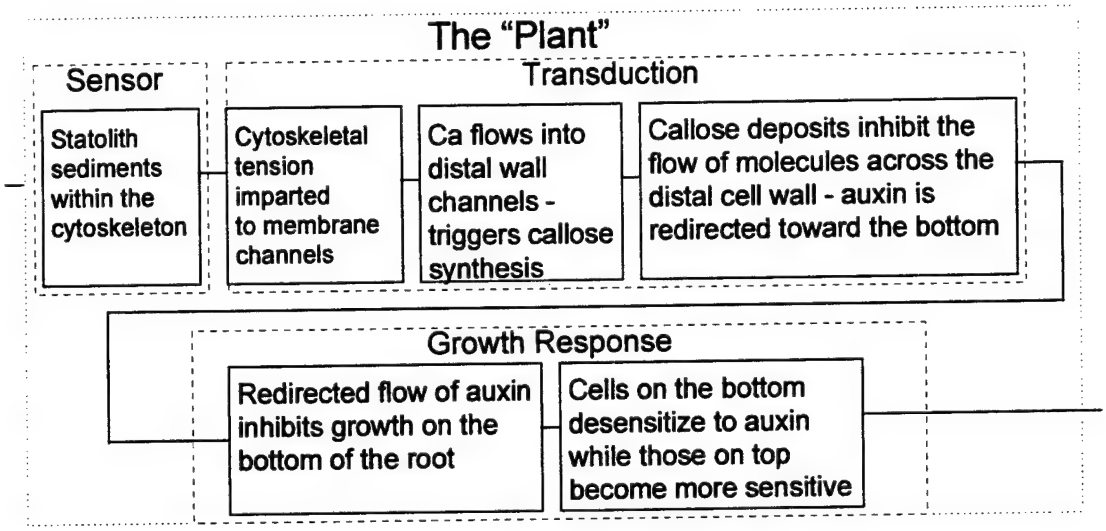

Figure 5.4 - Model Set with Further Details

The order of events that occur during the gravitropic response provides some guidance as to the general form of model set to develop. Table 5-1 provides a summary of some of the events that are found to occur during the graviresponse of the plant root. Further detail for these events can be found in Chapter 2.

Table 5.1 - Order of Events During Gravitropism

Order	Event	Context	References
1	Statolith Sedimentation	immediate movement after placing horizontal - 5 mm/sec full sedimentation NOT required for response	(Sack *et al.*, 1986) (Sievers *et al.*, 1989) (Sack *et al.*, 1985)
2	Cell Membrane Potential Changes	8 sec in *Lepidium* 30 sec in *Vigna mungo* 1 min in *Zea mays*	(Behrens *et al.*, 1985) (Ishikawa & Evans, 1990) (Ishikawa & Evans, 1994)
3	Current Changes	few minutes in *Lepidium* / 2-6 min in *Zea mays* 3-4 minutes in *Zea mays*	(Moore & Evans, 1986) (Bjorkman & Leopold, 1987) (Weisenseel & Meyer, 1997)
4 ??	Ca^{++} flux	distal wall accumulation within 5 min in maize 1.5:1 top:bottom accumulation in the mucilage after 2 hours	(Moore & Fondren, 1986) (Moore, 1986) (Moore & Fondren, 1988) (Weisenseel & Meyer, 1997)
5 ??	pH changes	8-9 min in *Phleum pratense* and *Lepidium* - proceeds differential growth by 10 min *Zea mays* produces a 4.5 pH prior to curvature on convex side (acid growth begins at 5.0)	(Weisenseel *et al.*, 1992) (Weisenseel & Meyer, 1997) (Taylor *et al.*, 1996)
6 ??	Auxin Gradient	15-20 minutes in maize - quantity only NOT flow rate - cap NOT elongation zone auxin rates of 1 cm/hr time to establish auxin gradient of exogenously applied auxin roughly equal to the time curvature appears	(Evans, 1991) (Evans & Ishikawa, 1997) (Zieschang & Sievers, 1991) (Young *et al.*, 1990)
7	Differential elongation / curvature	20-30 minutes in maize	(Barlow *et al.*, 1993) (Evans & Ishikawa, 1997)

The questions marks next to event numbers 4, 5, and 6 in Table 5.1 indicate the uncertainty of the specific order of these events relative to each other.

Experimental resolution accomplished in these areas is low enough to demand a level of uncertainty as to which of these specific events occurs first. What is clear is that initial events occur quickly after gravistimulation; far too quickly to be caused by hormonal (auxin) redistribution as the simple Cholodny-Went model would indicate. Therefore, the following modification to the model set is proposed.

Because of the events that occur very rapidly following statolith sedimentation, an ionic pathway, in parallel with the classic hormonal pathway is introduced into the model set. Figure 5.5 diagrams this modification. Total root curvature is the integration of differential elongation growth caused by both dual path mechanisms along the length of the root. It is also likely that these paths individually contain their own feedback mechanisms (i.e. catabolic regulation, etc.) that help govern their characteristics, but these mechanisms remain beyond the scope of this thesis. Response characteristics differ greatly between these two parallel paths. For example, the relatively rapid appearance of membrane potential changes and current fluctuations following gravistimulation lead to the conclusion that the time constant involved with the ionic path is small compared to that of the hormonal path since auxin gradients seem to occur much more slowly. This model is analogous to other models of biological mechanisms such as the maintenance of arterial blood pressure or neuron action. Blood pressure maintenance has short-term autonomic nervous system mechanisms, medium-term heart rate mechanisms, and a third, very large time constant hormonal controlled mechanism of the kidneys (Milhorn, 1966). The motor neuron also displays this dual response modality with a short-term electrical response and a longer-term hormonal response for bridging the neuronic cleft (Kernan, 1997).

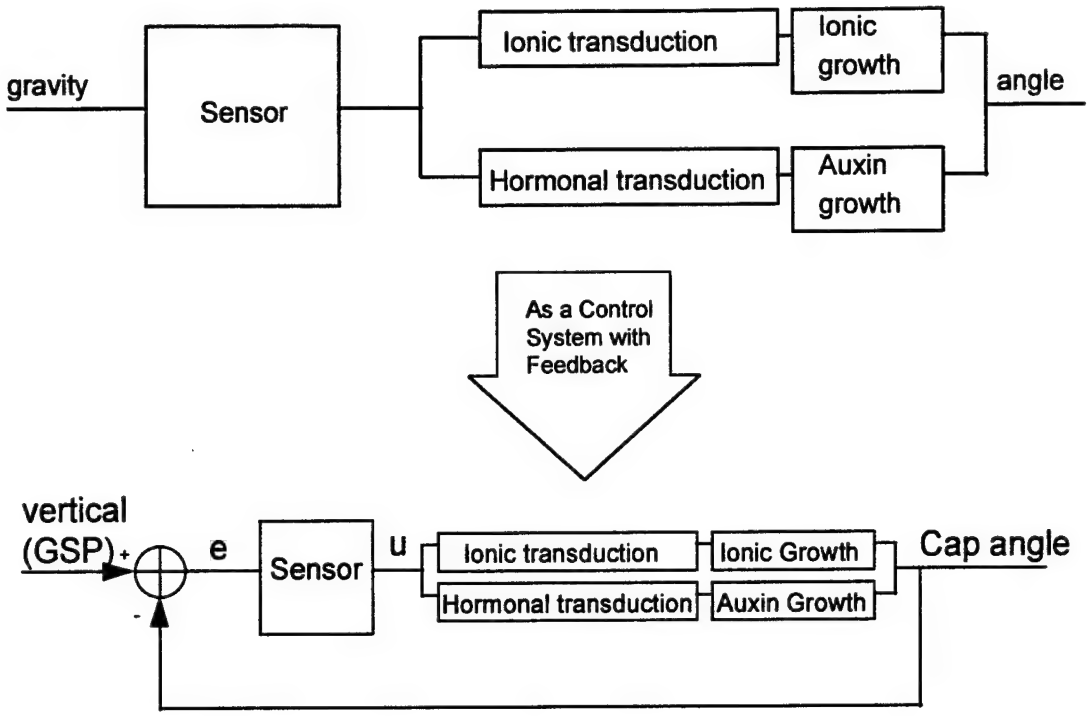

Figure 5.5 - Dual Path Model Set for Gravitropism
This dual path model allows for a parallel path for transduction and growth. The ionic path having a smaller time constant than the hormonal path. The GSP (gravitropic set-point) remains as vertical (0 degrees) in this model. The error signal (e) is the difference between the GSP and the actual angle of the root cap. The sensor produces a control signal (u) which is required for both of the parallel paths.

A gravitropic response path independent of the classical, chemical hormone path has been proposed at various times in the past few years, but primarily from the basis of the sensor. Dr. Barbara Pickard has proposed for many years that the root as a whole can function as a sensor (Pickard & Ding, 1992; Pickard & Ping Ding, 1993; Pickard, 1994). Her theoretical plasmalemmal control centers serve as mechano-sensors that detect minute changes in the stresses imposed on individual cell membranes. These sensors are then integrated over the entire root allowing the root as a whole to serve as a gravity sensor. While helping to explain various phenomena that the classic Cholodny-Went theory cannot, such as the rapidity of the growth

response in a specialized zone of cells millimeters from the classic sensor, the efficacy of the Pickard hypothesis remains to be shown in a number of areas. An example of such an area includes determining whether gravity imparts large enough changes in stress on individual cell membranes distinguishable above the local noise created by numerous sources such as the plant cell's own modulation of turgor stress. A leading research scientist has also concluded that some alteration to the classic Cholodny-Went theory is required. Citing phenomena such as those discussed in Table 5.1, Dr. Michael Evans also concludes that either gravity must be directly perceived by individual cells throughout the root or the signal must move from the root cap to the root proper much more rapidly than can be accounted for by known auxin transport rates (Evans, 1992).

Further arguments that support the need for a parallel response path with ionic versus hormonal properties comes from work on characterizing hormonal pathways and induction of gravitropism in agravitropic species. It is assumed that only two physical pathways exist by which substances can move from the root cap to the root proper; a symplastic pathway through plasmodesmata, and an apoplastic pathway through cell walls and mucilage. After studying the morphology of the Yellow Dent cultivar of *Zea mays* L., the symplastic pathway is found to be restricted to the center of the cap, occurring only between protodermal cells and meristematic cells, and only involves approximately 400 protodermal cells covering 110,000 square microns (0.11 square mm) (Moore & McClelen, 1989). Therefore, if gravitropic effectors move from the root cap to the root symplastically, they must move exclusively through the meristematic cells in the center of the cap. Since this is opposed by extensive

experiments showing the opposite is true (see section 2.4.3.1) and this area, functionally only 10% of the entire root-root cap interface, cannot serve to provide a pathway for all the effector running both into and out of the root cap, another pathway must exist. For these same reasons, the Moore group suggests an apoplastic pathway through the mucilage as detailed in section 2.4.3.1 of this thesis. This apoplastic pathway was characterized on work with an agravitropic cultivar of maize and was found to likely be the mucilage that covers the root tip (Moore *et al.*, 1990). The agravitropic cultivar became as graviresponsive as its parent wild-type (Kys) with only the application of mucilage (lacking in the agravitropic) or K-Y Jelly to the root-root cap junction. These media, found to accumulate large amounts of calcium and share electrical properties, established normal electrical patterns and time responses following gravistimulation. These data force a conclusion that a dual path model set must be investigated. This thesis concentrates on the classic sensor (Chapter 3) and creates a model set (Figure 5.5) that provides a path for more rapid signal transduction and differential growth by a means independent of the classic hormonal (auxin-based) path. This chapter describes this overall model by empirical means. First, by examining historical gravitropic time responses and then by examining the raw data of new time responses, the time response characteristics of this overall model are determined, examined, and discussed.

5.4 Experimental and Mathematical Procedures

Both experimental and mathematical techniques were used to accomplish the objective of this chapter. Laboratory materials and methods along with computational

software developed to visualize and analyze the empirical data are discussed in the following subsections.

5.4.1 Experimental Methods

Two cultivars, Yellow Dent and Merit, of corn (*Zea mays*) were obtained from the East Texas Seed Company (Tyler, Texas, {800}888-1371). Seeds were disinfected and washed for 6 minutes using 5.25% NaOCl and 1.0% Triton X-100 solution (100 μl of Triton per 10 ml of commercial bleach) by continuously agitating the seeds in solution. Following the wash, the seeds were rinsed using 6, 2 minute washes of sterilized, distilled water (dH_2O) under a sterile hood. Six seeds were imbibed between 2 sheets of filter paper (90mm Whatman Qualitative #1) in a 100 mm x 15 mm Petri dish using 5 ml of sterilized, ultra-filtered water. The filter paper, dH_2O, and milli-Q water were sterilized by autoclave using a 10 minute wet-cycle. Petri dishes were sealed with Parafilm™ sheets and placed in a vertical position. This method of imbibing produced less than one fungal contamination per 100 petri dishes (600 seeds). For the same reasons as those outlined in section 3.4.1 of this thesis, all seedlings were used within 5 days of germination.

The vertical Petri dishes were kept at 25 ± 1.5^0C. Germinating seeds of Yellow Dent remained in darkness while those of Merit were placed under 1000 lux fluorescent lighting (4 Duro-Test 40W Vitalites). Germination of both cultivars occurs at approximately the 36 hour point after imbibing. Vertically growing, primary roots in three different length categories were selected for study. The three categories

were 20-29 mm lengths, 30-39 mm lengths, and 40-55 mm lengths. Growth rates of roots within the germination dishes ranged from 1 to 2 mm/hr.

Selected seedlings were then transferred to a plant Growth Chamber/Shadow Box(GC/SB) constructed to hold individual seedlings, maintain a constant growth environment, and provide proper photographic conditions for recording the plant root gravicurvatures. Figure 5.6 shows the details of this growth chamber. The chamber provided a temperature of 25 ± 1.5^0C and relative humidity (RH) of $92.5 \pm 2.5\%$.

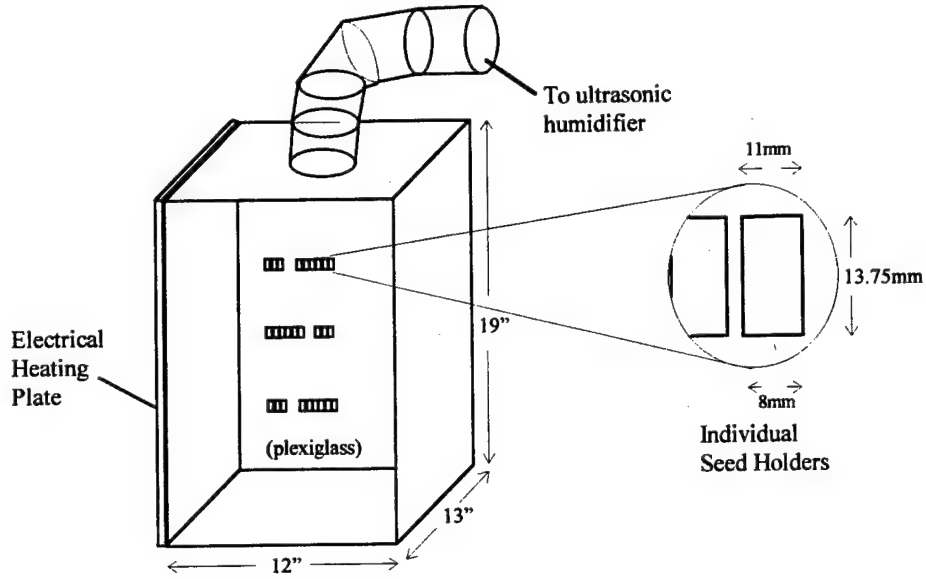

Figure 5.6 - The Plant Growth Chamber/Shadow Box (GC/SB)
The entire chamber is placed within a temperature controlled room (25^{0}C), but the electrical heating plate is required to counter the slightly cooler, humid air coming from the humidifier. The vinyl tube at the top of the chamber leads to the ultrasonic humidifier output vent. Individual seed holders are cut from large, wide orifice, 5ml pipet tips allowing entry of the seedling from the top with the bottom slightly smaller and friction fitting the seed, thereby holding the entire seedling in the mounted position. The back of the chamber onto which the seed holders are adhered is a translucent plexiglass, behind which are 2, 50 Watt incandescent bulbs which are switched on to provide a shadow box effect for imaging the roots.

After placing the seedlings in the GC/SB, the roots were allowed to adapt by continuing to grow vertically for 3 hours. During this time digital imagery was taken to analyze the steady-state activities of the root in the vertical position. Digital imagery was accomplished with a Fuji MX-700 megapixel digital camera. This camera produces 1280x1024 pixel, 24-bit color images and focuses from 3.5 inches to infinity automatically with f-stop values ranging from 3.5 to 8. Serial transfer of the images were made to a Power Macintosh and NIH Image (ver. 1.67) software was used to analyze the root positions. Photographs were taken at a distance of 177.8 mm which

provided a subject field of view of 177.8 mm x 152.4 mm (horizontal x vertical). This provided 7.2 pixels/mm x 6.7 pixels/mm for root analysis. For practical matters of determining the angle of the root cap which is only approximately 1 mm in length, this resolution, along with the technique of angle measurement from NIH Image, produced an angular precision of approximately 5 degrees.

A gravistimulation of 90 degrees was applied to the roots by turning the GC/SB 90 degrees. Pictures were taken immediately following gravistimulation and every 10 minutes thereafter for a total of 6 hours. After processing the digital photos in NIH Image, the angle of the root cap was determined by recording, then analyzing, the pixel coordinates of the endpoints of a line that ran tangent to the root cap/root proper junction. Figure 5.7 details the technique. The pixel coordinates are then processed and analyzed by various computational techniques.

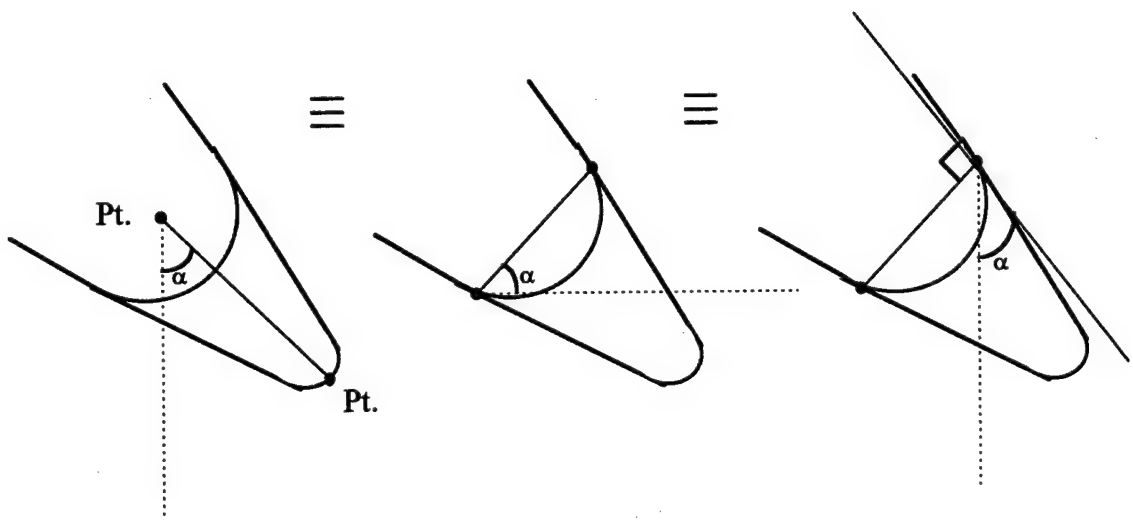

Figure 5.7 - Measurement of the Root Cap Angle
Three equivalent techniques for measuring the angle of the root cap with respect to vertical. Because of the contrast of the digital pictures, the first technique was used most often. The x-y coordinates of the two endpoints of the line drawn through the root's quiescent center and tip were recorded using NIH Image.

5.4.2 Computational Techniques

Processing of the digital pictures of root graviresponses began with the use of NIH Image software. The x-y coordinates of the two endpoints from Figure 5.7 were recorded. Each set of coordinates was separated with the time between images and this coordinate/time data was stored in data files. Each root's individual time-curvature response is recorded to separate data files with this format:

x-coordinate of Pt. 1 at time 0	y-coordinate of Pt. 1 at time 0
x-coordinate of Pt. 2 at time 0	y-coordinate of Pt. 2 at time 0
minutes to time 1	minutes to time 1
x-coordinate of Pt.1 at time 1	y-coordinate of Pt. 1 at time 0
x-coordinate of Pt. 2 at time 0	y-coordinate of Pt. 2 at time 0
minutes to time 2	minutes to time 2
etc.	etc.

These data files were then processed by a Pascal program, LABRESP.PAS (see Appendix VII). This program requires a text file (filelist.txt) that contains the names of all data files to be processed with a category designator (20 for roots in the 20-29 mm length category, 30 for roots in the 30-39 mm category, etc.) following the file name. The program reads in all the separate data file x-y coordinate data, creates a single listing of time and angle for every root processed, and then averages the time-angle information for all roots in the three length categories: 20-29 mm, 30-39 mm, and 40-55 mm. This program was run separately to process all the Yellow Dent responses and all the Merit responses.

Data files of processed data, both every single root response and the averaged responses for every root within a length category, have the following format:

time from gravistimulation (min)	angle of root cap

time from gravistimulation (min)	angle of root cap
etc.	etc.

These time response data are then analyzed using various MATLAB script files (see Appendix VIII). The first script file, "CURVEFIT.M", fits a polynomial curve to the response data until the coefficient of determination (r^2) is greater than 0.99. The coefficient of determination is defined as:

$$r^2 = 1 - \frac{SSE}{SS_{yy}} \;\; ; \;\; SS_{yy} = \sum (y_i - \bar{y})^2 \;\; ; \;\; \bar{y} \text{ - mean value}$$

$$SSE \text{ - sum of the squared errors} \equiv \Sigma(\text{residuals})^2 \equiv \Sigma(\text{polynomial fit point - actual point})^2$$

This 'best fit' polynomial is then used to determine the time response specifications of the graviresponse curve in "TRANS_FUNC.M." The input magnitude, rise time, percent overshoot, settling time, final value, and steady-state error is returned. TRANS_FUNC.M also returns a 'best fit' second-order transfer function based on the above specifications. A flag indicating whether the s-domain transfer function has 2 distinct, 2 repeated, or a complex-conjugate pair of poles is returned along with appropriate sigma or natural frequency/zeta values. "COMPENSATE.M" uses s-domain techniques to apply various 1st and 2nd order compensators to the 2nd-order transfer function to improve its fit to the experimental data. "AUTO_RESP_SPECS.M" automatically examines all individual root graviresponses found within an input file and creates a document containing all the time-domain specifications found in TRANS_FUNC.M and the frequency content of the response curve. Following use of these data analysis files, other MATLAB System Identification tools are used to create z-domain (discrete, sampled data) and s-domain

models from the individual responses. Some of these tools include the Prony discrete filter fit to a time response and the Steiglitz-McBride iteration method for ARMA modeling. MATLAB statistical data analysis tools were used to compile statistical summaries and compare data categories with the Student's t-test. Statistically significant population means were judged if the P-Value of the t-test was ≤ 0.05.

5.5 Results

The results section is divided into two subsections. The first examines the results of time response analysis on two historical studies of maize root graviresponse. This serves both as a basis for presenting the application of the system identification techniques and provides a comparison with the data acquired under the experimental procedures of this thesis. The second subsection presents these experimental results, system identification analysis, and a finalized s-domain model.

5.5.1 Historical Analysis Results

When attempting to compile a historical database of graviresponse time histories, numerous difficulties become apparent. Over one hundred years of research into gravitropism has produced very many graviresponse experiments, but many experiments use vastly different materials and methods. Although some standardization attempts have begun recently, the historical literature is full of experiments where the root angle is measured with vastly different methods, the temperature range is wide, root configurations are sometimes cantilevered and sometimes growing suspended on a media, media are of varying types, and sampling

rate of curvature angle is too low to provide precise data for system identification techniques. An example of historical data that uses the same method for "root angle" as shown in Figure 5.7, used the cantilevered root configuration which minimizes thigmotropic and media-induced reactions, and provided data with fairly high sampling rates is presented and analyzed here. This experiment (Ishikawa *et al.*, 1991) uses the maize cultivar, Merit, and was introduced in Chapter 4 of this thesis. Figure 5.8 shows the time history of the graviresponse after moving the root to 90^0 from vertical. Next, a curve is fit to the raw data until the conditions described for Equation 5-1 are met. These curves are found in Figure 5.9.

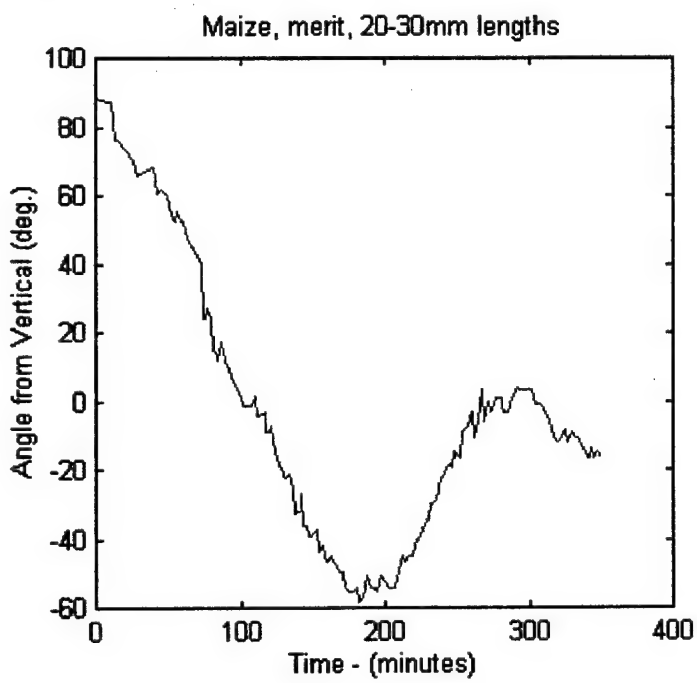

Figure 5.8 - Maize Merit Graviresponse Curve
Data from Ishikawa *et al.*, 1991.

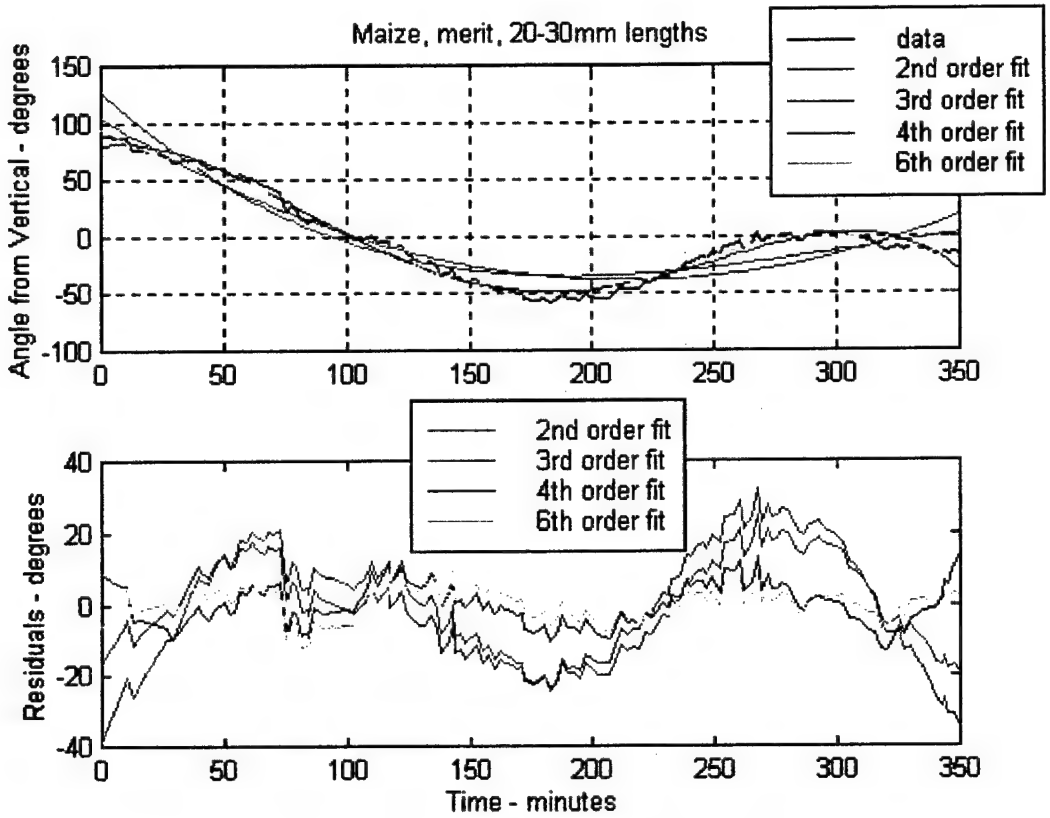

Figure 5.9 - Curve Matching with Residuals for Maize Merit

Note that a 6th order polynomial was required to bring the coefficient of determination within the 0.99 goal and that this model keeps the difference between actual and predicted values (residuals) to a maximum of approximately 5^0 throughout the time period. The next computational procedure (found in TRANS_FUNC.M) examines the time response of the polynomial model and computes the time response specifications along with an approximate 2nd-order, s-domain model. Figure 5.10 shows the 2nd-order transfer function step response along with the raw data. Note that the transfer function does not contain enough information to completely describe the actual data; specifically, the beginning and end of the time response is poorly modeled.

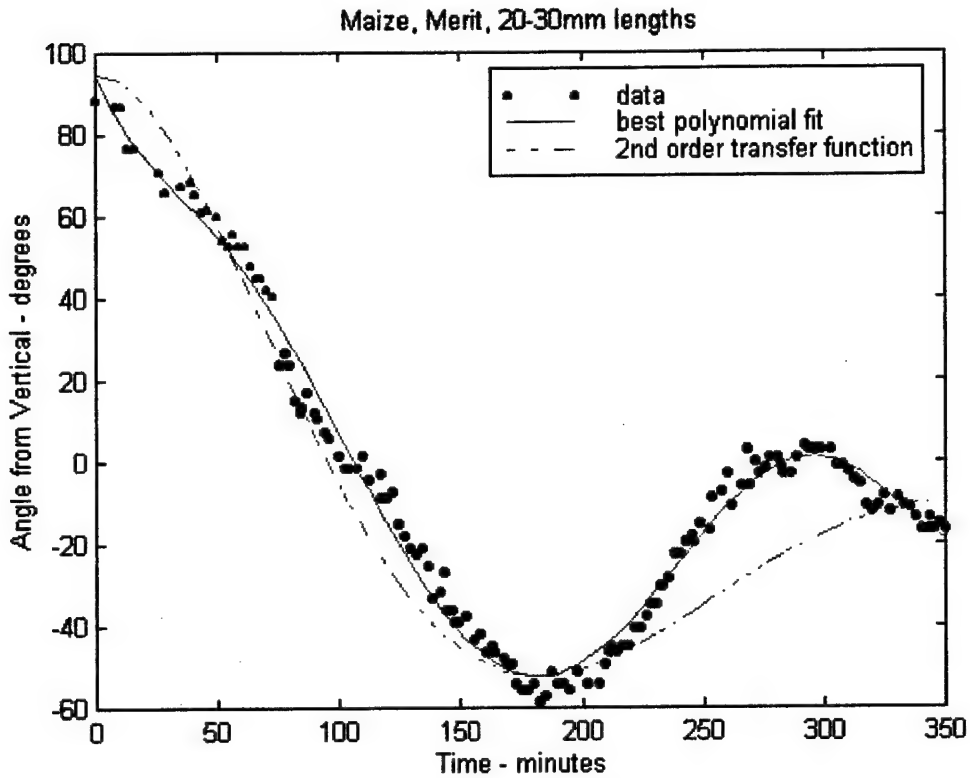

Figure 5.10 - Transfer Function Fit to Maize Merit Data

The time-domain analysis on the Ishikawa data of the previous figures provide the following time-response specifications:

Initial angle is: 88.5 degrees
Steady-state angle is: -24.4 degrees
Steady-state magnitude: 19.9 degrees
Response overshoots steady-state value...
Time-to-Peak: 183.0 minutes
Percent Overshoot: 30.6 percent
Damping Ratio(ζ): 0.352
Natural Frequency: 0.0183434 radians/min.
Transfer function:

$$\frac{0.03798}{s^2 + 0.01293\, s + 0.0003365}$$

A few observations are made from this summary. The steady-state magnitude, indicating the amplitude of any remaining oscillations in the response, is still rather high which indicates that the response was not complete and that further data should have been taken. This high value contains both remaining oscillations in the gravitropic reaction and any circumnutational oscillations underlying the graviresponse and they are difficult to separate. A negative steady-state (final) angle is not a typical response, with typical roots (see Chapter 2) reaching angles between 20^0 and vertical (0^0). For the 2nd-order transfer function (s-domain), the natural frequency (w_n) and the damping ratio (ζ) build the denominator (the transfer function's dynamics) from the form: $s^2 + 2\zeta w_n s + w_n^2$. It is evident from Figure 5.10 that even further terms are required for the transfer function to duplicate the data. Figure 5.11 examines the frequency spectrum of the data by analyzing the frequency content of the data's fast Fourier transform (FFT). Analysis is done on the entire response and then on the last third of the response in order to note any frequencies that only become dominant as the response approaches steady-state conditions. Note that in the entire response, three frequencies stand out: 0.05×10^{-3} Hz, 0.15×10^{-3} Hz, and 0.28×10^{-3} Hz. These frequencies convert to 333 minute, 111 minute, and 60 minute periods, respectively. Comparing this data with the time response in Figure 5.8, we note that the 333 minute period is the dominant, graviresponse period. The origin of the other 2 frequencies present within the data is problematic, although the 60 minute period can possibly be attributed to the circumnutational effects (with similar periods) discussed in Chapter 4

of this thesis. We are unable to confirm this with this data, since, as noted earlier, the graviresponse does not run to its full steady-state conditions.

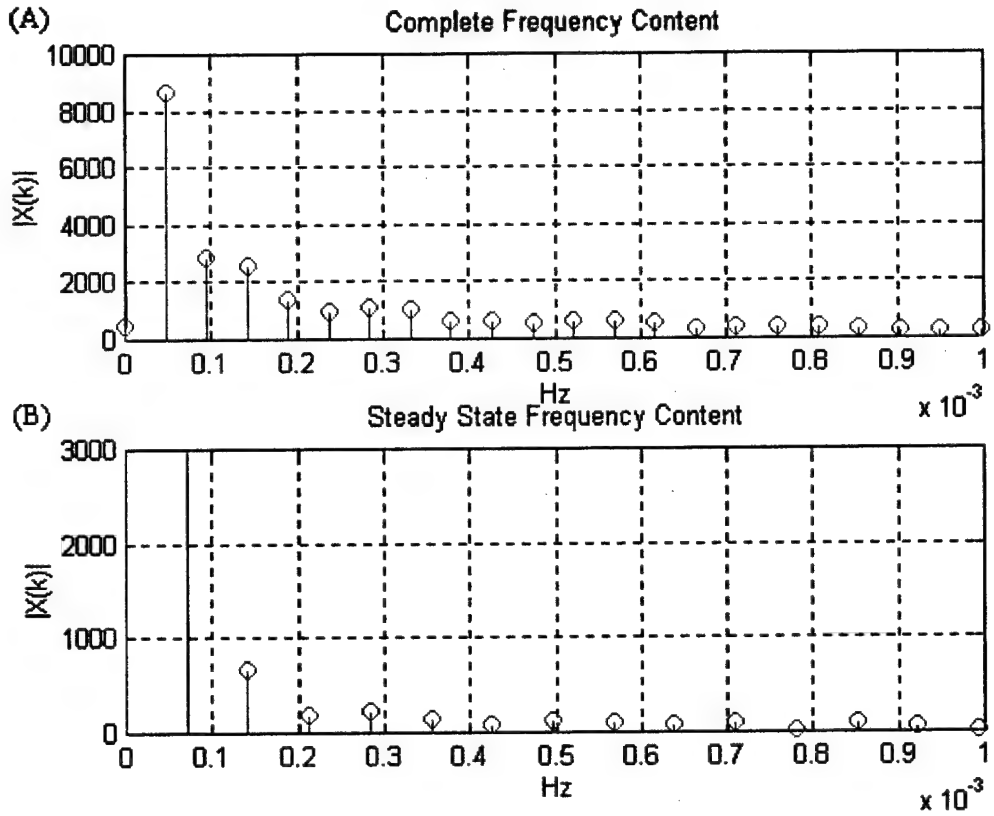

Figure 5.11 - Frequency Analysis of the Maize Merit Data
(A) displays relative frequency contributions in the entire data set, while (B) examines the final third of the response data.

In order to model the overall maize Merit historical data, a higher-order model must be designed. Two approaches can be applied for this. The first uses the design procedures introduced in Section 2.3 of this thesis and the second uses a more automated approach provided by the MATLAB Signal Processing and System Identification Toolboxes introduced in Section 5.4.2 of this Chapter. Using s-plane design approaches from Section 2.3 and attempting to place the poles of the system in

the locations required to produce the desired response becomes quite iterative and time-consuming with higher order systems. It was accomplished for this first set of data, but not for the remaining data. Figure 5.12 shows the effect of adding two compensators (additional transfer functions) to the original 2nd-order model. The primary compensator was approximately $\frac{0.0005(s+0.203)(s-0.189)}{(s-0.0569)(s+0.066)(s+0.0042\pm 0.071j)}$ with a ionic compensator of approximately $\frac{0.5}{s+0.009}$ placed in a parallel path with the primary dynamics. Part (B) of Figure 5.12 shows the results of using the Steiglitz-McBride iterative method within MATLAB to achieve the same results, a higher-order model of the maize Merit time response. This computational procedure produces a 8th-order transfer function (one order higher than manual design). The lack of resolution of the transfer functions to a specific structure such as a feed-forward path, 2 parallel paths, etc. is of little concern since any overall system description (a "black box") can be mathematically rearranged in an infinite set of configurations.

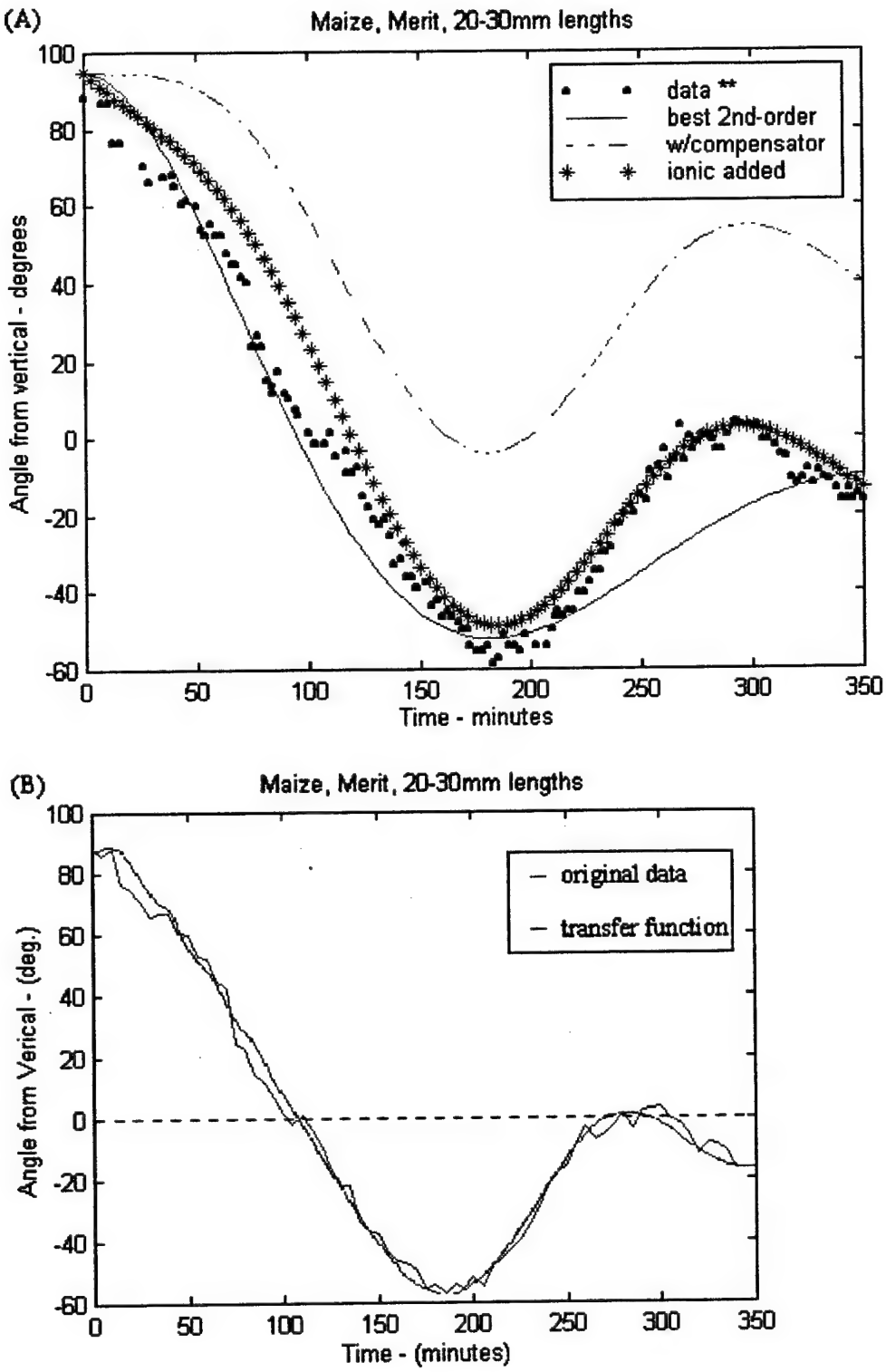

Figure 5.12 - Maize Merit as Higher Order Transfer Functions
(A) shows the manual technique of applied compensators, while (B) presents the results of the MATLAB computational design.

Two findings appear significant from this initial modeling analysis. First, the graviresponse must be allowed to complete its dynamic effects in order to fully analyze the frequency make-up of the steady-state. Secondly, the MATLAB System Identification tools appear equal to the task of developing transfer functions to describe the plant root gravitropic response data. This transfer function must then be analyzed and a structure given to it. The transfer function found in Figure 5.12(B) is:

$$\frac{0.2799s^8+0.0009867s^7+4.266\times10^{-5}s^6+9.939\times10^{-8}s^5+1.251\times10^{-9}s^4+9.977\times10^{-13}s^3+3.288\times10^{-16}s^2+4.87\times10^{-19}s+2.294\times10^{-23}}{s^9+0.00309s^8+0.0001495s^7+3.393\times10^{-7}s^6+4.272\times10^{-9}s^5+3.462\times10^{-12}s^4+1.735\times10^{-15}s^3+1.739\times10^{-18}s^2+2.649\times10^{-22}s+9.198\times10^{-26}}$$

The second historical example is briefly provided to highlight another problem found in some historical data. The circumnutational oscillations and other short-period oscillatory dynamics occurring beneath the main gravitropic response can be masked out of the data if the data is taken with too large a sampling rate or the data is time-averaged for numerous roots with varying initial angles upon gravistimulation. An example of the first problem is shown in Figure 5.13 and is data taken from (Moore, 1987). This data was sampled at 20-30 minute intervals and contains no frequency information other than the 0 Hz (DC) contribution of the nearly-linear response. The second sampling problem occurs when dozens of root responses are time-averaged to provide a single response curve. If the experimental methods do not standardize the initial angle and angular rate due to pre-gravistimulation curvatures and curvature rates, the offsets in these initial angles (phase angles) can be averaged

out in the time-averaging process and the dynamic is lost in the final product. Figure 5.14 highlights this effect.

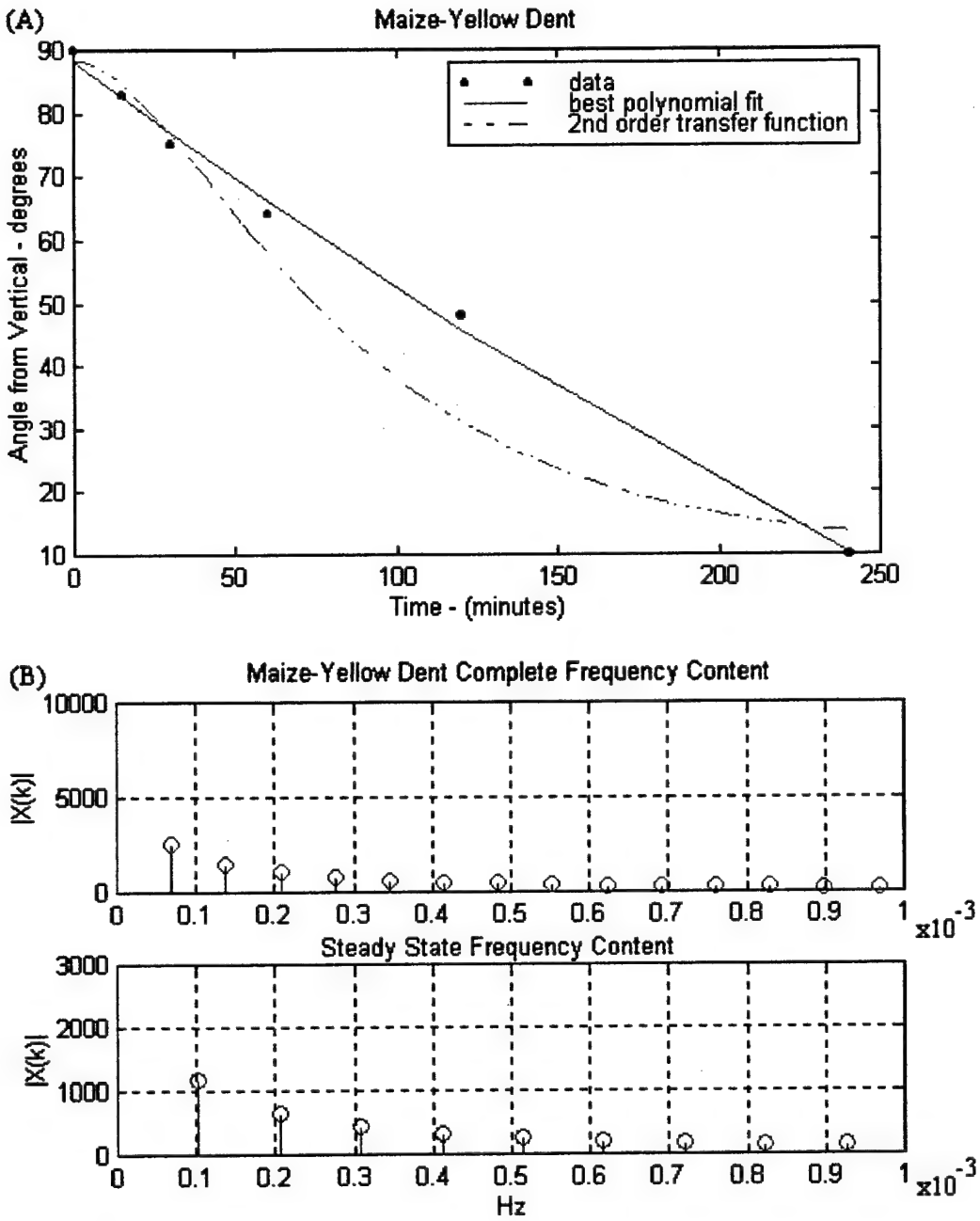

Figure 5.13 - Low Sampling Rate Problem
(A) shows the initial data taken from Moore, 1987, while (B) shows the lack of frequency data.

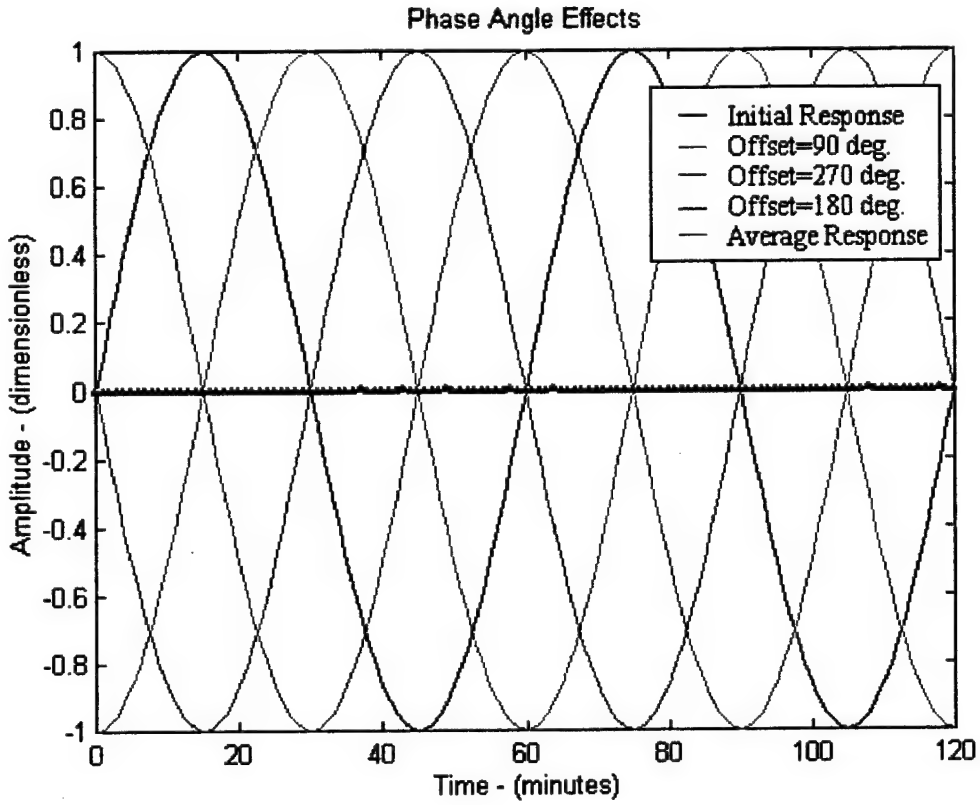

Figure 5.14 - Time-Averaging with Offset Initial Conditions

The previous illustrations point out that in order to accomplish system identification analysis on root graviresponse data, sampling rate must be high enough to capture any transient changes in the response (Dorf, 9180). For example, to properly sample a sinusoidal wave with a 60 minute period, a sampling period equal to 60 or 30 minutes, if in phase, would detect zero at every sample, therefore providing inaccurate information. The minimum usable sampling period is T/4, where T is the period of the transient response one wishes to accurately sample. As seen in Chapter 4, circumnutational periods can be on the order of 50 minutes, requiring an appropriate sampling period of 12 minutes to accurately capture the circumnutational dynamics. Additionally, the response must be allowed to reach steady-state conditions

so that the graviresponse can be fully distinguished from the circumnutational dynamics. Ideally, graviresponses should include the time previous to gravistimulation, continue until all transients have died out in the response, and be quite meticulous when time-averaging individual root graviresponses. Historical data is not rich in these properties.

5.5.2 Current Experimental Results

The statistical summary of the graviresponse experiments accomplished for this thesis are found in Table 5.2. The total number of maize, Yellow Dent graviresponses accomplished was approximately 130 with numerous responses not included because of various anomalies occurring during the 6 hours of graviresponse, such as the seed falling from the holder, total growth taking the root tip out of the camera's field of view, and growth rates significantly different from prestimulation growth due to unknown stress placed on the root. The actual numbers (shown in the table) reflect the anomalies and those roots whose initial angles were $90^0 \pm$circumnutation angle. Out of 107 maize, Merit seedlings photographed, 76 had responses without anomalies, and 70 of those had acceptable initial conditions: 22 roots of 20-29 mm lengths, 20 roots of 30-39 mm lengths, and 28 roots of 40-55 mm lengths. The time-domain specifications (introduced in Chapter 2) are α_{ss}(steady-state angle), M_{ss}(steady-state oscillatory amplitude), T_p(time-to-peak), PO(percent overshoot), ζ(damping ratio), w_n(natural frequency), the 2nd-order transfer function coefficients, the primary(overall1) and secondary(overall2) frequencies in the complete response and the primary frequency in the steady-state response(ss).

Table 5.2 - Summary of Time-domain Analysis on Graviresponses

Root Type	α_{ss} (deg)	M_{ss} (deg)	T_p (min)	PO (%)	ζ	w_n (rad/min)	2nd-order Num.	Transfer s^2	Function s	Coefs	Period Overall1	Period Overall2	(min) ss
Yellow Dent													
20-29 mm (n=25)													
mean:	27.3	8.4	141.9	25.7	0.43	0.027	0.051	1	0.0238	0.0008	179	64	66
standard deviation:	13.1	3.8	43.6	15.3	0.16	0.008	0.029	0	0.0136	0.0004	18	19	17
95% CI Error:	5.1	1.5	17.1	7.9	0.06	0.003	0.011	0	0.0053	0.0002	7	8	7
30-39 mm (n=21)													
mean:	20.8	7.6	161.5	21.7	0.47	0.025	0.053	1	0.0242	0.0007	173	61	60
standard deviation:	10.7	3.7	48.0	14.3	0.15	0.009	0.055	0	0.0173	0.0006	29	15	19
95% CI Error:	4.6	1.6	20.5	6.1	0.06	0.004	0.023	0	0.0074	0.0003	12	6	8
40-55 mm (n=17)													
mean:	24.1	6.9	139.8	24.1	0.45	0.029	0.063	1	0.0259	0.0009	168	65	57
standard deviation:	14.1	2.8	45.4	14.8	0.18	0.009	0.055	0	0.0175	0.0006	30	18	13
95% CI Error:	6.7	1.4	21.6	7.0	0.08	0.004	0.026	0	0.0083	0.0003	14	9	6
Merit													
20-29 mm (n=22)													
mean:	23.9	7.7	189.1	13.9	0.54	0.021	0.030	1	0.0234	0.0004	229	73	53
standard deviation:	15.8	3.4	36.0	5.7	0.08	0.005	0.016	0	0.0079	0.0003	33	20	12
95% CI Error:	6.6	1.4	15.8	2.5	0.04	0.002	0.007	0	0.0033	0.0001	14	9	5
30-39 mm (n=20)													
mean:	27.8	7.8	182.2	14.4	0.54	0.024	0.047	1	0.0257	0.0007	231	79	53
standard deviation:	7.5	3.5	57.7	6.8	0.09	0.012	0.058	0	0.0136	0.0008	29	24	12
95% CI Error:	3.3	1.5	25.3	2.9	0.04	0.005	0.025	0	0.0059	0.0003	13	10	5
40-55 mm (n=28)													
mean:	33.4	7.0	143.8	23.9	0.44	0.029	0.055	1	0.0251	0.001	222	81	54
standard deviation:	11.3	3.5	56.1	15.0	0.13	0.012	0.047	0	0.0142	0.0009	26	24	12
95% CI Error:	4.2	1.3	20.8	5.6	0.05	0.005	0.017	0	0.053	0.0003	10	9	5

Differences between the two cultivars of maize are readily apparent from Table 5.2. The Yellow Dent cultivar exhibits more of a tendency to approach the vertical following the graviresponse (smaller α_{ss}), a faster initial response (smaller T_p), and slightly more unstable characteristics (higher PO and lower ζ). The higher speed of the graviresponse is also reflected in the frequency analysis summary where Yellow Dent exhibits shorter periods in both the overall primary and secondary frequencies, but also note that Merit's steady-state primary frequency is higher (smaller period) than that of Yellow Dent indicating a shorter period circumnutation in the Merit cultivar. Table 5.3 summarizes the Student's t-Test results in determining whether a significant difference (P-value ≤ 0.05) exists between the various population categories. Statistical significance was tested between all categories of root length within a cultivar and between the two cultivars. Specifications examined included α_{ss}, M_{ss}, T_p, ζ, w_n, the primary and secondary frequencies in the complete response, and the primary steady-state frequency. Out of a total of 80 tests accomplished, the summary table displays only the results of those tests that produced significant differences between the tested categories. Note that the differences between Yellow Dent and Merit observed earlier in this paragraph have been given statistical corroboration. The Yellow Dent cultivar is faster, less stable, and has less steady-state error (final angle, α_{ss}, from vertical) than the Merit cultivar; a classical indication of higher gain within the Yellow Dent gravitropic mechanism.

Table 5.3 - Summary of Significant t-Test Results

Description	P-Value
Within Yellow Dent roots:	
secondary frequency(overall2) between	
20-29 mm & 30-39 mm lengths:	**<0.001**
Within Merit roots:	
α_{ss} between	
30-39 mm & 40-55 mm lengths:	**0.047**
T_p between	
30-39 mm & 40-55 mm lengths:	**0.03**
20-29 mm & 40-55 mm lengths:	**0.001**
ζ between	
30-39 mm & 40-55 mm lengths:	**0.004**
20-29 mm & 40-55 mm lengths:	**0.002**
w_n between	
20-29 mm & 40-55 mm lengths:	**0.004**
Between Yellow Dent & Merit roots:	
α_{ss}	
of all lengths:	**0.04**
of 30-39 mm lengths:	**0.02**
of 40-55 mm lengths:	**0.03**
T_p	
of all lengths:	**0.005**
of 20-29 mm lengths:	**<0.001**
ζ	
of all lengths:	**0.01**
of 20-29 mm lengths:	**0.005**
w_n	
of 20-29 mm lengths:	**0.004**
primary frequency(overall1)	
of all lengths:	**<0.001**
of 20-29 mm lengths:	**<0.001**
of 30-39 mm lengths:	**<0.001**
of 40-55 mm lengths:	**<0.001**
secondary frequency(overall2)	
of all lengths:	**<0.001**
of 30-39 mm lengths:	**0.008**
of 40-55 mm lengths:	**0.02**
steady-state frequency(ss)	
of all lengths:	**0.003**
of 20-29 mm lengths:	**0.005**

These tests appear to indicate a few conclusions concerning the responses within the same cultivar. Neither of the two cultivars show any significant change in their primary or secondary frequency components between the length categories. The Yellow Dent cultivar, although shown to be significantly different than the Merit, shows very little response differences between the three length categories. However, Merit appears to get significantly faster with a lower damping ratio (less stability) with age/root length. These observations would allow a single s-domain model to be estimated for Yellow Dent, but any model for Merit would need to include coefficients dependent upon root length. Further work needs to be accomplished to determine accurate dependency of the transfer function coefficients on root age/length, however, a model can be designed for a single length category.

The Yellow Dent overall s-domain model is developed to meet the average time-domain specifications and contain the proper frequency components identified within the time-response signal. Figure 5.15 displays the time response of this model. The results (see Table 5.2) provide the target specifications as $\alpha_{ss} \approx 24^0$, $M_{ss} \approx 7.6^0$, $T_p \approx 145$ minutes, PO≈24%, $\zeta \approx 0.45$, a dominant overall response frequency of 0.8×10^{-4} Hz, and a steady-state dominant frequency of approximately 2.8×10^{-4} Hz. Figure 5.15 confirms the time-domain specifications for the model and Figure 5.16 confirms the frequency components. The transfer function that models the primary gravitropic response is shown in Equation 5-4, while the transfer function that models the frequency component of circumnutation is found in Equation 5-5. The complete s-domain response function to a unit step (90^0 or 1g) is shown in Equation 5-6.

$$CLTF_{grav} = \frac{6.161x10^{-18}}{s^6 + 0.0022s^5 + 2.812x10^{-6}s^4 + 2.373x10^{-9}s^3 + 1.313x10^{-12}s^2 + 4.91x10^{-16}s + 9.128x10^{-20}} \quad (5-4)$$

$$CLTF_{circ} = \frac{0.01375s}{s^2 + 3.04617x10^{-6}} \quad (5-5)$$

$$Y_{overall}(step) = Y_{grav}(step) + Y_{circ}(step) = CLTF_{grav} * 1/s + CLTF_{circ} * 1/s$$
$$= 1/s(CLTF_{grav} + CLTF_{circ}) \quad (5-6)$$

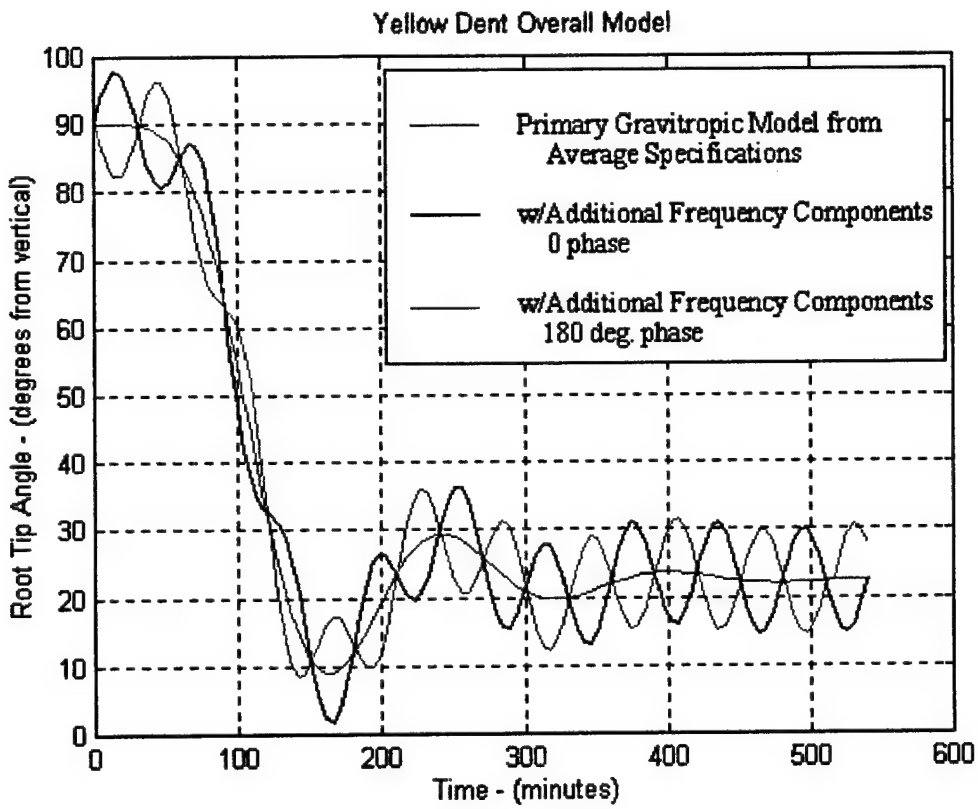

Figure 5.15 - Yellow Dent Overall Model
The blue curve represents the average of all 2nd-order characteristics from the empirical, Yellow Dent, results. The black curve represents the complete model after including the rapid, low damped dynamics found prevalent in the Yellow Dent frequency analysis and shows the dramatic effect these dynamics create in the overall appearance of the response curve. The rapid, low damped dynamics (linked to circumnutation) is superimposed with the primary curve at a point 0 radians into the wavelength of the circumnutation, but can be superimposed at any other point, changing the appearance of the curve (such as the green curve).

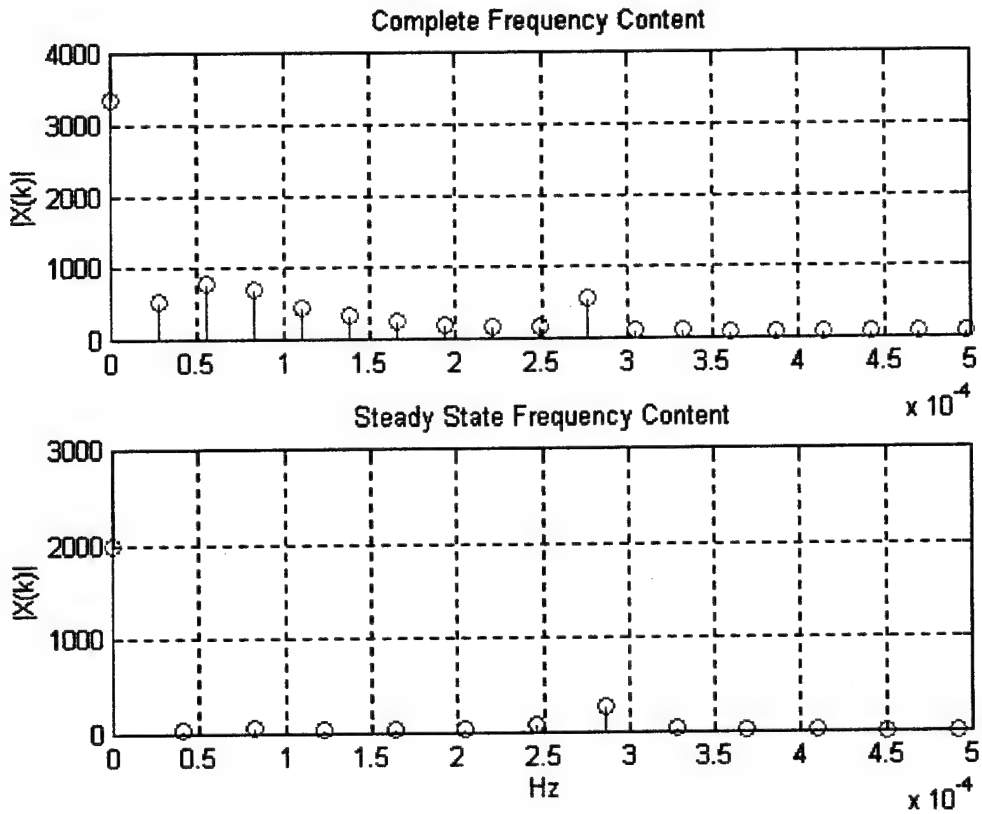

Figure 5.16 - Frequency Components of the Yellow Dent Model

Note that by convention, the model shown in Equation 5-6 is the parallel connection or superposition of the circumnutational and primary gravitropic dynamics to the overall response. Under this convention, the resulting "overall" response is as shown by the black line in Figure 5-15. Producing the response requires a 90^0 shift in the step output since the transfer functions implicitly contain zero initial conditions and the convention for displaying gravitropic responses is that horizontal roots are at 90^0. When accomplishing reduction operations in Chapter 6 to infer transduction properties, this overall model will be operated upon by the s-domain model found in Chapter 4 for the differential growth response.

5.6 Summary and Discussion

During the initial theoretical development, a dual-path model set was chosen to represent the overall root gravitropism system. From past research, it appeared evident that the overall system displays rapid, less stable, low amplitude dynamics and less rapid, higher amplitude primary gravitropic dynamics with greater stability. Historically, the secondary dynamics tend to be treated as only noise or the effects of other plant movements. The accepted method of examining graviresponses has been to develop averaged responses over time. This technique along with inadequately small sampling times was shown to mask certain dynamics present within the graviresponse. The conclusion is affirmed in the final modeling effort for Yellow Dent. Instead of time-averaging the individual root response data, the modeling was accomplished by statistically compiling time specifications (refer back to Table 5.2) and creating model that duplicated the specifications. When the time-averaged response is examined, the time-domain specifications were $\alpha_{ss} = 28.2^0$, $M_{ss} = 5.1^0$, $T_p =$ 231.0 minutes, PO = 7.9%, $\zeta = 0.628$, and $w_n = 0.0174677$ radians/min. These are from 20-66 % off from the compiled time specifications and the frequency information in this time-averaged response did not contain the expected frequency content (approximately 180 minute and 60 minute periods) of circumnutation seen in the individual responses.

The empirical gravitropic response data indicates that the response characteristics of the two cultivars differ significantly. This is not surprising, but of more interest is the finding that Yellow Dent responses are not mediated by root

length/age. Alternatively, Merit responses appear significantly dependent upon the length of the root. Further research is required to define a precise relationship between the s-domain model coefficients and the root length/age.

The s-domain response function represented in Equation 5-4 is the final model for the overall maize, Yellow Dent, graviresponse. It must be kept in mind that this represents the overall system response function to a unit impulse (1 in the s-domain). The root tip angle (θ) is described by the response function (RF), where θ = (unit impulse)*(RF) = 1RF. Therefore, since the horizontal placement of the root is defined as a unit step input for the graviresponse, the overall closed-loop transfer function (CLTF) is found by RF*s. The open-loop transfer function (OLTF) is CLTF/(1-CLTF). Figure 5.17 outlines the progression of s-domain descriptions.

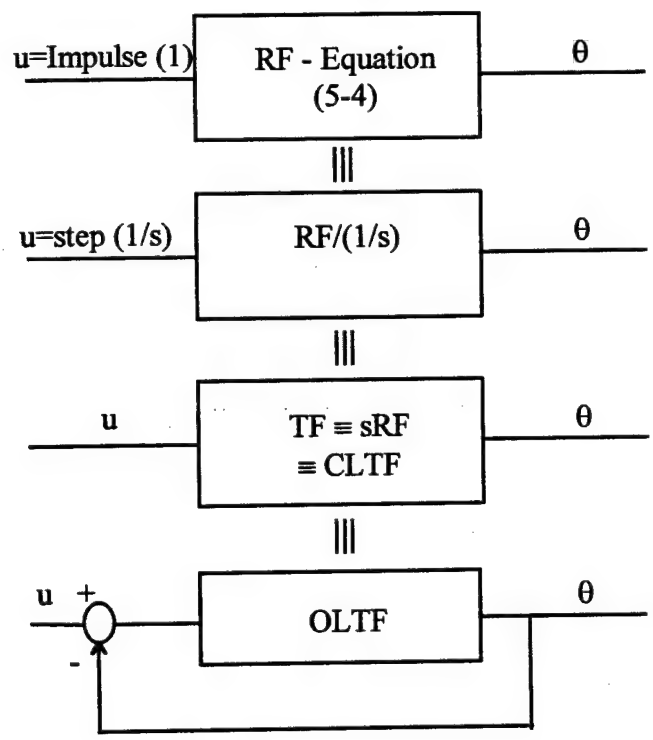

Figure 5.17 - Block Diagram Conversion of s-Domain Model

5.7 Conclusions

The objective of this chapter has been successfully achieved. Both historical and current gravitropic responses appear to corroborate the existence of a dual-path gravitropic system. This chapter has produced a s-domain model that successfully duplicates the time- and frequency-domain characteristics of the individual maize, Yellow Dent, root graviresponses. With similar models produced for the sensor (Chapter 3) and the differential growth response (Chapter 4), Chapter 6 will compare and operate on these models in order to provide a coherent model that can also provide some insight into the gravitropic transduction mechanism.

CHAPTER 6

INFERENCES TO THE TRANSDUCTION MECHANISM

6.1 Introduction and Objective

The transduction mechanism which receives the gravity signal perceived by the sensor and eventually induces the differential growth response within the distal elongation zone (DEZ) is the most elusive of the three mechanisms that make up the gravitropic system. Transduction involves a complex chain of biochemical signals, with, more than likely, some signals operating in parallel to others. Much work in the field of molecular biology is required to piece together the structure and chemistry of this mechanism. Some components of this structure and chemistry are presumed. Auxin is believed to be the primary agent for differential growth (Taiz & Zeiger, 1991). At a microscopic level, the auxins create membrane hyperpolarization and by stimulating the plasma membrane's H^+ ATPase, creates cell wall acidification. This brings about cell wall loosening and, along with turgor pressure within the cell, promotes elongation growth in these tissues (Millner, 1995). Indole-3-acetic acid (IAA) is the most important of the naturally occurring hormones in the gravitropic process. As introduced in Chapter 2 of this thesis, much evidence exists pointing to IAA as the growth response effector (Bandurski *et al.*, 1984; Lee *et al.*, 1984; Evans *et al.*, 1986; McClure & Guilfoyle, 1989; Cosgrove, 1990; Nick *et al.*, 1990; Young *et al.*, 1990; Evans, 1991). Calcium and membrane potentials are also most certainly involved with the transduction mechanism (Lee *et al.*, 1983; Lee *et al.*, 1983; Lee *et al.*, 1984; Moore, 1986; Moore *et al.*, 1987; Stinemetz *et al.*, 1987; Hasenstein &

Evans, 1988; Leopold & Wettlaufer, 1988; Wendt & Sievers, 1989; Wayne *et al.*, 1990; Bjorkman & Cleland, 1991; Ishikawa & Evans, 1992; Suzuki *et al.*, 1994; Zieschang & Sievers, 1994)

The objective of this chapter is to develop a "black-box" model of the plant root's transduction mechanisms. Because of the complexity and lack of causal data discussed in the previous paragraph and in Chapter 2 of this thesis, the goal is not to develop a precise representation of all the processes and mechanisms involved in transduction, but to examine the general characteristics that the complete transduction mechanism exhibits. By applying the mathematical model for the sensor from objective 1 (Chapter 3) and the mathematical model for the differential growth response from objective 2 (Chapter 4) to the overall model achieved for objective 3 (Chapter 5), a simple input/output model (the transfer function) of the root's transduction processes is obtained. This model's characteristics are then discussed.

6.2 Mathematical Techniques

The overall gravitropic system is partitioned into 3 separate mechanisms: sensor, transduction, and differential growth. Recall from Chapter 2 that one of the advantages of obtaining s-domain descriptions of time-domain differential equations is that the s-domain representations can be solved and manipulated algebraically versus the need for integration and convolution in the time-domain. This leads to block diagram algebra. If the overall system, G(s), is known along with two other subsystems, P(s) and D(s), then a third subsystem can be inferred by the relationship in

Equation 6-1. Figure 6.1 illustrates this relationship and its specific application to the gravitropic system.

$$G(s) = P(s) * T(s) * D(s)$$

$$\therefore \quad T(s) = \frac{G(s)}{P(s) * D(s)} \tag{6-1}$$

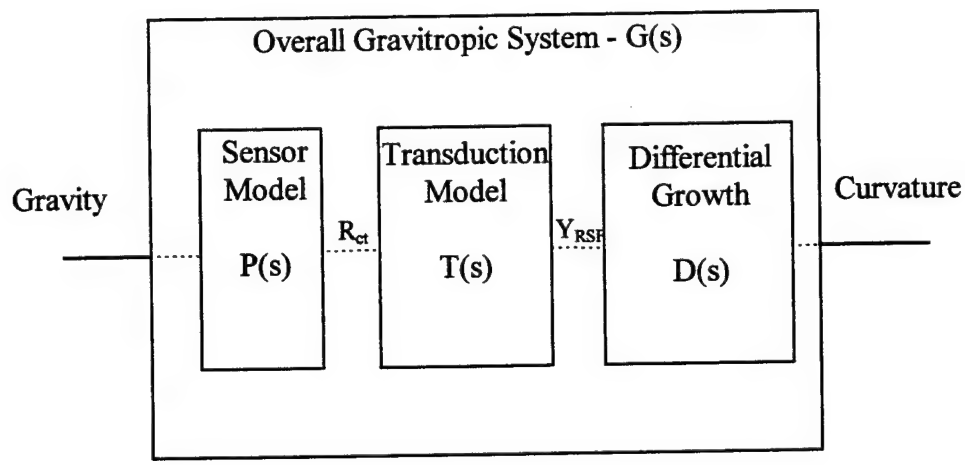

$$T(s) \equiv \frac{Y_{RSF}(s)}{R_{ct}(s)} = \frac{G(s)}{P(s) * D(s)}$$

Figure 6.1 - Development of the Transduction Model

The transduction transfer function, T(s), describes a linear input-to-output relationship in the s-domain with zero initial conditions. The input variable ($R_{ct}(s)$) is the output variable from the sensor (perception) model, P(s), which to the resolution of this thesis is overall cytoskeletal tensions produced in the columella cells (see Section 3.5.4). The output variable ($Y_{RSF}(s)$) is the input variable for the differential growth model, D(s), which is a generic "RELEL Stimulus Factor" (see Section 4.3.2).

One further operation of block diagram algebra is required because Chapter 5 does not conclude with the same overall model, G(s), as that shown in Figure 6.1.

The overall gravitropic response modeling accomplished in Chapter 5 is for the complete gravitropic system which is certainly a closed-loop feedback system. The overall transfer function shown in Figure 6.1 is the open-loop transfer function (OLTF). The relationship between the closed-loop transfer function (CLTF) and the OLTF for a linear, single negative feedback loop system (specifically, the root tip angle, α, for this system) is given by Equation 6-2. However, one must remember that when examining a "black box" containing complex systems with nonlinearities and multiple input-to-output pathways, the OLTF derived from Equation 6-2 may not be an accurate open-loop model. This is most probably the situation for the gravitropic mechanism.

$$\begin{aligned} \mathrm{CLTF} &= \frac{\mathrm{OLTF}}{1+\mathrm{OLTF}} \\ \mathrm{OLTF} \equiv G(s) &= \frac{\mathrm{CLTF}}{1-\mathrm{CLTF}} \end{aligned} \tag{6-2}$$

Once the transduction model is derived, the model's time-domain characteristics are described. These specifications are reviewed in Table 2.1 of Chapter 2. This information such as any time delays or rate specifications can be used to provide insight into the complex and elusive transduction mechanisms at work in root gravitropism.

6.3 Results and Discussion

This section is divided into three subsections; a review and discussion of the previous chapter's final s-domain (linear, time-invariant, zero initial condition models), a discussion of inferred transduction time-domain characteristics following block diagram reduction, and a section on possible transduction subsystems such as a possible stimulus for the circumnutational differential growth and a description of possible growth dynamics that could lead to RELEL perturbations seen in the differential growth model.

6.3.1 Review and Discussion of Various s-Domain Models

Equation 6-3 is the transfer function (s-domain) model developed for the root's differential growth in Chapter 4. It includes both the dynamics of primary gravitropism and those of circumnutation. Equations 6-4 and 6-5, respectively, are the separate transfer functions for circumnutation and primary gravitropism. It should be noted that these are CLTF's since they were developed using a differential growth model that was time-variant, where the time variability is in itself a result of feedback of the root tip angle. When the time variability is removed from the differential growth model, thereby only using the initial RELEL perturbations as computed by the weighted average method (results in Table 4.7 and Figure 4.12), we have an appropriate s-domain model of the OLTF for differential growth; Equation 6-6.

$$\frac{90s^6+0.03435s^5+0.002705s^4+8.972\text{x}10^{-7}s^3+6.472\text{e-}9s^2+2.483\text{x}10^{-12}s+3.591\text{x}10^{-16}}{s^7+0.0003935s^6+3.026\text{x}10^{-5}s^5+1.018\text{x}10^{-8}s^4+7.795\text{x}10^{-11}s^3+2.443\text{x}10^{-14}s^2+1.097\text{x}10^{-17}s+2.079\text{e-}25} \quad (6\text{-}3)$$

$$\text{Circumnutation:} \quad \frac{1.181\, s^2 - 0.007685\, s - 9.852\text{x}10^{-8}}{s^3 + 5.54\text{x}10^{-5}\, s^2 + 2.679\text{x}10^{-6}\, s + 1.538\text{x}10^{-10}} \tag{6-4}$$

$$\text{Graviresponse:} \quad \frac{88.5\, s^2 + 0.03495\, s + 5.081\text{x}10^{-6}}{s^3 + 0.0003336\, s^2 + 1.496\text{x}10^{-7}\, s - 6.463\text{x}10^{-15}} \tag{6-5}$$

$$\text{OLTF}_{grav}: \quad \frac{90s^3 + 0.9627s^2 - 0.0001385s}{s^3 + 0.01084s^2 + 1.464\text{x}10^{-15}s + 4.207\text{x}10^{-20}} \equiv \frac{90s^2+0.9627s-0.0001385}{s^2 + 0.01084\, s} \tag{6-6}$$

Note that OLTF_{grav} is "unstable." This is expected since without feedback, the root will continue to curve. This is corroborated by experiments that continue to rotate the root as it curves, keeping the root tip at a horizontal position to the gravity vector. These experiments result in roots (and stems) that curve into tight spirals as the curvature mechanism continues, unchecked by a feedback mechanism (Simmons *et al.*, 1995). Figure 6.2 is the resulting step response of OLTF_{grav}. Note that the poles of OLTF_{grav} ($s=-1.08\text{x}10^{-2}$, $s=-6.73\text{x}10^{-14} \pm 1.97\text{x}10^{-9}i$) contain a very slightly unstable pole that is also slightly oscillatory ($w_d=1.97\text{x}10^{-9}$ rad/sec. or $3.13\text{x}10^{-10}$ Hz), but the frequency is too low to be noticeable in the response.

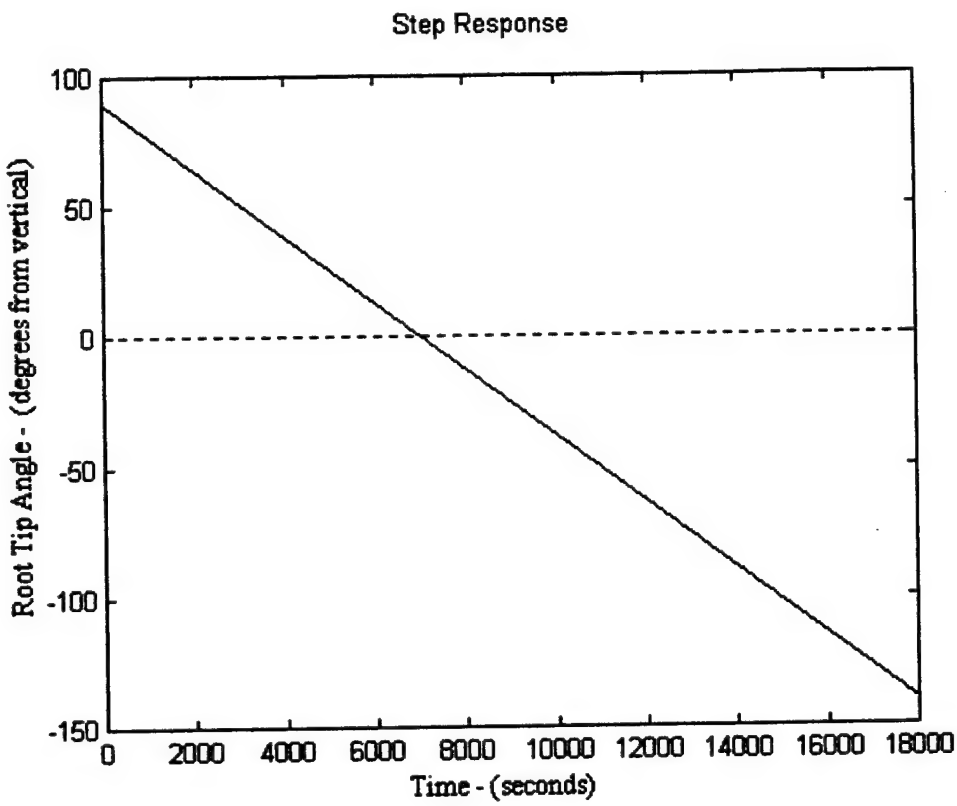

Figure 6.2 - Differential Growth Gravitropic OLTF - Step Response

The issue remains as to whether the s-domain model for circumnutation (Equation 6-4, with the impulse response shown in Figure 4.23) is the result of feedback of the tip angle (a closed-loop transfer function, $CLTF_{circ}$) or is independent of tip angle feedback ($OTLF_{circ}$)? Since experiments have never been designed to target this question, further research should be accomplished to verify this assumption (see Chapter 8). Recall that this research has found that statolith motions between vertical (diffusion only) and 10^0 displacement angles are statistically insignificant (see Chapter 3, Table 3.12 and text). Since circumnutational angles are $\leq 10^0$, this appears to indicate that circumnutational dynamics are not dependent upon feedback angle and Equation 6-4 is also $OLTF_{cir}$. It should be noted that $OLTF_{cir}$ is actually a response

function to an impulse input. It is doubtful that a physical transduction signal exists in the form of an impulse function. Further efforts to refine the form of the transduction signal at this final point prior to actuating a circumnutational RELEL perturbation would be required to describe the s-domain model of circumnutational differential growth. One such idea is introduced in Section 6.3.3.

Because of the complexity of the statolith dynamics found in Chapter 3, the sensor s-domain model must remain quite generalized. Further finite-element model work in this area may yield a more refined model for cytoskeletal tensions during statolith sedimentations, but for now the model is assumed to be 1st-order and is shown in Equation 6-7 (see Figure 3.28, and text):

$$G_{sensor} \equiv \frac{C}{g} = \frac{0.01}{s + 0.01} \qquad (6\text{-}7)$$

where, output C is a generic variable for the fraction of longitudinally redirected cytoskeletal tensions and g is gravity input (a step of amplitude 1 being complete horizontal rotation of the root while amplitude of $\sin\theta$ are rotations of θ degrees). The fraction of tensions being directed laterally within the columella cell would be (1.0-C). Further refinements of this model require not only the finite-element resolution, but the integration of all the columella cells within a typical root cap (approximately 50 in maize) and an appropriate weighting to various storeys of columella cells over those of other storeys (Blancaflor *et al.*, 1998).

The s-domain model for the overall, closed-loop response (developed in Chapter 5, Equation 5-6) represents the response for unit step input (90^0 of gravistimulation, full 1g). The primary gravitropic closed-loop model is repeated in

Equation 6-8 and Figure 6.3 shows the result of a 1g step input on the overall closed loop system repeated in Equation 6-9a and the complete, overall s-domain model is shown in Equation 6-9b.

$$CLTF_{grav} = \frac{6.161x10^{-18}}{s^6 + 0.0022s^5 + 2.812x10^{-6}s^4 + 2.373x10^{-9}s^3 + 1.313x10^{-12}s^2 + 4.91x10^{-16}s + 9.128x10^{-20}} \quad (6-8)$$

$$CLTF_{circ} = \frac{0.01375s}{s^2 + 3.04617x10^{-6}}$$

$$Y_{overall}(step) = Y_{grav}(step) + Y_{circ}(step) = CLTF_{grav} * 1/s + CLTF_{circ} * 1/s$$
$$= 1/s(CLTF_{grav} + CLTF_{circ}) \quad (6-9a)$$

$$CLTF_{overall} = \frac{-0.01375s^7 - 3.025x10^{-5}s^6 - 3.866x10^{-8}s^5 - 3.262x10^{-11}s^4 - 1.805x10^{-14}s^3 - 5.896x10^{-19}s^2 - 1.255x10^{-21}s + 1.877x10^{-23}}{s^8 + 0.0022s^7 + 5.858x10^{-6}s^6 + 9.074x10^{-9}s^5 + 9.877x10^{-12}s^4 + 7.718x10^{-15}s^3 + 4.09x10^{-18}s^2 + 1.496x10^{-21}s + 2.781x10^{-25}} \quad (6-9b)$$

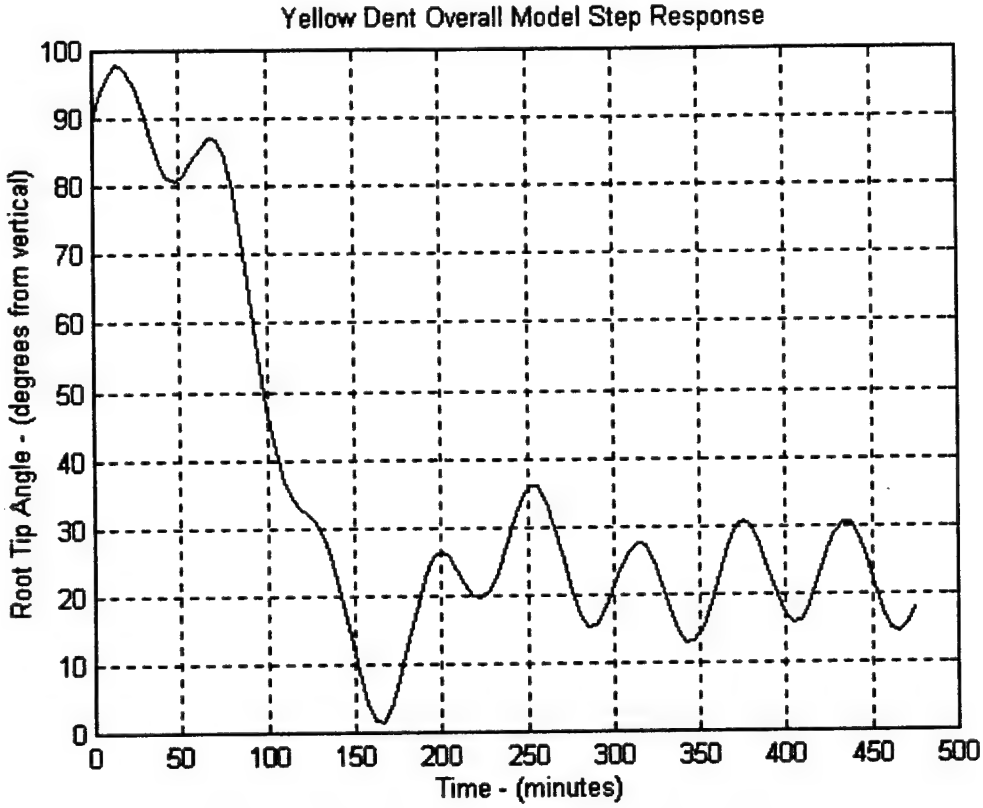

Figure 6.3 - Overall, Closed-Loop Model Step Response

6.3.2 Time-domain Characteristics of the Transduction Mechanism

Figure 6.4 summarizes the s-domain models and their interconnections following the discussion of the previous section and the overall model set discussed in Chapter 5. The diagram reflects the dual-path model set discussed in Chapter 5. The output, θ, root tip curvature angle from vertical is the superposition of both the ionic growth (modeled from the rapid, oscillatory circumnutational dynamics) and the hormonal growth (modeled from the slower, more stable primary gravitropic dynamics). Remember, as discussed in Chapter 2 and Chapter 5, that the gravitropic set-point (GSP or θ_{ref}) may also be dynamic in nature and subject to environmental and

gravitropic change. Using the block diagram algebra introduced in Equations 6-1 and 6-2, G_{trans}, the transduction s-domain model is found as shown in Equation 6-10.

$$CLTF_{overall} = \frac{G_{sensor} * G_{trans} * G_{dg}}{1 + G_{sensor} * G_{trans} * G_{dg}}$$

$$CLTF_{overall} = G_{sensor} * G_{trans} * G_{dg} - G_{sensor} * G_{trans} * G_{dg} * CLTF_{overall}$$

$$\therefore \quad G_{trans} = \frac{CLTF_{overall}}{G_{sensor} * G_{dg} * (1 - CLTF_{overall})} \equiv \frac{G_{overall}}{G_{sensor} * G_{dg}} \qquad (6\text{-}10)$$

where, $G_{DG}=OLTF_{cir}+OLTF_{grav}$.

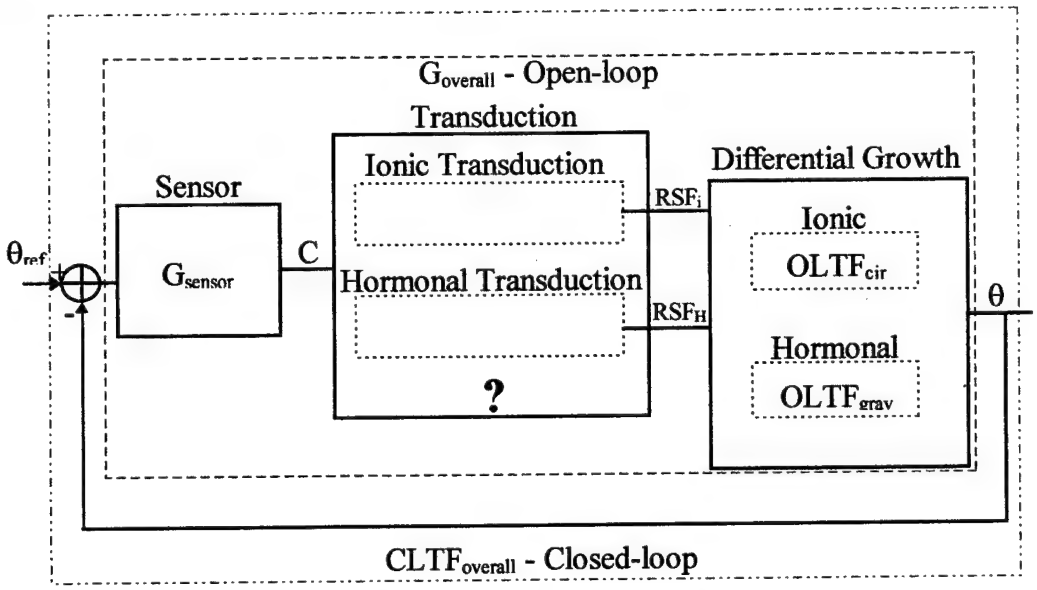

Figure 6.4 - Summary of s-Domain Models
θ_{ref} is the gravitropic set-point (GSP). G_{sensor} is Equation 6-7. $OLTF_{cir}$ and $OLTF_{grav}$ are Equations 6-4 and 6-6, respectively. The outputs from the transduction mechanism (RSF_i and RSF_H) represent the RELEL stimulus factors from ionic and hormonal sources, respectively. C, the output from the sensor model, is redirected longitudinal cytoskeletal. $CLTF_{overall}$ is Equation 6-9b.

In operating on these s-domain models, one problem still remains and that is the form of the differential growth models and their inputs. The overall model was developed with zero initial conditions and the response is adjusted 90^0 for gravitropic

conventions of horizontal roots. The Steiglitz-McBride auto-recursive algorithm used to develop the s-domain models for differential growth following their simulation does not place the dynamics at zero initial conditions. Adjustment of these models is required along with the assumption that the input to their parallel subsystem, G_{dg} can be viewed as the linear combination of both the ionic and hormonal factors. The adjusted open-loop model from the differential growth simulation is Equation 6-11. Recall that the response to this model will need corrected by 90^0 (y=90-y) in order to remain consistent with gravitropic convention (see Figure 6.5).

$$RSF_{Total} = RSF_i + RSF_H$$

$$G_{dg} \equiv \frac{\theta}{RSF_{total}} = OLTF_{cir} + OLTF_{grav}$$

$$G_{dg} = \frac{s(-3.012s^3 + 0.02022s^2 - 3.429x10^{-6}s + 3.425x10^{-8})}{s^4 - 1.938x10^{-6}s^3 + 2.679x10^{-6}s^2 + 1.219x10^{-13}s - 7.051x10^{-18}} \qquad (6\text{-}11)$$

Following reduction using Equation 6-10, the open-loop transfer function for the transduction mechanism is shown in Equation 6-12 with its step response in Figure 6.6. The instability of the response is immediately noted. This is expected because of the assumptions and operations accomplished in this derivation, but in actuality, the biological processes within the transduction mechanism are subject to catabolic regulation and reaction limitations that limit the production of all stimulus factors. However, the characteristics of early portions of this response are worth examination. The curve is characteristic of an exponential rise with a time-constant, $T_c \approx 3.5$ minutes, where the response, $y = e^{time/T_c}$. The unexpected level of instability in this inferred process demands another approach to reducing the s-domain models.

$G_{trans} =$

$$\frac{0.4564s^{12} + 0.005568s^{11} + 1.254\times10^{-5}s^{10} + 2.881\times10^{-8}s^{9} + 4.174\times10^{-11}s^{8} + 4.327\times10^{-14}s^{7} + 3.085\times10^{-17}s^{6} + 1.59\times10^{-20}s^{5} - 5.593\times10^{-24}s^{4} - 5.409\times10^{-28}s^{3} - 1.669\times10^{-29}s^{2} - 7.579\times10^{-37}s + 4.393\times10^{-41}}{s^{12} + 0.009237s^{11} - 6.983\times10^{-5}s^{10} - 1.879\times10^{-7}s^{9} - 4.182\times10^{-10}s^{8} - 6.158\times10^{-13}s^{7} - 6.627\times10^{-16}s^{6} - 4.826\times10^{-19}s^{5} - 3.246\times10^{-22}s^{4} + 7.405\times10^{-26}s^{3} - 5.232\times10^{-29}s^{2} + 2.102\times10^{-31}s} \quad (6\text{-}12)$$

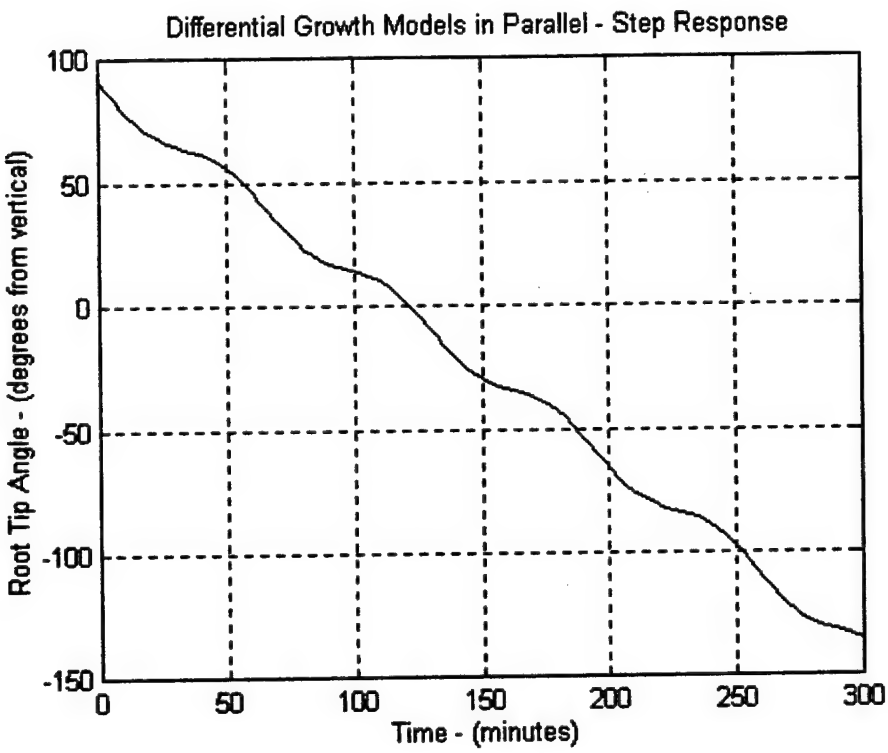

Figure 6.5 - Complete Open-Loop Differential Growth Model

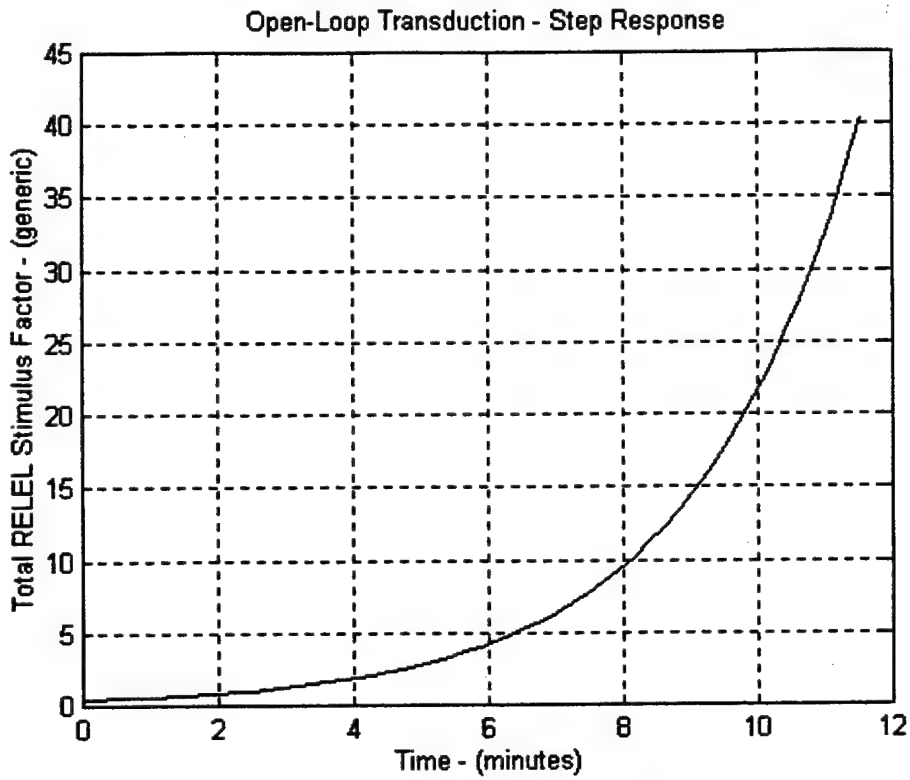

Figure 6.6 - Open-Loop Transduction Dynamics

The second approach is to begin the block diagram reduction not with the $CLTF_{overall}$, but with the open-loop model, $G_{overall}$. If $G_{overall}$ is computed with Equation 6-2 ($G = \frac{CLTF}{1 - CLTF}$), the computed open-loop response displays fast, unstable dynamics that the actual root does not display. The dynamics indicate that the root would spiral at a much higher rate than indicated empirically and in the differential growth simulation (refer back to Figure 6.2). Therefore, an open loop model is designed using the TRANS_FUNC.M routine from Chapter 5 and s-plane design techniques introduced Chapter 2. Additionally, the circumnutational dynamics are removed from both the overall model and the differential growth model in order to

explore just those characteristics in transduction which lead to the primary gravitropic curvatures. Therefore, the s-domain models used in this analysis are Equation 6-7 for the G_{sensor}, Equation 6-6 for G_{dg}, and $G_{overall}$ is designed using the first 100 minutes of the modeled closed-loop response from Equation 5.4 in Chapter 5 (the blue curve in Figure 5.15). Equation 6-13 is the resulting open-loop model with unstable dynamics (spiraling root without feedback) that are designed to approximate the initial stages of a gravitropic response prior to any decrease in curvature acceleration (approximately the 2 hour point, see Figure 5.15 in Chapter 5). Equation 6-14 is the resulting G_{trans} following removal of the G_{sensor} and G_{dg} models. Figure 6.7 is the step response for this altered G_{trans}. Note the change in time constant to a more reasonable value of ≈67 minutes. Also of interest is the fact that the RELEL stimulus does not appear until after the 20 minute point. This delay correlates with the beginning of noticeable gravitropic curvatures beginning within the elongation zone. This model should be used for future work in identifying candidate subsystems of biochemical pathways composing the transduction mechanism.

$G_{overall}$(designed)=

$$\frac{5.3958e\text{-}018\ (s-0.0008678)}{(s+0.001644)\ (s-0.0008678)\ (s-0.00076)\ (s^2 + 0.001968s + 2.509\times10^{-6})\ (s^2 - 0.0005442s + 1.696\times10^{-6})} \qquad (6\text{-}13)$$

G_{trans}(adjusted)=

$$\frac{-4.2228\times10^{-14}s\ (s-0.0008678)\ (s+0.01)}{(s+0.001644)\ (s-0.0008678)\ (s-0.00076)\ (s^2 + 0.001968s + 2.509\times10^{-6})\ (s\text{^}2 - 0.0005442s + 1.696e\text{-}006)} \qquad (6\text{-}14)$$

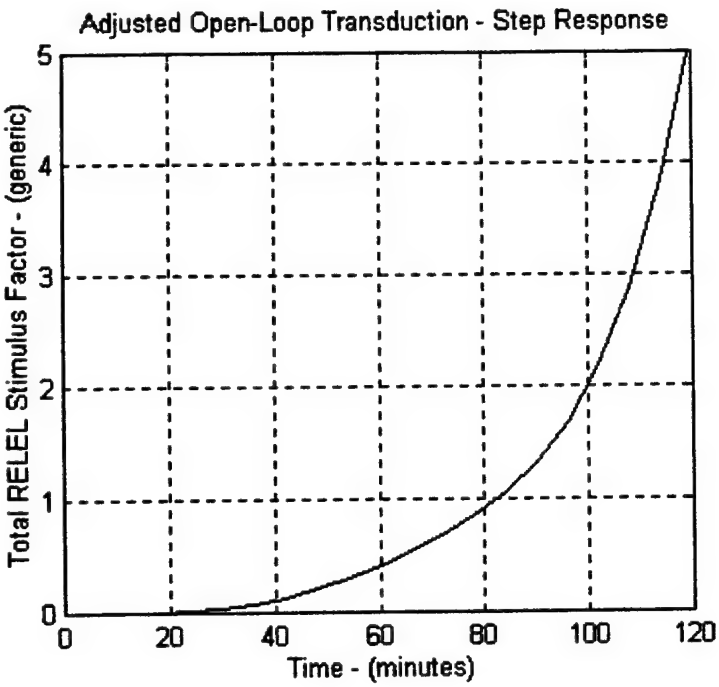

Figure 6.7 - Altered Open-Loop Transduction Dynamics

6.3.3 Discussion of Possible Transduction Subsystems

The transduction mechanism is the most elusive section of the gravitropic system. Biochemical complexity is one reason for this elusiveness. A systems model for transduction will require numerous subsystems, with various interconnections, in order to accurately model the mechanism. One approach is to describe the dynamics of various growth effectors (e.g. auxin, Ca^{++}, etc.) believed to contribute to gravitropism. Descriptions (models) such as this would provide a link from the RELEL perturbations, in the growth response model, to specific hormone (or ion) gradients produced in the transduction mechanism. This would replace the generic RELEL stimulus factor (RSF) used in the present model. Cell volumetric increase begins with an increase in turgor pressure within the cell causing an increase in cell

wall stress until some growth effector causes the bonds between the cell wall polysaccharides (cellulose, hemicellulose, pectin, etc.) to loosen. Once loosened the polysaccharide network of the cell wall is allowed to stretch inelastically, thereby reducing the turgor pressure within the cell (Brett & Waldron, 1990; Taiz & Zeiger, 1991; Alberts *et al.*, 1994). Debate still exists as to the mechanism(s) involved with the cell wall loosening, but a lowered pH appears to be involved. Two equations describe the volumetric growth rate (GR) of a cell under the turgor pressure-relaxation model (Taiz & Zeiger, 1991):

$$GR \equiv \frac{\dot{V}}{V} = \frac{AL_p}{V}\Delta\Psi = L\Delta\Psi \qquad (6\text{-}15)$$

$$GR = m(TP - TP_{min}) \qquad (6\text{-}16)$$

where, $\frac{\dot{V}}{V}$ - a relative volumetric rate of growth { /sec.}

A - cell surface area {μm^2}
L_p - specific hydraulic conductivity of the cell {μm/(sec-Pa)}
L - relative cell hydraulic conductivity { /(sec-Pa)}
TP - turgor pressure {Pa}
OP - osmotic pressure {Pa}
TP_{min} - minimum yield turgor pressure {Pa}
m - growth coefficient (growth signal dependent) { /(sec-Pa)}
ψ - water potential, (TP-OP); ψ_o - outside the cell, ψ_I - inside the cell
$\Delta\psi$ - $(\psi_o - \psi_i) \equiv \Delta TP - \Delta OP$

Solving Equations 6-15 and 6-16 simultaneously produces Equation 6-17:

$$GR \equiv \frac{\dot{V}}{V} = \frac{Lm}{L+m}(\Delta OP - TP_{min}) \qquad (6\text{-}17)$$

This description of growth rate requires extensive empirical data to determine the values for TP_{min}, ΔOP, m, and L for a particular cell type (or location) and any

changes in these parameters under changing concentrations of auxins (or ions). A more practical method would be to describe growth in the elongation zone (isodiametric) of the root as a linear function of a given hormone (or ion).

In the root elongation zone, growth is known to be predominantly isodiametric, especially over the time period of a gravitropic reaction. Therefore, growth may be described in 1-dimension; lengthwise (L):

$$\dot{L} - \dot{L}_i = m_{effector}(C - C_i)$$

$$\frac{\dot{L} - \dot{L}_i}{L_i} = \frac{m_{effector}\Delta C}{L_i}$$

$$\therefore \quad RELEL_{perturbation} = \frac{m_{effector}\Delta C}{L_i} \qquad (6\text{-}18)$$

where, $\dot{L}$ - rate of elongation {μm/min.}
$\dot{L}_i$ - initial rate of elongation {μm/min.}
L_i - initial length of cell {μm}
C - growth effector concentration {M}
$m_{effector}$ - growth effector coefficient {μm/(min-M)}

The change or perturbation in RELEL ($RELEL_{perturbation}$) is the same as that used to model differential growth in Chapter 4 of this thesis and would allow a direct connection between that and a hormone (or ion) gradient produced within transduction processes. In the example of the hormone IAA, once believed to have a logarithmic effect on root growth, it has clearly been shown that roots respond to auxin in an inverse arithmetic manner; small changes in concentration of IAA produce significant growth rate changes (Pilet & Saugy, 1987; Pilet, 1989; Evans, 1991; Evans, 1992; Evans & Ishikawa, 1997). These findings support the efficacy of the above model. Table 6.1 reviews some of the literature from which quantitative values for $m_{effector}$ were derived; data on endogenous concentrations versus growth is scarce.

Table 6.1 - Derivation of $m_{effector}$ from Historical Data

Effector	$m_{effector}$	linear range of C	Reference
Auxin (IAA)	-5.75×10^{6} mm/hr-M	$1\text{-}2.5 \times 10^{-7}$ M	(Pilet & Saugy, 1987)
Abscisic Acid (ABA)	-8.35×10^{5} mm/hr-M	$1.3\text{-}1.0 \times 10^{-6}$ M	(Pilet & Saugy, 1987)

One final proposal for a specific transduction subsystem has been highlighted during this research. Chapter 4 highlighted the significantly large perturbations in RELEL (comparable with that of primary gravitropism) that must be present to produce the circumnutational amplitudes ($\pm 5^{0}$-10^{0}) found empirically, but with the short periods inherent in circumnutation (50-70 minutes). Along with this, Chapter 3 presented the finding that the sensor appears unable to differentiate between these amplitudes of root tip displacement and, therefore, the existence of circumnutation is probably independent of feedback of the root tip angle. Although it may provide insight into the nature of the ionic pathway for gravitropism, a separate transduction mechanism for circumnutational perturbations RELEL parameters may exist. One such idea is proposed in Figure 6.8. The dynamics of circumnutation calls for a wave of growth effector that rotates around the root. The effector could either stimulate or retard growth in specific root tissue, but the overall effect would be a wave of increased turgor pressure in those cells stimulated to higher growth rates. This wave would need to propagate in a circular pattern in the cross-sectional plane of the root. Figure 6.8 shows an example of an effector with a negative $m_{effector}$ value. The proposal includes a relationship between this circumnutational "wave" and the same effector's role in the primary gravitropic RELEL perturbation. These waves are

envisioned as being ionic in nature, again, because of the rapid frequency shown in circumnutation and the slower rates of plant hormone transport (see Chapter 2). The effect these ions have on primary gravitropism can be seen as an established bias created in the oscillatory nature of the original wave following detection of gravistimulation in the root cap. This bias would follow the dynamics found in the differential growth model of gravitropic perturbations.

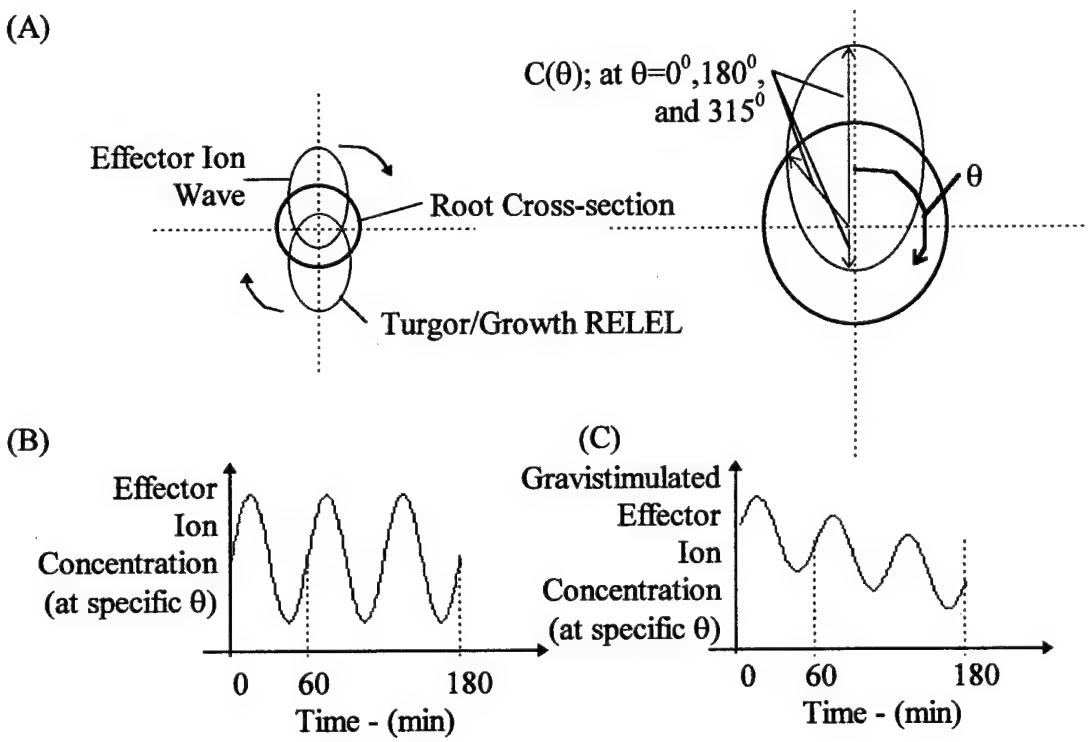

Figure 6.8 - Proposed Ionic Signal Properties
(A) shows the progression of an ion wave around a root circumference along with its subsequent growth wave. The radial distance from the ellipse focus to the surface at a given angle (θ) around the root section represents the concentration of the ion, C(θ). (B) shows a typical time history of this proposed ion wave with dynamics commensurate with those of circumnutation. (C) shows the same ion dynamics linearly-biased because of perception of gravistimulation.

This concept may be mathematical justified by some recent work accomplished by Sharon Lubkin from the Department of Mathematics and Statistics at the University of Pittsburgh (Lubkin, 1994). Although she worked with the morphology of twining stems, the findings should also relate to root circumnutation. As noted earlier in Chapters 2 and 4, root circumnutation displays a strong directional preference, with maize displaying predominantly clockwise oscillations in the root tip. For the above model (Figure 6.8) to apply , some proof must be found to indicate that the wave travel can be supported in one direction and not the other. At the least, the wave propagation should be stable in the preferred direction, but some circumferential asymmetry must exist to make wave travel in the opposite direction unstable. Lubkin showed by applying excitable reaction-diffusion equations operating near a Hopf bifurcation, unidirectional waves are supported on an isotropic annulus, analogous to the outer cortex and epidermis region of the elongation zone. The requirement for a excitable system is easily met in the dynamic biochemical environment of the root. The root sensor has already been shown (see Chapter 3) to be significantly dynamic in the vertical, ungravistimulated state due only to diffusive forces and recently, various enzymes are being shown to follow reactive periods that are not circadian, but mediated only by temperature (Morre & Morre, 1998), a characteristic shared by circumnutation. As detailed in Chapter 8, further research along these lines could further refine the application to the root elongation zone and identify the circumferential asymmetry (such as plasmodesmata concentrations or alignment of cell wall polysaccharides) that can lead to the unidirectional wave stability.

6.4 Summary and Conclusions

The complexity encountered within the topics of this chapter and the numerous assumptions made in order to progress through a legitimate analysis of the transduction mechanism provide confirmation as to the complexity (and probable nonlinearities) inherent to the gravitropic mechanism. The fact that the overall closed-loop model for gravitropism could not be converted algebraically to an open-loop model with dynamics generally close to those expected confirms that the system is not linear nor may it be a single-input-single-output feedback system. However, once the input and output units between the three operating models (sensor, differential growth, and overall) were made comparable and the overall open-loop model was designed to meet the initial dynamics of a gravitropic response, some insight into transduction dynamics was possible.

The various biochemical processes of transduction appear to create a delay of approximately 20 minutes. Additionally, a time constant of $\approx$67 minutes indicates that over 20 minutes are required to double the amount of RELEL stimulus factor. Overall, the delay and this time constant indicate that approximately 40 minutes are required to produce a significant gradient in RELEL stimulus. The fact that curvature appears in maize between 20 and 30 minutes confirms the model set of a separate, parallel ionic pathway. The ionic pathway, with faster dynamics, would transduce a signal into the growth zone faster than the hormonal dynamics would allow. This would allow the root to begin curving prior to the presence of a hormonal (IAA, etc.) gradient. The high frequency circumnutational dynamics provide evidence that this

pathway does exist and that the RELEL perturbations can be just as significant as those produced in primary gravitropism.

Two additional subsystems of the transduction mechanism were introduced. The first is a refinement of the "RELEL stimulus factor" into actual growth mediation caused by various hormones (or ions). The immediate effect of integrating these relationships into the end of the transduction mechanism is to create a multiple-input-multiple-output subsystem. The other subsystem, a "rotating wave" model of ions moving circumferentially around the root might provide insight into the characteristics of the proposed ionic pathway.

CHAPTER 7

SUMMARY AND CONCLUSIONS

7.1 Introduction

This summary is divided into four main subsections; the overall model (Chapter 5), the sensor model (Chapter 3), the differential growth model (Chapter 4), and the inferred characteristics of transduction (Chapter 6). Following this review of previous chapters, a summary section reviews the overall gravitropic model and how this thesis has contributed to the evolving structure of the gravitropic mechanism. A final conclusions section lists the findings that are considered the most significant or novel in this field of research.

7.2 Overall Model

Review of historical modeling of the overall gravitropic response showed a preponderance of imitative approaches to modeling and an almost complete lack of systems engineered models. While the imitative models duplicate the graviresponse very well, they provide little insight into the subsystems creating the response nor the true interconnections among the subsystems. The speed of the gravitropic response in light of relatively slow hormonal transport values, few physical hormonal pathways, and rapidly occurring events following gravistimulation (altered membrane potentials and asymmetric current flow) indicate the need for a model set that contains not a simple, single-input-single-output (SISO) set of subsystems, but a multiple-input-multiple-output (MIMO). At the very least, an "ionic" pathway with a faster response

(and possibly less stable) must operate in parallel with the classic "hormonal" pathway (parallel or feed-forward).

Time-response data acquisition for gravitropism has been 100 years in compilation. However, numerous problems appear to plague the historical data. The research field has begun to address the lack of standardization in environmental control, experimental methods, and gravitropic angle descriptions, but this research has found that further standardization is required. Because of the various frequency components identified within the graviresponses during this research, the historical data have been found to contain sampling rates that are too low to detect certain key components of the responses and the age-old experimental method of time-averaging the graviresponse data is found to mask certain characteristics within the responses. Along these same lines, the prevalent circumnutational dynamic is ignored in most cases, but must not be. Graviresponses must be recorded with continuity between motions prior to gravistimulation and the primary gravitropic reaction after gravistimulation. Additionally, data collection must continue until all transient effects of the graviresponse have concluded. The novel approach of this research was to examine and statistically measure the time response characteristics instead of time-averaging curvature-time data points. It was shown that the averaged time response specifications were significantly different from those characteristics obtained from time-averaged data points.

Time responses were accomplished on 130 Yellow Dent seedlings and 107 Merit seedlings. Synchronization of the initial circumnutational position and

anomalous events caused a loss of approximately 25% of these data sets. Little significant difference was found between the time response specifications of the three length categories investigated for Yellow Dent, but the length categories of Merit show that this cultivar becomes faster and less stable with increasing length. Yellow Dent was also found to be faster and less stable than Merit. Additionally, frequency analysis of the graviresponses indicated a frequency component conspicuous in nearly every data set of both species. This frequency (2.8×10^{-4}Hz) was later found to coincide with the separately witnessed circumnutational dynamics with periods of approximately 1 hour. Frequency analysis of the steady-state portions of the response data sets showed the greater prevalence of this frequency component as the primary gravitropic dynamics reached their conclusion.

7.3 Sensor Model

The feasibility of the maize amyloplast as a statolith was confirmed in a variety of different ways. A single amyloplast sedimenting 0.74 μm equates to 1000x more energy than the thermal background noise of the columella cell. The calculated tension within an actin fiber attached to an amyloplast approaches the tensions, measured in current patch-clamp experiments that open mechano-sensitive channels. A single amyloplast sedimenting only 0.025 μm converts the equivalent amount of energy from potential to kinetic as the hydrolysis of a single ATP molecule produces. These energy and force comparisons, along with the low diffusivity and Peclet ratios indicate that the amyloplasts are susceptible enough to gravity to serve as statoliths; the gravity sensors.

After establishing the feasibility of the statolith as a sensor, a force balance model was created. This model was intended to prove or disprove Model Set #1 for amyloplast-cytoskeletal interaction; the "tethered" model (see Figure 3.2 #1). Two equations of motion (EOMs) result and are shown in Equations 3-13 (unforced EOM; no gravity) and 3-15 (gravity forced) of Chapter 3. A computer simulation of the gravity-forced EOM was accomplished which showed that an actin property correction factor of 10^{-6} was required to achieve amyloplast sedimentation rates on the order of 1-20 μm/min. Additionally, the unforced simulation model was used in an attempt to duplicate the TEXUS rocket experiments of Volkmann and Sievers (Volkmann *et al.*, 1991). Duplication of results was accomplished only after the actin elastic modulus was decreased 10^{6}-fold. The fact that both of these simulations required the same adjustment to actin properties indicated a need to correct the actin property or correct the model set of amyloplast-cytoskeletal interaction. Because the methods used to measure the actin properties appeared to be above reproach and an independent determination of this value is beyond the scope of this thesis, Model Set #1 was rejected and work continued toward identifying a more appropriate model set.

With the goal of refining the amyloplast-cytoskeletal interaction model set, an in depth study was made of the columella cell internal environment by using the amyloplasts as 2 μm probes. A total of 566 amyloplasts were observed in their sedimentation through 75 different columella cells. Additionally, the diffusive motions of 10 cells (43 amyloplasts) were studied. An extensive MATLAB script file was developed that processes the raw position versus time coordinate information into

various position and velocity profile analysis. Six separate data formulations that test, visualize, and quantify four different behaviors of amyloplast motion were constructed. The four behaviors of amyloplast motion that were investigated were (1) channeling behavior, (2) group movement behavior, (3) velocity within specific cellular domains, and (4) terminal velocity behavior. Three different root length categories were included in order to identify any parameters that may be root length/age dependent.

The results of the sedimentation study indicate that only the absolute velocity of sedimentation is significantly different among the length categories. Because neither the x-velocities nor the y-velocities were found to be significantly different, it appears that the length of the root does not significantly affect the amount of cytoskeletal interaction experienced by the amyloplasts, but that it may significantly effect the viscosity (η) of the cytoplasm, with the youngest roots showing the lowest η followed by an increase in the 30-39 mm length category and then a decrease again as the root ages further. Overall, side-to-side and distal-to-basal profiles produce sedimentation velocities significantly lower than those witnessed in distal-to-side profiles. This indicates that a central obstruction within the cell is present to slow the plastids that must traverse the columella's central regions. It is proposed that this obstruction is of cytoskeletal origin; a more dense region of cytoskeletal network being toward the cell center with the cell periphery being a more "privileged" zone of amyloplast movement. The data on channeling behavior confirmed this model set.

The conclusion that root length/age doesn't affect the cytoskeletal interaction is confirmed by the fact that channeling behavior was shown to be only marginally

affected by root length. Additionally, channeling behavior was significantly different between normal roots and those treated with cytochalasin D (CD). The roots treated with CD had significantly lower channeling coefficients which indicates that the central obstructions which lead to channeled motion are associated with actin. Amyloplasts that must undergo motion through the central regions of the cell display lower velocities at the upper part of the cell as if obstructed by a central domain that blocks their free vertical sedimentation. Channeling appears to be the result of mutual action on the part of the amyloplasts to create a local deformation in the cytoskeletal network until a "pore" can be created to allow passage of the group of statoliths. The point of closest approach of these channeling plastids, the point of greatest channeling, occurs on the average at approximately cell vertical center.

The group behavior of the amyloplasts was also studied and established in two separate ways. Y-position over time was found to be highly correlated (correlation coefficient > 0.95). Keeping in mind the highly obstructive environment of sedimentation established with the channeling behaviors, this appears to strongly indicate that the plastids act as a group. However, whether this group action is because of direct physical connection between the plastids or indirect mutual motion caused by the group effort at deforming the cytoskeletal network is still open for debate. Correlation between y-velocity over time, although much lower because of inherent data collection noise and diffusive forces, appears large enough (≈ 0.6) to confirm the notion of group action among the plastids. Additionally, this correlation is found to be significantly higher in distal-to-side profiles and, in side-to-side (or distal-

to-basal) profiles, those roots treated with CD show significantly higher correlation. These two significant differences confirm the hypothesized model set of a centrally higher concentration of actin fibers leaving a privileged zone of movement along the cell periphery (especially the distal end).

A final confirmation of the model set is found when examining the amyloplast velocity as it passes through five separate vertical domains of the cell. Amyloplasts undergoing distal-to-side sedimentation show consistently higher velocities in the top 4 domains than those amyloplasts sedimenting through the central region of the cell (side-to-side and distal-to-basal profiles). Distal-to-side profiles show monotonically decreasing velocities as the statolith descends within the cell. Side-to-side (or distal-to-basal) profiles begin with the slowest speed at the top of the cell, reaching a maximum in sector 3, the cell center, coincident with the point of maximum channeling. The application of CD creates a significant increase in the second sector velocities of centrally traversing profiles. Again, this appears to indicate that the central obstruction is actin as this increase in second sector velocity is probably due to a slight increase in actin network pore-size.

During the study of viscosity and diffusion, data found both with velocity matching techniques and with diffusion analysis appear to indicate a cytoplasmic viscosity of $\approx$34 cp. This is approximately 50% higher than the assumptions of Chapter 1, lowering the diffusion coefficient and placing the Peclet number at a more reasonable value of 10. Additionally, no significant difference was found in overall plastid motion between vertical root caps and those rotated 10° to the gravity vector.

This indicates that the sensor may not be able to detect a root tip angle of ±10° and therefore, circumnutational oscillations may not be subject to root tip angle feedback.

The final model set chosen to describe the sensor is a modification of the "network" model (see Figure 3.2, #3). The modification requires an increase in the concentration of actin toward the cell center. This higher gradient of amyloplast-cytoskeletal interaction in the columella central regions, with more privileged zones of movement along the cell periphery, is indicated by virtually every data formulation of the sedimentation study. Analysis of a cylindrical cell model with evenly spaced actin attachments along the cell surface indicates that 3726 actin fibers, 3% by cell volume, would provide the appropriate amount of elastic accelerations to duplicate the average velocities seen in the empirical study.

7.4 Differential Growth Model

Both elastic and inelastic contributions to the actual curvature in the root were investigated. Elastic contributions were found to be negligible. Concentrating on inelastic or differential growth effects led to the selection of a model set that is analogous to bi-metallic bending. The elemental contributions of elongation in finite lengths of material separated by a constant distance provide the mathematical basis for the model set. The existence of RELEL (relative elemental elongation) data is advantageous to the selection of this model set. RELEL data provide relative elongation growth rate for finite segments of length along the root. Also advantageous is the fact that the RELEL data can be accurately estimated as a

Gaussian curve with parameters $RELEL_{max}$, μ mean position of $RELEL_{max}$ along the root, and σ (standard deviation of the curve) fully describing the growth data.

The finite-elemental growth model was programmed using MATLAB so that both quantitative analysis and visualization could be accomplished. Historical RELEL data were used, but found to be lacking in standardization and time-variant varieties. Five different model/simulation studies were accomplished; vertical growth (to test the basics of the model), time-invariant gravicurvatures, a sensitivity study, time-variant curvatures, and circumnutational effects. The time-invariant gravicurvatures used single, averaged, and weighted averages of historical RELEL data, and the results highlighted the sensitivity of the resulting root curvature characteristics to specific RELEL parameters. Following a thorough sensitivity study, the curvature profiles were found to be extremely sensitive to small changes in any or all of the three RELEL parameters. This appears to be the primary reason why graviresponses can vary widely with very small differences in methods and environmental conditions. Time variant RELEL data are extremely rare and need to be gathered in future research. However, the model/simulation produces results comparable with existing historical experiments. Finally and most strikingly, it was found that in order to create circumnutational effects comparable with empirical findings (5° - 10° amplitudes with periods of $\approx$60 minutes), perturbations in vertical RELEL conditions need to be as large as those seen in primary gravitropism. This indicates that a faster, ionic pathway does exist in the root that can affect root RELEL as significantly as the primary gravitropic auxin gradients.

7.5 Inferences on Transduction

The process of seeking characteristics of the transduction mechanism required the sensor and differential growth models to be simplified and linearized. Additionally, the dual-path nature of the gravitropic mechanism, indicated by multiple findings both historically and in this research, had to be ignored in order for the linear system operations to provide a reduced model for the transduction mechanism. However, this process, although resulting in a loss of accuracy in the modeling, was still useful in highlighting some interesting characteristics of the elusive transduction system. The delay and time-constant of the transduction response provides further proof that a hormonal (single-path) model of transduction cannot possibly create the growth response within the time known for appearance of the initial gravitropic curvature. Additionally, arguments were made that the system model set may not only require multiple feed-forward paths, but also multiple feedback pathways.

7.6 Summary

Figure 7.1 outlines the evolving structure of the gravitropic mechanism model. Throughout this research effort, the mechanism has developed from a simple "black-box" into various models with increasing levels of complexity. Results from the historical literature and current experiments pertaining to the gravitropic sensor, curvature mechanism, and the overall response characteristics were used to evolve the model through each progressive level of complexity.

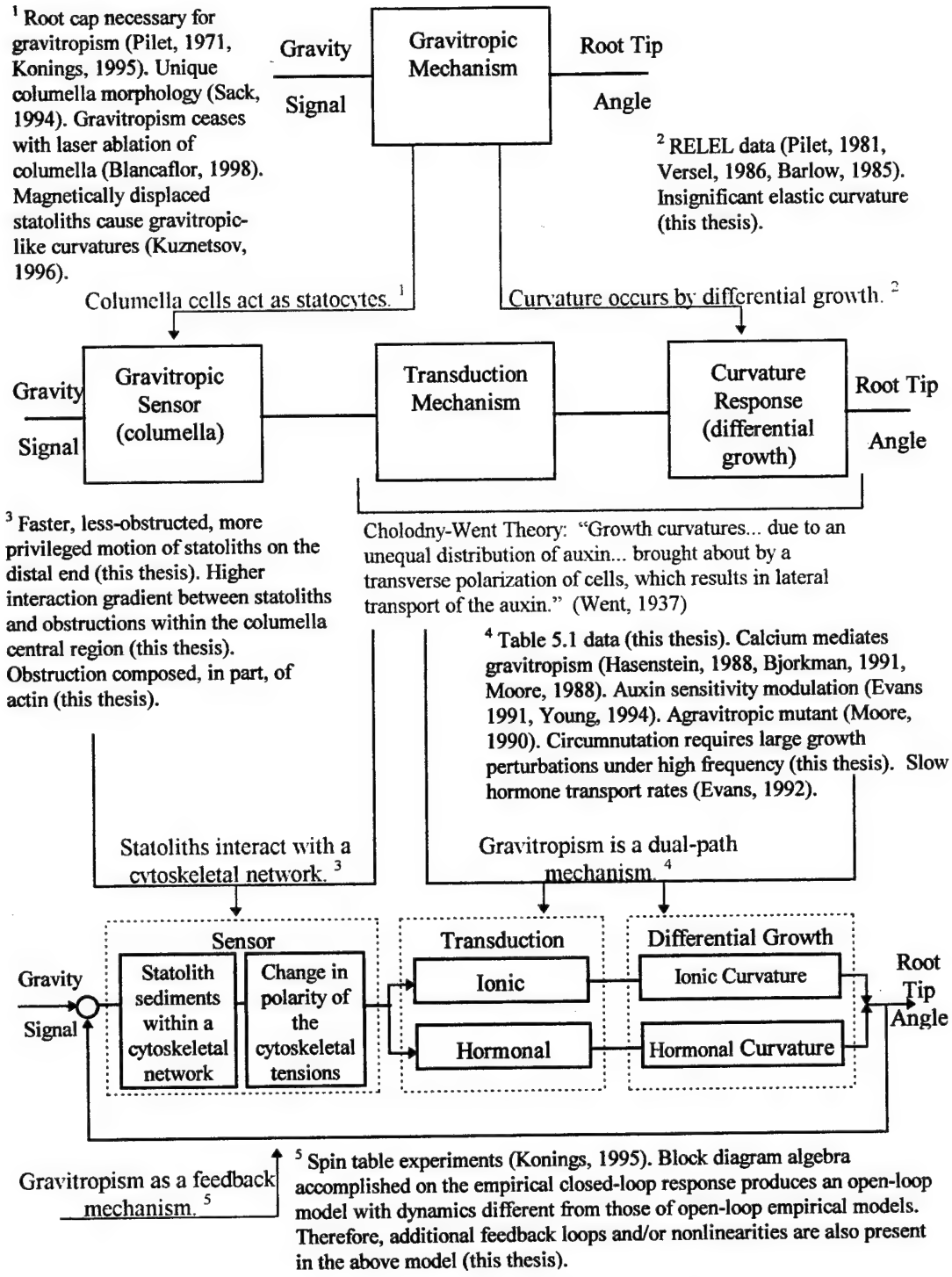

Figure 7.1 - The Evolving Model of Plant Root Gravitropism
This figure diagrams the evolving structure of the root gravitropic mechanism. Each arrowhead in blue identifies a point where logical inference or experimental results have indicated an additional modification to the present model structure. Some of the data sources that infer the modification are identified and summarized where indicated by superscripts.

The model evolved from a simple, input-to-output black-box into a system with three sub-mechanisms: (1) sensor, (2) transduction, and (3) curvature response. The sensor model is in line with the classic starch-statolith hypothesis (see Section 2.4.1) while classical models concerning the last two subsystems (Cholodny-Went Theory) appear incomplete. Analyses of the dynamics of amyloplast motion throughout the columella cell accomplished in this thesis provide more insight into the interaction between the statoliths and the cytoskeletal network of the cell. Numerous pieces of circumstantial evidence, both observed and found in the historical literature, also indicate the existence of a dual response pathway governing gravitropic transduction and growth. One pathway, the ionic pathway, which was heretofore uncharacterized, provides response characteristics of higher frequency, a faster time constant, and less stability than those hormonal characteristics empirically established through decades of research supporting the classic Cholodny-Went Theory. These response characteristics could help explain the numerous gravitropic observations established over the years that cannot be explained through hormonal signaling alone, such as rapid membrane potential and current pattern alterations following gravistimulation, the sensitivity of the graviresponse to Ca^{++} and other ions, cellular specificity to auxin effects, and curvature occurring earlier than can be accounted for by established hormone transport rates.

7.7 Conclusions

This research has established the efficacy of a gravitropic system model with multiple feed-forward and possibly multiple feedback pathways. The overall system

modeling work has highlighted the need for data collection and analysis that takes into account the frequency components of the gravitropic response and the inaccuracies inherent with averaging the time-curve data. The work to model the sensor has produced a coherent picture of the amyloplast-cytoskeletal interactions that goes well beyond the classic "tethered" model. A model set that includes an increasing gradient of actin fibers within the central regions of the columella cell is an appropriate model set that can duplicate the empirical behaviors of channeling, group action, and velocity changes within different cellular regions. Additionally, the sensor modeling efforts have produced a more refined value for maize cytoplasmic viscosity and has shown that circumnutational motion is likely to be independent of root tip angle feedback. Finally, the surprising result that circumnutationally-derived RELEL perturbations must be of the same magnitude (but higher frequency) than those of primary gravitropism confirms the existence of a faster, ionically driven, feed-forward signal pathway within the root.

CHAPTER 8

RECOMMENDED FURTHER RESEARCH

8.1 Introduction

Toward the goal of providing more quantitative data for improved model resolution, this chapter proposes some areas for further research. The suggested research topics are categorized by the specific model the research is intended to enhance; the overall gravitropic model, the gravitropic sensor model, and the differential growth model.

8.2 Overall Model

Because of the effects of time-point averaging the gravitropic response curves as discussed in Chapter 5 of this thesis, it is highly recommended that the following experiments be accomplished with the data analysis including the oscillations prior to gravistimulation and well after the steady state curvature is attained. Time-curvature data points should not be averaged, but the time response specifications (T_p, PO, frequency components, etc.) can be analyzed to develop conclusions concerning experimental groups.

The first experiment proposed is designed to expand the database of response dependency on various environmental parameters. Within a given species (e.g. Yellow Dent) and a given age/length category(e.g. 20-30 mm), develop the time-response specifications for corn growing in different growth media such as sucrose, calcium, IAA, humidity, temperature, and light conditions. Again, as with the work done for

this thesis, most of these conditions have been examined before, but not without time-curvature data point averaging and without time-response specification analysis.

The next experiment proposed is designed to further pinpoint the columella cells as the predominant sensor in the gravitropic mechanism versus a systemic stress distribution sensor. Graviresponse curvatures should be examined within a given species (e.g. Yellow Dent) and a given age/length category(e.g. 20-30 mm), but in different mounting media. Gravicurvature time response experiments in this thesis used only a cantilevered configuration of the corn root responding to gravity. If this response is significantly altered when the root is supported, for instance, on a plate of agar, then the response mechanism might also include a systemic stress distribution component.

Similarly, another area of research could investigate the memory component of the graviresponse mechanism, by developing a finer value for corn's presentation time. Results in this thesis indicate that presentation time could be simply an artifact of experimental accuracy and if the amyloplasts are truly the statoliths of the system, and they begin their movement almost instantly, then presentation time or the minimum time for gravistimulus to produce a gravitropic response could be significantly closer to zero than presently believed. To prove this, a microgravity experiment along with a ground experiment based on use of a clinostat could be used to refine the presentation time for corn. Previously, presentation time was developed by giving a small dose of gravistimulation to a root and seeing if it reacted. As increasing amounts of gravistimulation produced more curvature in progressive roots, a regression line was

placed on the curvature vs. duration-of-gravistimulation plot and the intercept of this line to the duration-of-gravistimulation axis was determined as the presentation time. This proposed research provides smaller and smaller durations of gravistimulation to a single root separated by times of microgravity or clinorotation. If the curvature response appears to result as cumulative effect of gravistimulation versus the actual length of the gravistimulation pulses, then a memory component to either the sensor or the transduction process is highlighted, and presentation time becomes only an artifact of experimental procedures. Noting the location of statoliths within the statocytes during various stages of this experiment would also be noteworthy. The Sievers and Hejnowicz laboratories have done some unpublished work in this area with cress and a clinostat.

The development of the parallel mechanisms of ionic and hormonal paths in this thesis, brings the need to develop experiments designed to further prove or disprove such a model's validity. The analysis of a corn cultivar or mutant that displays the characteristics of one path, but not the other would go far in establishing the hypothesis of the dual path system. Specifically, the analysis of a species that displayed no pre-gravistimulation oscillations, no post-steady-state oscillations, and no rapid shift in electrical current symmetry following gravistimulation, but continued to display the predominant form of gravitropism could establish the parallel and independent nature of this dual path model.

Finally, it is suggested that if a long-term study of gravitropism is desired, computational software should be obtained (or designed) to convert directly from

digital pictures to curvature data files. One such computational package is available from the Michael Evans laboratory at Ohio State University; the SECANT and ADAPT software (Evans & Ishikawa, 1997).

8.3 The Sensor

Changing the environment in which the amyloplasts sediment could lead to further understanding of the amyloplast-cytoskeletal interactions taking place within the columella cell. Research suggestions along this direction include the study of sedimentation characteristics following clinorotation. Since previous experiments have shown detrimental effects of clinorotation (Smith, 1996), sedimentation characteristics might be mediated by the clinorotation process. Likewise, the sedimentation characteristics might alter significantly upon introduction of actin polymer-destabilizing drugs such as the cytochalasins and latrunculin A, a marine sponge derivative. Alternatively, sedimentation characteristics might be equally mediated by the introduction of actin stabilizing agents such as potassium, magnesium, or the phalloidins. Further study is also possible on untreated columella cells.

With the significant channeling effects seen during sedimentation of the statoliths, it is suggested that future video capture the side-to-side (and distal-to-basal) profiles followed immediately by turning the specimen 180^0 and capturing the sedimentation in reverse. The aim of this study is to determine if the "channels" are caused by permanent features of the cell's interior or a temporary deformation of the cytoskeleton created by group action of the statoliths on the actin network. With the same goal, a 3-D reconstructive EM study could be accomplished on those cell

specimens whose sedimentation profiles display channeling effects. Fixation would have to occur immediately following the video procedures outlined in this thesis.

Toward the goal of enhancing the sensor model, the diffusion study of section 3.5.3 could be expanded to compare the diffusion motions between vertical roots and those gravistimulated at 15^0, 20^0, and higher. Since, this thesis showed no significant difference between vertical root diffusive motions of the statoliths and their motions when gravistimulated 10^0, it would be interesting to note the point where significant differences do occur and this study could further refine the duality of the response paths as it provides further evidence of circumnutation's relationship to gravitropism.

The need for more detailed finite-element modeling was introduced in Chapter 3. Refinement of a finite-element model could lead to better simulation of the statolith interaction with the columella cell boundaries, its cytoskeleton, and other plastids, providing a better imitation of the amyloplast dynamics. This model could better simulate the nuances of amyloplast motion and provide an integrated measure of tensions occurring within the actin network, including how these tensions are perturbed with gravistimulation.

8.5 Differential Elongation

As introduced in Chapter 4, refined RELEL data for the maize root are desired. The RELEL data taken following gravistimulation should not be time-averaged over long sampling periods, but should be within short sampling periods ($\approx$15 min). This will provide refined RELEL data with temporal dependence, because as shown in Chapter 4, data on the time progression of RELEL curves following

gravistimulation is sparse. Additionally, in order to establish coefficients that weight the RELEL data based upon environmental factors (temperature, water content, sucrose and other nutrient, electrolytes, etc.), a study should be undertaken that establishes the effect that these various environmental factors have on the vertical RELEL, the circumnutationally-perturbed RELEL, and the gravitropically-perturbed RELEL. The study of Ca^{++} and IAA effects on the various root cell types (distance from the root tip) and how time mediates these effects should establish a link between the final stages of transduction and the differential growth mechanism.

8.6 Transduction

Circumnutation is assumed in this thesis not to be a result of feedback of the tip angle. This may not be the case. An experiment could be accomplished to verify this hypothesis. The root must be mounted on rotating platform in the vertical plane. In response to the circumnutational curvatures of the root tip, the root could be turned in order to keep the root aligned with the original angle of tip position. Recording the rotation angles induced on the rotating platform in order to maintain root tip angle is comparable to measuring the 2-dimensional circumnutational motions. The resulting circumnutational dynamics would be effectively without a feedback loop for tip angle and are then compared with circumnutational controls. Understanding how circumnutations are (or are not) related to gravitropic reactions could provide some keen insight into the gravitropic mechanism.

An additional experiment geared toward integrating how circumnutational dynamics could be related to gravitropic dynamics is to establish a 3-D video study of

the circumnutational characteristics of the root while it undergoes a gravitropic reaction. With one camera mounted to capture the primary gravitropic reaction and another oriented toward the axis of the root to capture circumnutations, it would be interesting to note any changes to the circumnutational dynamics during a graviresponse. Fidelity would require that the second camera "track" the root tip as it undergoes downward curvature. Figure 8.1 roughly diagrams this suggested experiment. Since it is already noted that the primary graviresponse "washes out" the dynamics of circumnutation in the root's vertical plane, this experiment could verify that it truly is a superposition of dynamics and not that circumnutation ceases (all planes) during a graviresponse.

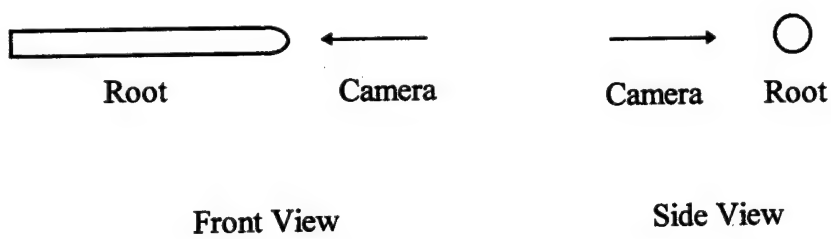

Figure 8.1 - Circumnutations During Gravitropism

Lubkin's work on the stability of wave propagation around the circumference of plant tissue (Lubkin, 1994) could be applied to the root elongation zone in order to discover the results for the root's specific tissues and identify the excitable phenomena or discrete oscillators within the root required to initiate the wave propagation. Since directional (around the root circumference) stability requires some level of circumferential asymmetry (such as plasmodesmata concentrations or alignment of cell

wall polysaccharides) that leads to unidirectional wave stability, research could be directed toward identifying such an asymmetry in the tissues of the root elongation zone.

8.7 Summary and Conclusions

The modeling of the root gravitropic mechanism is obviously not an easy task. Plenty of work remains to be done to bring us closer to a comprehensive model that explains many of the nuances of gravitropism. The work has only started.

BIBLIOGRAPHY

Agoram, B. (1998). Mathematical Model of Amyloplast Sedimentation in Root-cap Cells, University of Colorado.

Alberts, B., Bray, D., Lewis, J., Raff, M., Roberts, K. and Watson, J.D. (1994) Molecular Biology of the Cell. Garland Publishing, Inc., New York.

Bandurski, R.S., Schulze, A., Dayanandan, P. and Kaufman, P.B. (1984) Response to Gravity by *Zea mays* Seedlings. *Plant Physiology,* **74**:284-288.

Barlow, P.W., Brain, P. and Adam, J.S. (1989) Differential Growth and Plant Tropisms: A Study Assisted by Computer Simulation. *Environmental and Experimental Botany,* **29**:71-83.

Barlow, P.W., Parker, J.S., Butler, R. and Brain, P. (1993) Gravitropism of Primary Roots of *Zea mays* L. at Different Displacement Angles. *Annals of Botany,* **71**:383-388.

Barlow, P.W. and Rathfelder, E.L. (1985) Distribution and Redistribution of Extension Growth Along Vertical and Horizontal Gravireacting Maize Roots. *Planta,* **165**:134-141.

Barlow, P.W. and Sargent, J.A. (1978) The Ultrastructure of the Regenerating Root Cap of *Zea mays* L. *Annals of Botany,* **42**:791-799.

Behrens, H.M., Gradmann, D. and Sievers, A. (1985) Membrane-potential Responses Following Gravistimulation in Roots of *Lepidium sativum* L. *Planta,* **163**:463-472.

Behrens, H.M., Weisenseel, M.H. and Sievers, A. (1982) Rapid Changes in the Pattern of Electric Current Around the Root Tip of *Lepidium sativum* L. Following Gravistimulation. *Plant Physiology,* **70**:1079-1083.

Bjorkman, T. (1988) Perception of Gravity by Plants. *Advances in Botanical Research,* **15**:1-41.

Bjorkman, T. and Cleland, R.E. (1991) The Role of Extracellular Free-calcium Gradients in Gravitropic Signalling in Maize Roots. *Planta,* **85**:379-384.

Bjorkman, T. and Leopold, A.C. (1987) An Electric Current Associated with Gravity Sensing in Maize Roots. *Plant Physiology,* **84**:841-846.

Blancaflor, E.B., Fasano, J.M. and Gilroy, S. (1998) Mapping the Functional Roles of Cap Cells in the Response of Arabidopsis Primary Roots to Gravity. *Plant Physiology,* **116**:213-222.

Buchen, B., Hejnowicz, Z., Braun, M. and Sievers, A. (1991) Cytoplasmic Streaming in *Chara* Rhizoids. *Protoplasma,* **165**:121-126.

Caspar, T. and Pickard, B.G. (1989) Gravitropism in a Starchless Mutant of *Arabidopsis*. *Planta,* **177**:185-197.

Cosgrove, D.J. (1990) Gravitropism of Cucumber Hypocotyls: Biophysical Mechanism of Altered Growth. *Plant, Cell and Environment,* **13**:235-241.

Ding, J.P. and Pickard, B.G. (1993) Mechanosensory Calcium-slective Cation Channels in Epidermal Cells. *The Plant Journal,* **3**:83-110.

Dorf, R.C. (9180) Modern Control Systems. Addison-Wesley Publishing Co., Reading, MA.

Dutcher, F.R., Hess, E.L. and Halstead, T.W. (1994) Progress in Plant Research in Space. *Advances in Space Research,* **14**:159-171.

Edwards, K.L. and Pickard, B.G. (1987) Detection and Transduction of Physical Stimuli in Plants. *The Cell Surface in Signal Transduction,* **H12**:41-66.

Erickson, R.O. and Sax, K.B. (1956) Elemental Growth Rate of the Primary Root of *Zea mays*. *Proceedings of the American Philosophical Society,* **100**:487-498.

Eshbach, O.W. and Souders, M., Eds. (1975) Handbook of Engineering Fundametals. Wiley Engineering Handbook Series. John Wiley & Sons, New York.

Evans, M.L. (1991) Gravitropism: Interaction of Sensitivity Modulation and Effector Redistribution. *Plant Physiology,* **95**:1-5.

Evans, M.L. (1992) What Remains of the Cholodny-Went Theory? *Plant, Cell and Environment,* **15**:767-768.

Evans, M.L. and Ishikawa, H. (1997) Cellular Specificity of the Gravitropic Motor Response in Roots. *Planta,* **203**:S115-S122.

Evans, M.L. and Ishikawa, H. (1997) Computer Based Imaging and Analysis of Root Gravitropism. *Gravitational and Space Biology Bulletin,* **10**:65-73.

Evans, M.L., Moore, R. and Hasenstein, K.-H. (1986) How Roots Respond to Gravity. *Scientific American,* **December**:112-119.

Falke, L., Edwards, K.L., Misler, S. and Pickard, B.G. (1986) A Mechanotransductive Ion Channel in Patches from Cultured Tobacco Cell Plamalemma. *Plant Physiology (Suppl),* **80**:9.

Gittes, F., Mickey, B., Nettleton, J. and Howard, J. (1993) Flexural Rigidity of Microtubules and Actin Filaments Measured from Thermal Fluctuations in Shape. *The Journal of Cell Biology,* **120**:923-934.

Green, P.B. (1976) Growth and Cell Pattern Formation on an Axis: Critique of Concepts, Terminology, and Modes of Study. *Botanical Gazette,* **137**:187-202.

Guharay, F. and Sachs, F. (1984) Stretch-activated Single Ion Channel Currents in Tissue-cultured Embryonic Chick Skeletal Muscle. *Journal of Physiology,* **352**:685-701.

Guikema, J.A., Hilaire, E. and Odom, W.R. (1993) Cytoskeleton-Amyloplast Interactions in Sweet Clover. *Transactions of the Kansas Academy of Science,* **96**:13-19.

Haberlandt, G. (1900) Uber die Perzeption des Geotropischen Reizes. *Ber Deutsch Bot Ges,* **18**:261-272.

Hager, A., Debus, G., Edel, H.-G., Stransky, H. and Serrano, R. (1991) Auxin Induces Exocytosis and the Rapid Synthesis of a High-Turnover Pool of Plasma-membrane H^+-ATPase. *Planta,* **185**:527-537.

Hasenstein, K.H. and Evans, M.L. (1988) Effects of Cations on Hormone Transport in Primary Roots of *Zea mays*. *Plant Physiology,* **86**:890-894.

Hasenstein, K.-H. and Evans, M.L. (1986) Calcium Dependence of Rapid Auxin Action in Maize Roots. *Plant Physiology,* **81**:439-443.

Hibbeler, R.C. (1993) Statics and Mechanics of Materials. Prentice Hall, Englewood Cliffs, NJ.

Ishikawa, H. and Evans, M.L. (1990) Gravity-induced Changes in Intracellular Potentials in Elongating Crotical Cells of Mung Bean Roots. *Plant and Cell Physiology,* **31**:457-462.

Ishikawa, H. and Evans, M.L. (1992) Induction of Curvature in Maize Roots by Calcium or by Thigmostimulation. *Plant Physiology,* **100**:762-768.

Ishikawa, H. and Evans, M.L. (1994) Correlations Between Changes in Electrical Parameters and Changes in Cell Elongation Rates in Gravistimulated Roots. *Advances in Space Research,* **14**:125-133.

Ishikawa, H. and Evans, M.L. (1995) Specialized Zones of Development in Roots. *Plant Physiology,* **109**:725-727.

Ishikawa, H., Hasenstein, K.H. and Evans, M.L. (1991) Computer-based Video Digitizer Analysis of Surface Extension in Maize Roots. *Planta,* **183**:381-390.

Iversen, T.-H. (1969) Elimination of Geotropic Responsiveness in Roots of Cress (*Lepidium sativum*) by Removal of Statolith Starch. *Physiologia Plantarum,* **22**:1251-1262.

Janmey, P.A., Euteneuer, U., Traub, P. and Schliwa, M. (1991) Viscoelastic Properties of Vimentin Compared with Other Filamentous Biopolymer Networks. *The Journal of Cell Biology,* **113**:155-160.

Kernan, M. (1997) The Molecular Basis of the Mechanical Senses: One Mechanism or Many? *The Journal of NIH Research,* **9**:32-36.

Kiss, J.Z., Hertel, R. and Sack, F.D. (1989) Amyloplasts are Necessary for Full Gravitropic Sensitivity in Roots of *Arabidopsis thaliana*. *Planta,* **177**:198-206.

Kiss, J.Z., Wright, J.B. and Caspar, T. (1996) Gravitropism in Roots of Intermediate-starch mutants of *Arabidopsis*. *Physiologia Plantarum,* **97**:237-244.

Klaus, D.M., Todd, P. and Schatz, A. (1998) Functional Weightlessness During Clinorotation of Cell Suspensions. *Advances in Space Research,* **21**:1315-1318.

Konings, H. (1995) Gravitropism of Roots: an Evaluation of Progress During the Last Three Decades. *Acta Botanica Neerlandica,* **44**:195-223.

Kordyum, E.L. (1994) Effects of Altered Gravity on Plant Cell Processes: Results of Recent Space and Clinostatic Experiments. *Advances in Space Research,* **14**:77-85.

Kryder, A.M. and Evans, M.L. (1990). Computerized Analysis of Root Growth Parameters: Characterization of Circumnutation and Its Relationship to Gravity Sensing. Columbus, OH, Ohio State University.

Kuznetsov, O.A. and Hasenstein, K.H. (1996) Intracellular Magnetophoresis of Amyloplasts and Induction of Root Curvature. *Planta,* **198**:87-94.

Leach, H.W. and Schoch, T.J. (1961) Structure of the Starch Granule: II Action of Various Amylases on Granular Starches. *Cereal Chemistry,* **38**:34-46.

Lee, J.S., Mulkey, T.J. and Evans, M.L. (1983) Gravity-Induced Polar Transport of Calcium Across Root Tips of Maize. *Plant Physiology,* **73**:874-876.

Lee, J.S., Mulkey, T.J. and Evans, M.L. (1983) Reversible Loss of Gravitropic Sensitivity in Maize Roots After Tip Application of Calcium Chelators. *Science,* **220**:1375-1376.

Lee, J.S., Mulkey, T.J. and Evans, M.L. (1984) Inhibition of Polar Calcium Movement and Gravitropism in Roots Treated with Auxin-transport Inhibitors. *Planta,* **160**:536-543.

Leopold, A.C. and Wettlaufer, S.H. (1988) Diagravitropism in Corn Roots. *Plant Physiology,* **87**:803-805.

Lubkin, S. (1994) Unidirectional Waves on Rings: Models for Chiral Preference of Circumnutating Plants. *Bulletin of Mathematical Biology,* **56**:795-810.

Mason, D.W. (1976) A Diffusion Driven Instability in Systems that Separate Particles by Velocity Sedimenation. *Biophysical Journal,* **16**:407-416.

McClure, B.A. and Guilfoyle, T.J. (1989) Tissue Print Hybridization. A Simple Technique for Detecting Organ- and Tissue-specific Gene Expression. *Plant Molecular Biology,* **12**:517-524.

Meuwly, P. and Pilet, P.E. (1991) Local Treatment with Indole-3-acetic Acid Induces Differential Growth Responses in *Zea mays* L. Roots. *Planta,* **185**:58-64.

Milhorn, H.T.J. (1966) The Application of Control Theory to Physiological Systems. W. B. Saunders Company, Philadelphia.

Millner, P.A. (1995) The Auxin Signal. *Current Opinion in Cell Biology,* **7**:224-231.

Momonoki, Y.S. (1997) Asymmetric Distribution of Acetylcholinesterase in Gravistimulated Maize Seedlings. *Plant Physiology,* **114**:47-53.

Montgomery, D.C. and Runger, G.C. (1994) Applied Statistics and Probability for Engineers. John Wiley & Sons, Inc., New York.

Moore, R. (1983) A Morphometric Analysis of the Ultrastructure of Columella Statocytes in Primary Roots of *Zea mays* L. *American Journal of Botany,* **51**:771-778.

Moore, R. (1986) Calcium Movement, Graviresponsiveness, and the Structure of Columella Cells in Primary Roots of Amylomaize Mutants of *Zea mays*. *American Journal of Botany,* **73**:417-426.

Moore, R. (1986) A Morphometric Analysis of the Redistribution of Organelles in Columella Cells of Horizontally-oriented Roots of *Zea mays*. *Annals of Botany,* **57**:119-131.

Moore, R. (1987) Root Gravitropism in a Cultivar of *Zea mays*Whose Columella Cells Contain Starch-deficient Amyloplasts. *Annals of Botany,* **59**:661-666.

Moore, R. (1989) Root Graviresponsiveness and Cellular Differentiation in Wild-type and a Starchless Mutant of *Arabidopsis thaliana*. *Annals of Botany,* **64**:271-277.

Moore, R. and Evans, M.L. (1986) How Plants Perceive and Respond to Gravity. *American Journal of Botany,* **73**:574-587.

Moore, R., Evans, M.L. and Fondren, W.M. (1990) Inducing Gravitropic Curvature of Primary Roots of *Zea mays*cv Ageotropic. *Plant Physiology,* **92**:310-315.

Moore, R. and Fondren, W.M. (1986) The Possible Involvement of Root-cap Mucilage in Gravitropism and Calcium Movement Across Root Tips of *Allium cepa*L. *Annals of Botany,* **58**:381-387.

Moore, R. and Fondren, W.M. (1988) A Gradient of Endogenous Calcium Forms in Mucilage of Graviresponding Roots of *Zea mays*. *Annals of Botany,* **61**:113-116.

Moore, R., L., C.I., Hunter, K.E., Olmos, D. and Smith, N.K.R. (1987) The Locations and Amounts of Endogenous Ions and Elements in the Cap and Elongating Zone of Horizontally Oriented Roots of *Zea mays*L.: An Electron-probe EDS Study. *Annals of Botany,* **59**:667-677.

Moore, R. and McClelen, C.E. (1983) A Morphometric Analysis of Cellular Differentiation in the Root Cap of *Zea mays*. *American Journal of Botany,* **70**:611-617.

Moore, R. and McClelen, C.E. (1983) Ultrastructural Aspects of Cellular Differentiation in the Root Cap of *Zea mays*. *Canadian Journal of Botany,* **61**:1566-1572.

Moore, R. and McClelen, C.E. (1989) Characterizing Pathways by Which Gravitropic Effectors Could Move from the Root Cap to the Root of Primary Roots of *Zea mays*. *Annals of Botany,* **64**:415-423.

Moore, R., McClelen, C.E., Fondren, W.M. and Wang, C.-L. (1987) Influence of Microgravity on Root-cap Regeneration and the Structure of Columella Cells in *Zea mays*. *American Journal of Botany,* **74**:218-223.

Moore, R. and Pasieniuk, J. (1984) Graviresponsiveness and the Development of Columella Tissue in Primary and Lateral Roots of *Ricinus communis*. *Plant Physiology,* **74**:529-533.

Moore, R. and Pasieniuk, J. (1984) Structure of Columella Cells in Primary and Lateral Root of *Ricinus communis* (Euphorbiaceae). *Annals of Botany,* **53**:715-726.

Nelson, A.J. and Evans, M.L. (1986) Analysis of Growth Patterns During Gravitropic Curvature in Roots of *Zea mays* by Use of a Computer-based Video Digitizer. *Journal of Plant Growth Regulation,* **5**:73-83.

Nick, P., Bergfeld, R., Schafer, E. and Schopfer, P. (1990) Unilateral Reorientation of Microtubules at the Outer Epidermal Wall During Photo- and Gravitropic Curvature of Maize Coleoptiles and Sunflower Hypocotyls. *Planta,* **181**:162-168.

Perbal, G. and Driss-Ecole, D. (1989) Polarity of Statocytes in Lentil Seedling Roots Grown in Space (Spacelab D1 Mission). *Physiologia Plantarum,* **75**:518-524.

Perbal, G. and Driss-Ecole, D. (1994) Transduction of the Gravity Stimulus in the Root Statocyte. *Advances in Space Research,* **14**:11-19.

Pickard, B.G. (1994) Contemplating the Plasmalemmal Control Center Model. *Protoplasma,* **182**:1-9.

Pickard, B.G. and Ding, J.P. (1992) Gravity Sensing by Higher Plants. *Advances in Comparative and Environmental Physiology,* **10**:82-110.

Pickard, B.G. and Ping Ding, J. (1993) The Mechanosensory Calcium-selective Ion Channel: Key Component of a Plasmalemmal Control Centre? *Australian Journal of Plant Physiology,* **20**:439-459.

Pilet, P.E. (1989) Differential Growth and Hormone Redistribution in Gravireacting Maize Roots. *Environmental and Experimental Botany,* **29**:27-45.

Pilet, P.E. (1992) What Remains of the Cholodny-Went Theory? IAA in Growing and Gravireacting Maize Roots. *Plant, Cell and Environment,* **15**:779-780.

Pilet, P.E. and Ney, D. (1981) Differential Growth of Georeacting Maize Roots. *Planta,* **151**:146-150.

Poff, K.L. and Martin, H.V. (1989) Site of Graviperception in Roots: A Re-examination. *Physiologia Plantarum,* **76**:451-455.

Ransom, J.S. and Moore, R. (1983) Geoperception in Primary and lateral Rots of *Phaseolus vulgaris*(Fabaceae). I. Structure of Columella Cells. *American Journal of Botany,* **70**:1048-1056.

Robinson, D.G. (1985) Plant Membranes. John Wiley & Sons, Inc., New York, NY.

Roux, S.J. (1992) What Remains of the Cholodny-Went Theory? Riding the Transduction Train to the Answer. *Plant, Cell and Environment,* **15**:783-784.

Sack, F.D. (1994) Cell Biology of Plant Gravity Sensing. *Advances in Space Research,* **14**:117-119.

Sack, F.D. (1997) Plastids and Gravitropic Sensing. *Planta,* **203**:S63-S68.

Sack, F.D., Suyemoto, M.M. and Leopold, A.C. (1985) Amyloplast Sedimentation Kinetics in Gravistimulated Maize Roots. *Planta,* **165**:295-300.

Sack, F.D., Suyemoto, M.M. and Leopold, A.C. (1986) Amyloplast Sedimentation and Organelle Saltation in Living Corn Columella Cells. *American Journal of Botany,* **73**:1692-1698.

Salisbury, F.B. (1992a) What Remains of the Cholodny-Went Theory? A Potential Role for Changing Sensitivity to Auxin. *Plant, Cell and Environment,* **15**:785-786.

Salisbury, F.B. and Ross, C.W. (1992b) Plant Physiology. Wadsworth Publishing Co., Belmont, CA.

Schatz, A., Reitstetter, R., Linke-Hommes, A., Briegleb, W., Slenzka, K. and Rahmann, H. (1994) Gravity Effects on Membrane Processes. *Advances in Space Research,* **14**:35-43.

Schoukens, J. and Pintelon, R. (1991) Identification of Linear Systems; A Pratical Guideline to Accurate Modeling. Pergamon Press, New York.

Scott, T.K. (1992) What Remains of the Cholodny-Went Theory? Some Cause and Effect Relationships in Root Gravitropism. *Plant, Cell and Environment,* **15**:787-788.

Selker, J.M.L. and Sievers, A. (1987) Analysis of Extension and Curvature During the Graviresponse in Lepidium Roots. *American Journal of Botany,* **74**:1863-1871.

Sievers, A. and Hejnowicz, Z. (1992) How Well Does the Clinostat Mimic the Effect of Microgravity on Plant Cells and Organs? *ASGSB Bulletin,* **5**:69-75.

Sievers, A., Kruse, S., Kuo-Huang, L. and Wendt, M. (1989) Statoliths and Microfilaments in Plant Cells. *Planta,* **179**:275-278.

Sievers, A. and Zieschang, H.E. (1992) What Remains of the Cholodny-Went Theory? It Does Not Fit the Growth Pattern of Cells During Bending of a Root. *Plant, Cell and Environment,* **15**:789-790.

Smith, J.D. (1996) *Plant Gravity Perception and Sensitivity Control Under Low-Gravity and Clinorotated Conditions.* University of Colorado Doctoral Thesis, Boulder, CO.

Stinemetz, C.L., Kuzmanoff, K.M., Evans, M.L. and Jarrett, H.W. (1987) Correlation between Calmodulin Activity and Gravitropic Sensitivity in Primary Roots of Maize. *Plant Physiology,* **84**:1337-1342.

Stockus, A. (1994) Basic Assumptions and Comparison of Three Gravitropic Response Models. *Advances in Space Research,* **14**:145-148.

Stockus, A. and Moore, D. (1996) Comparison of Plant and Fungal Gravitropic Responses Using Imitational Modelling. *Plant, Cell and Environment,* **19**:787-800.

Suzuki, T., Takeda, C. and Sugawara, T. (1994) The Action of Gravity in Agravitropic *Zea* Primary Roots - Effect of Gravistimulation on Extracellular Free Ca Content in the 1-mm Root Tip in the Dark. *Planta,* **192**:379-383.

Taiz, L. and Zeiger, E. (1991) Plant Physiology. Benjamin/Cummings Pub. Co., Redwood City, CA.

Taylor, D.P., Slattery, J. and Leopold, A.C. (1996) Apoplasic pH in Corn Root Gravitropism: A Laser Scanning Confocal Microscopy Measurement. *Physiologia Plantarum,* **97**:35-38.

Todd, P. (1994) Mechanical Analysis of Statoliths Action in Roots and Rhizoids. *Advances in Space Research,* **14**:121-124.

Todd, P. and Klaus, D.M. (1996) Theories and Models on the Biology of Cells in Space. *Advances in Space Research,* **17**:3-10.

Versel, J.M. and Pilet, P.E. (1986) Distribution of Growth and Proton Efflux in Gravireacting Roots of Maize (*Zea mays* L.). *Planta,* **167**:26-29.

Volkmann, D., Buchen, B., Hejnowicz, Z., Tewinkel, M. and Sievers, A. (1991) Oriented Movement of Statoliths Studied in a Reduced Gravitational Field During Parabolic Flights of Rockets. *Planta,* **185**:153-161.

Wayne, R., Staves, M.P. and Leopold, A.C. (1990) Gravity-dependent Polarity of Cytoplasmic Streaming in *Nitellopsis*. *Protoplasma,* **155**:43-57.

Weisenseel, M.H., Becker, H.F. and Ehlgotz, J.G. (1992) Growth, Gravitropism, and Endogenous Ion Currents of Cress Roots (*Lepidium sativum* L.). *Plant Physiology,* **100**:16-25.

Weisenseel, M.H. and Meyer, A.J. (1997) Bioelectricity, Gravity, and Plants. *Planta,* **203**:S98-S106.

Wendt, M. and Sievers, A. (1986) Restitution of Polarity in Statocytes from Centrifuged Roots. *Plant, Cell and Environment,* **9**:17-23.

Wendt, M. and Sievers, A. (1989) The Polarity of Statocytes and the Gravisensitivity of Roots are Dependent on the Concentration of Calcium in Statocytes. *Plant and Cell Physiology,* **30**:929-932.

Went, F.W. and Thimann, K.W. (1937) Phytohormones. The MacMillan Company, New York, NY.

Yang, R.L. and Tepper, H.B. (1996) Effects of Circumnutation and Passive Bending on the Initial Stages of Gravitropism in Pea Stems. *Journal of Plant Physiology,* **147**:703-708.

Young, L.M. and Evans, M.L. (1994) Calcium-dependent Asymmetric Movement of ^{3}H-indole-3-acetic Acid Across Gravistimulated Isolated Root Caps of Maize. *Plant Growth Regulators,* **14**:235-242.

Young, L.M., Evans, M.L. and Hertel, R. (1990) Correlations Between Gravitropic Curvature and Auxin Movement Across Gravistimulated Roots of *Zea mays*. *Plant Physiology,* **92**:792-796.

Zieschang, H.E. and Sievers, A. (1991) Graviresponse and the Localization of its Initiating Cells in Roots of *Phleum pratense* L. *Planta,* **184**:468-477.

Zieschang, H.E. and Sievers, A. (1994) Differential Flank Growth. *Advances in Space Research,* **14**:135-144.

APPENDIX I - MATLAB SCRIPT FILES FOR PROCESSING AMYLOPLAST SEDIMENTATION

I.1 AMYLFALL.M

```
% amylfall.m  script file for reading in amyloplast sedimentation coordinates
%           and producing a plot of this sedimentation and statistics concerning
%           the form of the sedimentation.
% requires:
%   fileid; name of data files to process
%   {fileid}.tim - this file contains a single column of time(seconds) between
%           each frame in the data-set. Therefore, the number of rows
%           within this file should be number of frames of data minus 1.
%   {fileid}.sed - this file contains the x,y coordinate data of all plastids within
%           within this data-set.  The format required for this file is
%           stringent.  Basically, the file is two columns of data for an
%           indeterminant amount of rows.  The file begins with the x,y coordinates
%           of two reference points at each time frame of the data-set (time 1
%           through final time).  These reference points serve to remove any
%           specimen stage drift rates from the data. These reference data ends
%           with a 0,0 header and is followed by the first cell data.  Leading
%           each cell data is its axis system points and then the 1st plastid
%           x,y coordinate data from 1st to final time frames ending with another
%           0,0 header.  This is followed by any remaining plastid coordinates within
%           that same cell.  At the completion of all data within the cell,
%           a new cell begins with a double 0,0 header, its axis system points,
%           and that cell's first plastid coordinates.  This scheme repeats until
%           all cells within that root-tip are recorded.
%         The format for this data is:
%             x-coordinate    y-coordinate of reference point#1 at time 1
%             x-coorindate    y-coordinate of reference point#2 at time 1
%             x-coordinate    y-coordinate of reference point#1 at time 2
%               etc.          etc.
%             x-coordinate    y-coordinate of reference point#2 at final time
%               0             0
%             x-coordinate    y-coordinate of cell origin for 1st cell
%             x-coordinate    y-coordinate of x-axis endpoint for 1st cell
%             x-coordinate    y-coordinate of y-axis endpoint for 1st cell
%             x-coordinate    y-coordinate of 1st plastid at time 1
%             x-coordinate    y-coordinate of 1st plastid at time 2
%               etc.          etc.
%             x-coordinate    y-coordinate of 1st plastid at final time
%               0             0
%             x-coordinate    y-coordinate of 2nd plastid at time 1
%               etc.          etc.
%               etc.          etc.
%             x-coordinate    y-coordinate of last plastid at final time
%               0             0
%               0             0
%             x-coordinate    y-coordinate of cell origin for 2nd cell
%             x-coordinate    y-coordinate of x-axis endpoint for 2nd cell
```

```
%            x-coordinate    y-coordinate of y-axis endpoint for 2nd cell
%            x-coordinate    y-coordinate of 1st plastid at time 1
%            x-coordinate    y-coordinate of 1st plastid at time 2
%              etc.          etc.
%              etc.          etc.
%              etc.          etc.
%            x-coordinate    y-coordinate of last plastid in final cell at final time
%Minor internal variables include:
%       maxcells  - The total number of different cells that were processed within this data-set.
%       cellnum   - The current cell being processed; ranges from 1 to maxcells.
%       amylnum   - The current amyloplast being processed within a cell.
%
%The following is a listing of all figures created by running the script and any text files or plots that
are saved to disk during the creation of the figure:
%
%Figure#                Filename                        Description
%
%1->maxcells    {fileid}_pos{cellnum}.m  Reconstructed sedimentation profile within each
%  cell processed.
%
%50+(1->maxcells)        {fileid}_stats{cellnum}.m          Statistics for a cell (min, max, mean,
%  std dev x,y,abs velocities, total change in x & y positions) for the entire time of
%  the data-set.
%
%60+(1->maxcells)  {fileid}_stats1{cellnum}.m      Statistics for a cell (min, max, mean,
%  std dev x,y,abs velocities, total change in x & y positions) for the 1st 3rd of the
%  time of the data-set.
%
%70+(1->maxcells)  {fileid}_stats2{cellnum}.m      Statistics for a cell (min, max, mean,
%  std dev x,y,abs velocities, total change in x & y positions) for the 2nd 3rd of
%  the time of the data-set.
%
%80+(1->maxcells)  {fileid}_stats3{cellnum}.m      Statistics for a cell (min, max, mean,
%  std dev x,y,abs velocities, total change in x & y positions) for the final 3rd
%  of the time of the data-set.
%
%temporary  {fileid}_{cellnum}_{amylnum}.m  3x3 plots of          x-velocity/time, y-vel/time,
%  abs-vel/time, x-vel/x-position, y-vel/x-pos, abs-vel/x-pos,x-vel/y-pos, y-vel/y-pos,
%  abs-vel/y-pos
%
%100+(1->maxcells)  {fileid}_ChanA{cellnum}.m  Channeling Coefficient A for each cell
%  (histogram of standard dev. in x-position as a function of y-position standardized
%  to the starting value).
%
%110+(1->maxcells)  {fileid}_ChanB{cellnum}.m   Channeling Coefficient B for each cell
%  (Abs.x-velocity histogram as a function of x-position).
%
%120+(1->maxcells)  {fileid}_GrpA{cellnum}.m    Group Movement A for each cell (Traces of
%  y-velocity as a function of time for all amyloplasts in the cell).
%
%    n/a {fileid}_GrpA{cellnum}.txt          Correlation matrix for the GrpA plot described above
%
%150+(1->maxcells)  {fileid}_GrpB{cellnum}.m      Group Movement B for each cell (Traces of
%  y-position over time for all amyloplasts in the cell).
```

```
%
%200+(1->maxcells) {fileid}_3DVel{cellnum}.m  Color-coded contour plot of vector-velocity
%  for each amyloplast within a cell during its sedimentation profile.
%
%225+(1->maxcells) {fileid}_ChanC{cellnum}.m  Histogram of y-velocity as function of y
%
%250+(1->maxcells) {fileid_GrpC{cellnum}.m   Traces of y-velocity and abs-velocity over time
%  within the same columella cell.
%
%Major Internal Variables include:
%
%numframes      The number of frames of data within the sedimentation run; within the data-set.
%
%time           A matrix[numframes-1 x 1] storing the time between each frame in seconds.
%
%cum_time       A matrix[numframes x 1] storing the cumulative time during the run...beginning
with 0.0.
%
%reference1     A matrix[numframes x 2] storing the x,y coordinates of reference point #1.
%
%reference2     A matrix[numframes x 2] storing the x,y coordinates of reference point #2.
%
%origin         A matrix[maxcells x 2] storing the x,y coordinates of the origin of each cell.
%
%xend           A matrix[maxcells x 2] storing the x,y coordinates of the x-axis endpoint of each
cell.
%
%yend           A matrix[maxcells x 2] storing the x,y coordinates of the y-axis endpoint of each
cell.
%
%sedprofile     A matrix[(numframes+1)*total amyloplasts x 2] storing the raw x,y coordinates %
                        corrected only for drift for each
%                       amyloplast tracked. Each set of data is (numframes) long
%                       beginning with a header identifying the cell# (cellnum) in
%                       column 1 and amyloplast# (amylnum) in column 2.
%
%normal_sed     A matrix(same size as above) storing the x,y coordinates normalized to the origin
%                       within each cell. Same headers described above begin the data for
%                       each amyloplast.
%
%vel_sed        A matrix(same size as above) storing the velocity associated with each x,y position
%                       coordinate stored in normal_sed. The velocity is post-calculated
%                       and is the average velocity of the amyloplast between its present
%                       and previous position. The 1st position is arbitrarily assigned a
%                       velocity of 0.0. Velocity is in microns/minute.
%
%sed_stats      A matrix(7*total amyloplasts+5*maxcells x 3 ) storing:
%               cellnum, amylnum
%               min. x-velocity, min. y-velocity, min. abs-velocity
%               max. x-velocity, max. y-velocity, max. abs-velocity
%               mean x-vel, mean y-vel, mean abs-vel
%               standard dev. in x-vel, standard dev. in y-vel, standard dev. in abs-vel
%               starting x-position, ending x-position, change in x-position
%               starting y-position, ending y-position, change in y-position
```

```
%       last 7 rows repeated for each amyloplast within a cell, followed by a cellular average:
%                       min. x-vel for the cell, min. y-vel for the cell, min. abs-vel for the cell
%                       max. x-vel for the cell, max. y-vel for the cell, max. abs-vel for the cell
%                       mean x-vel for the cell, mean y-vel for the cell, mean abs-vel for the cell
%                       mean st.dev. of x-vel for the cell, mean st.dev. of y-vel for the cell, mean %
                                        st.dev. of abs-vel for the cell
%                       total change in plastid x-position for the cell, total change in plastid y-%
                                        position for the cell
%                       This matrix records data over the entire time of the data-set.
%
%sed_stats1     Same as sed_stats, but only for the 1st third of the sedimentation time.
%sed_stats2     Same as sed_stats, but only for the 2nd third of the sedimentation time.
%sed_stats3     Same as sed_stats, but only for the final third of the sedimentation time.


%develop the names of the time and sedimentation data files
timefile=strcat(fileid,'.tim');
sedfile=strcat(fileid,'.sed');

%open the time and sedimentation data files for input
timeid=fopen(timefile,'rt');
sedid=fopen(sedfile,'rt');

%scan in the entire time data file into a column vector; time
time=fscanf(timeid,'%3i',inf);
fclose(timeid);
numframes=length(time)+1;

%scan in the drift reference coordinates leading off the sedimentation data file
for i=1:numframes
  reference1(i,1)=fscanf(sedid,'%f',1);
  reference1(i,2)=fscanf(sedid,'%f',1);
  reference2(i,1)=fscanf(sedid,'%f',1);
  reference2(i,2)=fscanf(sedid,'%f',1);
end

%check for a proper placement of 0  0 ending the drift reference coordinates
integrity=fscanf(sedid,'%i',1);
integrity=fscanf(sedid,'%i',1);
if integrity~=0
  disp('WARNING...Data file in an incorrect format following reference data.')
  break
end

%scan in the first cell's x-y axis information
cellnum=1;
origin(cellnum,1)=fscanf(sedid,'%f',1);
origin(cellnum,2)=fscanf(sedid,'%f',1);
xend(cellnum,1)=fscanf(sedid,'%f',1);
xend(cellnum,2)=fscanf(sedid,'%f',1);
yend(cellnum,1)=fscanf(sedid,'%f',1);
yend(cellnum,2)=fscanf(sedid,'%f',1);
amylnum=1;
```

```
%place header information into sedimentation profile matrix; cell#   amyloplast#
sedprofile(1,1)=cellnum;
sedprofile(1,2)=amylnum;

%scan in the first amyloplast's sedimentation coordinates
sedprofile(2,1)=fscanf(sedid,'%f',1);
sedprofile(2,2)=fscanf(sedid,'%f',1);
xdrift_correction=0.0;
ydrift_correction=0.0;
for i=2:numframes
  xdrift_correction=xdrift_correction+(reference1(i,1)-reference1(i-1,1));
  ydrift_correction=ydrift_correction+(reference1(i,2)-reference1(i-1,2));
  sedprofile(i+1,1)=fscanf(sedid,'%f',1)-xdrift_correction;
  sedprofile(i+1,2)=fscanf(sedid,'%f',1)-ydrift_correction;
end
amylnum=2;

%scan in all other amyloplasts plotted within this data file while checking
%  for proper data integrity
k=1;
while integrity==0
  integrity=fscanf(sedid,'%i',1);
  if isempty(integrity)==1
    break
  else
    integrity=fscanf(sedid,'%i',1);
    if integrity~=0
      disp('WARNING...Data file in an incorrect format following a sed-profile.')
      break
    end
  end

  %check for a change in columella cell
  temp=fscanf(sedid,'%f',1)  ;
  if temp==0.0
    integrity=fscanf(sedid,'%i',1);
    cellnum=cellnum+1;
    origin(cellnum,1)=fscanf(sedid,'%f',1);
    origin(cellnum,2)=fscanf(sedid,'%f',1);
    xend(cellnum,1)=fscanf(sedid,'%f',1);
    xend(cellnum,2)=fscanf(sedid,'%f',1);
    yend(cellnum,1)=fscanf(sedid,'%f',1);
    yend(cellnum,2)=fscanf(sedid,'%f',1);
    temp=fscanf(sedid,'%f',1);
    amylnum=1;
  end

  %place header information again
  sedprofile(k*(numframes+1)+1,1)=cellnum;
  sedprofile(k*(numframes+1)+1,2)=amylnum;

  %continue scanning sedimenation coordinates
  sedprofile(k*(numframes+1)+2,1)=temp;
```

```
  sedprofile(k*(numframes+1)+2,2)=fscanf(sedid,'%f',1);
  xdrift_correction=0.0;
  ydrift_correction=0.0;
  for i=2:numframes
    xdrift_correction=xdrift_correction+(reference1(i,1)-reference1(i-1,1));
    ydrift_correction=ydrift_correction+(reference1(i,2)-reference1(i-1,2));
    sedprofile(k*(numframes+1)+i+1,1)=fscanf(sedid,'%f',1)-xdrift_correction;
    sedprofile(k*(numframes+1)+i+1,2)=fscanf(sedid,'%f',1)-ydrift_correction;
  end
  amylnum=amylnum+1;
  k=k+1;

end %all adjusted-for-drift sedimentation data in now scanned into the 'sedprofile' matrix which
corresponds
% with the 'time' vector and the axis information in the 'origin', 'xend', and 'yend' matrices.
fclose(sedid);



%create color table for plotting amyloplasts
color(1,:)='gO';
color(2,:)='rO';
color(3,:)='mO';
color(4,:)='kO';
color(5,:)='bO';
color(6,:)='gh';
color(7,:)='rh';
color(8,:)='mh';
color(9,:)='kh';
color(10,:)='bh';
color(11,:)='g^';
color(12,:)='r^';
color(13,:)='m^';
color(14,:)='k^';
color(15,:)='b^';
%create a cell id table for saving plots
stringid=['01';'02';'03';'04';'05';'06';'07';'08';'09';'10';'11';'12';'13';'14';'15'];



%normalize the sedimentation coordinates to the origin and plot sedimentation
% within each columella cell
k=1;
oldcell=0.0;
while k<=length(sedprofile)
  cellnum=sedprofile(k,1);
  amylnum=sedprofile(k,2);
  normal_sed(k,1)=cellnum;
  normal_sed(k,2)=amylnum;
  k=k+1;

  %compute this columella's x-y axes' start and end points along with the cell's boundary
  if oldcell~=cellnum
    oldcell=cellnum;
```

```
%check for correction for data taken with distal end to the right
if origin(cellnum,1)>xend(cellnum,1)
  mirrorflag=-1;
else
  mirrorflag=1;
end
xaxis_start=mirrorflag*(yend(cellnum,1)-origin(cellnum,1));
xaxis_end=mirrorflag*(xend(cellnum,1)-origin(cellnum,1));
yaxis_start=xend(cellnum,2)-origin(cellnum,2);
yaxis_end=yend(cellnum,2)-origin(cellnum,2);
topright=[xaxis_end,yaxis_start];
lowerleft=[xaxis_start,yaxis_end];
lowerright=[xaxis_end,yaxis_end];

%plot this columella's cell boundaries relative to the origin
figure
if xend(cellnum,2)>=origin(cellnum,2)
  if yend(cellnum,1)>=origin(cellnum,1)
    %right and bottom cell wall inside + coordinates
    axis([0 xaxis_end 0 yaxis_end])
  else
    %right, but not bottom cell wall inside +coordinates
    axis([xaxis_start xaxis_end 0 yaxis_end])
  end
else
  if yend(cellnum,1)>=origin(cellnum,1)
    %not right, but bottom cell wall inside +coordinates
    axis([0 xaxis_end yaxis_start yaxis_end])
  else
    %neither right, nor bottom cell wall inside +coordinates
    axis([xaxis_start xaxis_end yaxis_start yaxis_end])
  end
end
plot([0;topright(1,1)],[0;topright(1,2)],'b-');
axis ij
plotid=strcat(fileid,'-',stringid(cellnum,:));
title(plotid);
xlabel('microns from top-distal corner of cell')
ylabel('microns from top-distal corner of cell')
hold on
plot([0;lowerleft(1,1)],[0;lowerleft(1,2)],'b-');
plot([lowerleft(1,1);lowerright(1,1)],[lowerleft(1,2);lowerright(1,2)],'b-');
plot([topright(1,1);lowerright(1,1)],[topright(1,2);lowerright(1,2)],'b-');
end

%normalize the sedimentation coordinates to the origin
for i=1:numframes
  normal_sed(k,1)=mirrorflag*(sedprofile(k,1)-origin(cellnum,1));
  normal_sed(k,2)=sedprofile(k,2)-origin(cellnum,2);
  k=k+1;
end

%plot this amyloplast's sedimentation path
plot(normal_sed(k-numframes:k-1,1),normal_sed(k-numframes:k-1,2),color(amylnum,:));
```

```
end

%save the figures created above
for i=cellnum:-1:1
  figure(i)
  plotid=strcat(fileid,'_pos',stringid(i,:));
  print(plotid);
end



%develop velocity profiles
%create cumulative time array (in minutes) to correspond to sedimentation frames
cum_time(1)=0.0;
for i=2:numframes
  cum_time(i)=cum_time(i-1)+time(i-1)/60;
end

%compute & plot velocity profiles along with sedimentation velocity statistics
k=1;
kk=1;
oldcell=0.0;
while k<=length(normal_sed)
  cellnum=normal_sed(k,1);
  %calculate last cell's stats when changing to next cell
  if cellnum~=oldcell
    if oldcell~=0
      %calculate the cellular x-vel statistics over all time
      sed_stats(kk,1)=min(sed_stats(kk-7*amylnum+1:7:kk-1,1));
      sed_stats(kk+1,1)=max(sed_stats(kk-7*amylnum+2:7:kk-1,1));
      sed_stats(kk+2,1)=mean(sed_stats(kk-7*amylnum+3:7:kk-1,1));
      sed_stats(kk+3,1)=mean(sed_stats(kk-7*amylnum+4:7:kk-1,1));
      %calculate the cellular x-vel statistics over 1st third time
      sed_stats1(kk,1)=min(sed_stats1(kk-7*amylnum+1:7:kk-1,1));
      sed_stats1(kk+1,1)=max(sed_stats1(kk-7*amylnum+2:7:kk-1,1));
      sed_stats1(kk+2,1)=mean(sed_stats1(kk-7*amylnum+3:7:kk-1,1));
      sed_stats1(kk+3,1)=mean(sed_stats1(kk-7*amylnum+4:7:kk-1,1));
      %calculate the cellular x-vel statistics over 2nd third time
      sed_stats2(kk,1)=min(sed_stats2(kk-7*amylnum+1:7:kk-1,1));
      sed_stats2(kk+1,1)=max(sed_stats2(kk-7*amylnum+2:7:kk-1,1));
      sed_stats2(kk+2,1)=mean(sed_stats2(kk-7*amylnum+3:7:kk-1,1));
      sed_stats2(kk+3,1)=mean(sed_stats2(kk-7*amylnum+4:7:kk-1,1));
      %calculate the cellular x-vel statistics over 3rd third time
      sed_stats3(kk,1)=min(sed_stats3(kk-7*amylnum+1:7:kk-1,1));
      sed_stats3(kk+1,1)=max(sed_stats3(kk-7*amylnum+2:7:kk-1,1));
      sed_stats3(kk+2,1)=mean(sed_stats3(kk-7*amylnum+3:7:kk-1,1));
      sed_stats3(kk+3,1)=mean(sed_stats3(kk-7*amylnum+4:7:kk-1,1));

      %calculate the cellular y-vel statistics over all time
      sed_stats(kk,2)=min(sed_stats(kk-7*amylnum+1:7:kk-1,2));
      sed_stats(kk+1,2)=max(sed_stats(kk-7*amylnum+2:7:kk-1,2));
      sed_stats(kk+2,2)=mean(sed_stats(kk-7*amylnum+3:7:kk-1,2));
```

```
sed_stats(kk+3,2)=mean(sed_stats(kk-7*amylnum+4:7:kk-1,2));
%calculate the cellular y-vel statistics over 1st third time
sed_stats1(kk,2)=min(sed_stats1(kk-7*amylnum+1:7:kk-1,2));
sed_stats1(kk+1,2)=max(sed_stats1(kk-7*amylnum+2:7:kk-1,2));
sed_stats1(kk+2,2)=mean(sed_stats1(kk-7*amylnum+3:7:kk-1,2));
sed_stats1(kk+3,2)=mean(sed_stats1(kk-7*amylnum+4:7:kk-1,2));
%calculate the cellular y-vel statistics over 2nd third time
sed_stats2(kk,2)=min(sed_stats2(kk-7*amylnum+1:7:kk-1,2));
sed_stats2(kk+1,2)=max(sed_stats2(kk-7*amylnum+2:7:kk-1,2));
sed_stats2(kk+2,2)=mean(sed_stats2(kk-7*amylnum+3:7:kk-1,2));
sed_stats2(kk+3,2)=mean(sed_stats2(kk-7*amylnum+4:7:kk-1,2));
%calculate the cellular y-vel statistics over 3rd third time
sed_stats3(kk,2)=min(sed_stats3(kk-7*amylnum+1:7:kk-1,2));
sed_stats3(kk+1,2)=max(sed_stats3(kk-7*amylnum+2:7:kk-1,2));
sed_stats3(kk+2,2)=mean(sed_stats3(kk-7*amylnum+3:7:kk-1,2));
sed_stats3(kk+3,2)=mean(sed_stats3(kk-7*amylnum+4:7:kk-1,2));

%calculate the cellular abs-vel statistics over all time
sed_stats(kk,3)=min(sed_stats(kk-7*amylnum+1:7:kk-1,3));
sed_stats(kk+1,3)=max(sed_stats(kk-7*amylnum+2:7:kk-1,3));
sed_stats(kk+2,3)=mean(sed_stats(kk-7*amylnum+3:7:kk-1,3));
sed_stats(kk+3,3)=mean(sed_stats(kk-7*amylnum+4:7:kk-1,3));
%calculate the cellular abs-vel statistics over 1st third time
sed_stats1(kk,3)=min(sed_stats1(kk-7*amylnum+1:7:kk-1,3));
sed_stats1(kk+1,3)=max(sed_stats1(kk-7*amylnum+2:7:kk-1,3));
sed_stats1(kk+2,3)=mean(sed_stats1(kk-7*amylnum+3:7:kk-1,3));
sed_stats1(kk+3,3)=mean(sed_stats1(kk-7*amylnum+4:7:kk-1,3));
%calculate the cellular abs-vel statistics over 2nd third time
sed_stats2(kk,3)=min(sed_stats2(kk-7*amylnum+1:7:kk-1,3));
sed_stats2(kk+1,3)=max(sed_stats2(kk-7*amylnum+2:7:kk-1,3));
sed_stats2(kk+2,3)=mean(sed_stats2(kk-7*amylnum+3:7:kk-1,3));
sed_stats2(kk+3,3)=mean(sed_stats2(kk-7*amylnum+4:7:kk-1,3));
%calculate the cellular abs-vel statistics over 3rd third time
sed_stats3(kk,3)=min(sed_stats3(kk-7*amylnum+1:7:kk-1,3));
sed_stats3(kk+1,3)=max(sed_stats3(kk-7*amylnum+2:7:kk-1,3));
sed_stats3(kk+2,3)=mean(sed_stats3(kk-7*amylnum+3:7:kk-1,3));
sed_stats3(kk+3,3)=mean(sed_stats3(kk-7*amylnum+4:7:kk-1,3));

kk=kk+4;
%calculate the cellular total x- & y-movement over all time
sed_stats(kk,1)=sum(sed_stats(kk-7*amylnum+1:7:kk-1,3));
sed_stats(kk,2)=sum(sed_stats(kk-7*amylnum+2:7:kk-1,3));
%calculate the cellular total x- & y-movement 1st third time
sed_stats1(kk,1)=sum(sed_stats1(kk-7*amylnum+1:7:kk-1,3));
sed_stats1(kk,2)=sum(sed_stats1(kk-7*amylnum+2:7:kk-1,3));
%calculate the cellular total x- & y-movement 2nd third time
sed_stats2(kk,1)=sum(sed_stats2(kk-7*amylnum+1:7:kk-1,3));
sed_stats2(kk,2)=sum(sed_stats2(kk-7*amylnum+2:7:kk-1,3));
%calculate the cellular total x- & y-movement 3rd third time
sed_stats3(kk,1)=sum(sed_stats3(kk-7*amylnum+1:7:kk-1,3));
sed_stats3(kk,2)=sum(sed_stats3(kk-7*amylnum+2:7:kk-1,3));
kk=kk+1;
end
oldcell=cellnum;
```

```
  end
  amylnum=normal_sed(k,2);
  vel_sed(k,1)=cellnum;
  vel_sed(k,2)=amylnum;

sed_stats(kk,1)=cellnum;sed_stats1(kk,1)=cellnum;sed_stats2(kk,1)=cellnum;sed_stats3(kk,1)=cellnu
m;

sed_stats(kk,2)=amylnum;sed_stats1(kk,2)=amylnum;sed_stats2(kk,2)=amylnum;sed_stats3(kk,2)=a
mylnum;
  k=k+1;
  kk=kk+1;

  %initial velocity is zero
  vel_sed(k,1)=0.0;
  vel_sed(k,2)=0.0;
  vel_sed(k,3)=0.0;
  k=k+1;

  %check for correction for data taken with distal end to the right
  if origin(cellnum,1)>xend(cellnum,1)
    mirrorflag=-1;
  else
    mirrorflag=1;
  end

  %velocity for remaining frames
  for i=2:numframes
    vel_sed(k,1)=mirrorflag*(normal_sed(k,1)-normal_sed(k-1,1))/time(i-1)*60;
    vel_sed(k,2)=(normal_sed(k,2)-normal_sed(k-1,2))/time(i-1)*60;
    vel_sed(k,3)=sqrt(vel_sed(k,1)^2+vel_sed(k,2)^2);
    k=k+1;
  end

  %plot this amyloplast's velocity and compute its statistics
  figure
  subplot(3,3,1)
  plot(cum_time,vel_sed(k-numframes:k-1,1),'b.')
  sed_stats(kk,1)=min(vel_sed(k-numframes+1:k-1,1));   %store min x-velocity all time
  sed_stats(kk+1,1)=max(vel_sed(k-numframes+1:k-1,1)); %store max x-velocity all time
  sed_stats(kk+2,1)=mean(vel_sed(k-numframes+1:k-1,1));%store mean x-velocity all time
  sed_stats(kk+3,1)=std(vel_sed(k-numframes+1:k-1,1)); %store std of x-velocities all time
  sed_stats1(kk,1)=min(vel_sed(k-numframes+1:k-fix(2*numframes/3)-1,1)); %store min x-velocity
1st third time
  sed_stats1(kk+1,1)=max(vel_sed(k-numframes+1:k-fix(2*numframes/3)-1,1)); %store max x-
velocity 1st third time
  sed_stats1(kk+2,1)=mean(vel_sed(k-numframes+1:k-fix(2*numframes/3)-1,1));%store mean x-
velocity 1st third time
  sed_stats1(kk+3,1)=std(vel_sed(k-numframes+1:k-fix(2*numframes/3)-1,1)); %store std of x-
velocities 1st third time
  sed_stats2(kk,1)=min(vel_sed(k-fix(2*numframes/3):k-fix(numframes/3)-1,1));   %store min x-
velocity 2nd third time
  sed_stats2(kk+1,1)=max(vel_sed(k-fix(2*numframes/3):k-fix(numframes/3)-1,1)); %store max x-
velocity 2nd third time
```

```
sed_stats2(kk+2,1)=mean(vel_sed(k-fix(2*numframes/3):k-fix(numframes/3)-1,1));%store mean x-velocity 2nd third time
sed_stats2(kk+3,1)=std(vel_sed(k-fix(2*numframes/3):k-fix(numframes/3)-1,1)); %store std of x-velocities 2nd third time
sed_stats3(kk,1)=min(vel_sed(k-fix(numframes/3):k-1,1));   %store min x-velocity 3rd third time
sed_stats3(kk+1,1)=max(vel_sed(k-fix(numframes/3):k-1,1)); %store max x-velocity 3rd third time
sed_stats3(kk+2,1)=mean(vel_sed(k-fix(numframes/3):k-1,1));%store mean x-velocity 3rd third time
sed_stats3(kk+3,1)=std(vel_sed(k-fix(numframes/3):k-1,1)); %store std of x-velocities 3rd third time
ylabel('x-velocity - (u/min)')
subplot(3,3,2)
plot(cum_time,vel_sed(k-numframes:k-1,2),'b.')
sed_stats(kk,2)=min(vel_sed(k-numframes+1:k-1,2));   %store min y-velocity all time
sed_stats(kk+1,2)=max(vel_sed(k-numframes+1:k-1,2)); %store max y-velocity all time
sed_stats(kk+2,2)=mean(vel_sed(k-numframes+1:k-1,2));%store mean y-velocity all time
sed_stats(kk+3,2)=std(vel_sed(k-numframes+1:k-1,2)); %store std of y-velocities all time
sed_stats1(kk,2)=min(vel_sed(k-numframes+1:k-fix(2*numframes/3)-1,2)); %store min y-velocity 1st third time
sed_stats1(kk+1,2)=max(vel_sed(k-numframes+1:k-fix(2*numframes/3)-1,2)); %store max y-velocity 1st third time
sed_stats1(kk+2,2)=mean(vel_sed(k-numframes+1:k-fix(2*numframes/3)-1,2));%store mean y-velocity 1st third time
sed_stats1(kk+3,2)=std(vel_sed(k-numframes+1:k-fix(2*numframes/3)-1,2)); %store std of y-velocities 1st third time
sed_stats2(kk,2)=min(vel_sed(k-fix(2*numframes/3):k-fix(numframes/3)-1,2)); %store min y-velocity 2nd third time
sed_stats2(kk+1,2)=max(vel_sed(k-fix(2*numframes/3):k-fix(numframes/3)-1,2)); %store max y-velocity 2nd third time
sed_stats2(kk+2,2)=mean(vel_sed(k-fix(2*numframes/3):k-fix(numframes/3)-1,2));%store mean y-velocity 2nd third time
sed_stats2(kk+3,2)=std(vel_sed(k-fix(2*numframes/3):k-fix(numframes/3)-1,2)); %store std of y-velocities 2nd third time
sed_stats3(kk,2)=min(vel_sed(k-fix(numframes/3):k-1,2));   %store min y-velocity 3rd third time
sed_stats3(kk+1,2)=max(vel_sed(k-fix(numframes/3):k-1,2)); %store max y-velocity 3rd third time
sed_stats3(kk+2,2)=mean(vel_sed(k-fix(numframes/3):k-1,2));%store mean y-velocity 3rd third time
sed_stats3(kk+3,2)=std(vel_sed(k-fix(numframes/3):k-1,2)); %store std of y-velocities 3rd third time
ylabel('y-velocity - (u/min)')
xlabel('time - (min)');
subplot(3,3,3)
plot(cum_time,vel_sed(k-numframes:k-1,3),'b.')
sed_stats(kk,3)=min(vel_sed(k-numframes+1:k-1,3));   %store min abs-velocity all time
sed_stats(kk+1,3)=max(vel_sed(k-numframes+1:k-1,3)); %store max abs-velocity all time
sed_stats(kk+2,3)=mean(vel_sed(k-numframes+1:k-1,3));%store mean abs-velocity all time
sed_stats(kk+3,3)=std(vel_sed(k-numframes+1:k-1,3)); %store std of abs-velocities all time
sed_stats1(kk,3)=min(vel_sed(k-numframes+1:k-fix(2*numframes/3)-1,3)); %store min abs-velocity 1st third time
sed_stats1(kk+1,3)=max(vel_sed(k-numframes+1:k-fix(2*numframes/3)-1,3)); %store max abs-velocity 1st third time
sed_stats1(kk+2,3)=mean(vel_sed(k-numframes+1:k-fix(2*numframes/3)-1,3));%store mean abs-velocity 1st third time
```

```
sed_stats1(kk+3,3)=std(vel_sed(k-numframes+1:k-fix(2*numframes/3)-1,3)); %store std of abs-velocities 1st third time
sed_stats2(kk,3)=min(vel_sed(k-fix(2*numframes/3):k-fix(numframes/3)-1,3)); %store min abs-velocity 2nd third time
sed_stats2(kk+1,3)=max(vel_sed(k-fix(2*numframes/3):k-fix(numframes/3)-1,3)); %store max abs-velocity 2nd third time
sed_stats2(kk+2,3)=mean(vel_sed(k-fix(2*numframes/3):k-fix(numframes/3)-1,3));%store mean abs-velocity 2nd third time
sed_stats2(kk+3,3)=std(vel_sed(k-fix(2*numframes/3):k-fix(numframes/3)-1,3)); %store std of abs-velocities 2nd third time
sed_stats3(kk,3)=min(vel_sed(k-fix(numframes/3):k-1,3)); %store min abs-velocity 3rd third time
sed_stats3(kk+1,3)=max(vel_sed(k-fix(numframes/3):k-1,3)); %store max abs-velocity 3rd third time
sed_stats3(kk+2,3)=mean(vel_sed(k-fix(numframes/3):k-1,3));%store mean abs-velocity 3rd third time
sed_stats3(kk+3,3)=std(vel_sed(k-fix(numframes/3):k-1,3)); %store std of abs-velocities 3rd third time
kk=kk+4;
ylabel('abs vel. - (u/min)')

subplot(3,3,4)
plot(normal_sed(k-numframes:k-1,1),vel_sed(k-numframes:k-1,1),'b.')
sed_stats(kk,1)=normal_sed(k-numframes,1);          %store starting x-position all time
sed_stats(kk,2)=normal_sed(k-1,1);                  %store ending x-position all time
sed_stats(kk,3)=sed_stats(kk,2)-sed_stats(kk,1);    %store change in x-position all time
sed_stats1(kk,1)=normal_sed(k-numframes,1);         %store starting x-position 1st third time
sed_stats1(kk,2)=normal_sed(k-fix(2*numframes/3)-1,1);%store ending x-position 1st third time
sed_stats1(kk,3)=sed_stats1(kk,2)-sed_stats1(kk,1); %store change in x-position 1st third time
sed_stats2(kk,1)=normal_sed(k-fix(2*numframes/3),1); %store starting x-position 2nd third time
sed_stats2(kk,2)=normal_sed(k-fix(numframes/3)-1,1); %store ending x-position 2nd third time
sed_stats2(kk,3)=sed_stats2(kk,2)-sed_stats2(kk,1); %store change in x-position 2nd third time
sed_stats3(kk,1)=normal_sed(k-fix(numframes/3),1);  %store starting x-position 3rd third time
sed_stats3(kk,2)=normal_sed(k-1,1);                 %store ending x-position 3rd third time
sed_stats3(kk,3)=sed_stats3(kk,2)-sed_stats3(kk,1); %store change in x-position 3rd third time
kk=kk+1;
ylabel('x-velocity - (u/min)')
subplot(3,3,5)
plot(normal_sed(k-numframes:k-1,1),vel_sed(k-numframes:k-1,2),'b.')
ylabel('y-velocity - (u/min)')
xlabel('x-position - (microns from origin)')
subplot(3,3,6)
plot(normal_sed(k-numframes:k-1,1),vel_sed(k-numframes:k-1,3),'b.')
ylabel('abs vel. - (u/min)')

subplot(3,3,7)
plot(normal_sed(k-numframes:k-1,2),vel_sed(k-numframes:k-1,1),'b.')
sed_stats(kk,1)=normal_sed(k-numframes,2);          %store starting y-position all time
sed_stats(kk,2)=normal_sed(k-1,2);                  %store ending y-position all time
sed_stats(kk,3)=sed_stats(kk,2)-sed_stats(kk,1);    %store change in y-position all time
sed_stats1(kk,1)=normal_sed(k-numframes,2);         %store starting y-position 1st third time
sed_stats1(kk,2)=normal_sed(k-fix(2*numframes/3)-1,2);%store ending y-position 1st third time
sed_stats1(kk,3)=sed_stats1(kk,2)-sed_stats1(kk,1); %store change in y-position 1st third time
sed_stats2(kk,1)=normal_sed(k-fix(2*numframes/3),2); %store starting y-position 2nd third time
sed_stats2(kk,2)=normal_sed(k-fix(numframes/3)-1,2); %store ending y-position 2nd third time
```

```
 sed_stats2(kk,3)=sed_stats2(kk,2)-sed_stats2(kk,1);  %store change in y-position 2nd third time
 sed_stats3(kk,1)=normal_sed(k-fix(numframes/3),2);   %store starting y-position 3rd third time
 sed_stats3(kk,2)=normal_sed(k-1,2);                  %store ending y-position 3rd third time
 sed_stats3(kk,3)=sed_stats3(kk,2)-sed_stats3(kk,1);  %store change in y-position 3rd third time
 kk=kk+1;
 ylabel('x-velocity - (u/min)')
 subplot(3,3,8)
 plot(normal_sed(k-numframes:k-1,2),vel_sed(k-numframes:k-1,2),'b.')
 ylabel('y-velocity - (u/min)')
 xlabel('y-position - (microns from origin)')
 subplot(3,3,9)
 plot(normal_sed(k-numframes:k-1,2),vel_sed(k-numframes:k-1,3),'b.')
 ylabel('abs vel. - (u/min)')
 %save the figure
 plotid=strcat(fileid,'_',stringid(cellnum,:),'_',stringid(amylnum,:));
 print(plotid);
 close
end

%calculate final cell's stats
%calculate the cellular x-vel statistics over all time
sed_stats(kk,1)=min(sed_stats(kk-7*amylnum+1:7:kk-1,1));
sed_stats(kk+1,1)=max(sed_stats(kk-7*amylnum+2:7:kk-1,1));
sed_stats(kk+2,1)=mean(sed_stats(kk-7*amylnum+3:7:kk-1,1));
sed_stats(kk+3,1)=mean(sed_stats(kk-7*amylnum+4:7:kk-1,1));
%calculate the cellular x-vel statistics over 1st third time
sed_stats1(kk,1)=min(sed_stats1(kk-7*amylnum+1:7:kk-1,1));
sed_stats1(kk+1,1)=max(sed_stats1(kk-7*amylnum+2:7:kk-1,1));
sed_stats1(kk+2,1)=mean(sed_stats1(kk-7*amylnum+3:7:kk-1,1));
sed_stats1(kk+3,1)=mean(sed_stats1(kk-7*amylnum+4:7:kk-1,1));
%calculate the cellular x-vel statistics over 2nd third time
sed_stats2(kk,1)=min(sed_stats2(kk-7*amylnum+1:7:kk-1,1));
sed_stats2(kk+1,1)=max(sed_stats2(kk-7*amylnum+2:7:kk-1,1));
sed_stats2(kk+2,1)=mean(sed_stats2(kk-7*amylnum+3:7:kk-1,1));
sed_stats2(kk+3,1)=mean(sed_stats2(kk-7*amylnum+4:7:kk-1,1));
%calculate the cellular x-vel statistics over 3rd third time
sed_stats3(kk,1)=min(sed_stats3(kk-7*amylnum+1:7:kk-1,1));
sed_stats3(kk+1,1)=max(sed_stats3(kk-7*amylnum+2:7:kk-1,1));
sed_stats3(kk+2,1)=mean(sed_stats3(kk-7*amylnum+3:7:kk-1,1));
sed_stats3(kk+3,1)=mean(sed_stats3(kk-7*amylnum+4:7:kk-1,1));

%calculate the cellular y-vel statistics over all time
sed_stats(kk,2)=min(sed_stats(kk-7*amylnum+1:7:kk-1,2));
sed_stats(kk+1,2)=max(sed_stats(kk-7*amylnum+2:7:kk-1,2));
sed_stats(kk+2,2)=mean(sed_stats(kk-7*amylnum+3:7:kk-1,2));
sed_stats(kk+3,2)=mean(sed_stats(kk-7*amylnum+4:7:kk-1,2));
%calculate the cellular y-vel statistics over 1st third time
sed_stats1(kk,2)=min(sed_stats1(kk-7*amylnum+1:7:kk-1,2));
sed_stats1(kk+1,2)=max(sed_stats1(kk-7*amylnum+2:7:kk-1,2));
sed_stats1(kk+2,2)=mean(sed_stats1(kk-7*amylnum+3:7:kk-1,2));
sed_stats1(kk+3,2)=mean(sed_stats1(kk-7*amylnum+4:7:kk-1,2));
%calculate the cellular y-vel statistics over 2nd third time
sed_stats2(kk,2)=min(sed_stats2(kk-7*amylnum+1:7:kk-1,2));
sed_stats2(kk+1,2)=max(sed_stats2(kk-7*amylnum+2:7:kk-1,2));
```

```
sed_stats2(kk+2,2)=mean(sed_stats2(kk-7*amylnum+3:7:kk-1,2));
sed_stats2(kk+3,2)=mean(sed_stats2(kk-7*amylnum+4:7:kk-1,2));
%calculate the cellular y-vel statistics over 3rd third time
sed_stats3(kk,2)=min(sed_stats3(kk-7*amylnum+1:7:kk-1,2));
sed_stats3(kk+1,2)=max(sed_stats3(kk-7*amylnum+2:7:kk-1,2));
sed_stats3(kk+2,2)=mean(sed_stats3(kk-7*amylnum+3:7:kk-1,2));
sed_stats3(kk+3,2)=mean(sed_stats3(kk-7*amylnum+4:7:kk-1,2));

%calculate the cellular abs-vel statistics over all time
sed_stats(kk,3)=min(sed_stats(kk-7*amylnum+1:7:kk-1,3));
sed_stats(kk+1,3)=max(sed_stats(kk-7*amylnum+2:7:kk-1,3));
sed_stats(kk+2,3)=mean(sed_stats(kk-7*amylnum+3:7:kk-1,3));
sed_stats(kk+3,3)=mean(sed_stats(kk-7*amylnum+4:7:kk-1,3));
%calculate the cellular abs-vel statistics over 1st third time
sed_stats1(kk,3)=min(sed_stats1(kk-7*amylnum+1:7:kk-1,3));
sed_stats1(kk+1,3)=max(sed_stats1(kk-7*amylnum+2:7:kk-1,3));
sed_stats1(kk+2,3)=mean(sed_stats1(kk-7*amylnum+3:7:kk-1,3));
sed_stats1(kk+3,3)=mean(sed_stats1(kk-7*amylnum+4:7:kk-1,3));
%calculate the cellular abs-vel statistics over 2nd third time
sed_stats2(kk,3)=min(sed_stats2(kk-7*amylnum+1:7:kk-1,3));
sed_stats2(kk+1,3)=max(sed_stats2(kk-7*amylnum+2:7:kk-1,3));
sed_stats2(kk+2,3)=mean(sed_stats2(kk-7*amylnum+3:7:kk-1,3));
sed_stats2(kk+3,3)=mean(sed_stats2(kk-7*amylnum+4:7:kk-1,3));
%calculate the cellular abs-vel statistics over 3rd third time
sed_stats3(kk,3)=min(sed_stats3(kk-7*amylnum+1:7:kk-1,3));
sed_stats3(kk+1,3)=max(sed_stats3(kk-7*amylnum+2:7:kk-1,3));
sed_stats3(kk+2,3)=mean(sed_stats3(kk-7*amylnum+3:7:kk-1,3));
sed_stats3(kk+3,3)=mean(sed_stats3(kk-7*amylnum+4:7:kk-1,3));
%calculate the cellular total x- & y-movement over all time
sed_stats(kk+4,1)=sum(sed_stats(kk-7*amylnum+5:7:kk-1,3));
sed_stats(kk+4,2)=sum(sed_stats(kk-7*amylnum+6:7:kk-1,3));
%calculate the cellular total x- & y-movement 1st third time
sed_stats1(kk+4,1)=sum(sed_stats1(kk-7*amylnum+5:7:kk-1,3));
sed_stats1(kk+4,2)=sum(sed_stats1(kk-7*amylnum+6:7:kk-1,3));
%calculate the cellular total x- & y-movement 2nd third time
sed_stats2(kk+4,1)=sum(sed_stats2(kk-7*amylnum+5:7:kk-1,3));
sed_stats2(kk+4,2)=sum(sed_stats2(kk-7*amylnum+6:7:kk-1,3));
%calculate the cellular total x- & y-movement 3rd third time
sed_stats3(kk+4,1)=sum(sed_stats3(kk-7*amylnum+5:7:kk-1,3));
sed_stats3(kk+4,2)=sum(sed_stats3(kk-7*amylnum+6:7:kk-1,3));

save(strcat(fileid,'_stats.txt'),'sed_stats','-ascii');
save(strcat(fileid,'_stats1.txt'),'sed_stats1','-ascii');
save(strcat(fileid,'_stats2.txt'),'sed_stats2','-ascii');
save(strcat(fileid,'_stats3.txt'),'sed_stats3','-ascii');

%plot the sedimentation velocity statistics for each columella cell
kk=length(sed_stats);
maxcells=sed_stats(kk-11,1);
while kk>=1
  cellnum=sed_stats(kk-11,1);
  amylnum=sed_stats(kk-11,2);
  %plot for all time
  figure(50+cellnum)
```

```
subplot(2,2,1)
plot(cellnum,sed_stats(kk-4,1),'b^');
cur_axis=gca;set(cur_axis,'xtick',[0:1:maxcells])
hold on
plot(cellnum,sed_stats(kk-3,1),'rv');
errorbar(cellnum,sed_stats(kk-2,1),sed_stats(kk-1,1),'ko');
xlabel('Columella Cell Number')
ylabel('x-velocity - (microns/min)')
title('X-velocity Statistics for Each Cell')

subplot(2,2,2)
plot(cellnum,sed_stats(kk-4,2),'b^');
cur_axis=gca;set(cur_axis,'xtick',[0:1:maxcells])
hold on
plot(cellnum,sed_stats(kk-3,2),'rv');
errorbar(cellnum,sed_stats(kk-2,2),sed_stats(kk-1,2),'ko');
xlabel('Columella Cell Number')
ylabel('y-velocity - (microns/min)')
title('Y-velocity Statistics for Each Cell')

subplot(2,2,3)
plot(cellnum,sed_stats(kk-4,3),'b^');
cur_axis=gca;set(cur_axis,'xtick',[0:1:maxcells])
hold on
plot(cellnum,sed_stats(kk-3,3),'rv');
errorbar(cellnum,sed_stats(kk-2,3),sed_stats(kk-1,3),'ko');
xlabel('Columella Cell Number')
ylabel('abs-velocity - (microns/min)')
title('Absolute Velocity Statistics for Each Cell')

subplot(2,2,4)
text(0.2,0.7,'Total x-movement:')
text(0.4,0.6,num2str(sed_stats(kk,1)))
text(0.2,0.4,'Total y-movement:')
text(0.4,0.3,num2str(sed_stats(kk,2)))

%plot for 1st third time
figure(60+cellnum)
subplot(2,2,1)
plot(cellnum,sed_stats1(kk-4,1),'b^');
cur_axis=gca;set(cur_axis,'xtick',[0:1:maxcells])
hold on
plot(cellnum,sed_stats1(kk-3,1),'rv');
errorbar(cellnum,sed_stats1(kk-2,1),sed_stats1(kk-1,1),'ko');
xlabel('Columella Cell Number')
ylabel('x-velocity - (microns/min)')
title('X-velocity Stats(1/3 time) for Each Cell')

subplot(2,2,2)
plot(cellnum,sed_stats1(kk-4,2),'b^');
cur_axis=gca;set(cur_axis,'xtick',[0:1:maxcells])
hold on
plot(cellnum,sed_stats1(kk-3,2),'rv');
errorbar(cellnum,sed_stats1(kk-2,2),sed_stats1(kk-1,2),'ko');
```

```
xlabel('Columella Cell Number')
ylabel('y-velocity - (microns/min)')
title('Y-velocity Stats(1/3 time) for Each Cell')

subplot(2,2,3)
plot(cellnum,sed_stats1(kk-4,3),'b^');
cur_axis=gca;set(cur_axis,'xtick',[0:1:maxcells])
hold on
plot(cellnum,sed_stats1(kk-3,3),'rv');
errorbar(cellnum,sed_stats1(kk-2,3),sed_stats1(kk-1,3),'ko');
xlabel('Columella Cell Number')
ylabel('abs-velocity - (microns/min)')
title('Absolute Velocity Stats(1/3 time) for Each Cell')

subplot(2,2,4)
text(0.2,0.7,'Total x-movement:')
text(0.4,0.6,num2str(sed_stats1(kk,1)))
text(0.2,0.4,'Total y-movement:')
text(0.4,0.3,num2str(sed_stats1(kk,2)))

%plot for 2nd third time
figure(70+cellnum)
subplot(2,2,1)
plot(cellnum,sed_stats2(kk-4,1),'b^');
cur_axis=gca;set(cur_axis,'xtick',[0:1:maxcells])
hold on
plot(cellnum,sed_stats2(kk-3,1),'rv');
errorbar(cellnum,sed_stats2(kk-2,1),sed_stats2(kk-1,1),'ko');
xlabel('Columella Cell Number')
ylabel('x-velocity - (microns/min)')
title('X-velocity Stats(2/3 time) for Each Cell')

subplot(2,2,2)
plot(cellnum,sed_stats2(kk-4,2),'b^');
cur_axis=gca;set(cur_axis,'xtick',[0:1:maxcells])
hold on
plot(cellnum,sed_stats2(kk-3,2),'rv');
errorbar(cellnum,sed_stats2(kk-2,2),sed_stats2(kk-1,2),'ko');
xlabel('Columella Cell Number')
ylabel('y-velocity - (microns/min)')
title('Y-velocity Stats(2/3 time) for Each Cell')

subplot(2,2,3)
plot(cellnum,sed_stats2(kk-4,3),'b^');
cur_axis=gca;set(cur_axis,'xtick',[0:1:maxcells])
hold on
plot(cellnum,sed_stats2(kk-3,3),'rv');
errorbar(cellnum,sed_stats2(kk-2,3),sed_stats2(kk-1,3),'ko');
xlabel('Columella Cell Number')
ylabel('abs-velocity - (microns/min)')
title('Absolute Velocity Stats(2/3 time) for Each Cell')

subplot(2,2,4)
text(0.2,0.7,'Total x-movement:')
```

```
text(0.4,0.6,num2str(sed_stats2(kk,1)))
text(0.2,0.4,'Total y-movement:')
text(0.4,0.3,num2str(sed_stats2(kk,2)))

%plot for 3rd third time
figure(80+cellnum)
subplot(2,2,1)
plot(cellnum,sed_stats3(kk-4,1),'b^');
cur_axis=gca;set(cur_axis,'xtick',[0:1:maxcells])
hold on
plot(cellnum,sed_stats3(kk-3,1),'rv');
errorbar(cellnum,sed_stats3(kk-2,1),sed_stats3(kk-1,1),'ko');
xlabel('Columella Cell Number')
ylabel('x-velocity - (microns/min)')
title('X-velocity Stats(3/3 time) for Each Cell')

subplot(2,2,2)
plot(cellnum,sed_stats3(kk-4,2),'b^');
cur_axis=gca;set(cur_axis,'xtick',[0:1:maxcells])
hold on
plot(cellnum,sed_stats3(kk-3,2),'rv');
errorbar(cellnum,sed_stats3(kk-2,2),sed_stats3(kk-1,2),'ko');
xlabel('Columella Cell Number')
ylabel('y-velocity - (microns/min)')
title('Y-velocity Stats(3/3 time) for Each Cell')

subplot(2,2,3)
plot(cellnum,sed_stats3(kk-4,3),'b^');
cur_axis=gca;set(cur_axis,'xtick',[0:1:maxcells])
hold on
plot(cellnum,sed_stats3(kk-3,3),'rv');
errorbar(cellnum,sed_stats3(kk-2,3),sed_stats3(kk-1,3),'ko');
xlabel('Columella Cell Number')
ylabel('abs-velocity - (microns/min)')
title('Absolute Velocity Stats(3/3 time) for Each Cell')

subplot(2,2,4)
text(0.2,0.7,'Total x-movement:')
text(0.4,0.6,num2str(sed_stats3(kk,1)))
text(0.2,0.4,'Total y-movement:')
text(0.4,0.3,num2str(sed_stats3(kk,2)))

kk=kk-7*amylnum-5;
end
%save the velocity statistics plots
for i=1:maxcells
  figure(50+i)
  plotid=strcat(fileid,'_stats',stringid(i,:));
  print(plotid)
  figure(60+i)
  plotid=strcat(fileid,'_stats1',stringid(i,:));
  print(plotid)
  figure(70+i)
  plotid=strcat(fileid,'_stats2',stringid(i,:));
```

```
  print(plotid)
  figure(80+i)
  plotid=strcat(fileid,'_stats3',stringid(i,:));
  print(plotid)
end


%recreate color table for plotting channeling and group movement info
clear color
color(1,:)='g- ';
color(2,:)='r- ';
color(3,:)='m- ';
color(4,:)='k- ';
color(5,:)='b- ';
color(6,:)='g: ';
color(7,:)='r: ';
color(8,:)='m: ';
color(9,:)='k: ';
color(10,:)='b: ';
color(11,:)='g--';
color(12,:)='r--';
color(13,:)='m--';
color(14,:)='k--';
color(15,:)='b--';


% Compute & plot the channeling and group movement behavior specs for each cell
k=1.0;
oldcell=0.0;
clear x,clear y,clear X
while k<=length(normal_sed)
  cellnum=normal_sed(k,1);
  amylnum=normal_sed(k,2);
  k=k+1;
  %check for the completion of a cell plot and save it
  if cellnum~=oldcell
    j=1;
    if oldcell~=0.0  %save old data if not at the beginning
      %save the Group Movement plots for the previous cell
      % start with Group Movement plot A (y-velocity per time)
      figure(120+cellnum-1)
      xlabel('Time - (minutes)')
      ylabel('y-velocity - (microns/min)')
      plotid=strcat(fileid,'GrpA',stringid(cellnum-1,:));
      title(plotid)
      print(plotid)
      correlation=corrcoef(y_vels);
      save(strcat(plotid,'.txt'),'correlation','-ascii')
      clear y_vels
      % next, Group Movement plot B (y-position per time)
      figure(150+cellnum-1)
      xlabel('Time - (minutes)')
      ylabel('y-position - (microns)')
      plotid=strcat(fileid,'GrpB',stringid(cellnum-1,:));
```

```
title(plotid)
axis ij
print(plotid)
correlation=corrcoef(y_pos);
save(strcat(plotid,'.txt'),'correlation','-ascii')
clear y_pos
%next, Group Movement plot C (y-vel & abs-vel over time)
figure(250+cellnum-1)
xlabel('Time - (minutes)')
ylabel('Velocity - (microns/minute)')
plotid=strcat(fileid,'GrpC',stringid(cellnum-1,:));
title(plotid)
print(plotid)
close

%compute, plot, & save the Channeling plots for the previous cell
%start with Channeling plot A (channeling coefficient; the normalized variance
%     of x-position per y-position)
[y_sorted,yidx]=sort(y);
x_sorted=x(yidx);
spread=y_sorted(length(y_sorted))-y_sorted(1);
incr=spread/10;
ybins=[2*incr+y_sorted(1):incr:y_sorted(length(y_sorted))];
jj=2;
i=1;
while i<=length(y_sorted)
  ii=1;
  while y_sorted(i)<=jj*incr+y_sorted(1)
    X(ii)=x_sorted(i);
    ii=ii+1;
    i=i+1;
    if i>length(y_sorted)
      break
    end
  end
  if ii==1
    X(1)=0;
  end
  if jj==2
    std1=std(X);
    chan_coef(jj-1)=1;
  elseif std(X)<.02
    chan_coef(jj-1)=0;
  else
    chan_coef(jj-1)=std(X)/std1;
  end
  jj=jj+1;
  clear X
end
figure(100+cellnum-1)
barh(ybins,chan_coef,1,'b')
axis ij
ylabel('y-position - (microns down from origin)')
xlabel('Channeling Coefficient')
```

```
plotid=strcat(fileid,'ChanA',stringid(cellnum-1,:));
title(plotid)
print(plotid)
clear chan_coef
%next, Channeling plot B (abs x-velocity per x-position) &
%     Channeling plot C (y-velocity per y-position)
[x_sorted,xidx]=sort(x); [y_sorted,yidx]=sort(y);
xvel_sorted=xvel(xidx); yvel_sorted=yvel(yidx);
spreadx=x_sorted(length(x_sorted))-x_sorted(1);
spready=y_sorted(length(y_sorted))-y_sorted(1);
incrx=spreadx/20; incry=spready/5;
xbins=[incrx+x_sorted(1):incrx:x_sorted(length(x_sorted))];
ybins=[incry+y_sorted(1):incry:y_sorted(length(y_sorted))];
jj=1;
i=1;
while i<=length(x_sorted)
  ii=1;
  while x_sorted(i)<=jj*incrx+x_sorted(1)
    X(ii)=xvel_sorted(i);
    ii=ii+1;
    i=i+1;
    if i>length(x_sorted)
      break
    end
  end
  if ii==1
    X(1)=0;
  end
  mean_xvel(jj)=mean(X);
  errx(jj)=0.5*(std(X));
  jj=jj+1;
  clear X
end
jj=1;
i=1;
while i<=length(y_sorted)
  ii=1;
  while y_sorted(i)<=jj*incry+y_sorted(1)
    Y(ii)=yvel_sorted(i);
    ii=ii+1;
    i=i+1;
    if i>length(y_sorted)
      break
    end
  end
  if ii==1
    Y(1)=0;
  end
  mean_yvel(jj)=mean(Y);
  erry(jj)=0.5*(std(Y));
  jj=jj+1;
  clear Y
end
figure(110+cellnum-1)
```

```
    bar(xbins(2:length(xbins)-1),mean_xvel(2:length(xbins)-1),1,'b')
    hold on
    errorbar(xbins(2:length(xbins)-1),mean_xvel(2:length(xbins)-1),errx(2:length(xbins)-1),'k.')
    hold off
    xlabel('x-position - (microns basally from origin)')
    ylabel('|x-velocity| - (u/min)')
    plotid=strcat(fileid,'ChanB',stringid(cellnum-1,:));
    title(plotid)
    print(plotid)
    figure(225+cellnum-1)
    bar(ybins,mean_yvel,1,'b')
    hold on
    errorbar(ybins,mean_yvel,erry,'k.')
    hold off
    xlabel('y-position - (microns down from origin)')
    ylabel('y-velocity - (u/min)')
    plotid=strcat(fileid,'ChanC',stringid(cellnum-1,:));
    title(plotid)
    print(plotid)
    close
    clear x,clear y,clear x_vel,clear y_vel,clear mean_xvel,clear mean_yvel,clear errx,clear erry
  end
  oldcell=cellnum;
end

%plot this amyloplast's Group Movement plots
% start with Group Movement plot A (y-velocity per time)
figure(120+cellnum)
hold on
plot(cum_time,vel_sed(k:k+numframes-1,2),color(amylnum,:))
y_vels(:,amylnum)=vel_sed(k:k+numframes-1,2);%storing all y-velocities for later
%                                    correlation
% next, Group Movement plot B (y-position per time)
figure(150+cellnum)
hold on
plot(cum_time,normal_sed(k:k+numframes-1,2),color(amylnum,:))
y_pos(:,amylnum)=normal_sed(k:k+numframes-1,2);%storing all y-positions for later
%                                    correlation
% next, Group Movement plot C (y-velocity & abs-velocity over time)
figure(250+cellnum)
hold on
plot(cum_time,vel_sed(k:k+numframes-1,2),color(amylnum,:))
hold on
plot(cum_time,vel_sed(k:k+numframes-1,3),color(amylnum,:))

%store this amyloplast's x,y positions and abs x-velocity into storage arrays for later
% analysis for Channeling plots
for i=1:numframes
  x(j)=normal_sed(k,1);
  y(j)=normal_sed(k,2);
  xvel(j)=abs(vel_sed(k,1));
  yvel(j)=abs(vel_sed(k,2));
  j=j+1;
  k=k+1;
```

```
  end
end

%save the Group Movement plots for the final cell
% start with Group Movement plot A (y-velocity per time)
figure(120+cellnum)
xlabel('Time - (minutes)')
ylabel('y-velocity - (microns/min)')
plotid=strcat(fileid,'GrpA',stringid(cellnum,:));
title(plotid)
print(plotid)
correlation=corrcoef(y_vels);
save(strcat(plotid,'.txt'),'correlation','-ascii')
% next, Group Movement plot B (y-position per time)
figure(150+cellnum)
xlabel('Time - (minutes)')
ylabel('y-position - (microns)')
plotid=strcat(fileid,'GrpB',stringid(cellnum,:));
title(plotid)
axis ij
print(plotid)
correlation=corrcoef(y_pos);
save(strcat(plotid,'.txt'),'correlation','-ascii')
% next, Group Movement plot C (y-velocity & abs-velocity per time)
figure(250+cellnum)
xlabel('Time - (minutes)')
ylabel('Velocity - (microns/minute)')
plotid=strcat(fileid,'GrpC',stringid(cellnum,:));
title(plotid)
print(plotid)
close

%compute, plot, & save the Channeling plots for the final cell
% start with Channeling plot A start with Channeling plot A (channeling coefficient; the normalized
variance of x-position per y-position)
[y_sorted,yidx]=sort(y);
x_sorted=x(yidx);
spread=y_sorted(length(y_sorted))-y_sorted(1);
incr=spread/10;
ybins=[2*incr+y_sorted(1):incr:y_sorted(length(y_sorted))];
jj=2;
i=1;
while i<=length(y_sorted)
  ii=1;
  while y_sorted(i)<=jj*incr+y_sorted(1)
    X(ii)=x_sorted(i);
    ii=ii+1;
    i=i+1;
    if i>length(y_sorted)
      break
    end
  end
  if ii==1
    X(1)=0;
```

```
  end
  if jj==2
    std1=std(X);
    chan_coef(jj-1)=1;
  elseif std(X)<.02
    chan_coef(jj-1)=0;
  else
    chan_coef(jj-1)=std(X)/std1;
  end
  jj=jj+1;
  clear X
end
figure(100+cellnum)
barh(ybins,chan_coef,1,'b')
axis ij
ylabel('y-position - (microns down from origin)')
xlabel('Channeling Coefficient')
plotid=strcat(fileid,'ChanA',stringid(cellnum,:));
title(plotid)
print(plotid)
clear chan_coef
% next, Channeling plot B (abs x-velocity per x-position) &
%     Channeling plot C (y-velocity per y-position)
[x_sorted,xidx]=sort(x); [y_sorted,yidx]=sort(y);
xvel_sorted=xvel(xidx); yvel_sorted=yvel(yidx);
spreadx=x_sorted(length(x_sorted))-x_sorted(1);
spready=y_sorted(length(y_sorted))-y_sorted(1);
incrx=spreadx/20; incry=spready/5;
xbins=[incrx+x_sorted(1):incrx:x_sorted(length(x_sorted))];
ybins=[incry+y_sorted(1):incry:y_sorted(length(y_sorted))];
jj=1;
i=1;
while i<=length(x_sorted)
  ii=1;
  while x_sorted(i)<=jj*incrx+x_sorted(1)
    X(ii)=xvel_sorted(i);
    ii=ii+1;
    i=i+1;
    if i>length(x_sorted)
      break
    end
  end
  if ii==1
    X(1)=0;
  end
  mean_xvel(jj)=mean(X);
  errx(jj)=0.5*(std(X));
  jj=jj+1;
  clear X
end
jj=1;
i=1;
while i<=length(y_sorted)
  ii=1;
```

```
  while y_sorted(i)<=jj*incry+y_sorted(1)
    Y(ii)=yvel_sorted(i);
    ii=ii+1;
    i=i+1;
    if i>length(y_sorted)
      break
    end
  end
  if ii==1
    Y(1)=0;
  end
  mean_yvel(jj)=mean(Y);
  erry(jj)=0.5*(std(Y));
  jj=jj+1;
  clear Y
end
figure(110+cellnum)
bar(xbins(2:length(xbins)-1),mean_xvel(2:length(xbins)-1),1,'b')
hold on
errorbar(xbins(2:length(xbins)-1),mean_xvel(2:length(xbins)-1),errx(2:length(xbins)-1),'k.')
hold off
xlabel('x-position - (microns basally from origin)')
ylabel('|x-velocity| - (u/min)')
plotid=strcat(fileid,'ChanB',stringid(cellnum,:));
title(plotid)
print(plotid)
figure(225+cellnum)
bar(ybins,mean_yvel,1,'b')
hold on
errorbar(ybins,mean_yvel,erry,'k.')
hold off
xlabel('y-position - (microns down from origin)')
ylabel('y-velocity - (u/min)')
plotid=strcat(fileid,'ChanC',stringid(cellnum,:));
title(plotid)
print(plotid)
close

clear x,clear y,clear xvel,clear yvel,clear mean_xvel,clear mean_yvel
clear errx,clear erry,clear y_vels,clear y_pos



%abs vel color/size plot data compiled and plotted for each columella cell
%first, create colormap (higher velocity...darker color)
s_axis=0.25;l_axis=0.45; %defines isosceles triangle marker's short and long axis
corner1=3*pi/4;corner2=5*pi/4; %defines angular location of triangle's 2, short end corners
k=1.0;
oldcell=0.0;
clear x,clear y,clear z
while k<=length(vel_sed)
  cellnum=vel_sed(k,1);
  amylnum=vel_sed(k,2);
```

```
 k=k+1;
 if cellnum~=oldcell  %start new x,y, and z compilation
   j=1;
   if oldcell~=0.0   %plot and save the old data if not at the beginning
     figure(200+cellnum-1)
     colormap(hot);
     map=colormap;
     velmap=map(64:-1:1,:);
     colormap(velmap);
     for i=1:length(x)
       if i/numframes~=fix(i/numframes)
         angle=atan2(y(i+1)-y(i),x(i+1)-x(i));
         x_tri=[l_axis*cos(angle);s_axis*cos(angle+corner1);s_axis*cos(angle+corner2)];
         y_tri=[l_axis*sin(angle);s_axis*sin(angle+corner1);s_axis*sin(angle+corner2)];
         fill(x_tri+x(i),y_tri+y(i),velmap(64-round((fastest-z(i))*63/fastest),:))
         hold on
       else
         fill(0.2*sin((1/8:2/8:15/8)*pi)+x(i),0.2*cos((1/8:2/8:15/8)*pi)+y(i),velmap(64-
round((fastest-z(i))*63/fastest),:))
       end
     end
     hold off
     axis ij
     caxis([0 fastest])
     colorbar
     xlabel('x-position - (microns from origin)')
     ylabel('y-position - (microns from origin)')
     title('Absolute Velocity wrt Cellular Position')
     plotid=strcat(fileid,'_3Dvel',stringid(cellnum-1,:));
     print(plotid);
     clear x,clear y,clear z
   end
   oldcell=cellnum;
   fastest=0.0;
  end
  for i=1:numframes
   x(j)=normal_sed(k,1);
   y(j)=normal_sed(k,2);
   z(j)=vel_sed(k,3);
   if z(j)>fastest
     fastest=z(j);
   end
   j=j+1;
   k=k+1;
  end
end

%save that last columella cell's pseudocolor abs vel plot
figure(200+cellnum)
colormap(hot);
map=colormap;
velmap=map(64:-1:1,:);
colormap(velmap);
for i=1:length(x)
```

```
  if i/numframes~=fix(i/numframes)
    angle=atan2(y(i+1)-y(i),x(i+1)-x(i));
    x_tri=[l_axis*cos(angle);s_axis*cos(angle+corner1);s_axis*cos(angle+corner2)];
    y_tri=[l_axis*sin(angle);s_axis*sin(angle+corner1);s_axis*sin(angle+corner2)];
    fill(x_tri+x(i),y_tri+y(i),velmap(64-round((fastest-z(i))*63/fastest),:))
    hold on
  else
    fill(0.2*sin((1/8:2/8:15/8)*pi)+x(i),0.2*cos((1/8:2/8:15/8)*pi)+y(i),velmap(64-round((fastest-
z(i))*63/fastest),:))
  end
end
hold off
axis ij
caxis([0 fastest])
colorbar
xlabel('x-position - (microns from origin)')
ylabel('y-position - (microns from origin)')
title('Absolute Velocity wrt Cellular Position')
plotid=strcat(fileid,'_3Dvel',stringid(cellnum,:));
print(plotid);
clear x,clear y,clear z
```

I.2 AMYLFALL_SPEC.M

```
%amyfall_spec.m - same as amylfall, but provides information on only specific amyloplasts
%
%Input requirements include: amyfall_spec must be run immediately after amyfall
% is run for a specific data-file. This script file is then executed to
% examine specific amyloplasts from that data only. The following variables,
% created in amylfall.m must exist: fileid, normal_sed, vel_sed, color, & numframes
% User can only examine the plastids in one columella cell at a time from a set of
% sedimentation data.
%Output includes only on-screen plots and variables, no files are written to disk.
%

k_amy=1;
while k_amy>=1
  k_amy=0;
  col_specific=input('Enter the number of the columella cell to analyze (e.g. 2) ');
  amy_specific=input('Enter a column vector of amyloplast numbers to analyze (e.g. [1;2;4;7]) ')
  if (length(amy_specific)==0 | amy_specific==0 | col_specific==0 )
    disp('You`ve entered an invalid number for columella # or amyloplast #....')
    break
  end
  % Compute & plot the channeling and group movement behavior specs for each set of plastids
  k=1.0;
  j=1.0;
  clear x,clear y,clear X
  while k<=length(normal_sed)
    cellnum=normal_sed(k,1);
    amylnum=normal_sed(k,2);
    k=k+1;
    compute_flag=0;
    for i=1:length(amy_specific)
      if amy_specific(i)==amylnum
        compute_flag=1;
      end
    end
    if (cellnum==col_specific) & (compute_flag==1)
      %plot this amyloplast's Group Movement plots
      % start with Group Movement plot A (y-velocity per time)
      figure(120+cellnum)
      hold on
      plot(cum_time,vel_sed(k:k+numframes-1,2),color(amylnum,:))
      y_vels(:,amylnum)=vel_sed(k:k+numframes-1,2);%store for future correlation analysis
      % next, Group Movement plot B (y-position per time)
      figure(150+cellnum)
      hold on
      plot(cum_time,normal_sed(k:k+numframes-1,2),color(amylnum,:))
      y_pos(:,amylnum)=normal_sed(k:k+numframes-1,2);%store for future correlation analysis

      %store this amyloplast's x,y positions and abs x-velocity into storage arrays for later
      % analysis for Channeling plots
      for i=1:numframes
        x(j)=normal_sed(k,1);
```

```
        y(j)=normal_sed(k,2);
        xvel(j)=abs(vel_sed(k,1));
        j=j+1;
        k=k+1;
      end
    else
      k=k+numframes;
    end
  end

  %display the Group Movement plots for the desired cell
  % start with Group Movement plot A (y-velocity per time)
  figure(120+col_specific)
  xlabel('Time - (minutes)')
  ylabel('y-velocity - (microns/min)')
  plotid=strcat(fileid,'GrpA',stringid(cellnum,:));
  title(plotid)
  correlation_vel=corrcoef(y_vels)
  % next, Group Movement plot B (y-position per time)
  figure(150+col_specific)
  xlabel('Time - (minutes)')
  ylabel('y-position - (microns)')
  plotid=strcat(fileid,'GrpB',stringid(cellnum,:));
  title(plotid)
  axis ij
  correlation_pos=corrcoef(y_pos)


  %compute & plot the Channeling plots for the final cell
  % start with Channeling plot A start with Channeling plot A (channeling coefficient; the
normalized variance of x-position per y-position)
  [y_sorted,yidx]=sort(y);
  x_sorted=x(yidx);
  spread=y_sorted(length(y_sorted))-y_sorted(1);
  incr=spread/10;
  ybins=[2*incr+y_sorted(1):incr:y_sorted(length(y_sorted))];
  jj=2;
  i=1;
  while i<=length(y_sorted)
    ii=1;
    while y_sorted(i)<=jj*incr+y_sorted(1)
      X(ii)=x_sorted(i);
      ii=ii+1;
      i=i+1;
      if i>length(y_sorted)
        break
      end
    end
    if ii==1
      X(1)=0;
    end
    if jj==2
      std1=std(X);
      chan_coef(jj-1)=1;
```

```
  else
    chan_coef(jj-1)=std(X)/std1;
  end
  jj=jj+1;
  clear X
end
figure(100+col_specific)
barh(ybins,chan_coef,1,'b')
axis ij
ylabel('y-position - (microns down from origin)')
xlabel('Channeling Coefficient')
plotid=strcat(fileid,'ChanA',stringid(cellnum,:));
title(plotid)
clear chan_coef
% next, Channeling plot B (abs x-velocity per x-position)
[x_sorted,xidx]=sort(x);
xvel_sorted=xvel(xidx);
spread=x_sorted(length(x_sorted))-x_sorted(1);
incr=spread/20;
xbins=[incr+x_sorted(1):incr:x_sorted(length(x_sorted))];
jj=1;
i=1;
while i<=length(x_sorted)
  ii=1;
  while x_sorted(i)<=jj*incr+x_sorted(1)
    X(ii)=xvel_sorted(i);
    ii=ii+1;
    i=i+1;
    if i>length(x_sorted)
      break
    end
  end
  if ii==1
    X(1)=0;
  end
  mean_xvel(jj)=mean(X);
  err(jj)=0.5*(std(X));
  jj=jj+1;
  clear X
end
figure(110+col_specific)
bar(xbins(2:length(xbins)-1),mean_xvel(2:length(xbins)-1),1,'b')
hold on
errorbar(xbins(2:length(xbins)-1),mean_xvel(2:length(xbins)-1),err(2:length(xbins)-1),'k.')
hold off
xlabel('x-position - (microns basally from origin)')
ylabel('|x-velocity| - (u/min)')
plotid=strcat(fileid,'ChanB',stringid(cellnum,:));
title(plotid)
clear x,clear y,clear mean_xvel,clear err,clear y_vels,clear y_pos

end % overall while-loop
```

APPENDIX II - MATLAB SCRIPT FILES FOR SIMULATING AMYLOPLAST SEDIMENTATION

II.1 SEDIMENT.M

```
% Statolith sedimentation Script-M file
%
%
% This is the parent script for the EOM programmed into the function "STATE.M".
%Provision is made to include the x-axis as an additional state, but for now
% the 1st state is y-position and the second state is y-velocity. Units here
% and in "STATE.M" must be the same and presently are in microns and minutes.
%
%

%User-configured parameters
t0=0.0; %initial time
t_interm=15; %intermediate time...to display extreme initial dynamics
t_steady=4.e-6; %steady-state time...when dynamics slow
t_final=15;     %final time
%x0=[0; 10; 0; 0]; %4-state initial conditions
x0=[0; 0];      %2-state initial conditions

%integrator parameters..shouldn't change
tol=1.e-6;
trace=0;

% integrate and plot the dynamics of early sedimentation
tspan=[t0 t_interm];
[tout, xout]=ode23s('state',tspan,x0);
figure
plot(tout,xout(:,1))
xlabel('Time - (minutes)')
ylabel('Y-position - (microns from equilibrium)')
title('Numerical Solution of Y-Sedimentation')
figure
plot(tout,xout(:,2))
xlabel('Time - (minutes)')
ylabel('Y-velocity - (microns/minute)')
title('Numerical Solution of Y-Sedimentation')
t_all=tout;
x_all=xout;

pause
% allow the early dynamics to arrive at steady values
x_interm=xout(length(xout),1:2)';
[tout, xout]=ode78('state',t_interm,t_steady,x_interm,tol,trace);
figure
plot(tout,xout)
t_all=[t_all;tout(2:length(tout),:)];
x_all=[x_all;xout(2:length(xout),:)];
```

II.2 STATE.M

```
function xdot=state(t,x)
%
%This function provides the state equations of motion for the amyloplast
%  within the columella cell.  Initial lines contain morphological parameters.
%  Provision is provided to expand to the x-dimension.
%
%
format compact
format short e

a=1.884; %maize      %amloplast radius {microns}
%a=2.1;  %cress
V=28;  %maize      %amyloplast volume {microns^3}
%V=38.8;  %cress
rho_amyl=1.364e-15;  %amyloplast density {kg/microns^3}
m=rho_amyl*V;       %mass of amyloplast {kg}

delta_rho=3.49E-16;  %difference between amyloplast & cytoplasmic density {kg/microns^3}
n=34E-09*60;        %cytoplasmic viscosity {kg/micron-min}

correction_factor=1; %correction factor for actin properties
num_actin=1;        %assumed number of actin attachments
actin_length=10;    %assumed initial actin fiber length {microns}
A_actin=1.88E-05;   %actin fiber cross-sectional area {microns^2}
E_actin=2.8E+09/1e+06*3600*correction_factor;%actin elastic modulus{kg/micron-min^2}
I_actin=3.07e-35*1e+24; %actin average moment of inertia {microns^4}
Gx=0;Gy=9.81E+06*3600;  %gravity forcing function {microns/min^2}
%Gx=0;Gy=0;            %no gravity forcing function

%tension_coefx=num_actin*A_actin*E_actin/actin_length/m; %spring constant in x
tension_coefy=num_actin*A_actin*E_actin/actin_length/m;  %spring constant in y
drag_coef=6*pi*a*n/m;          %drag-damping constant
%input_coefx=V*delta_rho/m*Gx;  %complete input accel for x {kg-microns/min^2}
input_coefy=V*delta_rho/m*Gy; %complete input accel for y {kg-microns/min^2}

%     MODEL SET #1
%Direct plastid/actin fiber attachment ("tethered") and spring constant is linear
%  with x & y position.  Following section is for model in both x & y dimensions
%  (states: x,y,xdot,ydot).
%if sign(x(1))==-1
%  Tr=tension_coefx*(-x(1));
%  Tl=0;
%else
%  Tr=0;
%  Tl=tension_coefx*(x(1));
%end
%if sign(x(2))==-1
%  Td=tension_coefy*(-x(2));
%  Tb=0;
```

```
%else
%  Td=0;
%  Tb=tension_coefy*(x(2));
%end
%tension_accelx=(Tr-Tl);
%tension_accely=(Td-Tb);

%Same model as above, but only y-dimension simulation(states are: y and ydot).
%if sign(x(1))==-1
%  Td=tension_coefy*(-x(1));
%  Tb=0;
%else
%  Td=0;
%  Tb=tension_coefy*(x(1));
%end
%tension_accely=(Td-Tb);


%     MODEL SET #3
%Cylindrical network of actin fibers creating a grid across the cell volume.
%This model set estimated as a constant spring deceleration due to contact
% with the grids. The following model is for only the y-dimension.
% (states are: y and ydot).
Vol_fraction=.03; %fraction of cell volume made of actin fibers
Cell_height=33; %(cylindrical cell height {microns})
Cell_diam=23;  %(cylindrical cell width/diameter {microns})
Area_lateral=Cell_height*2*pi*Cell_diam/2; %area of cylinder lateral surface
Area_ends=2*pi*(Cell_diam/2)^2;  %area of the cylinder end surfaces
Tot_area=Area_lateral+Area_ends; %total surface area
Lateral_fraction=Area_lateral/Tot_area; %fraction of surface area on lateral surface
End_fraction=1-Lateral_fraction;      %fraction of surface area on end surfaces
%Following code evenly distributes actin fiber connection points along the cell surface
%Num_ends is the number of fibers attached to the ends
%Num_lat is the number of fibers attached to the lateral wall
Num_ends=V*Vol_fraction/(A_actin*(Cell_height+Lateral_fraction*Cell_diam/End_fraction));
Num_lat=Lateral_fraction*Num_ends/End_fraction;
disp('Total Number of actin fibers per cell is:')
Num_tot=Num_ends+Num_lat   %Total number of actin fibers in the cell
disp('An actin fiber per XX micron^2:')
Grid_area=Tot_area/(2*Num_tot) %Grid size in {microns^2}
Grid_side=sqrt(Grid_area);  %Assume square grid...side length {microns}
Delta_r=a-Grid_side/2;     %extra amount to open grid for plastid to fall
Theta=acos(Grid_side/2/a);  %angle {rad} of grid contact on plastid (pi/2 is below)
if Grid_side<a/2*sin(Theta)
  contact_num=12;
elseif Grid_side<a*sin(Theta)
  contact_num=8;
else
  contact_num=4;
end
% calculate force required to deflect the fiber (ref. Eschbach, 1975)
W=Delta_r*192*E_actin*I_actin/cos(Theta)/(Cell_diam)^3;
% total vertical acceleration of plastid is contact# x the above plus angular component
disp('Vertical acceleration is:')
```

```
tension_accely=-contact_num*W*sin(Theta)/m


%The state equation of motion
%Use this when including the x-dimension
%xdot=[x(3);
%  x(4);
%  tension_accelx-drag_coef*x(3)+input_coefx;
%  tension_accely-drag_coef*x(4)+input_coefy];

%Use this for only the y-dimension
xdot=[x(2);
  tension_accely-drag_coef*x(2)+input_coefy];
```

APPENDIX III - DERIVATION OF CURVATURE IN THE CANTILEVERED ROOT

Let:

w - applied load
- -- mg (mass times gravity for a point load)
- -- dg (density times gravity for a distributed load)

v - vertical deflection (downward, if due to gravity)
x,y - horizontal, vertical axes
M - internal moment
V - shear stress
θ - curvature angle (horizontal is zero radians)
EI - flexural rigidity (E - Young's modulus, I - moment of inertia)
L - length of root
ρ - radius of curvature

Relationships (Hibbeler, 1993):

$$V(x) = EI\frac{d^3v}{dx^3}$$

$$M(x) = EI\frac{d^2v}{dx^2}$$

$$\theta(x) = \frac{dv}{dx}; \quad \rho(x) = \frac{EI}{M(x)}$$

$$-\frac{dV}{dx} = w$$

Therefore,

$$V(x) = \frac{dM}{dx}$$

$$w = -\frac{d^2M}{dx^2}$$

For a cantilevered root,

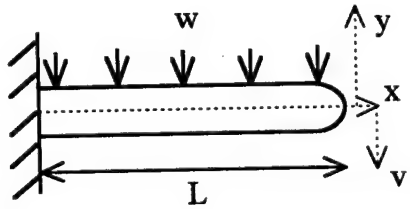

The distributed load of plant tissue can be assumed to act through a point or center of gravity at l/2:

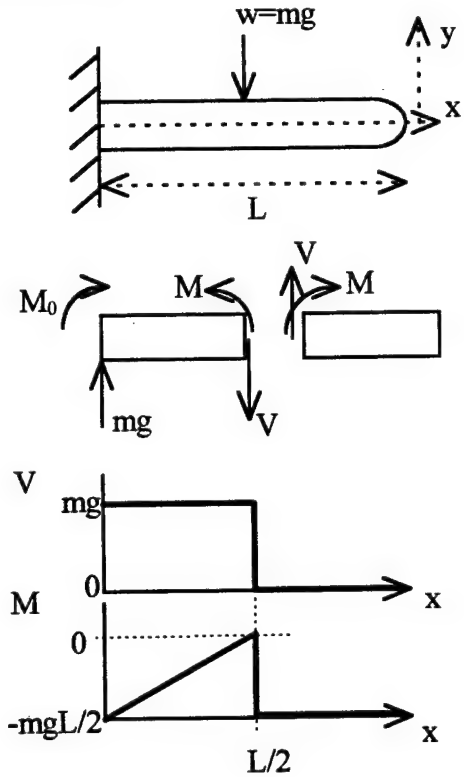

For x = 0 through L / 2:

$\sum F_y = 0$

$mg - V = 0$

$V = mg;$

$\therefore\ \mathbf{V(x) = mg}$

$\sum M = 0\ ;\ M_0 = -\frac{mgL}{2}$

$M - mgx - M_0 = 0$

$\therefore\ \mathbf{M(x) = mgx - \frac{mgL}{2}}$

For x > L / 2 through L:

$\mathbf{V = 0}$

$\mathbf{M = 0}$

or, the distributed load can be treated as a mass function distributed along x:

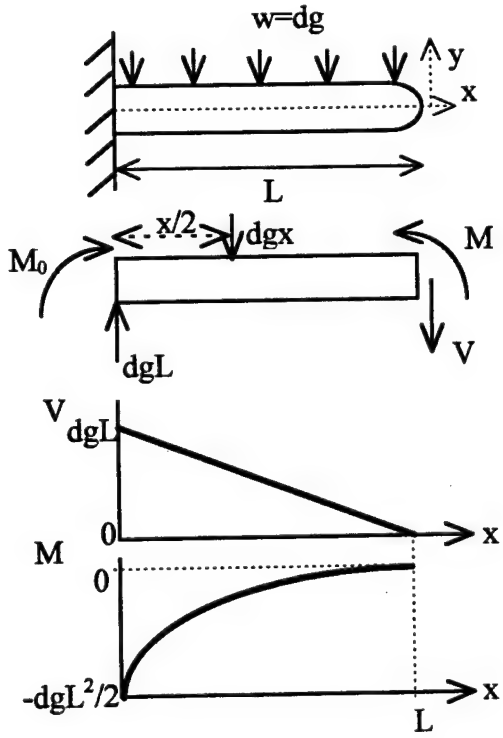

$\sum F_y = 0$

$dgL - dgx - V = 0$

$\mathbf{V = dg(L - x)}$

$\sum M = 0\ ;\ M_0 = -dLg(L/2)$

$M + dgx(\frac{x}{2}) - dgL(x) - M_0 = 0$

$\mathbf{M = dgx(L - \frac{x}{2}) - dg\frac{L^2}{2}}$

Deriving the elastic curve using the distributed load scheme:

$$M(x) = EI\frac{d^2v}{dx^2} = dgx(L - \frac{x}{2}) - dg\frac{L^2}{2}$$

$$EI\frac{dv}{dx} = \frac{dgLx^2}{2} - \frac{dgx^3}{6} - \frac{dgL^2x}{2} + c_1 \quad ; \quad \text{substitute } \theta(x) = \frac{dv}{dx};$$

$$EI\theta(x) = \frac{dgLx^2}{2} - \frac{dgx^3}{6} - \frac{dgL^2x}{2} + c_1 \quad ; \quad \text{boundary condition of } \frac{dv}{dx} = 0,\ x = 0;$$

$$\therefore\ 0 = c_1$$

$$\therefore\ \theta(x) = \frac{dg}{2EI}(-L^2x + Lx^2 - \frac{x^3}{3}) \quad ; \quad \text{describes the curvature as a function of x}$$

APPENDIX IV - DERIVATION OF ROOT THREE-POINT BENDING

Let,

- p - centered load (N)
- w - distributed load (weight of root/mm)
- L - length of root
- wL - total weight of root
- v - downward deflection distance
- EI - flexural rigidity
- E - elastic (Young's) modulus
- I - moment of inertia
- V - internal stress
- M - internal moment
- x - horizontal axis

3-point bending setup:

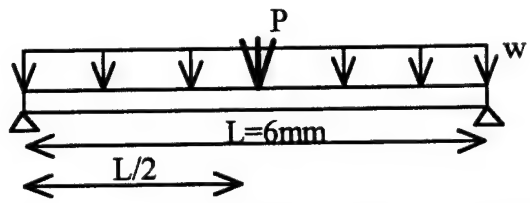

- typical maize elongation zone is 6 mm in length, starting 2.3 mm from tip (Ishikawa & Evans, 1995).

Freebody diagram:

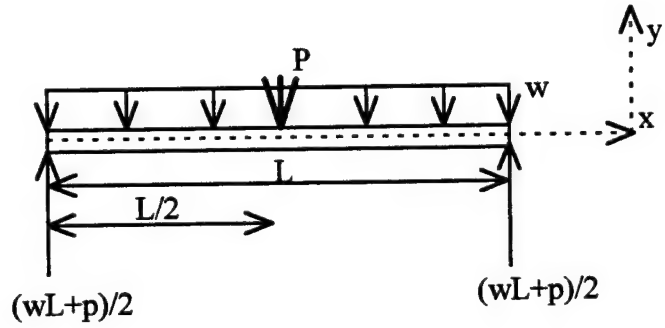

up to P (center):

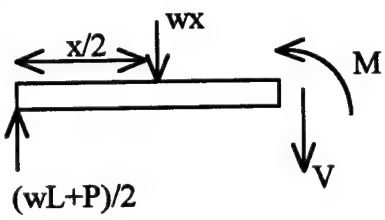

after P:

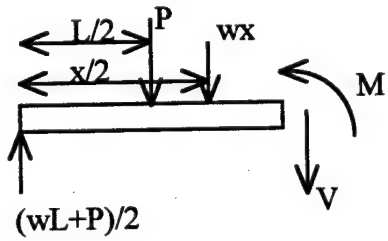

up to x=L/2:

$$\sum F_y = 0 \quad ; \quad \sum M = 0$$

$$\frac{wL+P}{2} - V - wx = 0 \qquad M + wx(\frac{x}{2}) - \frac{wL+P}{2}(x) = 0$$

$$V = w(\frac{L}{2} - x) + \frac{P}{2} \qquad M = \frac{w}{2}(Lx - x^2) + \frac{P}{2}x$$

$x \geq L/2$:

$$\sum F_y = 0 \quad ; \quad \sum M = 0$$

$$\frac{wL+P}{2} - wx - P - V = 0 \qquad M + wx(\frac{x}{2}) - \frac{wL+P}{2}(x) + P(x - \frac{L}{2}) = 0$$

$$V = w(\frac{L}{2} - x) - \frac{P}{2} \qquad M = \frac{w}{2}(Lx - x^2) + \frac{P}{2}(L - x)$$

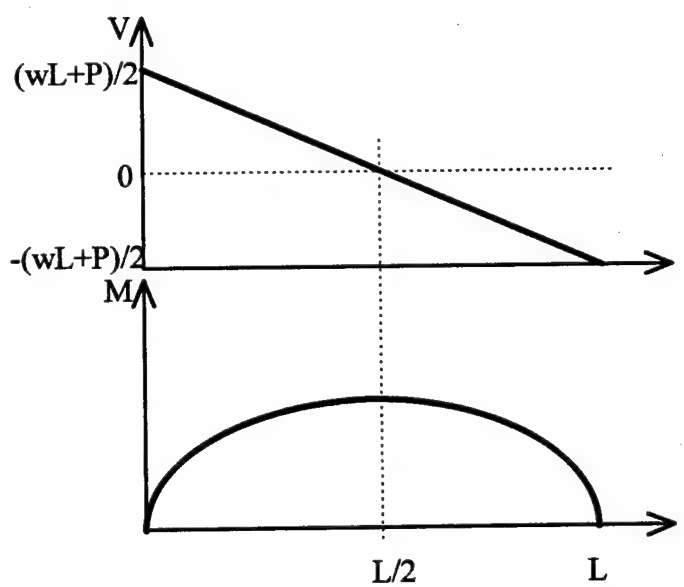

Therefore, M_{max} occurs at $\frac{dM}{dx} = 0 = V$ @ x=L/2:

$$M = \frac{w}{2}(Lx - x^2) + \frac{P}{2}(L - x)$$

$$M_{max} = \frac{w}{2}(L(\frac{L}{2}) - (\frac{L}{2})^2) + \frac{P}{2}(L - (\frac{L}{2}))$$

$$M_{max} = \frac{wL^2}{8} + \frac{PL}{4}$$

Derive the elastic curve using:

$$V(x) = EI\frac{d^3v}{dx^3}$$

$$M(x) = EI\frac{d^2v}{dx^2}$$

$$\theta(x) = \frac{dv}{dx}; \quad \rho(x) = \frac{EI}{M(x)}$$

<u>Prior to L/2</u>:

$$M = EI\frac{d^2v}{dx^2} = \frac{w}{2}(Lx - x^2) + \frac{P}{2}x$$

$$EI\frac{dv}{dx} = \frac{w}{2}(L\frac{x^2}{2} - \frac{x^3}{3}) + \frac{P}{4}x^2 + c_1 \qquad (1)$$

$$EIv = \frac{w}{2}(L\frac{x^3}{6} - \frac{x^4}{12}) + \frac{P}{12}x^3 + c_1x + c_2 \qquad (2)$$

<u>After L/2</u>:

$$M = EI\frac{d^2v}{dx^2} = \frac{w}{2}(Lx - x^2) + \frac{P}{2}(L - x)$$

$$EI\frac{dv}{dx} = \frac{w}{2}(\frac{Lx^2}{2} - \frac{x^3}{3}) + \frac{P}{2}(Lx - \frac{x^2}{2}) + c_3 \qquad (3)$$

$$EIv = \frac{w}{2}(\frac{Lx^3}{6} - \frac{x^4}{12}) + \frac{P}{2}(\frac{Lx^2}{2} - \frac{x^3}{6}) + c_3x + c_4 \qquad (4)$$

Find integration constants by applying boundary conditions (no deflection at the endpoints):

@ x=0 on the interval x<L/2, v=0
@ x=L on the interval x>L/2, v=0

and, continuity conditions:

@ x=L/2, v=v on both intervals and dv/dx=dv/dx on both intervals

1. @ x=0 on the interval x<L/2, v=0:

Equation (2) gives c_2=0.

2. @ x=L on the interval x>L/2, v=0:

Equation (4) gives:

$$0 = \frac{w}{2}(\frac{L(L)^3}{6} - \frac{L^4}{12}) + \frac{P}{2}(\frac{L(L)^2}{2} - \frac{L^3}{6}) + c_3L + c_4$$

$$c_3 = -\frac{c_4}{L} - \frac{WL^3}{24} - \frac{PL^2}{6} \qquad (5)$$

3. @ x=L/2, dv/dx=dv/dx:

Equations (1) and (3) give:

$$\frac{w}{2}(L\frac{x^2}{2}-\frac{x^3}{3})+\frac{P}{4}x^2+c_1=\frac{w}{2}(\frac{Lx^2}{2}-\frac{x^3}{3})+\frac{P}{2}(Lx-\frac{x^2}{2})+c_3$$

$$\frac{Px^2}{2}+c_1=\frac{PLx}{2}+c_3 \;\; ; \;\; \text{at } x=L/2;$$

$$\frac{PL^2}{8}+c_1=\frac{PL^2}{4}+c_3$$

$$c_1=\frac{PL^2}{8}+c_3 \qquad (6)$$

4. @ x=L/2, v=v:

Equations (2) and (4) give:

$$\frac{w}{2}(L\frac{x^3}{6}-\frac{x^4}{12})+\frac{P}{12}x^3+c_1x+c_2=\frac{w}{2}(\frac{Lx^3}{6}-\frac{x^4}{12})+\frac{P}{2}(\frac{Lx^2}{2}-\frac{x^3}{6})+c_3x+c_4$$

$$\frac{Px^3}{6}+c_1x=\frac{PLx^2}{4}+c_3x+c_4 \;\; ; \;\; \text{at } x=L/2;$$

$$\frac{PL^3}{48}+c_1\frac{L}{2}=\frac{PL^3}{16}+c_3\frac{L}{2}+c_4$$

$$c_4=\frac{PL^3}{48}+c_1\frac{L}{2}-\frac{PL^3}{16}-c_3\frac{L}{2} \;\; ; \;\; \text{substitute Equation (6) here;}$$

$$c_4=\frac{PL^3}{48}+(\frac{PL^2}{8}+c_3)\frac{L}{2}-\frac{PL^3}{16}-c_3\frac{L}{2}$$

$$\therefore \;\; c_4=\frac{PL^3}{48}$$

From Equation (5) above:

$$c_3=-\frac{c_4}{L}-\frac{wL^3}{24}-\frac{PL^2}{6}$$

$$c_3=-\frac{PL^2}{48}-\frac{wL^3}{24}-\frac{PL^2}{6}$$

$$\therefore \;\; c_3=-\frac{L^2(9P+2wL)}{48}$$

From Equation (6) above:

$$c_1 = \frac{PL^2}{8} + c_3$$

$$c_1 = \frac{PL^2}{8} - \frac{L^2(9P + 2wL)}{48}$$

$$\therefore \quad c_1 = -\frac{L^2(3P + 2wL)}{48}$$

Therefore, from Equation (2), v_{max} can be determined:

$$EIv = \frac{w}{2}(L\frac{x^3}{6} - \frac{x^4}{12}) + \frac{P}{12}x^3 + c_1x + c_2 \quad ; \; v_{max} \text{ occurs at } x = L/2;$$

$$EIv_{max} = \frac{w}{2}(L\frac{(L/2)^3}{6} - \frac{(L/2)^4}{12}) + \frac{P}{12}(L/2)^3 + (c_1)(L/2) + (0)$$

$$v_{max} = -\frac{L^3(8P + 5wL)}{384EI} \tag{7}$$

Equation (7) serves as the basis for experiments to determine the EI of the elongation zone of the maize root. A specific center load (P) and specimen length (L) is chosen. Fulcrums are mounted on a microscope slide at L distance apart and the center load is applied to all specimens placed onto the fulcrums under a vertical microscope stage. A graduated reticle is used to measure the vertical deflection of the root at the centerpoint. The flexural rigidity of the root is calculated using Equation (7).

APPENDIX V - DERIVATION OF CURVATURE DUE TO DIFFERENTIAL EXPANSION

Let,

- u - upper layer subscript and initial length of upper layer
- ℓ - lower layer subscript and initial length of lower layer
- d - distance between layers
- S - length ($=r\theta$)
- r - radius of curvature
- θ - angle of tangent line to surface
- ΔL - change in length

Initially,

$$S_u = S_\ell$$

$$\theta_u = \theta_\ell = 0 \text{ rad}$$

A change in length occurs on the upper side, but θ_u must remain equal to θ_l :

$$\theta_u = \theta_\ell$$

$$\frac{S_u}{r_u} = \theta_\ell$$

$$\frac{u + \Delta L}{r_u} = \theta_\ell$$

For the upper and lower side to subtend the same angle, their radii of curvature must only differ by d; $r_u = r_\ell + d$.

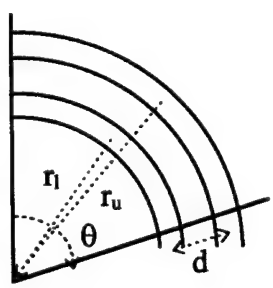

Therefore, completing the derivation:

$$\frac{u+\Delta L}{r_u} = \theta_\ell$$

$$\frac{u+\Delta L}{r_l + d} = \theta_\ell$$

$$\frac{u+\Delta L}{\frac{\ell}{\theta_\ell} + d} = \theta_\ell$$

$$\frac{\theta_l(u+\Delta L)}{\ell + \theta_l d} = \theta_\ell$$

$$\theta_\ell(u+\Delta L) = \theta_\ell(\theta_\ell d + \ell)$$

$$u + \Delta L = \theta_\ell d + \ell \quad ; \text{ but } u = \ell$$

$$\therefore \quad \theta \equiv \theta_u = \theta_\ell = \frac{\Delta L}{d} \qquad (1)$$

APPENDIX VI - MATLAB DIFFERENTIAL GROWTH AND RELEL SCRIPT FILES

VI.1 GROWTH.M

```
% Growth.m script file
%   This M-file simulates the growth and bending of a root undergoing the elongation
% parameters programmed into the RELEL.M file.  Based on that elongation data, a root
% of provided length and diameter is "grown" in finite-element fashion over a provided
% time period, length increment, and cirumferential increment.
%
% Internal units are consistently:
%                 for time - minutes
%                for angles - radians
% output angles(text and graphs) - degrees
%               for distance - mm
%
% Minor internal variables include:
%      root_length - the initial length of root
%      s_incr      - elemental lengths that the root length is divided into
%      d           - diameter of root
%      theta0      - initial angle of root to vertical
%      theta1      - angle of gravitstimulation
%      t_final     - total simulation time (initial time always zero)
%      t_incr      - time increment/calculation step size
%      t_stim      - time until gravistimulation occurs
%      plot_incr   - number of time increments until a simulation plot is drawn
%      c_incr      - angle increments around circumference (allows future expansion to 3D)
%      num_time    - number of time frames in simulation
%      numsegs     - number of elements in root's length
%      s           - vector containing distance of length element from base
%      angle       - vector containing circumferential element's angular position
%      c           - vector containing cumulative circumferential distance corresponding with angle
% The following variables share the same structure.  Columns correspond contain data
%  during each progressive time frame while rows contain data for each progressive
%  element along the root length.
%      root_s      - length of elements and growth rate in format:
%              length,element#1,upper/right side,time#1     time#2     etc.
%              length,element#2,lower/left side,time#1      time#2     etc.
%              rate,element#1,upper/right side,time#1       time#2     etc.
%              rate,element#2,lower/left side,time#1        time#2     etc.
%                      etc.                    etc.    etc.
%              rate,final element,lower/left side,time#1     etc.     etc.
%
%      root_x      -  x-coordinate of element endpoints in format:
%              x-position,element#1,upper side,time#1       time#2     etc.
%              x-position,element#1,lower side,time#1       time#2     etc.
%                      etc.                    etc.    etc.
%              x-position,final element,lower side,time#1     etc.     etc.
%
%      root_y      -  same as root_x, but for y-coordinates
%
%    tot_length  - row vector with the root total length at each time frame
```

```
%    top_length  - row vector with the root top-side length at each time frame
%    bot_length  - "    "    "   " "  bottom-side "   " "   "   "
%    top_rate    - "    "    "   " "  top-side growth rate at each time frame
%    bot_rate    - "    "    "   " "  bottom-side "   "   "  "  "    "
%    grow_rate   - "    "    "   " "  total      "   "   "  "  "    "
%    tip_angle   - "    "    "   " " tip curvature angle at each time frame
%    angle_rate  - "    "    "   " "  "    "       "  rate at each time frame
%    curveloc    - "    "    "   " location of the root's maximum curvature from the tip
%    growth_data - matrix with each row being the above 9 vector's
%                  This matrix is output to the text-file: "growth_data.txt"
%
% Minor variables used within calculations include:
%  c_top & c_bot       - angles of the top and bottom side of the root
%  rel_top & rel_bot   - rate of elongation of the top and bottom side elements
%  cumx_top & cumx_bot - cumulative storage of x-position for top and bottom sides
%  cumy_top & cumy_bot -   "        "    " y-position  "  "  "   "    "
%  maxcurve & maccurve_loc - temporary storage of the maximum curvature and location
%  init_angle   - initial angle for x-y coordinate processing (angle of rootbase)
%
% Required External Functions and Routines:
%  RELEL   -  contains the gravitropic perturbations to steady-state Relel parameters
%  RELEL_VERT - steady-state Relel parameters and circumnutational perturbations
%


% Begin the User-defined Parameters Section
%define the root dimensions
root_length=20; %initial length of root {mm}
d=1;          %diameter of root cylinder {mm}
theta1=pi/2;   %gravistimulation displacement angle of root{radians - vertical is 0.0}

%define the extent and step size of the calculations
t_final=420;  %final time {min}
%t_final=180;
t_incr=10;
t_stim=0;
%t_incr=10;    %time increment {min}
%t_stim=90;    %time until gravistimulation {min} MUST BE >= ZERO!!!
plot_incr=4;  %plot increment (how many time increments until a plot of result)
c_incr=10;    %angle increment around circumference {deg}
s_incr=0.5;   %length increment down length of root {mm}; MUST DIVIDE EVENLY WITH
%                                                         ROOT_LENGTH!!
% End the User-defined Parameters Section


theta0=0.0; %root initially vertical
num_time=t_final/t_incr+1; %compute the number of time slots
angle=0:c_incr*pi/180:2*pi;  %circumference of root divided into c_incr increments {rads}
s=0:s_incr:root_length;     %root length divided in elements of incremental length {mm}
numsegs=root_length/s_incr;  %number of finite elements the root's divided into
c=angle*d/2;                %cumulative circumference of the root along angle increment {mm}
```

```
%Requested RELEL functions plotted for all root length and circumference angle
%following requests display gravi-dependent perturbed RELELs
relel(s,angle,0,pi) %pre-gravistimulated time
relel(s,angle,(t_final-t_stim)/4,pi)   %1/4 time
relel(s,angle,(t_final-t_stim)/2,pi)   %1/2 time
relel(s,angle,3*(t_final-t_stim)/4,pi) %3/4 time; 4/4 time assumed same as initial time
%following requests display vertical, circumnutational RELELs
relel_vert(s,angle,0,pi)  %neutral point of circumnutation (vertical,steady-state RELEL)
relel_vert(s,angle,12,pi) %max amplitude point of circumnutation (assumes 50 min period)



%calculate and plot the root cylinder growth/curvature over time
%  given the RELEL conditions in functions 'relel' & 'relel_vert'

%first...build the root elemental length matrix
%compute for initial time
k=1;
tot_length(1,k)=root_length;top_length(1,k)=root_length;bot_length(1,k)=root_length;
grow_rate(1,k)=0.0;top_rate(1,k)=0.0;bot_rate(1,k)=0.0;
for i=s_incr:s_incr:root_length %start at base of root; i becomes distance from base
  root_s(k,1)=s_incr;
  root_s(k+1,1)=s_incr;
  %compute REL for this s_incr
  c_top=pi/2;
  c_bot=3*pi/2;
  if 0<t_stim
    rel_top=quad('relel_vert',root_length-i,root_length-i+s_incr,[],[],angle,0,c_top);
    rel_bot=quad('relel_vert',root_length-i,root_length-i+s_incr,[],[],angle,0,c_bot);
  else
    rel_top=quad('relel',root_length-i,root_length-
i+s_incr,[],[],angle,0,c_top)+quad('relel_vert',root_length-i,root_length-i+s_incr,[],[],angle,0,c_top);
    rel_bot=quad('relel',root_length-i,root_length-
i+s_incr,[],[],angle,0,c_bot)+quad('relel_vert',root_length-i,root_length-i+s_incr,[],[],angle,0,c_bot);
  end
  root_s(k+2,1)=rel_top;
  root_s(k+3,1)=rel_bot;
  k=k+4;
end
k=2;
for i=t_incr:t_incr:t_final
  root_length_adj=tot_length(1,k-1); %adjust root length with previous growth
  s_incr_adj=root_length_adj/numsegs;%adjust length increment with previous growth
  tot_length(1,k)=0.0;top_length(1,k)=0.0;bot_length(1,k)=0.0;
  kk=1;
  for j=s_incr_adj:s_incr_adj:root_length_adj %start at base of root; j becomes distance from base
    root_s(kk,k)=root_s(kk,k-1)+root_s(kk+2,k-1)*t_incr;
    root_s(kk+1,k)=root_s(kk+1,k-1)+root_s(kk+3,k-1)*t_incr;

    %Classic-RELEL definition (Erikson & Sachs, 1967)
    %temp=root_s(kk+2,k-1)*t_incr/2;
    %root_s(kk,k)=-root_s(kk,k-1)*(temp+1)/(temp-1);
    %temp=root_s(kk+3,k-1)*t_incr/2;
```

```
    %root_s(kk+1,k)=-root_s(kk+1,k-1)*(temp+1)/(temp-1);

    %Log-RELEL definition (Nelson & Evans, 1989)
    %temp=root_s(kk+2,k-1)*t_incr/s_incr_adj;
    %root_s(kk,k)=exp(temp)*root_s(kk,k-1);
    %temp=root_s(kk+3,k-1)*t_incr/s_incr_adj;
    %root_s(kk+1,k)=exp(temp)*root_s(kk+1,k-1);


    top_length(1,k)=top_length(1,k)+root_s(kk,k);
    bot_length(1,k)=bot_length(1,k)+root_s(kk+1,k);
    tot_length(1,k)=tot_length(1,k)+(root_s(kk,k)+root_s(kk+1,k))/2;
    %compute REL for this s_incr
    c_top=pi/2;
    c_bot=3*pi/2;
    if i<t_stim
      rel_top=quad('relel_vert',root_length_adj-j,root_length_adj-j+s_incr_adj,[],[],angle,i,c_top);
      rel_bot=quad('relel_vert',root_length_adj-j,root_length_adj-j+s_incr_adj,[],[],angle,i,c_bot);
    else
      rel_top=quad('relel',root_length_adj-j,root_length_adj-j+s_incr_adj,[],[],angle,i-
t_stim,c_top)+quad('relel_vert',root_length_adj-j,root_length_adj-j+s_incr_adj,[],[],angle,i,c_top);
      rel_bot=quad('relel',root_length_adj-j,root_length_adj-j+s_incr_adj,[],[],angle,i-
t_stim,c_bot)+quad('relel_vert',root_length_adj-j,root_length_adj-j+s_incr_adj,[],[],angle,i,c_bot);
    end
    root_s(kk+2,k)=rel_top;
    root_s(kk+3,k)=rel_bot;
    kk=kk+4;
  end
  top_rate(1,k)=(top_length(1,k)-top_length(1,k-1))/t_incr;
  bot_rate(1,k)=(bot_length(1,k)-bot_length(1,k-1))/t_incr;
  grow_rate(1,k)=(tot_length(1,k)-tot_length(1,k-1))/t_incr;
  k=k+1;
end


%second...build the x&y coordinate matrices based on the elemental length
if 0<t_stim
  init_angle=theta0;
else
  init_angle=theta1;
end
rootbase_x(1,1)=d/2*cos(init_angle);
rootbase_x(2,1)=-d/2*cos(init_angle);
rootbase_y(1,1)=-d/2*sin(init_angle);
rootbase_y(2,1)=d/2*sin(init_angle);
cumx_top=rootbase_x(1,1);
cumx_bot=rootbase_x(2,1);
cumy_top=rootbase_y(1,1);
cumy_bot=rootbase_y(2,1);
%compute for initial time
k=1;
tip_angle(1,k)=init_angle*180/pi;
angle_rate(1,k)=0.0;
for i=s_incr:s_incr:root_length
```

```
  root_x(k,1)=root_s(k*2-1,1)*cos(init_angle-pi/2)+cumx_top;
  root_x(k+1,1)=root_s(k*2,1)*cos(init_angle-pi/2)+cumx_bot;
  root_y(k,1)=root_s(k*2-1,1)*cos(init_angle)+cumy_top;
  root_y(k+1,1)=root_s(k*2,1)*cos(init_angle)+cumy_bot;
  cumx_top=root_x(k,1);
  cumx_bot=root_x(k+1,1);
  cumy_top=root_y(k,1);
  cumy_bot=root_y(k+1,1);
  %create root-tip by bringing the final coordinates together
  if i==root_length
    avg_x=(root_x(k,1)-root_x(k+1,1))/2;
    avg_y=(root_y(k,1)-root_y(k+1,1))/2;
    root_x(k,1)=root_x(k,1)-avg_x;
    root_x(k+1,1)=root_x(k+1,1)+avg_x;
    root_y(k,1)=root_y(k,1)-avg_y;
    root_y(k+1,1)=root_y(k+1,1)+avg_y;
  end
  k=k+2;
end
%compute for all remaining time
k=2;
for i=t_incr:t_incr:t_final
  if i<t_stim
    init_angle=theta0;
  else
    init_angle=theta1;
  end
  rootbase_x(1,k)=d/2*cos(init_angle);
  rootbase_x(2,k)=-d/2*cos(init_angle);
  rootbase_y(1,k)=-d/2*sin(init_angle);
  rootbase_y(2,k)=d/2*sin(init_angle);
  cumx_top=rootbase_x(1,k);
  cumx_bot=rootbase_x(2,k);
  cumy_top=rootbase_y(1,k);
  cumy_bot=rootbase_y(2,k);
  cum_theta=init_angle;
  kk=1;
  for j=s_incr:s_incr:root_length
    theta=cum_theta-(root_s(kk*2-1,k)-root_s(kk*2,k))/d;
    root_x(kk,k)=root_s(kk*2-1,k)*cos(theta-pi/2)+cumx_top;
    root_x(kk+1,k)=root_s(kk*2,k)*cos(theta-pi/2)+cumx_bot;
    root_y(kk,k)=root_s(kk*2-1,k)*cos(theta)+cumy_top;
    root_y(kk+1,k)=root_s(kk*2,k)*cos(theta)+cumy_bot;
    cumx_top=root_x(kk,k);
    cumx_bot=root_x(kk+1,k);
    cumy_top=root_y(kk,k);
    cumy_bot=root_y(kk+1,k);
    cum_theta=theta;
    %create root-tip by bringing the final coordinates together
    if j==root_length
      avg_x=(root_x(kk,k)-root_x(kk+1,k))/2;
      avg_y=(root_y(kk,k)-root_y(kk+1,k))/2;
      root_x(kk,k)=root_x(kk,k)-avg_x;
      root_x(kk+1,k)=root_x(kk+1,k)+avg_x;
```

```
      root_y(kk,k)=root_y(kk,k)-avg_y;
      root_y(kk+1,k)=root_y(kk+1,k)+avg_y;
    end
    kk=kk+2;
  end
  tip_angle(1,k)=cum_theta*180/pi;
  angle_rate(1,k)=(tip_angle(1,k)-tip_angle(1,k-1))/t_incr;
  k=k+1;
end
%insert the x-y coordinates for the rootbase
root_x=[rootbase_x;root_x];
root_y=[rootbase_y;root_y];

%create color table for line drawing
color(1,:)='k-';
color(2,:)='b-';
color(3,:)='g-';
color(4,:)='r-';
color(5,:)='c-';
color(6,:)='m-';
color(7,:)='y-';

%plot the x-y coordinates above for each time interval to display the differential growth
figure
k=1;
kk=1;
for i=0:plot_incr*t_incr:t_final
  plot(root_x(1:2:size(root_x,1),k),root_y(1:2:size(root_y,1),k),color(kk,:))
  axis ij
  hold on
  plot(root_x(2:2:size(root_x,1),k),root_y(2:2:size(root_y,1),k),color(kk,:))
  %axis([0 2*root_length -10*d/2 10*d/2])
  axis equal
  k=k+plot_incr;
  kk=kk+1;
  if kk>7
    kk=1;
  end
end
box off
title('Root Growth and Curvature')
xlabel('x(horizontal)-axis - (mm from base)')
ylabel('y(vertical)-axis - (mm from base)')

%Search and record the location of maximum curvature change
k=1;
for i=0:t_incr:t_final
  kk=1;
  maxcurve=0.005;
  maxcurve_loc=numsegs*4-3;
  for j=s_incr:s_incr:root_length
    if abs(root_s(kk,k)-root_s(kk+1,k))>maxcurve
      maxcurve=abs(root_s(kk,k)-root_s(kk+1,k));
      maxcurve_loc=kk;
```

```
    end
    kk=kk+4;
  end
  curveloc(1,k)=(sum(root_s(numsegs*4-3:-4:maxcurve_loc+1,k))+sum(root_s(numsegs*4-2:-
4:maxcurve_loc+1,k)))/2+(root_s(maxcurve_loc,k)+root_s(maxcurve_loc+1,k))/4;
  k=k+1;
end


%Save the growth data
growth_data=[tot_length;top_length;bot_length;top_rate;bot_rate;grow_rate;tip_angle;angle_rate;cur
veloc];
save('Growth_data.txt','growth_data','-ascii')

%Plot the top- and bottom-side growth rates
figure
plot(t_incr:t_incr:t_final,top_rate(1,2:num_time)*60,'k')
hold on
plot(t_incr:t_incr:t_final,bot_rate(1,2:num_time)*60,'b:')
title('Elongation Rates over Time')
xlabel('Time - (min)')
ylabel('Elongation Rate - (mm/hr)')
legend('Top','Bottom')

%Plot the tip angle from vertical
figure
Haxis=axes;
plot(0:t_incr:t_final,tip_angle(1,1:num_time),'g-')
set(Haxis,'YAxisLocation','right')
title('Root Angle')
xlabel('Time - (min)')
ylabel('Root Tip Angle - (deg. from vertical)')


%Produce response functions if requested
tf_flag=0;
if tf_flag==1
  %RF for tip angle
  [num,den]=prony(tip_angle,2,3);
  sysd=tf(num,den,t_incr*60);
  sysc=d2c(sysd);
  [yy,tt]=impulse(sysc,t_final*60);
  rf_angle=sysc*max(tip_angle)/max(yy);
  %RF for tip angle rate
  [num,den]=prony(angle_rate(2:num_time),2,3);
  sysd=tf(num,den,t_incr*60);
  sysc=d2c(sysd);
  [yy,tt]=impulse(sysc,t_final*60);
  rf_anglerate=sysc*max(angle_rate(2:num_time))/max(yy);
  %RF for upper- and lower-side lengths
  [num,den]=prony(top_length,2,3);
  sysd=tf(num,den,t_incr*60);
  sysc=d2c(sysd);
  [yy,tt]=impulse(sysc,t_final*60);
```

```
rf_toplength=sysc*max(top_length)/max(yy);
[num,den]=prony(bot_length,2,3);
sysd=tf(num,den,t_incr*60);
sysc=d2c(sysd);
[yy,tt]=impulse(sysc,t_final*60);
rf_botlength=sysc*max(bot_length)/max(yy);
%RF for upper- and lower-side growth rates
[num,den]=prony(top_rate(2:num_time)*60,2,3);
sysd=tf(num,den,t_incr*60);
sysc=d2c(sysd);
[yy,tt]=impulse(sysc,t_final*60);
rf_toprate=sysc*max(top_rate(2:num_time)*60)/max(yy);
[num,den]=prony(bot_rate(2:num_time)*60,2,3);
sysd=tf(num,den,t_incr*60);
sysc=d2c(sysd);
[yy,tt]=impulse(sysc,t_final*60);
rf_botrate=sysc*max(bot_rate(2:num_time)*60)/max(yy);

%plot the resulting impulse responses
impulse(rf_angle,rf_anglerate,rf_toprate,rf_botrate,t_final*60)
%save the response functions in a MAT-file
rfs=[rf_angle;rf_anglerate;rf_toplength;rf_botlength;rf_toprate;rf_botrate];
save rfs rfs

end
```

VI.2 RELEL.M

```
function y=relel(length_segs,circum_segs,time,circum_angle)
%RELEL Relative Elemental Elongation
%  relel(length_segs,circum_segs,time,circum_angle)
%        generates a vector of output values corresponding to the RELELs at
%        a given circumference angular location (circum_angle) along a length
%        section(length_segs) at a given time(time).
%Input arguments:
%  length_segs - vector of segmental distances along length of root that is of interest
%  circum_segs - vector containing the root circumference segment divisions
%                from zero to 2*pi radians.
%        time - scalar containing the specific time of interest
%  circum_angle - scalar angle {radians} designating the specific circumference
%                location(measured as an angle from front middle thru
%                top of the root) to output a 2D function of RELEL to root length vector.
%
% This function contains the RELEL parameter perturbations from vertical,steady-state
%  conditions. In order to obtain the surface plot of gravitropic RELEL, the
%  steady-state parameters must also be included for that section. These steady-state
%  parameters should be the same as those programmed into function 'RELEL_VERT'. The
%  user must enter the RELEL_max magnitude (RELEL_norm), the mean RELEL location
%  (u_norm), and the RELEL standard deviation (sigma_norm) along with the functions
%  describing how these parameters are perturbed with time and circumferential position.
%

if nargin~=4, error('Four input arguments are required.'),end


% Begin Section for Vertical, Unperturbed Root RELEL Parameters
%define the parameters of the RELEL Gaussian function for steady-state root growth
relel_norm=0.004;    %Barlow,1985 and the weighted average of Barlow,Versel,& Nelson
%relel_norm=0.0034;   %averaged Barlow and Versel data
%u_norm=4;            %Ishikawa,1991/Barlow,1985/Barlow,1989 also averaged Barlow & Versel
u_norm=3.8;          %weighted average of Barlow,Versel, & Nelson
%sigma_norm=1.5;      %Barlow,1985/Versel,1986
sigma_norm=1.4;      %weighted average of Barlow,Versel, & Nelson



% Begin Section on Gravitropic RELEL Parameter Perturbations
%define RELEL parameters as a function of circumferential distance and time after
%    gravitropic stimulation.
%1st-model: no gravitropic perturbation: u, sigma, & relel_max are constant over c
%u=u_norm;            %u as a function of c defined here {constant if no change}
%sigma=sigma_norm;    %sigma{c} defined here {constant if no change}
%relel_max=relel_norm; %relel_max{c} defined here {constant if no change}
%2nd-model: u, relel_max, and sigma dependent on c (averaged Barlow & Versel)
%        gravitropic shifts of +0.2 %/min top & -0.2 %/min bottom in max RELEL,
%        -0.7 mm top & +0.7 mm bottom in location,
%        and -0.4 mm top & +0.4 mm bottom in sigma.
%relel_max=relel_norm+0.002*sin(circum_segs);
```

```
%u=u_norm-0.7*sin(circum_segs);
%sigma=sigma_norm-0.4*sin(circum_segs);
%3rd-model: Weighted average of Barlow, Versel, and Nelson data
%           gravitropic shifts of +0.2 %/min top & -0.2 %/min bottom in max RELEL,
%           -0.5 mm top & +0.5 mm bottom in location,
%           and -0.3 mm top and +0.3 mm bottom in sigma.
%relel_max=relel_norm+0.002*sin(circum_segs);
%u=u_norm-0.5*sin(circum_segs);
%sigma=sigma_norm-0.3*sin(circum_segs);
%4th-model: relel_max, u, & sigma dependent on c AND time
%           Same weighted average data as part 3, but time-variable.
time_coef=1.8*exp(-(time/100))*sin(pi/150*time);
relel_max=relel_norm+0.002*sin(circum_segs)*time_coef;
u=u_norm-0.5*sin(circum_segs)*time_coef;
sigma=sigma_norm-0.3*sin(circum_segs)*time_coef;
%5th-model: relel_max, u, & sigma dependent on c AND time, but NOT uniformly
%           data taken from Ishikawa, 1991
%half_length=fix(length(circum_segs)/2);
%full_length=fix(length(circum_segs));
%if (time<=0)|(time>=430)
%  relel_max(1:full_length)=0.00375;
%else
%  lower=0.00375-sin(circum_segs(half_length+1:full_length))*polyval([-8.8228e-016  3.0882e-012
-2.3804e-009  7.0997e-007 -8.0518e-005  1.4192e-017],time);
%  if time<=60
%    upper(1:full_length-half_length)=0.00375;
%  else
%    upper=0.00375+sin(circum_segs(1:half_length))*polyval([-1.8807e-014  2.0571e-011 -
7.4554e-009  9.8187e-007 -3.6272e-005 -3.6685e-017],time);
%  end
%  relel_max=[upper lower];
%end
%if (time<=0)|(time>=430)
%  u(1:full_length)=4;
%else
%  upper=4+sin(circum_segs(1:half_length))*polyval([4.5117e-012 -2.9888e-009  1.0903e-007
2.1540e-004 -2.9396e-002  1.8417e-014],time);
%  lower=4-sin(circum_segs(half_length+1:full_length))*polyval([-1.4428e-011  1.2390e-008 -
2.6495e-006 -1.3694e-004  5.6932e-002 -4.8151e-014],time);
%  u=[upper lower];
%end
%if (time<=0)|(time>=430)
%  sigma(1:full_length)=1.0;
%else
%  upper=1.0+sin(circum_segs(1:half_length))*polyval([-3.0515e-012  3.1786e-009 -1.0872e-006
1.2371e-004  1.0766e-005 -6.7603e-015],time);
%  lower=1.0-sin(circum_segs(half_length+1:full_length))*polyval([-5.1003e-012  5.6871e-009 -
2.3216e-006  4.1243e-004 -2.5884e-002 -5.7131e-015],time);
%  sigma=[upper lower];
%end


if nargout==0 %just display 3D graph
  figure
```

```
[S,C]=meshgrid(length_segs,circum_segs);
%RELEL must be defined in this section as a function of S and C
%        (root length position and circumferential position). This section
%        obtains a surface plot of the RELEL perturbed by gravity.  Therefore,
%        the 'RELEL=' line must also include the steady-state parameters.
%1st-model: no gravitropic perturbation: u, sigma, & relel_max are constant over c
%RELEL=relel_max*exp(-(S-u).^2/(2*sigma^2));
%2nd-model: u, relel_max, and sigma dependent on c (averaged Barlow & Versel)
%        gravitropic shifts of +0.2 %/min top & -0.2 %/min bottom in max RELEL,
%        -0.7 mm top & +0.7 mm bottom in location,
%        and -0.4 mm top & +0.4 mm bottom in sigma.
%RELEL=(relel_norm+0.002*sin(C)).*exp(-(S-(u_norm-0.7*sin(C))).^2./(2*(sigma_norm-
%            0.4*sin(C)).^2));
%3rd-model: Weighted average of Barlow, Versel, and Nelson data
%          gravitropic shifts of +0.2 %/min top & -0.2 %/min bottom in max RELEL,
%          -0.5 mm top & +0.5 mm bottom in location,
%          and -0.3 mm top and +0.3 mm bottom in sigma.
%RELEL=(relel_norm+0.002*sin(C)).*exp(-(S-(u_norm-0.5*sin(C))).^2./(2*(sigma_norm-
%         0.3*sin(C)).^2));
%4th-model: u & relel_max dependent on c and time
%         Same weighted average data as part 3, but time-variable.
RELEL=(relel_norm+0.002*sin(C)*time_coef).*exp(-(S-(u_norm-
0.5*sin(C)*time_coef)).^2./(2*(sigma_norm-0.3*sin(C)*time_coef).^2));
%5th-model: relel_max, u, & sigma dependent on c AND time, but NOT uniformly
%          data taken from Ishikawa, 1991
%if (time<=0)|(time>=430)
% relel_max=0.00375*ones(full_length,length(length_segs));
%else
% lower=0.00375-sin(C(half_length+1:full_length,:))*polyval([-8.8228e-016  3.0882e-012 -
%              2.3804e-009  7.0997e-007 -8.0518e-005  1.4192e-017],time);
% if time<=60
%   upper=0.00375*ones(half_length,length(length_segs));
% else
%   upper=0.00375+sin(C(1:half_length,:))*polyval([-1.8807e-014  2.0571e-011 -7.4554e-009
%              9.8187e-007 -3.6272e-005 -3.6685e-017],time);
% end
% relel_max=[upper;lower];
%end
%if (time<=0)|(time>=430)
% u=4.0*ones(full_length,length(length_segs));
%else
% upper=4+sin(C(1:half_length,:))*polyval([4.5117e-012 -2.9888e-009  1.0903e-007  2.1540e-
%              004 -2.9396e-002  1.8417e-014],time);
% lower=4-sin(C(half_length+1:full_length,:))*polyval([-1.4428e-011  1.2390e-008 -2.6495e-006
%              -1.3694e-004  5.6932e-002 -4.8151e-014],time);
% u=[upper;lower];
%end
%if (time<=0)|(time>=430)
% sigma=ones(full_length,length(length_segs));
%else
% upper=1.0+sin(C(1:half_length,:))*polyval([-3.0515e-012  3.1786e-009 -1.0872e-006  1.2371e-
%              004  1.0766e-005 -6.7603e-015],time);
% lower=1.0-sin(C(half_length+1:full_length,:))*polyval([-5.1003e-012  5.6871e-009 -2.3216e-
%              006  4.1243e-004 -2.5884e-002 -5.7131e-015],time);
```

```
  %  sigma=[upper;lower];
  %end
  %RELEL=relel_max.*exp(-(S-u).^2./(2*sigma.^2));
  %
  mesh(S,C*180/pi,RELEL*100)
  colormap(hot);map=colormap;revmap=map(64:-1:1,:);colormap(revmap)
  view(-30,45)
  clear S,clear C,clear RELEL
else
  s=length_segs;
  %Y (RELEL) must be defined in this section as a function of s for a given
  %         circumferential position.  This section is evaluated by the integration
  %         routine across a elemental length segment to calculate a rate of
  %         elongation for the element.  Since, the function "RELEL_VERT" is also
  %         evaluated, the magnitude programmed into the line 'y=...' should NOT
  %         include the steady-state magnitude (RELEL_NORM) which is included in
  %         this second function call.
  %1st-model: no gravitropic perturbation: u, sigma, & relel_max are constant over c
  %y=0.0;
  %2nd-model: u, relel_max, and sigma dependent on c (averaged Barlow & Versel)
  %        gravitropic shifts of +0.2 %/min top & -0.2 %/min bottom in max RELEL,
  %        -0.7 mm top & +0.7 mm bottom in location,
  %        and -0.4 mm top & +0.4 mm bottom in sigma.
  %y=(0.002*sin(circum_angle))*exp(-(s-(u_norm-0.7*sin(circum_angle))).^2/(2*(sigma_norm-
%            0.4*sin(circum_angle)).^2));
  %3rd-model: Weighted average of Barlow, Versel, and Nelson data
  %          gravitropic shifts of +0.2 %/min top & -0.2 %/min bottom in max RELEL,
  %          -0.5 mm top & +0.5 mm bottom in location,
  %          and -0.3 mm top and +0.3 mm bottom in sigma.
  %y=(0.002*sin(circum_angle))*exp(-(s-(u_norm-0.5*sin(circum_angle))).^2/(2*(sigma_norm-
%            0.3*sin(circum_angle)).^2));
  %4th-model: u & relel_max dependent on c and time
  %         Same weighted average data as part 3, but time-variable.
  y=(0.002*sin(circum_angle)*time_coef)*exp(-(s-(u_norm-
0.5*sin(circum_angle)*time_coef)).^2/(2*(sigma_norm-0.3*sin(circum_angle)*time_coef).^2));
  %5th-model: relel_max, u, & sigma dependent on c AND time, but NOT uniformly
  %          data taken from Ishikawa, 1991
  %if (time<=0)|(time>=430)
  %  relel_max=0.00375;
  %elseif (circum_angle>pi)&(circum_angle<=2*pi)
  %  relel_max=0.00375-sin(circum_angle)*polyval([-8.8228e-016  3.0882e-012 -2.3804e-009
%            7.0997e-007 -8.0518e-005  1.4192e-017],time);
  %elseif time<=60
  %  relel_max=0.00375;
  %else
  %  relel_max=0.00375+sin(circum_angle)*polyval([-1.8807e-014  2.0571e-011 -7.4554e-009
%            9.8187e-007 -3.6272e-005 -3.6685e-017],time);
  %end
  %if (time<=0)|(time>=430)
  %  u=4;
  %elseif (circum_angle>=0)&(circum_angle<=pi)
  %  u=4+sin(circum_angle)*polyval([4.5117e-012 -2.9888e-009  1.0903e-007  2.1540e-004 -
%            2.9396e-002  1.8417e-014],time);
  %else
```

```
  %  u=4-sin(circum_angle)*polyval([-1.4428e-011  1.2390e-008 -2.6495e-006 -1.3694e-004
%          5.6932e-002 -4.8151e-014],time);
  %end
  %if (time<=0)|(time>=430)
  %  sigma=1.0;
  %elseif (circum_angle>=0)&(circum_angle<=pi)
  %  sigma=1.0+sin(circum_angle)*polyval([-3.0515e-012  3.1786e-009 -1.0872e-006  1.2371e-004
%          1.0766e-005 -6.7603e-015],time);
  %else
  %  sigma=1.0-sin(circum_angle)*polyval([-5.1003e-012  5.6871e-009 -2.3216e-006  4.1243e-004 -
%          2.5884e-002 -5.7131e-015],time);
  %end
  %y=relel_max*exp(-(s-u).^2/(2*sigma^2));
end
```

VI.3 RELEL_VERT.M

```
function y=relel_vert(length_segs,circum_segs,time,circum_angle)
%RELEL Relative Elemental Elongation
%  relel(length_segs,circum_segs,time,circum_angle)
%        generates a vector of output values corresponding to the RELELs at
%        a given circumference angular location (circum_angle) along a length
%        section(length_segs) at a given time(time).
%Input arguments:
%  length_segs - vector of segmental distances along length of root that is of interest
%  circum_segs - vector containing the root circumference segment divisions
%                from zero to 2*pi radians.
%        time - scalar containing the specific time of interest
%  circum_angle - scalar angle {radians} designating the specific circumference
%                location(measured as an angle from front middle thru
%                top of the root) to output a 2D function of RELEL to root length vector.
%
% This function contains the RELEL parameters for vertical,steady-state and circumnutational
%  perturbations. These steady-state parameters should be the same as those programmed
%  into function "RELEL".  The user must enter the RELEL_max magnitude (RELEL_norm),
%  the mean RELEL location (u_norm), and the RELEL standard deviation (sigma_norm)
%  along with the functions describing how these parameters are perturbed with
%  time and circumferential position.
%

if nargin~=4, error('Four input arguments are required.'),end


% Begin Section for Vertical, Unperturbed Root RELEL Parameters (should be same as 'RELEL' %
        function)
%define the parameters of the RELEL Gaussian function for steady-state root growth
relel_norm=0.004;    %Barlow,1985 and the weighted average of Barlow,Versel,& Nelson
%relel_norm=0.0034;   %averaged Barlow and Versel data
%u_norm=4;            %Ishikawa,1991/Barlow,1985/Barlow,1989 also averaged Barlow & Versel
u_norm=3.8;          %weighted average of Barlow,Versel, & Nelson
%sigma_norm=1.5;      %Barlow,1985/Versel,1986
sigma_norm=1.4;      %weighted average of Barlow,Versel, & Nelson



% Begin Section on Circumnutational RELEL Parameter Perturbations
%define RELEL parameters as a function of circumferential distance and time.
%1st-model: no circumnutation: u, sigma, & relel_max are constant over c and time
%relel_max=relel_norm; %relel_max{c} defined here {constant if no change}
%u=u_norm;            %u as a function of c defined here {constant if no change}
%sigma=sigma_norm;    %sigma{c} defined here {constant if no change}
%2nd-model: u, relel_max, and sigma dependent on c and time {Barlow,85 data}
%        circumnutational shifts of +0.075 %/min top & -0.075 %/min bottom in max RELEL
%        and -0.75 mm top & +0.75 mm bottom in location. Time is an undamped
%        sinusoid with a 50 minute period with initial condition of maximum
%        curvature occurring on right-side.
time_coef=sin(pi/32*time+pi/1.7);
```

```
relel_max=relel_norm+0.0012*sin(circum_segs)*time_coef;
u=u_norm-0.75*sin(circum_segs)*time_coef;
sigma=sigma_norm;


if nargout==0 %just display 3D graph
  figure
  [S,C]=meshgrid(length_segs,circum_segs);
  %
  %RELEL must be defined in this section as a function of S and C
  %        (root length position and circumferential position). This section
  %        obtains a surface plot of the steady-state RELEL perturbed only by
  %        circumnutational effects. Therefore, the 'RELEL=' line must
  %        include the steady-state parameters.
  %1st-model: no circumnutation: u, sigma, & relel_max are constant over c and time
  %RELEL=relel_max*exp(-(S-u).^2/(2*sigma^2));
  %2nd-model: u, relel_max, and sigma dependent on c and time {Barlow,85 data}
  %        circumnutational shifts of +0.075 %/min top & -0.075 %/min bottom in max RELEL
  %        and -0.75 mm top & +0.75 mm bottom in location. Time is an undamped
  %        sinusoid with a 50 minute period.
  RELEL=(relel_norm+0.0012*sin(C)*time_coef).*exp(-(S-(u_norm-
0.75*sin(C)*time_coef)).^2/(2*sigma^2));
  %
  mesh(S,C*180/pi,RELEL*100)
  colormap(hot);map=colormap;revmap=map(64:-1:1,:);colormap(revmap)
  view(-30,45)
  clear S,clear C,clear RELEL
else
  s=length_segs;
  %
  %Y (RELEL) must be defined in this section as a function of s for a given
  %         circumferential position.
  %1st-model: no circumnutation: u, sigma, & relel_max are constant over c and time
  %y=relel_max*exp(-(s-u).^2/(2*sigma^2));
  %2nd-model: u, relel_max, and sigma dependent on c and time {Barlow,85 data}
  %        circumnutational shifts of +0.075 %/min top & -0.075 %/min bottom in max RELEL
  %        and -0.75 mm top & +0.75 mm bottom in location. Time is an undamped
  %        sinusoid with a 50 minute period.
  y=(relel_norm+0.0012*sin(circum_angle)*time_coef)*exp(-(s-(u_norm-
0.75*sin(circum_angle)*time_coef)).^2/(2*sigma^2));
  %
end
```

APPENDIX VII - PASCAL SOURCE CODE FOR PROCESSING EMPIRICAL ROOT CURVATURE RESPONSES

```
Program Labresp;

Type
  MatrixDataPtr = ^MatrixData;
  MatrixData    = RECORD
                    Index    : Integer;
                    Number   : single;
                    Next,Last : MatrixDataPtr;
                  END;
  MatrixPtr     = RECORD
                    NumRows,NumCols : Integer;
                    DPtr            : MatrixDataPtr;
                    Head,Tail       : MatrixDataPtr;
                  END;
  Matrix        = ^MatrixPtr;


Var
        I, J, K, numfiles, numpoints, index  :  integer;
        filen, filed, out                    :  text;
        names  :  array[1..400] of string[14];
        group  :  array[1..400] of byte;
        rawdata, timecurve : Matrix;
        avg20, avg30, avg40 : Matrix;
        elapsedtime,deltax,deltay  :  single;
    temp1,temp2 : single;
        s : string[20];

{ ------------------------------------------------------------------------
|
|                    PROCEDURE INITIALIZEMATRIX
|
| This procedure initializes a matrix by allocating space on the heap for the
|   matrix pointer records and placing a zero in each element.
|
| Author  :  Maj Tom Yoder  USAFA/DFAS  719 495-0156   Fall 1996
|        Ref: Vallado, David. "Methods of Astrodynamics, A Computer
|              Approach."  Department of Astronautics, USAFA, 14 Mar 92.
| Inputs  :
|   M,N  - Rows and Columns of the desired matrix
|
| OutPuts :
|   A    - Matrix initialized
|
| Local Variables :
|   I,J  - indices
|   NextValue - pointer to next data value
|
| Constants:
```

```
|  None.
|
| Other Procedures:
|  None.
|
 ------------------------------------------------------------------------ }
PROCEDURE INITIALIZEMATRIX(VAR A : MATRIX;
                           M,N : INTEGER);
  VAR
    I,J : INTEGER;
    NEXTVALUE : MatrixDataPtr;

  BEGIN
    NEW(A);
    A^.NUMROWS:=M;
    A^.NUMCOLS:=N;
    A^.DPTR:=NIL;
    A^.HEAD:=NIL;
    A^.TAIL:=NIL;
    FOR I:=1 TO M DO
          BEGIN
             FOR J:=1 TO N DO
                   BEGIN
                         NEW(NEXTVALUE);
                         WITH NEXTVALUE^ DO
                            BEGIN
                                  INDEX:=(I-1)*A^.NUMCOLS+J;
                                  NUMBER:=0.0;
                                  NEXT:=NIL;
                                  LAST:=NIL;
                            END;
                         IF A^.DPTR=NIL THEN
                            BEGIN
                                  NEXTVALUE^.LAST:=NIL;
                                  A^.HEAD:=NEXTVALUE;
                            END
                            ELSE
                            BEGIN
                                  NEXTVALUE^.LAST:=A^.TAIL;
                                  A^.TAIL^.NEXT:=NEXTVALUE;
                            END;
                         A^.TAIL:=NEXTVALUE;
                         A^.TAIL^.NEXT:=NIL;
                         A^.DPTR:=NEXTVALUE;
                   END;
          END;
  END; {procedure initializematrix}


{ ------------------------------------------------------------------------
|
|                 PROCEDURE DELETEMATRIX
|
| This procedure deletes a matrix, thereby freeing up the space on the heap.
```

```
|
| Author  :  Maj Tom Yoder  USAFA/DFAS  719 495-0156   Fall 1996
|          Ref: Vallado, David. "Methods of Astrodynamics, A Computer
|                 Approach."  Department of Astronautics, USAFA, 14 Mar 92.
| Inputs  :
|   A  - matrix to be deleted
|
| OutPuts :
|
|
| Local Variables :
|   I,J  - indices
|   Temp, Next - pointers to data values
|
| Constants:
|  None.
|
| Other Procedures:
|  None.
|
 ------------------------------------------------------------------------ }
PROCEDURE DELETEMATRIX(VAR A:Matrix);

VAR
  I,J : INTEGER;
  TEMP, NEXT : MatrixDataPtr;

BEGIN
  TEMP:=A^.HEAD;
  WHILE TEMP^.NEXT<>NIL DO
    BEGIN
          NEXT:=TEMP^.NEXT;
          DISPOSE(TEMP);
          TEMP:=NEXT;
    END;
  DISPOSE(TEMP);
  DISPOSE(A);
END;  {procedure deletematrix}


{ ------------------------------------------------------------------------
|
|                    FUNCTION GETVALUE
|
| This procedure retrieves a value from the matrix record.
|
| Author  :  Maj Tom Yoder  USAFA/DFAS  719 495-0156   Fall 1996
|          Ref: Vallado, David. "Methods of Astrodynamics, A Computer
|                 Approach."  Department of Astronautics, USAFA, 14 Mar 92.
|
| Inputs  :
|   A   - Matrix
|   M   - Row of desired element
|   N   - Column of desired element
```

```
|
| OutPuts :
|   GETVALUE - Value of desired element
|
| Local Variables :
|   I,J  - indices
|
| Constants:
|  None.
|
| Other Procedures:
|  None.
|
 ------------------------------------------------------------------------ }
FUNCTION GETVALUE(VAR A : Matrix; M,N : INTEGER) : single;

 VAR
   I,J : INTEGER;

 BEGIN
   J:=(M-1)*A^.NUMCOLS+N;
   WHILE (J>A^.DPTR^.INDEX) AND (A^.DPTR^.NEXT<>NIL) DO
          A^.DPTR:=A^.DPTR^.NEXT;
   WHILE (J<A^.DPTR^.INDEX) AND (A^.DPTR^.LAST<>NIL) DO
          A^.DPTR:=A^.DPTR^.LAST;
   GETVALUE:=A^.DPTR^.NUMBER;
 END; {function getvalue}


{ ------------------------------------------------------------------------
|
|                    PROCEDURE ASSIGNVALUE
|
| This procedure places a value into the matrix record.
|
| Author  :  Maj Tom Yoder  USAFA/DFAS  719 495-0156   Fall 1996
|          Ref: Vallado, David. "Methods of Astrodynamics, A Computer
|                  Approach."  Department of Astronautics, USAFA, 14 Mar 92.
|
| Inputs  :
|   A   -  Matrix to place value in
|   M,N  -  Row and Column to place the value
|   VALUE -  Value to be placed into the matrix
|
| OutPuts :
|   A   -  Altered A matrix
|
| Local Variables :
|   Temp - value holder in order to set the matrix pointer correctly
|
| Constants:
|
|
| Other Procedures:
```

```
|   GetValue
|
 ------------------------------------------------------------------------ }
PROCEDURE ASSIGNVALUE(VAR A   : MATRIX;
                      M,N : INTEGER; VALUE : single);
  VAR
    TEMP : single;

  BEGIN
    TEMP:=GETVALUE(A,M,N);
    A^.DPTR^.NUMBER:=VALUE;
  END; {procedure assignvalue}

{-----------------------------------------------------------}


Begin {main program}
  Chdir('C:\work\phd\dissert\data\temp');
        Assign(filen,'filelist.txt');
        Reset(filen);
        numfiles:=0;

  {read in the list of file names to be processed along to their stat-group}

        While Not EOF(filen) Do
                Begin
                numfiles:=numfiles+1;
                Readln(filen,names[numfiles],group[numfiles]);
                End;
        Close(filen);
        Assign(out,'timecurv.txt');
        Rewrite(out);
        InitializeMatrix(rawdata,100,2);
        InitializeMatrix(timecurve,7000,2);
        InitializeMatrix(avg20,73,3);
        InitializeMatrix(avg30,73,3);
        InitializeMatrix(avg40,73,3);
        J:=1;

  {for each datafile, read in the raw xy coordinate data, count the number}
  {  of xy coordinates, and build the timecurve matrix which contains     }
  {  processed time,curvature information for each datafile}

        For I:=1 to numfiles Do
                Begin
                Assign(filed,names[I]);
                Reset(filed);
                K:=0;
                While Not EOF(filed) Do  {reads in the raw, x-y coordinate data}
                        Begin
                        K:=K+1;
                        Readln(filed,temp1,temp2);
                        AssignValue(rawdata,K,1,temp1);
                        AssignValue(rawdata,K,2,temp2);
```

```
                End;
            numpoints:=Round(K/3); {number of x-y coordinate data points in this file}
            Close(filed);
            AssignValue(timecurve,J,1,I);
            AssignValue(timecurve,J,2,numpoints);
            Writeln(out,names[I],' ',numpoints);
            elapsedtime:=0.0;
            For K:=1 to numpoints Do
                Begin
Writeln('Processing file# ',I,'  at datapoint# ',K,' J+K= ',J+K);
                AssignValue(timecurve,J+K,1,elapsedtime);
deltax:=GetValue(rawdata,3*K-1,1)-GetValue(rawdata,3*K-2,1);
deltay:=GetValue(rawdata,3*K-1,2)-GetValue(rawdata,3*K-2,2);
If (deltay=0.0) then
  AssignValue(timecurve,J+K,2,90.0)
  Else
  Begin
  temp1:=180/Pi*Arctan(deltax/deltay);
  AssignValue(timecurve,J+K,2,temp1);
  {simple quadrant check for roots higher than horizontal}
  If (deltay<0) then AssignValue(timecurve,J+K,2,180.0+temp1);
  End;

                Writeln(out,GetValue(timecurve,J+K,1),' ',GetValue(timecurve,J+K,2));

{Now process the stats for the three group populations}

index:=1+Round(GetValue(timecurve,J+K,1)/5);
If (group[I]=20) then
  Begin
  temp1:=GetValue(avg20,index,1);
  temp2:=GetValue(timecurve,J+K,2);
  AssignValue(avg20,index,1,temp1+temp2);  {sum of Xi's}
  temp1:=GetValue(avg20,index,2);
  AssignValue(avg20,index,2,temp1+Sqr(temp2));  {sum of squared Xi's}
  temp1:=GetValue(avg20,index,3);
  AssignValue(avg20,index,3,temp1+1);  {n}
  End
  Else
  If (group[I]=30) then
    Begin
        temp1:=GetValue(avg30,index,1);
        temp2:=GetValue(timecurve,J+K,2);
        AssignValue(avg30,index,1,temp1+temp2);  {sum of Xi's}
        temp1:=GetValue(avg30,index,2);
        AssignValue(avg30,index,2,temp1+Sqr(temp2));  {sum of squared Xi's}
        temp1:=GetValue(avg30,index,3);
        AssignValue(avg30,index,3,temp1+1);  {n}
    End
    Else
    If (group[I]=40) then
      Begin
                temp1:=GetValue(avg40,index,1);
                temp2:=GetValue(timecurve,J+K,2);
```

```
                    AssignValue(avg40,index,1,temp1+temp2);  {sum of Xi's}
                    temp1:=GetValue(avg40,index,2);
                    AssignValue(avg40,index,2,temp1+Sqr(temp2));  {sum of squared Xi's}
                    temp1:=GetValue(avg40,index,3);
                    AssignValue(avg40,index,3,temp1+1);  {n}
            End;

                        If (K<numpoints) then
elapsedtime:=elapsedtime+GetValue(rawdata,3*K,1);
                        End;
                J:=J+numpoints+1;
                End;
  Close(out);

  {Finally, print out the population group's averaged time-curve data}
  {   and statistics}

  Assign(out,'Group20.txt');
  Rewrite(out);
  Writeln(out,'    Averaged time-curvature Data for Group 20');
  Writeln(out,'Time(min)  ','Mean Curve(deg)  ',' n   ','Variance');
  For I:=1 to 73 do
    Begin
    index:=I*5-5;
    If (GetValue(avg20,I,3)<>0) then
      Begin
      Write(out,index:9,'  ',GetValue(avg20,I,1)/GetValue(avg20,I,3):10:1,'
',Round(GetValue(avg20,I,3)):3);
      If (GetValue(avg20,I,3)=1.0) then
        Writeln(out,'          -')
        Else
        Writeln(out,'  ',(GetValue(avg20,I,2)-
Sqr(GetValue(avg20,I,1))/GetValue(avg20,I,3))/(GetValue(avg20,I,3)-1):8:1);
      End;
    End;
  Close(out);
  Assign(out,'Group30.txt');
  Rewrite(out);
  Writeln(out,'    Averaged time-curvature Data for Group 30');
  Writeln(out,'Time(min)  ','Mean Curve(deg)  ',' n   ','Variance');
  For I:=1 to 73 do
    Begin
    index:=I*5-5;
    if (GetValue(avg30,I,3)<>0) then
      Begin
      Write(out,index:9,'  ',GetValue(avg30,I,1)/GetValue(avg30,I,3):10:1,'
',Round(GetValue(avg30,I,3)):3);
      If (GetValue(avg30,I,3)=1.0) then
        Writeln(out,'          -')
        Else
        Writeln(out,'  ',(GetValue(avg30,I,2)-
Sqr(GetValue(avg30,I,1))/GetValue(avg30,I,3))/(GetValue(avg30,I,3)-1):8:1);
      End;
    End;
```

```
  Close(out);
  Assign(out,'Group40.txt');
  Rewrite(out);
  Writeln(out,'    Averaged time-curvature Data for Group 40');
  Writeln(out,'Time(min)  ','Mean Curve(deg)  ',' n   ','Variance');
  For I:=1 to 73 do
     Begin
     index:=I*5-5;
     if (GetValue(avg40,I,3)<>0) then
        Begin
        Write(out,index:9,'  ',GetValue(avg40,I,1)/GetValue(avg40,I,3):10:1,'
',Round(GetValue(avg40,I,3)):3);
        If (GetValue(avg40,I,3)=1.0) then
          Writeln(out,'          -')
          Else
          Writeln(out,'  ',(GetValue(avg40,I,2)-
Sqr(GetValue(avg40,I,1))/GetValue(avg40,I,3))/(GetValue(avg40,I,3)-1):8:1);
        End;
     End;
  Close(out);

End. {program ends}
```

APPENDIX VIII - MATLAB SCRIPT FILES FOR CURVATURE RESPONSE ANALYSIS

VIII.1 CURVEFIT.M

```
% Curvefit.m script file to fit various polynomials to time response data.
%
% Required variable, timeresp, must first be loaded by executing 'timeresp' or
%     manually into nx2 matrix. Rootid must be entered for plot title.
% Output includes the best_poly vector that can be used by trans_func.m to
%     produce a transfer function approximation.

figure
format long e
x=timeresp(:,1);
y=timeresp(:,2);
subplot(2,1,1)
ylabel('Angle from Vertical - degrees')
title(rootid)
plot(x,y,'k')
hold on
grid

flag=0;
% evaluate the second order polynomial
p2=polyfit(x,y,2);
y2=polyval(p2,x);
subplot(2,1,1)
ylabel('Angle from Vertical - degrees')
title(rootid)
plot(x,y2,'b')
legend('data','2nd order fit')
resid2=y-y2;
subplot(2,1,2)
ylabel('Residuals - degrees')
xlabel('Time - minutes')
plot(x,resid2,'b')
legend('2nd order fit')
hold on
SSE2=sum(resid2.^2);        % compute sum of the square residuals...small is best fit
SSyy=sum((y-mean(y)).^2);
R2=sqrt(1-SSE2/SSyy);       % compute coefficient of determination...close to 1 is best fit
if R2 > 0.99
  flag=1;
  best_poly=y2;
  best_resid=resid2;
  best_SSE=SSE2
  best_R=R2
  disp('Best fit is 2nd order...')
end
```

```
% evaluate third order polynomial, if necessary
if flag == 0
  p3=polyfit(x,y,3);
  y3=polyval(p3,x);
  subplot(2,1,1)
  ylabel('Angle from Vertical - degrees')
  title(rootid)
  plot(x,y3,'g')
  legend('data','2nd order fit','3rd order fit')
  resid3=y-y3;
  subplot(2,1,2)
  ylabel('Residuals - degrees')
  xlabel('Time - minutes')
  plot(x,resid3,'g')
  legend('2nd order fit','3rd order fit')
  SSE3=sum(resid3.^2);   % compute sum of the square residuals...small is best fit
  R3=sqrt(1-SSE3/SSyy);  % compute coefficient of determination...close to 1 is best fit
  if R3 > 0.99
    flag=1;
    best_poly=y3;
    best_resid=resid3;
    best_SSE=SSE3
    best_R=R3
    disp('Best fit is 3rd order...')
  end
end

% evaluate fourth order polynomial, if necessary
if flag == 0
  p4=polyfit(x,y,4);
  y4=polyval(p4,x);
  subplot(2,1,1)
  ylabel('Angle from Vertical - degrees')
  title(rootid)
  plot(x,y4,'r')
  legend('data','2nd order fit','3rd order fit','4th order fit')
  resid4=y-y4;
  subplot(2,1,2)
  ylabel('Residuals - degrees')
  xlabel('Time - minutes')
  plot(x,resid4,'r')
  legend('2nd order fit','3rd order fit','4th order fit')
  SSE4=sum(resid4.^2);   % compute sum of the square residuals...small is best fit
  R4=sqrt(1-SSE4/SSyy);  % compute coefficient of determination...close to 1 is best fit
  if R4 > 0.99
    flag=1;
    best_poly=y4;
    best_resid=resid4;
    best_SSE=SSE4
    best_R=R4
    disp('Best fit is 4th order...')
  end
end
```

```
% evaluate sixth order polynomial, if necessary
if flag == 0
  p6=polyfit(x,y,6);
  y6=polyval(p6,x);
  subplot(2,1,1)
  ylabel('Angle from Vertical - degrees')
  title(rootid)
  plot(x,y6,'c')
  legend('data','2nd order fit','3rd order fit','4th order fit','6th order fit')
  resid6=y-y6;
  subplot(2,1,2)
  ylabel('Residuals - degrees')
  xlabel('Time - minutes')
  plot(x,resid6,'c')
  legend('2nd order fit','3rd order fit','4th order fit','6th order fit')
  SSE6=sum(resid6.^2);   % compute sum of the square residuals...small is best fit
  R6=sqrt(1-SSE6/SSyy);  % compute coefficient of determination...close to 1 is best fit
  if R6 > 0.99
    flag=1;
    best_poly=y6;
    best_resid=resid6;
    best_SSE=SSE6
    best_R=R6
    disp('Best fit is 6th order...')
  end
end

% evaluate eighth order polynomial, if necessary
if flag == 0
  p8=polyfit(x,y,8);
  y8=polyval(p8,x);
  subplot(2,1,1)
  ylabel('Angle from Vertical - degrees')
  title(rootid)
  plot(x,y8,'m')
  legend('data','2nd order fit','3rd order fit','4th order fit','6th order fit','8th order fit')
  resid8=y-y8;
  subplot(2,1,2)
  ylabel('Residuals - degrees')
  xlabel('Time - minutes')
  plot(x,resid8,'m')
  legend('2nd order fit','3rd order fit','4th order fit','6th order fit','8th order fit')
  SSE8=sum(resid8.^2);   % compute sum of the square residuals...small is best fit
  R8=sqrt(1-SSE8/SSyy);  % compute coefficient of determination...close to 1 is best fit
  if R8 > 0.99
    flag=1;
    best_poly=y8;
    best_resid=resid8;
    best_SSE=SSE8
    best_R=R8
    disp('Best fit is 8th order...')
  end
end
```

```
% evaluate tenth order polynomial, if necessary
if flag == 0
  p10=polyfit(x,y,10);
  y10=polyval(p10,x);
  subplot(2,1,1)
  ylabel('Angle from Vertical - degrees')
  title(rootid)
  plot(x,y10,'y')
  legend('data','2nd order fit','3rd order fit','4th order fit','6th order fit','8th order fit','10th order fit')
  resid10=y-y10;
  subplot(2,1,2)
  ylabel('Residuals - degrees')
  xlabel('Time - minutes')
  plot(x,resid10,'y')
  legend('2nd order fit','3rd order fit','4th order fit','6th order fit','8th order fit','10th order fit')
  SSE10=sum(resid10.^2);   % compute sum of the square residuals...small is best fit
  R10=sqrt(1-SSE10/SSyy);  % compute coefficient of determination...close to 1 is best fit
  if R10 > 0.99
    best_poly=y10;
    best_resid=resid10;
    best_SSE=SSE10
    best_R=R10
    disp('Best fit is 10th order...')
  else
    disp('No good fit found for this data.........')
  end
end
```

VIII.2 TRANS_FUNC.M

```
% trans_func.m script file for obtaining a guess at the TF (Transfer Function)
%            behind a timeresponse.
%
% The curve_fit.m script file must be run first (or best_poly vector manually produced)
%   to supply a polynomial vector that models the time response this script obtains
%   a TF for. Rootid must also exist to title the generated plot.

input=best_poly(1);
stepmag=input;
ss_value=best_poly(length(best_poly));
if min(best_poly)<ss_value
  % evaluated if the time response shows oscillations past the final value(zeta<1)
  [peak,index]=min(best_poly);
  Tp=x(index);
  PO=(ss_value-peak)/(input-ss_value)*100;
  zeta=-log(PO/100)/sqrt(pi^2+(log(PO/100))^2);
  Wn=pi/(Tp*sqrt(1-zeta^2));
  sigma=zeta*Wn;
  N=[(input-ss_value)*Wn^2]
  D=[1 2*sigma Wn^2]
else
  % evaluated if the time response shows no oscillations past the final value(zeta>1)
  % find the rise time, Tr, from 10% to 90% of steady state value
  ss_value10=0.10*(input-ss_value);
  ss_value90=0.90*(input-ss_value);
  flg=0;
  for ii=1:length(best_poly),
    if (flg==0) & (best_poly(ii)<=input-ss_value10)
        Tr_10=[best_poly(ii); ii];
        flg=1;
    end
    if best_poly(ii)<=(input-ss_value90)
      Tr_90=[best_poly(ii); ii];
      break
    end
  end
  Tr=x(Tr_90(2))-x(Tr_10(2));

  % find the settling time +-2% of the final value
  ss_value02=0.02*(input-ss_value);
  for ii=length(best_poly):-1:1
    if (best_poly(ii) > ss_value+ss_value02) | (best_poly(ii) < ss_value-ss_value02)
      Ts=[x(ii); ii];
      break
    end
  end

  sigma1=3.358/Tr;
  sigma2=4/Ts(1);
  N=[(input-ss_value)*sigma1*sigma2]
  D=[1 sigma1+sigma2 sigma1*sigma2]
```

```
end

% identify the LTI model under investigation
olsys=tf(N,D)
[ystep,tstep]=step(olsys,x(length(x)));

% convert the step response to gravitropic form
ystep=-ystep+stepmag;

% plot the system model response {green}
%   over the original data {black} and best poly fit {blue}
figure
plot(x,y,'k.')
hold on
plot(x,best_poly,'b-')
plot(tstep,ystep,'g-.')
title(rootid)
xlabel('Time - minutes')
ylabel('Angle from Vertical - degrees')
legend('data','best polynomial fit','2nd order transfer function')
```

VIII.3 COMPENSATE.M

```
% compensate.m compensator design script file
%
% The trans_func.m script file must be run prior to this or the open loop system (stored
%     in 'olsys' must be manually input.  Compensator values must be manually entered
%     below to analyze their impact on the overall system. The variable 'rootid' must
%     also exist to title the generated plot.


figure
% create plot of progressive matches to data
plot(x,y,'k.');
hold on
plot(tstep,ystep,'b-')
title(rootid)
xlabel('Time - minutes')
ylabel('Angle from Vertical - degrees')

% Compensator designed
G=feedback(olsys,[1],+1);
Kc=5.0e-03;
comp_num=conv([1 2.029395077178747e-01],[1 -1.894866279450010e-01]);
comp_den=conv(conv([1 -5.689829766567092e-02],[1 6.599911881000878e-02]),conv([1
4.176029314268038e-03-7.111380391334415e-02*i],[1 4.176029314268038e-
03+7.111380391334415e-02*i]));
comp=tf(Kc*comp_num,comp_den);
G_comp=series(comp,G);
% simplify the TF if needed
G_comp_ss=ss(G_comp);G_comp_ssmin=minreal(G_comp_ss);G_comp=tf(G_comp_ssmin);

clsys=feedback(G_comp,[1]);
[ycl,tcl]=step(clsys,x(length(x)));
ycl=-ycl+stepmag;
plot(tcl,ycl,'g-.')

% fast response of ionic pathway added in parallel
ionic_sys=tf(.5,[1 0.009]);
both_olsys=parallel(clsys,ionic_sys);
[yboth,tboth]=step(both_olsys,x(length(x)));
yboth=-yboth+stepmag;
plot(tboth,yboth,'r*')
legend('data **','best 2nd-order','w/compensator','ionic added')
```

VIII.4 AUTO_RESP_SPECS.M

```
% auto_resp_specs.m script file analyzes time response data for both time and frequency
%            response specifications, then saves the data in various files.
%   This script file accomplishes this analysis on several packets of time response
% data, sequentially, found in the INPUT FILE designated in the dataid=fopen( ); line of
% code below.  The format of this file must be as follows:
%      root id{typically a date & position from the growth chamber} [space] number of data points for
%                    this root
%      time1 {min} [space] root angle1 {degrees}
%      time2 {min} [space] root angle2 {degrees}
%        .          .        .
%      next root's id  [space] next root's number of time points
%      time1 {min} [space] root angle1 {degrees}
%         etc.      etc.      etc.
%
% Four output files are produced for each root identified within the INPUT FILE. Each
%   begins with the identifier found in the INPUT FILE and ends with either,
%          '_f.m', '_f.mat', '_t.m', or '_t.mat'
% Those files with '_f.m' and '_f.mat' are the script files and variable assignments
%   needed to reproduce the spectral frequency plot while those with '_t.m' and '_f.mat'
%   are needed to reproduce the time response plot for that root.
% Additionally, the file 'gravresp.txt' is produced that summarizes the time response
%   specifications for all roots analyzed within the INPUT FILE.  This file should
%   be renamed immediately (e.g. yellow_dent_specs.txt, etc.) to avoid overwriting
%   the data upon the next execution of this script.


dataid=fopen('c:\apps\science\matlab\toolbox\phd\timecurv_mrt.txt','rt');
rootid='start';
while isempty(rootid)==0
  rootid=fscanf(dataid,'%s',1);
  if isempty(rootid)==1
    break
  end
  rootnumpts=fscanf(dataid,'%2i',1);
  for timept=1:rootnumpts
    timeresp(timept,1)=fscanf(dataid,'%e',1);
    timeresp(timept,2)=fscanf(dataid,'%e',1);
  end

format long e
FID=fopen('gravresp.txt','a');
fprintf(FID,'File processed: ');
fprintf(FID,rootid);
fprintf(FID,'\n');
x=timeresp(:,1);
y=timeresp(:,2);
subplot(3,1,1)
plot(x,y,'k.')
hold on
grid
```

```
% interpolate between data using cubic spline
x_new=0:1:x(length(x));
y_new=interp1(x,y,x_new,'spline');
subplot(3,1,1)
plot(x_new,y_new,'b'),title(rootid),xlabel('Time (min)'),ylabel('Angle from vertical (deg)')


% conduct frequency analysis over entire response
Fourier=fft(y_new);
magF=abs(Fourier);
N=length(y_new);
k=0:N-1;
T=60;  % spline sample is at 1 per minute or 60 sec/sample
hertz=k*(1/(N*T));
subplot(3,1,2)
stem(hertz(1:fix(N/2)),magF(1:fix(N/2))),title('Complete Frequency
Content'),xlabel('Hz'),ylabel('|X(k)|'),grid
axis([0 1e-3 0 10000])

% conduct frequency analysis over steady state portion
transient_y_new=y_new(1:fix(length(y_new)*2/3));
steady_y_new=y_new(fix(length(y_new)/3):length(y_new)); % steady-state defined as last 3rd of
%                                                        response
steady_Fourier=fft(steady_y_new);
magF=abs(steady_Fourier);
N=length(steady_y_new);
k=0:N-1;
T=60;  % spline sample is at 1 per minute or 60 sec/sample
hertz=k*(1/(N*T));
subplot(3,1,3)
stem(hertz(1:N/2),magF(1:N/2)),title('Steady State Frequency
Content'),xlabel('Hz'),ylabel('|X(k)|'),grid
axis([0 1e-3 0 3000])
plotid=strcat(rootid,'_f');
print(plotid)
close

% response specs calculated

ss_value=mean(steady_y_new);
ss_mag=std(steady_y_new);
input=max(y_new);
type_flag=0;
if min(transient_y_new)<ss_value
  % evaluated if the time response shows oscillations past the final value(zeta<1)
  type_flag=1;
  [peak,index]=min(transient_y_new);
  Tp=x_new(index);
  PO=(ss_value-peak)/(input-ss_value)*100;
  zeta=-log(PO/100)/sqrt(pi^2+(log(PO/100))^2);
  Wn=pi/(Tp*sqrt(1-zeta^2));
  sigma=zeta*Wn;
  N=[(input-ss_value)*Wn^2];
  D=[1 2*sigma Wn^2];
```

```
else
  % evaluated if the time response shows no oscillations past the final value(zeta>1)
  % find the rise time, Tr, from 10% to 90% of steady state value
  type_flag=2;
  ss_value10=0.10*(input-ss_value);
  ss_value90=0.90*(input-ss_value);
  flg=0;
  for ii=1:length(y_new),
    if (flg==0) & (y_new(ii)<=input-ss_value10)
        Tr_10=[y_new(ii); ii];
        flg=1;
    end
    if y_new(ii)<=(input-ss_value90)
      Tr_90=[y_new(ii); ii];
      break
    end
  end
  Tr=x_new(Tr_90(2))-x_new(Tr_10(2));
  % find the settling time +-2% of the final value
  ss_value02=0.02*(input-ss_value)+ss_mag;
  for ii=length(y_new):-1:1
    if (y_new(ii) > ss_value+ss_value02) | (y_new(ii) < ss_value-ss_value02)
      Ts=[x_new(ii); ii];
      break
    end
  end

  sigma1=3.358/Tr;
  sigma2=4/Ts(1);
  N=[(input-ss_value)*sigma1*sigma2];
  D=[1 sigma1+sigma2 sigma1*sigma2];
end

% summary output of all time response specifications
fprintf('Initial angle is:      %5.1f degrees \n',input)
fprintf('Steady-state angle is:  %5.1f degrees \n',ss_value)
fprintf('Steady-state magnitude: %5.1f degrees \n',ss_mag)
fprintf(FID,'Initial angle is:      %5.1f degrees \n',input);
fprintf(FID,'Steady-state angle is:  %5.1f degrees \n',ss_value);
fprintf(FID,'Steady-state magnitude: %5.1f degrees \n',ss_mag);
if type_flag==1
  disp('Response overshoots steady-state value...')
  fprintf('Time-to-Peak is:     %5.1f minutes \n',Tp)
  fprintf('Percent Overshoot:   %5.1f percent \n',PO)
  fprintf('Damping Ratio(zeta): %5.3f \n',zeta)
  fprintf('Natural Frequency:   %g radians/min \n',Wn)
  fprintf(FID,'Time-to-Peak is:     %5.1f minutes \n',Tp);
  fprintf(FID,'Percent Overshoot:   %5.1f percent \n',PO);
  fprintf(FID,'Damping Ratio(zeta): %5.3f \n',zeta);
  fprintf(FID,'Natural Frequency:   %g radians/min \n',Wn);

 else
   if type_flag==2
     disp('Response never overshoots steady-state value...')
```

```
    fprintf('Rise Time:       %5.1f minutes \n',Tr)
    fprintf('Settling Time:   %5.1f minutes \n',Ts)
    fprintf(FID,'Rise Time:       %5.1f minutes \n',Tr);
    fprintf(FID,'Settling Time:   %5.1f minutes \n',Ts);
  else
    disp('WARNING....unidentified response type; dubious accuracy in computed specs!!!')
  end
end

fprintf(FID,'Numerator: %g   %g   %g \n',N);
fprintf(FID,'Denominator: %g   %g   %g \n',D);

% identify the LTI model under investigation
olsys=tf(N,D)
[ystep,tstep]=step(olsys,x(length(x)));

% convert the step response to gravitropic form
ystep=-ystep+input;
% plot the system model response {green}
%   over the original data {black} and cubic spline {blue}
figure
plot(x,y,'k.')
hold on
grid
plot(x_new,y_new,'b-')
plot(tstep,ystep,'g-.')
legend('data','cubic spline fit','2nd order transfer function')
title(rootid),xlabel('Time - (min)'),ylabel('Curvature - (deg)')
plotid=strcat(rootid,'_t');
print(plotid)
close

fprintf(FID,'\n \n');
fclose(FID);
clear timeresp

end %entire datafile processing while-loop
fclose(dataid);
```

APPENDIX IX - DERIVATION OF PROPER 1-D CLINOSTAT PARAMETERS FOR MAIZE ROOTS

The objective of these calculations is to determine the proper rotational speed for a maize root on a 1-D clinostat. If the clinostat is intended to produce effective weightlessness in the columella region, specifically, create conditions of effective weightlessness for the amyloplasts within the columella cells, the results of these calculations should be used in designing a clinostat experiment for a maize root. The morphological parameters required in this derivation are found in Table 1.1, Chapter 1, of this thesis. The development of these equations and a thorough discussion of the aspects of clinorotation was accomplished by Klaus *et al.* in 1998 (Klaus *et al.*, 1998). A list of the goals when designing a rotation speed on a 1-D clinostat include the following:

(1) The rotation speed should not be great enough to achieve centrifugation.

(2) Relative sedimentation distance of the particle under observation should remain within the same order as diffusive distance for an equivalent time period.

(3) For effective weightlessness, sedimentation distance should be within the radius of the particle under observation.

Determination of Maximum Rotation Rate:

When comparing the effects of centrifugation to diffusion, it is convenient to express the result as an equilibrium between diffusion and sedimentation due to accelerative forces in a isothermal environment. This equilibrium is expressed as a ratio which measures the density lapse rate between one point in the medium and

another. For example, in a vessel of colloidal particles where the acceleration is gravity, isothermal equilibrium will produce a density increase in the particles from the top to the bottom of the vessel along an exponential curve:

$$\frac{N_z}{N_0} = e^{-(V\Delta\rho a_c z/kT)}$$

where, N_z is the concentration (or density) as a function of vertical distance from the bottom (z-axis), N_0 is the standardized density, V is the volume of the vessel, $\Delta\rho$ is the difference between the particle's density and the medium it sediments within, a_c is the acceleration applied to the particle, z is the distance over which the ratio is computed, k is Boltzmann's Constant = 1.3807×10^{-23} J/^{0}K, and T is the temperature in ^{0}K. This shows that as height (z) approaches zero, the ratio approaches 1 and as height approaches infinity, the ratio approaches zero. Ratio of 1 indicates that there is no difference in the particle density across the distance, z. Ratios less than 1 indicate greater and greater particle density differences along the distance, z. For the problem of a maize root cap in a clinostat, the distance, z, is the radius of the root and the acceleration, a_c, is the applied centripetal acceleration due to spinning the root. The goal is to have a ratio as close to 1 as possible, and, in practical terms, to provide the same ratio as would be achieved in a typical microgravity environment (1×10^{-5} g's).

$$\frac{N_R}{N_0} = e^{-(V\Delta\rho a_c R/kT)} \equiv e^{-(V\Delta\rho a\omega^2 R^2/kT)}; \text{ where } a_c = \omega^2 R$$

$$\therefore \; a_c = \omega^2 R = -\ln\left(\frac{N_R}{N_0}\right)\frac{kT}{V\Delta\rho R}$$

$$\text{where } R = 1\text{mm}, \; \frac{kT}{V\Delta\rho R} = 4.1681 \times 10^{-4} \frac{\text{m}}{\text{sec}^2} \text{ at } 70^0\text{F}$$

The above equation is then analyzed at various values of N_R/N_0 and the results are below:

N_R/N_0	a (m/s2)	w (rad/sec)	w (rpm)
1	0	0	0
0.99	4.18E-06	9.53E-02	9.10E-01
0.97	1.27E-05	1.66E-01	1.58E+00
0.95	2.13E-05	2.15E-01	2.06E+00
0.93	3.02E-05	2.56E-01	2.45E+00
0.91	3.92E-05	2.92E-01	2.79E+00
0.89	4.85E-05	3.25E-01	3.10E+00
0.87	5.79E-05	3.55E-01	3.39E+00
0.85	6.76E-05	3.83E-01	3.66E+00
0.83	7.75E-05	4.10E-01	3.92E+00
0.81	8.76E-05	4.36E-01	4.17E+00
0.79	9.80E-05	4.62E-01	4.41E+00
0.77	1.09E-04	4.86E-01	4.64E+00
0.75	1.20E-04	5.10E-01	4.87E+00

It is noted that a rotation rate of up to 3.5 RPM can still keep the acclerations on the amyloplasts down in the mid-10^{-5} g range. Next, we determine if 3 RPM is fast enough to provide effective weightlessness to the amyloplasts.

Determining Minimum RPM:

The minimum RPM required is found by requiring that the sedimentation distance be equal to or less than the distance the particle moves by diffusion:

$$\langle x\rangle^2=2Dt$$

where, x is diffusion distance over a time period, t, and D is the diffusivity constant:

$$D=kT/6\pi\eta r_{amyl}$$

where, η is the viscosity of the medium the particle sediments within (cytoplasmic viscosity in this case) and r_{amyl} is the particle radius (amyloplast radius in this case). Stokes drag provides a formula for the terminal velocity of gravity-induced sedimentation, V_{sed}:

$$V_{sed} = \frac{2\Delta\rho r_{amyl}^{2} g}{9\eta}$$

where, g is the acceleration of 1 g (9.81 m/sec^2). The sedimentation distance travelled over a time period, t, is $y=(V_{sed})t$, and since this distance is the circumference of the circle the particle traces during sedimentation in a 1-D clinostat, $y=(V_{sed})t=2\pi r$. The design goal is to allow this radius of sedimentation during clinorotation to be less than or equal to the diffusive radius, $\langle x \rangle$. Letting $\langle x \rangle = r$, the relationship becomes,

$$V_{sed} = \frac{2\Delta\rho r_{amyl}^{2} g}{9\eta}$$

$$\frac{y}{t} = \quad "$$

$$\frac{2\pi r}{t} = \quad "$$

$$\frac{2\pi r}{\langle x \rangle^2 / 2D} = \quad "$$

$$\frac{4D\pi r}{r^2} = \quad " \quad ; D = \frac{kT}{6\pi\eta r_{amyl}}$$

$$\therefore \quad r = \frac{3kT}{\Delta\rho g r_{amyl}^{3}} = 0.532\,\mu m$$

The RPM required to achieve a particle sedimentation radius of 0.532 μm is $2\pi r/V_{sed}$. The V_{sed} for η=40 cp (determined from this thesis) is 6.57×10^{-8} m/sec. Therefore, the minimum RPM required is given by:

$$49.52 \ \frac{\text{sec}}{\text{rev}} \equiv 1.21 \text{ RPM}$$

This minimum RPM is found to be less than the maximum RPM, minimizing centrifugation effects. Finally, a check is made to ensure that the 3rd goal, the sedimentation distance being on the same order as the particle radius, is achieved. The sedimentation radius is found to be 0.532 μm at an RPM of 1.2 and this is approximately 1/3 the amyloplast radius (1.884 μm), therefore it appears that an RPM of approximately 1.5 RPM should produce a functional weightlessness within the maize columella cell.